



HAL
open science

Improving the lifetime prediction methodology of Li-ion batteries for electric vehicles

Marc Haber

► **To cite this version:**

Marc Haber. Improving the lifetime prediction methodology of Li-ion batteries for electric vehicles. Materials. Université Grenoble Alpes [2020-...], 2023. English. NNT : 2023GRALY002 . tel-04120919

HAL Id: tel-04120919

<https://theses.hal.science/tel-04120919v1>

Submitted on 7 Jun 2023

HAL is a multi-disciplinary open access archive for the deposit and dissemination of scientific research documents, whether they are published or not. The documents may come from teaching and research institutions in France or abroad, or from public or private research centers.

L'archive ouverte pluridisciplinaire **HAL**, est destinée au dépôt et à la diffusion de documents scientifiques de niveau recherche, publiés ou non, émanant des établissements d'enseignement et de recherche français ou étrangers, des laboratoires publics ou privés.

THÈSE

Pour obtenir le grade de

DOCTEUR DE L'UNIVERSITÉ GRENOBLE ALPES

École doctorale : PHYS - Physique

Spécialité : Physique des matériaux

Unité de recherche : Laboratoire d'Innovation pour les Technologies des Energies Nouvelles (LITEN - CEA)

Amélioration de la méthodologie de prédiction de durée de vie des batteries de véhicules électriques

Improving the lifetime prediction methodology of Li-ion batteries for electric vehicles

Présentée par :

Marc HABER

Direction de thèse :

Olivier RACCURT

Ingénieur HDR, CEA Centre de Grenoble

Directeur de thèse

Sylvie GENIES

Ingénieur HDR, Université Grenoble Alpes

Co-encadrante de thèse

Philippe AZAIS

INGENIEUR HDR, CEA

Co-encadrant de thèse

Rapporteurs :

JEAN-MICHEL VINASSA

Professeur des Universités, BORDEAUX INP

SERGE PELISSIER

Directeur de recherche, UNIVERSITE GUSTAVE EIFFEL

Thèse soutenue publiquement le **9 janvier 2023**, devant le jury composé de :

JEAN-MICHEL VINASSA

Professeur des Universités, BORDEAUX INP

Rapporteur

SERGE PELISSIER

Directeur de recherche, UNIVERSITE GUSTAVE EIFFEL

Rapporteur

DELPHINE RIU

Professeur des Universités, GRENOBLE INP

Examinatrice

PASCAL VENET

Professeur des Universités, UNIVERSITE LYON 1 - CLAUDE BERNARD

Président



*Whenever you find yourself on the side of the majority,
it is time to reform.*

Mark Twain

This page was intentionally left blank

Special Acknowledgments

The Lebanese – American writer Kahlil Gibran once said: “You are the bows from which your children as living arrows are sent forth”. This being said, I would like to thank, first and foremost, my parents, who devoted all their life to my good being and my education. Despite all the difficulties the country (Lebanon) faced and still faces, they gave no excuses, and they fought for my brother and I. Their story is a life lesson for everyone, and without their dedication, this work couldn't even exist.

I would especially like to thank my mentor, my friend, one of the best blues guitarists I've known, and also, my thesis director, Dr. Olivier RACCURT. Throughout these years, he taught me everything I need to know about the scientific method and way of thinking, the rigor, the vision, the communication (that flows always better with coffee... yes, we had a lot of coffee together), and the professionalism at work. Throughout these years, I never stopped learning from him, and I strongly believe that if everyone listened to him carefully, they'll also learn a lot.

My gratitude is addressed to Dr. Sylvie GENIES and Dr. Philippe AZAIS. I would say that I was very lucky being between the hand of these giants in the field of Li-ion batteries. They taught me the basics and the knowhow of the field, from the single ion to the electric vehicle and its usage, from the basics of the aging mechanisms to their identification and analysis. Though, what I will mainly take from them, is their passion to their job, and their lovingness to helping the others.

I would also like to thank, in particular, Alexis MARTIN, as he was the only person from the modeling team that had the team spirit in him. He never hesitated to help me in understanding the fundamentals of the mathematical modeling of Li-ion batteries, and how to make the model converge. He also never hesitated or refused to have a beer (or more). I think that has something to do with success... Cheers my friend, wishing you all the best, and looking forward to be seeing you soon, somewhere in time!

A person that was also always present to follow my work and move mountains whenever a problem occurred, is our team leader Dr. Magali REYTIER. Thank you, Magali, I've learned a lot from your textbook leadership.

From the technical point of view, I would thank Mr. Kamel Bachir ELEZAAR, Mr. Pierre BALFET, Dr. Bertrand GAULUPEAU, and, last but not least, Mr. Frédéric GAILLARD who helped me, with all his experience and solid background, to design the batteries cell holder.

Finally, a very special thanks to one of my closest friends, sort of a brother from another mother, Abdelmounaim AKCHACH. Strong and solid friendships can result out of a thesis!

Last but not least, my deepest gratitude goes to Dr. Loic SIMONIN, my close friend and by far my favorite jazz soprano saxophonist and composer, and his lovely family, whom I consider as my family in France.

This work couldn't be done without the dedication that CEA – LITEN and the UGA had towards science and innovation.

To conclude, I dedicate this work to my parents and my brother.

To you, my family

Table of Contents

SPECIAL ACKNOWLEDGMENTS	3
LIST OF ABBREVIATIONS	12
CHAPTER 1 – GENERAL INTRODUCTION	15
CHAPTER 2 – LITERATURE REVIEW AND THESIS METHODOLOGY	17
1. INTRODUCTION.....	18
2. A LI-ION BATTERY OVERVIEW: FROM THE ION TO THE AUTOMOTIVE APPLICATIONS.....	18
2.1 BATTERY CELL OPERATING PRINCIPLES.....	18
2.2 GENERATIONS OF LI-ION BATTERIES.....	19
2.3 FORM THE BATTERY ASSEMBLY TO THE PACK	20
2.4 THE AUTOMOTIVE APPLICATIONS	22
<i>2.4.1 The Battery Electric Vehicle (BEV)</i>	<i>22</i>
<i>2.4.2 Hybrid Electric vehicle (HEV)</i>	<i>22</i>
<i>2.4.3 Plug in hybrid electric vehicle (PHEV)</i>	<i>22</i>
3. LI-ION BATTERY AGING: BASIC PRINCIPLES AND ISSUES	23
3.1 BASIC PRINCIPLES	23
3.2 AGING ISSUES	24
4. LI-ION BATTERY AGING: DETECTION AND MECHANISMS.....	25
4.1 DETECTING AGING MECHANISMS.....	25
4.2 AGING MECHANISMS	27
<i>4.2.1 The Solid Electrolyte Interphase (SEI)</i>	<i>27</i>
<i>4.2.2 Li-plating.....</i>	<i>28</i>
<i>4.2.3 PE structural changes and transition metal dissolution.....</i>	<i>29</i>
<i>4.2.4 Particle cracking and fracturing</i>	<i>30</i>
<i>4.2.5 Interaction between degradation mechanisms</i>	<i>30</i>
5. LI-ION BATTERY LIFETIME ESTIMATION.....	31
5.1 ACCELERATED AGING TESTS	31

5.2	AGING MECHANISMS CONSISTENCY	32
5.3	AGING MODELING.....	33
5.4	CUMULATIVE DAMAGE APPROACH	35
5.5	INTERDEPENDENCE BETWEEN CALENDAR AND CYCLE AGING	36
6.	OBSERVATIONS.....	37
7.	THESIS GOAL AND METHODOLOGY	38
CHAPTER 3 – LI-ION BATTERIES’ STRESS FACTORS DURING ELECTRIC VEHICLES’ SERVICE LIFETIME.....		41
1.	INTRODUCTION.....	42
2.	METHODOLOGY	42
3.	RESULTS AND DISCUSSION	47
3.1	CELL TEMPERATURE	47
3.1.1	<i>Parking conditions</i>	<i>47</i>
3.1.2	<i>Driving conditions.....</i>	<i>49</i>
3.1.3	<i>Charging conditions.....</i>	<i>51</i>
3.2	ENERGY CONSUMPTION	53
3.2.1	<i>Effect of ambient temperature on energy consumption.....</i>	<i>53</i>
3.2.2	<i>Effect of trip length on energy consumption</i>	<i>55</i>
3.2.3	<i>Effect of road type and vehicle mass on energy consumption</i>	<i>56</i>
3.2.4	<i>Effect of vehicle mass on energy consumption</i>	<i>58</i>
3.3	CHARGING POWER.....	61
3.4	STATE OF CHARGE (SOC) AND DEPTH OF DISCHARGE (DOD).....	63
4.	RISK PROBABILITY NUMBER (RPN) ANALYSIS.....	66
4.1	BREAKDOWN AND DISCUSSION OF THE RPN ANALYSIS.....	67
4.1.1	<i>The BEV batteries.....</i>	<i>67</i>
4.1.2	<i>The HEV batteries</i>	<i>68</i>
4.1.3	<i>The PHEV batteries</i>	<i>68</i>
4.1.4	<i>Limitation of the RPN analysis.....</i>	<i>69</i>
5.	CONCLUSION AND PERSPECTIVE ON BATTERY TESTING.....	70

CHAPTER 4 – BATTERY ELECTRIC VEHICLE DRIVING CAMPAIGN.	73
1. INTRODUCTION	74
2. METHODOLOGY	74
2.1 VEHICLE INSTRUMENTATION AND DATA HARNESSING	74
2.2 EXPERIMENTAL PROTOCOL	75
3. RESULTS AND DISCUSSION	76
3.1 RANGE IN FUNCTION OF TEMPERATURE	77
3.2 SOC	78
3.3 CHARGING DATA	80
<i>3.3.1 The two types of charging</i>	<i>80</i>
<i>3.3.2 Charging energy</i>	<i>80</i>
3.4 DISCHARGE	81
3.5 CELL TEMPERATURE IN FUNCTION OF TRIP LENGTH	82
4. GENERAL DISCUSSION	84
5. CONCLUSION, LIMITATIONS AND PERSPECTIVES	85
CHAPTER 5 – ACCELERATED AGING PROTOCOL AND PERFORMANCE LOSS	87
1. INTRODUCTION	88
2. METHODOLOGY	88
2.1 ACCELERATED AGING PROTOCOL: A GENERAL IDEA	88
2.2 CELL IDENTITY AND APPLICATION	89
2.3 PROTOCOL PARAMETRIZATION	90
<i>2.3.1 Identification of phases</i>	<i>90</i>
<i>2.3.2 Phases parametrization</i>	<i>91</i>
<i>2.3.3 Aging protocol cycle</i>	<i>94</i>
2.4 CHECKUP PROTOCOL	95
<i>2.4.1 Performance criteria</i>	<i>96</i>
<i>2.4.2 Primary checkup</i>	<i>97</i>
<i>2.4.3 Secondary checkup</i>	<i>99</i>

2.4.4	<i>Frequency and condition of checkups</i>	103
3.	EXPERIMENTAL SETUP	104
3.1	CELL COMPRESSION	104
3.2	CELL HOLDER DESIGN.	104
3.3	TEST BENCHES AND CLIMATIC CHAMBERS	105
3.4	DATA SAMPLING AND PROCESSING	105
4.	RESULTS AND DISCUSSION: CELL-TO-CELL VARIATION	107
5.	RESULTS AND DISCUSSION: ACCELERATED AGING	109
5.1	ENERGY EVOLUTION	109
5.1.1	<i>Cal conditions</i>	110
5.1.2	<i>Cal + ST + LT Conditions</i>	111
5.1.3	<i>Cal + HT Conditions</i>	112
5.1.4	<i>A note on the difference in the coulomb capacity (Ah) and the energy value (Wh)</i>	113
5.2	WLTP RANGE EVOLUTION	114
5.2.1	<i>WLTP range value in function of the setup</i>	114
5.2.2	<i>WLTP range loss</i>	116
5.2.3	<i>WLTP range loss compared to the energy loss</i>	116
5.2.4	<i>Impact of the resistive behavior on the WLTP profile</i>	117
5.2.5	<i>Outcomes of the WLTP results and perspective</i>	119
6.	CONCLUSION AND PERSPECTIVES	120
CHAPTER 6 – IDENTIFICATION OF THE DEGRADATION MECHANISMS		
123		
1.	GENERAL METHODOLOGY	124
2.	THE ELECTRODE BALANCING AND DIAGNOSIS (EBD) TOOL	124
2.1	EBD PRINCIPALS	125
2.2	EBD ALGORITHM AND USAGE METHODOLOGY	127
2.3	EBD CALIBRATION AT BOL	128
2.4	APPLICATION AND RESULTS	131

2.4.1	<i>Aging at 25 °C</i>	132
2.4.2	<i>Aging at 45 °C</i>	132
2.5	DISCUSSION	134
2.5.1	<i>Aging mechanism consistency</i>	134
2.5.2	<i>The impact of the ST and LT on the Cal aging</i>	135
2.6	THE KEY TAKE-AWAY POINTS	137
3.	APPLICATION OF THE ‘ALAWA TOOLBOX	137
3.1	CALIBRATION OF THE ‘ALAWA TOOL	138
3.2	IDENTIFICATION OF THE FEATURES OF INTEREST (FOI)	139
3.3	AGING MODES IDENTIFICATION	140
3.3.1	<i>FOI 1 – 3.47 V – Intensity and Voltage shift</i>	141
3.3.2	<i>FOI 2 – 3.63 V – Intensity and Voltage shift</i>	142
3.3.3	<i>FOI 3 – 3.78 V – Intensity and Voltage shift</i>	143
3.3.4	<i>FOI 4 – 4.0 to 4.1 V – Area evolution</i>	144
3.4	DISCUSSION AND CONFRONTATION WITH THE EBD	145
4.	THE LIMITATIONS OF THE EBD AND THE ‘ALAWA METHODS	146
5.	POST-MORTEM: A CRUCIAL VALIDATION	146
5.1	POST-MORTEM METHODOLOGY	147
5.1.1	<i>Battery dismantling and visual inspection</i>	147
5.1.2	<i>Electrode surface analyses by SEM</i>	148
5.1.3	<i>Coin-cell experiments</i>	148
5.2	VISUAL INSPECTION	150
5.2.1	<i>Cell thickness evolution</i>	150
5.2.2	<i>The physical state of the electrodes</i>	151
5.2.3	<i>The nature of the metallic deposition</i>	154
5.3	SEM ANALYSES	155
5.3.1	<i>Scrapped vs non-scrapped region</i>	156
5.3.2	<i>Negative electrode of the SPHEV 11</i>	156

5.3.3	<i>Negative electrode SPHEV 54</i>	158
5.3.4	<i>Positive electrodes of the SPHEV 11 and the SPHEV 54</i>	160
5.3.5	<i>SEM outcomes</i>	161
5.4	DISCUSSION ON THE RESULTS OBTAINED BY THE VISUAL INSPECTION AND THE SEM	161
5.5	COIN-CELL SAMPLING	162
5.5.1	<i>Electrodes' capacity evolution: results and discussion</i>	163
5.5.2	<i>HPPC resistance calculation: results and discussion</i>	165
5.5.3	<i>Positive electrode initial potential: a significant information</i>	168
6.	CONCLUSION, DISCUSSION AND PERSPECTIVES	170
	CHAPTER 7 – PERFORMANCE AND AGING MODELING	175
1.	INTRODUCTION	176
2.	MODEL DEVELOPMENT	176
2.1	THE CONTINUUM APPROACH	176
2.2	GOVERNING PRINCIPLES	178
2.3	ASSUMPTIONS AND LIMITATIONS	181
2.4	PROBLEM RESOLUTION AND VALIDATION	183
2.4.1	<i>Solution and expected outcomes</i>	183
2.4.2	<i>Operating process and tools</i>	184
2.4.3	<i>Validation strategy</i>	185
2.5	PARAMETERS EXTRACTION	186
2.5.1	<i>Geometrical parameters</i>	186
2.5.2	<i>Electrolyte related parameters</i>	187
2.5.3	<i>Separator related parameters</i>	190
2.5.4	<i>Electrodes related parameters</i>	192
2.5.5	<i>Parameters assessment</i>	199
3.	MODEL VALIDATION	200
4.	AGING MODELING	202
4.1	GENERAL PRINCIPLES AND HYPOTHESES	202

4.2	THE PRINCIPALS OF THE SEI MODEL.....	203
4.3	PARAMETERIZATION AND METHODOLOGY	205
4.4	CALIBRATION OF THE SEI MODEL	206
4.4.1	<i>General parameters</i>	<i>206</i>
4.4.2	<i>Kinetics parameters calibration</i>	<i>207</i>
4.5	LAM_{PE} AND LAM_{NE} MODELS	208
4.6	SEI SURFACE INCREASE MODELING	210
4.7	VALIDATION OF THE FULL MODEL.....	210
5.	CONCLUSION AND PERSPECTIVES	212
	CHAPTER 8 – GENERAL CONCLUSION AND PERSPECTIVES.....	215
	SCIENTIFIC PRODUCTION.....	217
	RESUME DE LA THESE EN FRANÇAIS	218
1.	CHAPITRE 1 – INTRODUCTION	218
2.	CHAPITRE 2 – BIBLIOGRAPHIE	218
3.	CHAPITRE 3 – FACTEURS DE STRESS VUS PAR UNE BATTERIE LI-ION EN FONCTION DE L’USAGE DANS UN VEHICULE ELECTRIQUE (EV).....	219
4.	CHAPITRE 4 – CAMPAGNE DE ROULAGE SUR UN BEV.....	223
5.	CHAPITRE 5 – CAMPAGNE DE VIEILLISSEMENT ACCELERE REPRESENTATIVE.....	224
6.	CHAPITRE 6 – IDENTIFICATION DES MECANISMES DE DEGRADATION	228
7.	CHAPITRE 7 – MODELISATION DE LA PERFORMANCE ET DU VIEILLISSEMENT.....	231
8.	CONCLUSION	235
	REFERENCE LIST	236

List of abbreviations

AM	Active Material
BEV	Battery Electric Vehicle
BMS	Battery Management System
BOL	Beginning Of Life
BTMS	Battery Thermal Management System
(C)	Combined profile
C	Current rate, or C-rate, expressed in h ⁻¹
Cal	Calendar aging
CC	Constant Current
CD	Charge Depletion
CP	Constant Power
CS	Charge Sustaining
CU	Checkup
CV	Constant Voltage
DOD	Depth of Discharge
DV	Differential Voltage
EBD	Electrode Balancing and Diagnosis
EDX	Energy Dispersive X-ray
EIS	Electrochemical Impedance Spectroscopy
EOL	End Of Life
EV	Electric Vehicle
FOI	Feature Of Interest
(H)	Highway profile
HEV	Hybrid Electric Vehicle
HPPC	Hybrid Power Pulse Characterization
HT	Hybrid Trip
IC	Incremental Capacity
ICE	Internal Combustion Engine

LAM	Loss of Active Material
LIB	Li-ion Batteries
LLI	Loss of Lithium Inventory
LR	Loading Ratio (N/P)
LT	Long Trip
N/P	Ratio of negative to positive capacities
NE	Negative Electrode
NMC	Nickel Manganese Cobalt
P	Power rate, or P-rate, expressed in h ⁻¹
P2D	Pseudo 2-dimensions
PE	Positive Electrode
PHEV	Plugin Hybrid Electric Vehicle
Q	Capacity
RPN	Risk Probabilistic Number
SEI	Solid Electrolyte Interphase
SEM	Scanning Electron Microscopy
SOC	State Of Charge
SOH	State Of Health
SOL	State Of Lithiation
SPHEV	Samsung 37 Ah PHEV
ST	Short Trip
T	Temperature
(U)	Urban profile
UCC	Usable Cell Capacity
WLTP	World harmonized Light vehicle Testing procedure

This page was intentionally left blank

Chapter 1 – General introduction

Since a decade or so, a huge endeavor is being invested into reducing the impact of road transport on climate change. According to the European Environment Agency [1], the domestic transport sector represents around 30 % of the EU greenhouse gas emissions, and 60.6 % of these emissions constitutes the passengers cars' share. In other words, 18.2 % of the EU greenhouse gas emission are generated from passengers' vehicles (Figure 1).

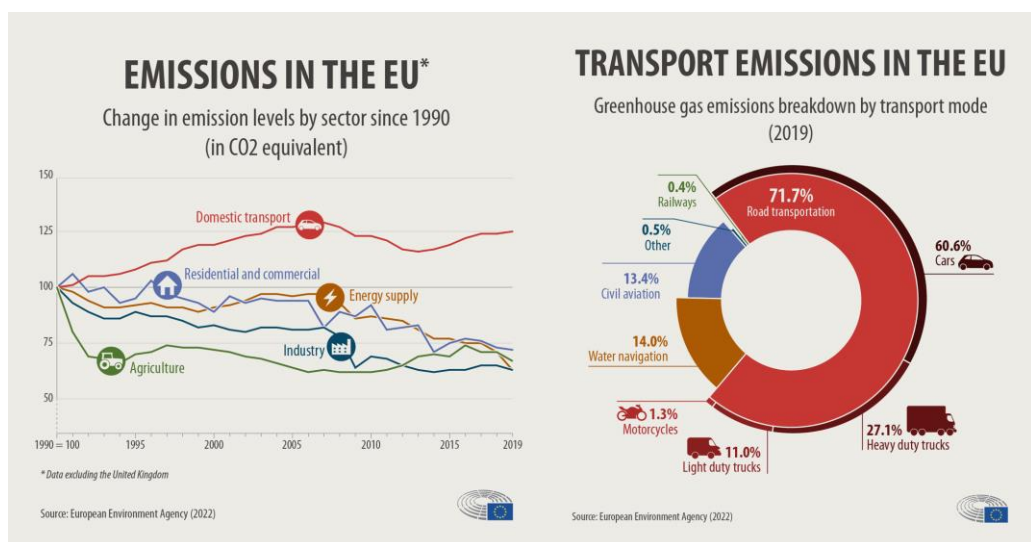


Figure 1. Numbers from the European Environment Agency concerning the EU emissions [1]

While many policies promote the use of public transportation and cycling, the vehicle remains sometimes a need. In sparsely populated areas, suburbs and rural locations, owning a car brings food to the table, education to the children and is vital during emergencies. That is also true for countries where public transport is barely developed and not reliable.

Electrifying road transport vehicles by relying on electrochemical energy storage is seen as a very favorable solution. With a quite reasonable reduction of greenhouse gas emissions from cradle-to-grave [2], Electric Vehicles (EVs) are finding their way into the market quite rapidly, leaving us with promising predictions for the next years.

As the internal combustion engine is the heart of conventional vehicles, the Li-ion battery is the heart of EVs and the key element behind their success [3]. However, the battery pack constitutes around 40% of the total vehicle price [4], [5]. Its main components' materials are scarce, bringing to the table the issues of shortages, and a further increase in its price [6], [7]. For these reasons, the matter of its durability is of utmost importance. Questions rise about warranty and battery replacement, but also about “second life” and circular economy applications.

Understanding the aging, or performance loss, of Li-ion batteries is inevitable to elucidate the answers to the these questions. However, battery aging remains a quite complicated field, and a huge amount of work is invested nowadays to try and understand it. The lack of comprehension of the aging mechanisms represents a considerable obstacle for their modeling, and thus, for the battery lifetime estimation.

The goal of the thesis is to develop a reliable methodology for the durability study of Li-ion batteries for automotive applications, in the goal of improving their aging modeling and lifetime estimation. The general idea relies on establishing the link between the durability experiments and the usage of the batteries in the field of passenger vehicles.

Chapter 2 – Literature Review and thesis methodology

A literature review is done in the purpose of investigating the existing works related to the aging and lifetime estimation methods of Li-ion batteries. This step is crucial to identify the gaps in literature, and to lay the foundation of the thesis' framework. Aging mechanisms detection, principles, and recent findings are covered. Accelerated aging tests and aging modeling technics are also reviewed. Finally the goal and the general methodology of the work are stated.

1. Introduction

Electrifying the road transport was evoked in the general introduction. It relies on the use of electrical energy storage, or a battery, designed to deliver energy for the propulsion and the auxiliary devices of the vehicle, and to last for a certain period of time. Battery based vehicles represent the leading direction towards the future of the automobile sector [8]. While road transport includes the entire range of vehicles, from the trucks to the motorcycles, the current work focuses on the passenger vehicles.

The concept of electric cars is not recent. The year 1859 saw the birth of the lead-acid batteries from the French physicist Gaston Planté. Electric Vehicles (EV) of the late 19th century were equipped with lead-acid batteries. However, the progress in this field flattened when thermal cars equipped with an Internal Combustion Engine (ICE) emerged due to the high rate of fossil fuel reservoirs findings in the 20th century [9].

Nowadays, the question of environment and fossil fuel dependency regained importance. As the Lead-acid acid batteries are very heavy and lack energy density, other technologies started emerging. Nickel Cadmium (Ni-Cd) batteries were used in the 1990s in city cars like the Peugeot 106. This technology is nowadays forbidden in the transport sector because of the toxicity of cadmium [8], [10].

The Nickel-Metal Hydride (Ni-MH) are used in today's industry for high power applications, but couldn't make their way to complete electrification of vehicles, especially due to their low capacity [8], [11].

The Li-ion battery makes its entrance in the market in 1991 with Sony [12], giving promising perspectives for its use in high energy and high power applications. It was labeled as a favorable technology also due to its vast operating temperature range, low self-discharge rate, high efficiency and long cycle life [8], [13].

2. A Li-ion battery overview: From the ion to the automotive applications

2.1 Battery cell operating principles

The principle components of a Li-ion battery are as follows. An ion-conducting electrolyte, containing a lithium conducting salt [14], fills the gap between two electrodes having a positive electric potential difference. A porous membrane, also called separator, shares the same space of the electrolyte in order to electrically isolate the electrodes from each other. The electrode is made of a current collector, an active material, binders and conductive additives.

In a nutshell, lithium ions alternate back and forth between the electrodes during charging and discharging. Concretely, they intercalate into and de-intercalate out of the active materials. This concept is called the "rocking-chair battery" and it was first

proposed by Michel Armand in the 1970's [15], and demonstrated by Lazzari and Scrosati in 1980 [16] (Figure 2).

The battery is first constructed when all the lithium ions are in the Positive Electrode (PE), therefore it is fully discharged. Charging the battery would then require to apply an external current via an outer electrical connection and pull electrons from the PE's current collector to the Negative Electrode's (NE) current collector. This imposes a driving force for the de-intercalation and migration of lithium ions from the positive active material to the negative one, passing by the electrolyte and the separator. For load delivery, electrons are released while lithium ions are de-intercalated from the negative active material and migrates to the positive one.

Concisely, the current collector of the PE is made of aluminum, and the one of the NE is made of copper (for carbon and/or silicon based electrodes). The active materials of the PE consist of lithiated metal oxides and those of the NE are generally carbon based [14]. The electrolyte is made mainly of a mixture of alkyl carbonates and one (or more) lithium salt to allow the transfer of lithium ions. Some additives are added to the electrolyte, having the purpose of improving the performance of the battery. The separator is usually made of polyethylene, or polypropylene, or layered combinations of both, with pores size in the range of 100 nm [17]. Its role is to be and remain mechanically and thermally stable to ensure safety and durability [18].

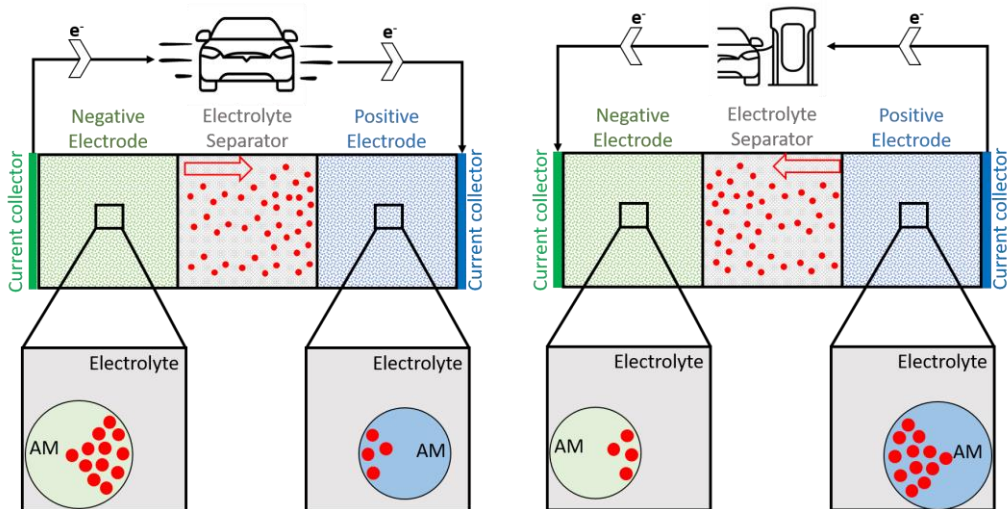


Figure 2. Illustrating the rocking chair principle, with the red dots illustrating the lithium ion. AM: Active Material

2.2 Generations of Li-ion batteries

Li-ion Batteries (LIB) are categorized with respect to their PE active material, as it is the major varying material nowadays. The NE active material is usually made of

Si-doped, or not, graphite. The first generation of LIB are made with a PE of Lithium Cobalt Oxide (LCO) and Lithium Manganese Oxide (LMO). They were followed by Lithium Iron Phosphate (LFP) and Nickel Cobalt Aluminum (NCA). NCA technology is known for its elevated power and energy density. Its reduced safety and elevated cost played against the rapid rise of this technology [10]. The generation 2a was dominated by the Nickel Manganese Cobalt (NMC) with a mass ratio of 1:1:1 (depicted as NMC 111). The NMC 532 and NMC 622 were labeled as generation 2b [19].

The generation 3a considers only nickel-rich PE (NMC 622, NMC 721 and NMC 811) with a NE of graphite with or without silicon components (less than 10% by mass). Generation 3b, scheduled for the year 2025 considers advanced technology lithium ion such as High-Voltage-Spinel (HVS) and High-Energy-NMC for the cathode with a Si-doped graphite. Generation 4 considers all-solid-state batteries. Finally, lithium air and the lithium-sulfur technology is kept for generation 5 [19].

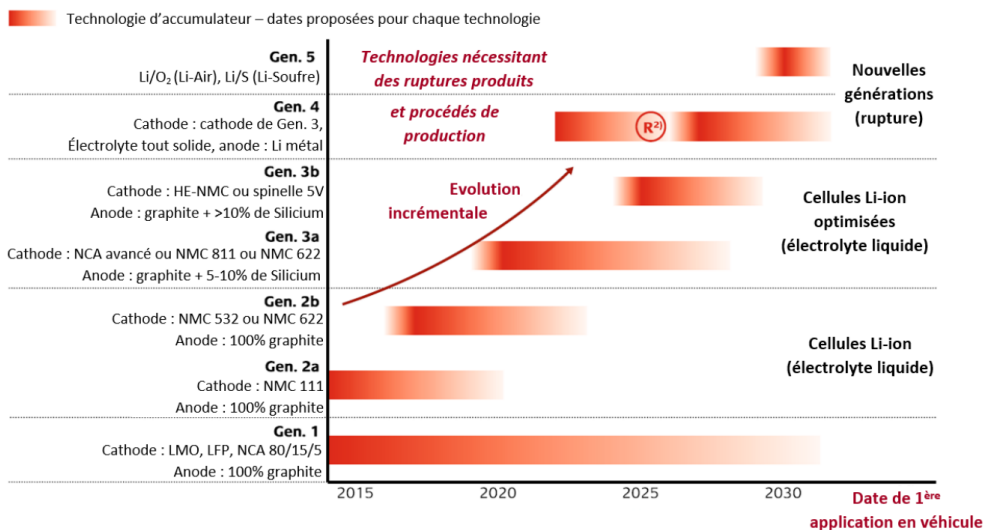


Figure 3. Battery generations listed with their cathode and anode material in function of their date of first application in vehicles [20]

2.3 Form the battery assembly to the pack

Another way to categorize LIB, is based on their different designs: the cylindrical, prismatic and pouch cells. Even if their core components can be very similar, their manufacturing processes differ [21].

After receiving the electrodes, the separator and the electrolyte from the manufacturing sector, the next step consists of assembling the parts into one of the three shapes aforementioned. The assembling process is divided into cutting, compound assembly, and packaging.

The pouch cell assembly consists of a stacking of single sheets electrodes. Electrodes are first cut, before being stacked together. Concerning the other designs, the electrodes and the separator material are coiled together inside the casing, either in a round winding (cylindrical cells) or in a flat winding (prismatic cells) [21], and cut afterwards.

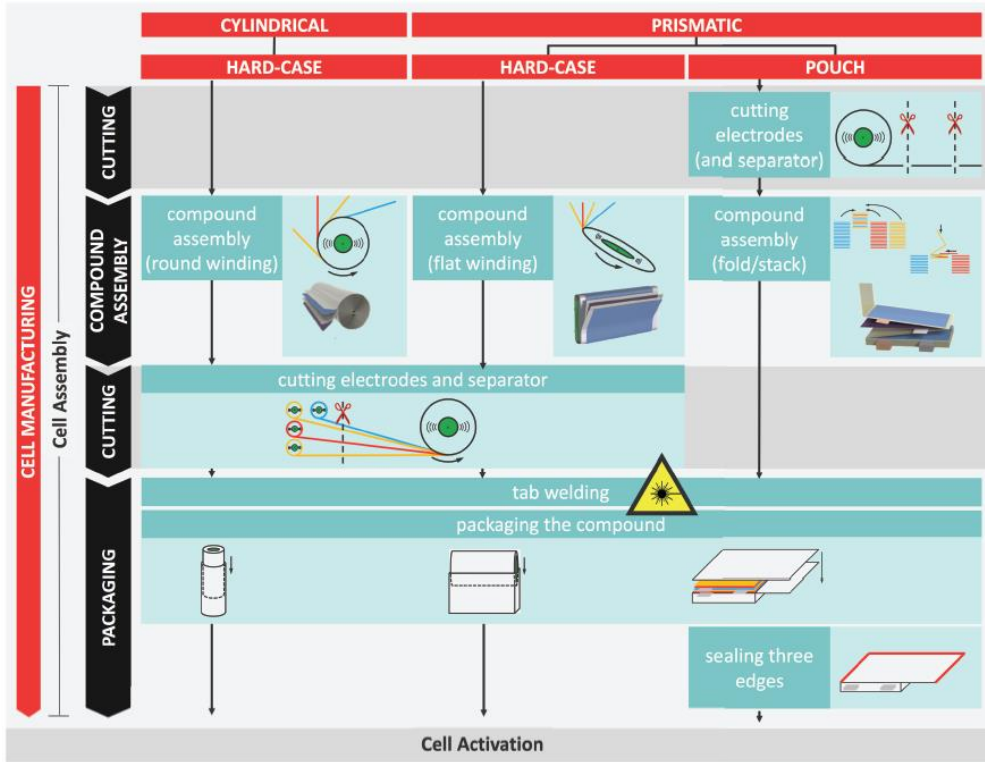


Figure 4. Overview of the assembling process of the three different shapes [21]

Usually those cells are connected together in series to form a module. A battery pack contains different modules connected in a series-parallel configuration, depending on the capacity and voltage of the single cell, and the demanded energy from the pack. Recently, the cell-to-pack architectures are being commercially proposed [22].

The battery pack is equipped with a Battery Management System (BMS), used for controlling and managing the electrical and thermal features of the battery system. Concretely, it balances the cell voltages, it manages the energy delivered (acceleration) or regenerated (braking), and it ensures the cells find themselves at their optimal working temperature for performance and safety purposes [13], [23]. It also provides communication between the battery system and the other vehicle devices such as the 12 V units (e.g. cabin heating/cooling) [14], [24].

2.4 The automotive applications

Three big families of EV exist, and each one uses the battery pack in a different fashion, hence exposing it to different operational conditions.

2.4.1 The Battery Electric Vehicle (BEV)

The BEVs, also known as the all-electric vehicles, are facing a rapid market propagation process [25]. Classified as the electrical homologue of conventional ICE vehicles, they use high energy Li-ion batteries as their energy source [24]. Besides being quieter than the ICE, the electric motor provides a much better driving efficiency (tank to wheel) [26] and an emission-free operation.

During its entire service life, the battery pack is in charge of delivering power for the three sub-systems of the drive train: the electric propulsion system, the BMS, the thermal management unit and the auxiliary system [24], [27].

With an elevated electric range (337 km in average, in November 2022 [28]), the BEVs are known for embarking the biggest battery (66 kWh in average, in November 2022 [28]) with high energy battery cells. With its big volume, the battery pack is located commonly in the lower part of the car, under the passengers seats.

2.4.2 Hybrid Electric vehicle (HEV)

The HEV seems to be the a very attractive design combining high power lithium ion batteries in an ICE/Electric Engine configuration, in order to reach a significant CO₂ decrease ratio. The battery in this vehicle is required to support the ICE during heavy loads such as in highways or in uphill roads, or even for cabin and pack thermalization. Different “levels” of hybridization exist, ranging from the micro to the full hybrid technologies [29]. With a small energy capacity of 1 to 4 kWh, the battery is constantly charging, with the help of the ICE and the regenerative braking process, and discharging when needed. Oppositely to the BEV, the battery does not need a charging unit. In order to withstand this continuous charge and discharge with a low capacity, the battery is designed for high power solicitations.

In terms of operating configuration, the wheels are directly linked to a transaxle, which is mechanically coupled to an ICE [30]. The ICE is mechanically combined to an electrical motor-generator via a belt-integrated starter generator (BISG), establishing a bi-directional energy transfer path between the wheels and the battery, which will open the way for its charging and discharging. While the electrical motor and the ICE are both located under the front hood of the vehicle, the battery pack is positioned in back of the car in order to prevent its exposure to high temperature caused by the motors [30].

2.4.3 Plug in hybrid electric vehicle (PHEV)

Considered as an alternative to the previously mentioned types, PHEVs have an electric motor fed by a Li-ion battery pack, and set in a parallel or series with an ICE

powered by a liquid fuel [31], [32]. PHEVs are known for two kinds of operating strategies. The first, called Charge Depleting (CD) mode, is similar to the operation of a BEV. The vehicle relies solely on electric power until the battery is partially depleted, providing full electrical autonomy for a certain distance. During this operating mode, the battery is charged either from an outside electric power source when parked, or through regenerative braking [31]. When a small amount of energy is remained in the battery, the second operating strategy, known as the Charge Sustaining (CS) mode, is automatically deployed. This strategy consists of running the car very similarly to an HEV. It relies mainly on the ICE to drive the vehicle [32] and uses the remaining energy of the battery for assistance.

PHEVs are classified and marketed based on their range. PHEV-20 have an electric range of 20 miles (32 km), the PHEV-40 have an electric range of 40 miles (64 km) and so on.

3. Li-ion battery aging: basic principles and issues

Indeed, the Li-ion technology is nowadays mature and commercially utilized in all its forms and chemistries in a wide range of automotive applications. Nevertheless, this technology faces aging issues, bringing to the table one of its main limitations [33].

3.1 Basic principles

Aging is defined by the loss of performance with time. Degradation processes, triggered and/or intensified by environmental and working conditions, tend to happen within the battery, deteriorating its main functionality. Conditions triggering and accelerating the aging of the battery are referred to as “stress factors”.

A battery starts aging as soon as it is assembled. When disconnected, it suffers from what is commonly referred to as “calendar aging”, e.g. when the vehicle is parked and tuned off. Two stress factors affect the life of the battery in such cases: its temperature and its State of Charge (SOC). The SOC refers to the ratio of the residual capacity to its maximum available capacity [34]. The higher the temperature, the faster the aging. The same can be said for the SOC level.

When the battery is charging or discharging, “cycling aging” occurs. The associated stress factors are the power rates that travels through the battery, its Depth Of Discharge (DOD), as well as its temperature and SOC window. The DOD refers to the energy throughput during a charge or discharge step. The higher these stresses, the faster the aging. Oppositely to calendar aging, here low temperature accelerates the aging.

The state of health (SOH) of the battery is the indicator of its condition. It is the ratio of the performance criteria value at its Beginning Of Life (BOL) to the performance criteria value at time t . When the SOH reaches a certain value (e.g. 80 %), the battery is considered to have attained its End Of Life (EOL) in a vehicle. It is either

transferred to its usage in a secondary application or recycled, and replaced by a newer battery.

3.2 Aging issues

The first issue resides in the cost of the battery pack, constituting nowadays around 40 % of the vehicle price [4], [5]. Concerns about pack replacement, warranty and pack-rental, decrease the attractiveness of the technology, leading to an economical obstacle for the evolution of EVs [14]. When warranty claims occur, customer satisfaction fails. One of the most important characteristic for the electric mobility to be successful is the customer satisfaction [14].

A concrete example is illustrated in Figure 5. 6,300 data points of SOH were retrieved from Geotab [35] for Tesla Model 3 and Nissan LEAF vehicles, both models being BEVs. The red arrow represents the warranty duration set at 8 years for these two vehicles.

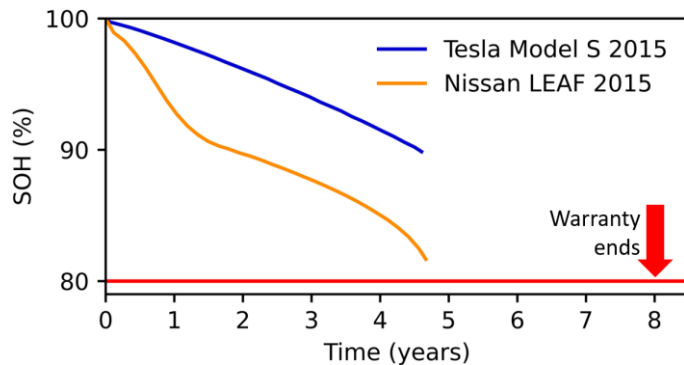


Figure 5. 6,300 data points illustrating the SOH evolution of the Tesla Model S 2015 and the Nissan LEAF 2015 [35]

The decrease rate in SOH is completely different for both vehicles. The usage conditions (SOC limitations, thermal management, discharged power rates etc.) and the battery chemistry have both a role to play in this decrease. This figure illustrates the issue of warranty, especially for the Nissan Leaf. A bad understanding of aging leads to bad estimations of the EOL, which is followed by a significant economic loss and a customer satisfaction problems.

The reuse of the battery in secondary applications (e.g. ESS (Energy Storage System), UPS (Uninterrupted Power Supply) etc.) rises some concerns. A good understanding of the battery aging and battery SOH is crucial to specify when and how the battery should be reused. This is also vital to ensure a long and safe secondary use. Operative limitations need to be reconditioned properly for the resulting application.

Comprehending battery aging is vital to surpass the economical obstacle, and guarantee a safe and long circular economy.

4. Li-ion battery aging: detection and mechanisms

For the reasons mentioned in the previous subsection, the aging mechanisms of Li-ion batteries are widely studied in literature [33], [36]–[43]. The purpose of the first subsection is to elaborate the aging mechanisms detection methods.

The second subsection focuses on the main aging mechanisms, and underlines the recent advancement in the understanding of each one of them. A focus is given on the impact these mechanisms have on the performance criteria.

It should be noted that the common performance criteria are the capacity (Ah) and the power (W), illustrated by the increase in internal resistance (Ohm, Ω). The EOL is reached either when the capacity reaches 80% of its initial value, or when the power capability attains 70 to 80% of its initial value (i.e. the resistance increased by 30 %) [14], [34].

Commonly, the capacity is obtained by integrating the applied current over the duration of a discharge or charge process, within the voltage limitation of the cell. The resistance is measured using the Ohm's law following a current or power pulse. Such measurements are usually based on methodologies described in standards [14], [44]–[48].

4.1 Detecting aging mechanisms

Two ways exist to detect the aging mechanisms of a Li-ion battery: the invasive or the non-invasive method.

Invasive methods. Also referred to as post-mortem analyses, these methods consists of dismantling the battery cell to access its core elements. Experiments are then performed and they range from simple weighing of the electrodes, to electrochemical tests, in depth microscopy and gas analyses. They were reviewed in details by [40].

Electrochemical tests consist of taking samples of the electrodes and the separator, along with samples of the electrolyte, and assemble them together in a coin cells or small format pouch cells. These are then connected to battery testing benches (galvanostats or potentiostats) to perform electrochemical tests. For example, analyzing results of the Electrochemical Impedance Spectroscopy (EIS) of a coin cell made of the aged NE vs Li metal, can help in identifying a slower kinetics within the NE, hinting at the thickening of a solid layer on the electrode surface (which is referred to as Solid Electrolyte Interphase (SEI)) [49].

Microscopy technics lie in the in-depth analysis of the electrodes surface either by surface sensitive methods (such as Scanning Electron Microscopy (SEM) or Energy

Dispersive X-ray (EDX) spectroscopy) or surface non-sensitive methods (such as X-ray diffraction (XRD)).

For example, in order to visualize cracks in the bulk of the NE [50] and the PE [51], SEM is performed on the aged electrodes of the mentioned publications. Transmission X-ray Microscopy (TXM) can be performed to identify some cracks within the particle itself [52].

Gas Chromatography-Mass Spectroscopy (GC-MS) can also be done on the electrolyte of the aged battery to identify products of side reactions for example [53].

Non-invasive methods. Non-invasive methods are also quite abundant, ranging from simple voltage and resistance measurements, to advance in-situ operando technics. They are exhaustively elaborated in these reviews [54], [55]. The focus here is made on the so called Electrochemical Voltage Spectroscopy (EVS) tests, as they are used in the further parts of this work.

EVS testing rely on the voltage response of the cell with aging during a certain solicitation (charge or discharge). The electrodes' potential are usually balanced at the BOL. With aging, they become unbalanced and the voltage response changes. Tracking the change in the voltage response hints at the cell's thermodynamic state, giving consequences of the aging mechanisms.

Voltage changes are in the order of mV, therefore very difficult to identify on a simple voltage vs capacity curve (with a span in the order of 2 V). Derivatives are then necessary to visualize clearly these changes.

The incremental capacity (IC) curve requires to plot the derivative of capacity (Q) with respect to the voltage (V) of the cell during a charge/discharge process, i.e. dQ/dV versus V. The peak and valley signature of this plot refers at the intercalation and de-intercalation stages of the material. This concept started to appear in the early 2000s [56] and was then developed by the works of Dubarry [57]–[60]. IC signature changes can then provide information about the Loss of Lithium Inventory (LLI) and the Loss in Active Material of both the PE (LAM_{pe}) and the NE (LAM_{ne}).

Oppositely to the IC curve, the differential voltage (DV) curve requires to plot the dV/dQ versus Q. Theoretically, both the IC and DV should provide the same information. However, practically, slight differences exist between these two technics.

First, IC curve is plotted in function of the voltage value, fixed for the entire aging process (e.g. always ranging from 3 to 4.2 V). The DV is plotted in function of the capacity, which is obviously variable with aging, making it less practical for comparisons. Second, the DV curve resemble to a huge “U” curve, where the signatures lie in the center region. A zoom in should then be applied to study the changes in the signature of the curve, hiding then the information of the two limits. Extra details about the comparison of both technics are elaborated in [54].

Ideally, both the IC and DV should be done at near equilibrium state for an reliable outcome. In other words, at very slow currents, in the order of $C/20$.

Other technics, such as the one developed by [61], [62] propose obtaining results about the electrode balancing changes during aging. This method requires using a near to equilibrium voltage curve of the cell with aging, along with half-cell data of each electrode (NE vs Li and PE vs Li) in the BOL.

4.2 Aging mechanisms

The aging mechanisms that are prone to happen in the battery are illustrated in Figure 6. The following subparts explain and elucidate the most critical ones, and underlines their interdependency.

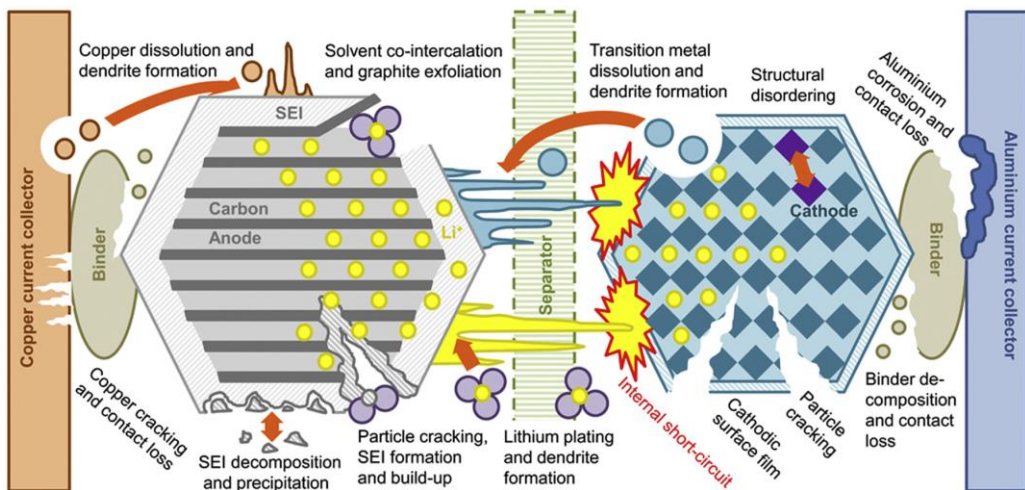


Figure 6. Illustrating the main degradation mechanisms of the Li-ion batteries [39]

4.2.1 The Solid Electrolyte Interphase (SEI)

Its formation. It has been widely accepted in literature that the Solid Electrolyte Interphase (SEI) formation on the carbon electrode is vital for the successful operation of Li-ion batteries [38]. As soon as the NE, made of carbon material, is immersed in a battery electrolyte and a negative potential is applied, electron exchange begins. The reduction of salts, solvents and impurities yields inorganic compounds like LiF and Li_2O that precipitates on the surface of the electrode. This is followed by the formation of partially soluble polymers and semi-carbonates, insoluble SEI components like Li_2CO_3 , as well as crystals of LiF salt which are very stable [63]. As mentioned by Peled and Menkin [38], after being formed, the SEI fulfil the job of preventing electron exchange from the electrode to the electrolyte, hence insuring a successful operation.

The widely adopted SEI model assumes that it is formed of an non-porous inorganic layer (on the electrode interphase) and a porous organic layer on top of the inorganic

one [38]. The inorganic layer was found to be more compact and thus has the advantage of limiting the electrolyte penetration. It has though a small ionic conductivity for lithium ions [64]. The organic layer is mainly much bigger and porous.

Although this SEI formation is important for the cycle life of Li-ion batteries, it consumes lithium ions and reduces the electrolyte, causing an initial loss of capacity.

Its growth. SEI growth is triggered at low NE potential (between 0.0 V and 0.4 V vs Li^+/Li , i.e. when the cell is charged), and accelerated at high temperatures ($> 35^\circ\text{C}$) [63], [64].

The growth mechanisms of the SEI layer is still not deeply understood, and it is based on different theories, as explained in details in [38].

The first suggests that its growth is due to a slow diffusion of electrolyte molecules through the SEI due to a concentration gradient, which leads to yielding SEI components at the electrode/SEI interface. However, it clashes with the conventional idea that the SEI is a compact polycrystalline material and solvent molecules cannot transport through it. The second, which is more accepted, was illustrated by Peled in 1979 [65]. It suggests that the growth of SEI is based on the conduction and diffusion of electrons from the electrode to the SEI/electrolyte interface, reducing the solvents and the salt anions at the top layer of the SEI.

Besides growing, the SEI layer can undergo a breakdown and repair process during the battery consumption. According to Peled and Menkin [38], the SEI layer can breakdown due to irregular retraction of the active material particle. This can be mainly caused by the volume changes during lithiation/delithiation processes, especially with Si-doped graphite anodes. Fast-forming cracks in the SEI layer opens the way for electrolyte to flow into the exposed anode surface, react with it, and form a fresh protective film. In the case of slow-forming cracks, the SEI becomes thinner, opening the way for electrons to pass through this local thin region and reduce faster the electrolyte, as the surface area of contact becomes bigger [38], [66].

In terms of performance, as the SEI layer grows, it consumes reversible lithium ion, what is mainly referred to as LLI (Loss of Lithium Inventory). This leads to a loss of capacity. Its width, density and uniformity impact heavily the resistance of the cell, as they limit the diffusion of the ions within the electrode [63].

4.2.2 Li-plating

One of the most unwanted mechanisms (on both aging and security levels) in the Li-ion battery is the deposition of metallic lithium on the NE. Also called lithium plating, it is enabled at an electrode potential of 0.0 vs Li^+/Li , so in a fully or overcharged cell. As the metallic lithium deposits on the SEI surface, dendrites formation follows. As the dendrites pass through the separator and reaches the positive electrode, short circuit occurs and can lead to thermal runaway [67]. Three

conditions favor the decrease of the NE potential: low temperature, elevated charging C-rates as well as high voltage and SOC levels [41], [63], [68], [69].

At low temperature, the electrolyte's ionic conductivity, the diffusion coefficients and the intercalation rate in the active material decrease, leading to an increase of the ionic flow and intercalation resistances. The limited electrode mobility blocks the diffusion paths in the graphite, accumulating the ions at the interface of the electrode. This causes concentration polarization of lithium and drives the anode potential below zero causing the metallic lithium to deposit on the anode surface [70].

An elevated charging C-rate will also cause lithium ions accumulation in front of the anode, favoring its deposition on the surface SEI/Electrolyte [68].

Finally, an increase SOC level or voltage is directly referred to an increased amount of intercalated lithium. According to Persson et al. [71], [72], for a low lithium content, the lithium migration is dependent on the slab space. However, at high lithium content, the Li-Li in plane intercalations play a repulsive role and increase the migration energy barrier. This pushes the lithium ions to accumulate on the surface of the anode [68].

Li-plating, similarly to the SEI, causes an LLI, and a loss in the capacity of the cell. Oppositely, it does not impact its resistance for the following two reasons. First, solid lithium is assumed to have a good conductivity when compared to the SEI [73]. Second, Li-plating appears in local fashion, without blocking any diffusion path.

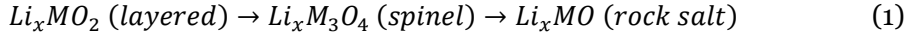
The NE is considered by many researchers, especially from the modeling sector [43], as the electrode that affects the most the loss of performance. This is probably due to the criticality of the electrode/electrolyte interface, as the organic electrolyte is highly reactive with the electrode material and lithium ions [67]. However, serious mechanisms happen at the PE that tend to decrease the available capacity of the battery cell.

4.2.3 PE structural changes and transition metal dissolution

If the active materials of the NE for automotive applications are mostly carbon based, a variety of active material exist for the PE (as mentioned previously). Here the focus is made on layered oxide NMC based electrodes ($\text{LiNi}_x\text{Mn}_y\text{Co}_z\text{O}_2$), since they are widely used in recent times (generation 2a to 3b) due to their promising performance [74].

The two most occurring mechanisms are underlined here: the PE structural change and the dissolution of transition metals. More details about the PE degradation mechanisms are provided in [41].

The mechanisms of the structural change and the oxygen release of the PE active material was estimated by [75]. It is summarized to take the following form [41], where oxygen is released in each step:



where M represents the transition metals

This mechanism of equation (1) is favored at highly de-lithiated states of the NMC.

The dissolution of transition metals (especially Mn) can be explained in two different mechanisms [76]. The first mechanism considers the reaction of the PE active material with the acid found in the electrolyte. Acid can be present due to the reaction between moisture and electrolyte fluoride contents. Following this mechanism, it was found that the dissolution of Mn accelerates with the increase in acid content in the electrolyte, the increase in the surface area, and the increase in temperature.

The second, well described in [77], is based on the phase transformation mechanism of $Li_xMn_2O_4$. It is proposed to occur at high PE potential, and to be accelerated at high temperatures.

On a performance level, this is usually affected to a loss of active material on the positive electrode (LAM_{pe}).

4.2.4 Particle cracking and fracturing

These mechanisms tend to happen on both electrodes [50]–[52]. The reason behind is the rapid and intensive change in volume of the particles, i.e. high current rates. It is a common issue for high theoretical capacity material (such as Si), and particles with large particle size [41]. High temperature can cause elevated thermal stress, and low temperature makes the material become more brittle and then prone to getting fractured [41].

Particle fracturing usually starts with some micro cracks, which can connect together to completely break and isolate a part of the particle from the rest of the electrode [41].

Particle fracturing is directly associated to a loss of active material on both electrode (LAM_{pe} and LAM_{ne}). In some cases where lithium ions are stuck in the AM particle that pulverized from the rest of the lot, LLI might happen. Dubarry et al. [58] refers to this as LAM_{li} or, loss of active material when lithiated. It is also seen to have a direct impact on the resistance of the cell, as the electrical contact between active particle can be disrupted [78].

4.2.5 Interaction between degradation mechanisms

Most of the time, aging mechanisms are studied independently in literature. However, in real life application, a multitude of stress factors coexist, and degradation mechanism never act on the battery independently. Edge et al. [41] allocates a good part of their review in detailing the interdependence of the aging mechanisms.

SEI growth is commonly referred to as the main degradation mechanism. It should be noted however, that its rate of growth or nature depends strongly on other mechanisms. Deposition of metallic lithium creates new surfaces where a secondary SEI can form and grow [79], [80], hence consuming lithium at a faster rate. In such manners the internal resistance is strongly affected as further SEI thickness can cause pore clogging, causing then a loss in the reachable active material (LAM_{ne}) [81].

High cycling rates can cause abrupt and uneven changes in the particle volume. Besides the breakdown and repair process evoked earlier on (part 4.2.1), if the particle itself cracks, it exposes the active material to the electrolyte, opening the way for the formation of a fresh SEI layer [82].

Zhang et al. [76] elaborated the dissolution, migration, and deposition (DMD) process of the PE's transition metals (Mn, especially), based on the finding of [83]. A process was described showing the Mn "pollutes" the SEI by increasing its electronic conductivity, acting as an electro-catalyst, and potentially increase its growth rate [84]. The SEI then becomes thicker and denser, increasing the resistance of the cell [85].

The interdependency of aging mechanisms does not always aggravate the aging rate. It is proposed in [86] that the more the SEI consumes lithium and grows, the less is the probability of Li-plating. As lithium is consumed, the potential of the NE increases and move away from the 0.0 V vs Li/Li⁺ region.

5. Li-ion battery lifetime estimation

As mentioned in part 3.2, the aging understanding and lifetime estimation is of extreme importance for the correct estimation of EOL, i.e. a correct dimensioning of the pack at BOL. To predict accurately the performance of the battery during its real usage, accelerated aging tests are needed.

5.1 Accelerated aging tests

Accelerated aging tests require testing the cells exposure to stress factors [14] and analyze the degradation mechanisms that occurs within the cell.

The most common type of accelerated testing technic used nowadays in the battery field is the overstress [87]. Accelerated aging by overstress is commonly used both in literature [88], [89] and in standards [45], [46], [90], [91]. This technic requires applying intensively a stress factor on the battery, by increasing its amplitude. The main stress factors are the temperature [34], [92]–[98], the current [99]–[101], the State Of Charge (SOC) [102]–[104] and the Depth Of Discharge (DOD) [88], [100].

Considerable care should be given to avoid generating aging mechanisms that do not happen in real service life. In order to visualize this, the analogy of the egg can be very telling. An egg needs around 20 days and 37 °C to yield a chick. Accelerating its

aging by increasing the temperature to 90 °C, for example, yields not a chick but a hardboiled egg in about 10 min. This is a typical example of a faster aging by overstress, but a totally different aging mechanism.

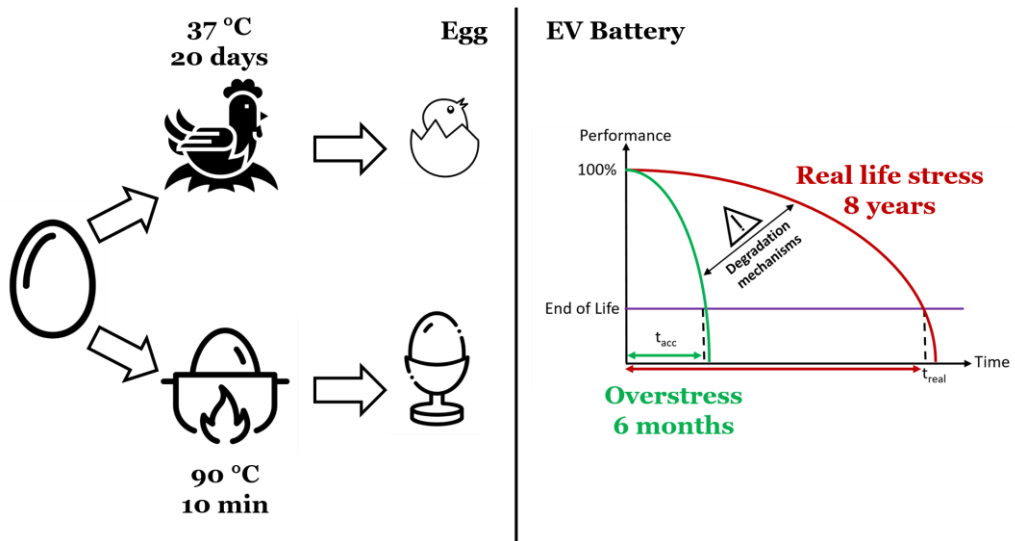


Figure 7. Aging mechanism consistency illustrated with the analogy of the egg

The final goal of accelerated aging tests is to parametrize a lifetime estimation model based on the observed outcomes in function of the different stress factors [44], [87], [105]. Characterizing the battery performance and aging is done by EV manufacturers as soon as they receive the battery cell, prior to its implementation in the vehicle. The pre marketing duration of an EV ranges from 3 to 5 years, where a big portion of the time (1 to 3 years), is dedicated to the qualification, validation and modeling of the cell [106].

5.2 Aging mechanisms consistency

As mentioned previously, for consistency purposes, durability tests have to represent real life aging. In other words, they should recreate the same aging mechanisms that happen in the batteries' real life, but in a faster manner. This aging-mechanism-consistency will insure accurate lifetime estimation and avoid misleading results.

Some examples from literature can be given to examine the consistency of these methods. Temperature is a very common overstress factor. At 25 °C the dominant aging mechanism is the SEI growth. Ideally, at 45 °C the SEI should grow in a faster manner. Gewalt et al. [92] suggest that increasing the temperature of the test might engender the production of gaseous products. It was seen previously that side reaction from the PE can produce gases at high temperature. The authors suggest then that the mechanism consistency is not fulfilled, and at high temperatures, the SEI is no more the dominant aging mechanism.

Snyder et al. [99] investigated the current overstress. It was proved that low current rates induces mainly SEI fracturing, while elevated currents can cause additional particle fracturing. As seen previously, particle fracturing can increase loss of capacity due to fresh and secondary SEI formation. The main degradation mechanism which was the SEI at low currents, is not anymore the dominant mechanism at high currents.

Finally, the DOD is another common stress. Nowadays, most of accelerated aging testing are done on a full DOD scale, from the lowest allowed cell voltage (usually 3.0 V for NMC/Graphite cells) to the highest (usually 4.2 V for NMC/Graphite cells). It was proved by [78], [107] that high DOD causes particle fracturing, especially for Si-doped graphite. This phenomena wasn't identified for low DOD values. Again, the mechanism consistency is not fulfilled.

5.3 Aging modeling

Accelerated aging tests outcomes are used to parametrize aging models. The role of aging models resides in estimating the loss in performance of the battery cell when confronted to real life stress factors. The following two publications reviewed exhaustively the modeling strategies used nowadays in the field of Li-ion battery [13], [37]. Five big categories of models can be identified and listed hereunder with some literature examples :

- Statistical [108]
- Empirical [109], [110]
- Semi-empirical [111]
- Equivalent Electric Circuit (EEC) [112]
- Multi-physical [113], [114]

Statistical models. Statistical models rely on a direct correlation between environmental or operational condition and the battery performance criterial. Such correlations are made using data from the terrain. Accelerated aging testing can be done to aliment these models with some extra data points.

Empirical models. Empirical models rely on some mathematical relationships linking stress factors to the performance criteria. Regressions between observed data points are done to estimate the Remaining Useful Life, commonly referred to as RUL.

In the previously elaborated models, no distinctions are made between the aging mechanisms. They both rely on mathematical correlations.

Semi-empirical models. Semi-empirical models gets a little deeper in understanding the mechanisms that happens inside the battery. They are based on simplified physical, chemical, or electrochemical equations.

Most of the semi-empirical models estimate that the SEI growth is the dominant degradation mechanism in the Li-ion battery, especially during calendar aging [95],

[102], [103], [115]–[117]. The idea of using an Arrhenius equation to model the loss of capacity with respect to the temperature is based on the Peled-Broussely model [65], [94], where the consumption of lithium ion by the SEI is proportional to the conductivity of the SEI which can be modeled by an Arrhenius equation. Arrhenius equations were also used to model the increase in internal resistance [118].

It was proved that the growth of SEI is not only proportional to temperature but also to the SOC level. The Eyring relationship, elaborated by [115], describes the loss in performance in function of different stress factors at once.

The Dakin approach is another example, elaborated in [93]. It is derived from the chemical kinetics, and used previously in the field of electrical insulation where thermal and electrical stresses are applied together [119].

Electric Equivalent Circuit models. Slightly less abstract than semi-empirical methods, the EEC models described the electrical behavior of a cell using the analogy of an electrical circuit made of an OCV source and a combination of passive components (resistors, perfect or imperfect capacitors and so on). The inputs to this model are ambient conditions such as cell temperature, and the solicitation levels, for example the current. The outputs are the SOC and the voltage. The idea behind the EEC models is that each component in the combination described in the circuit models a physical phenomenon [115].

As such, the model can describe the performance of the cell. Additional degradation mechanisms can be added to be able to describe the evolution of the performance with time. In depth explanation of ECC can be found in [13].

Multi-physics models. Considered as the less abstract method, these models are based on physical, electrochemical and transport equations to model the behavior of each compartment in a cell [115]. They rely on the porous electrode model theory [120]. The Newman Pseudo-2D [121] and the Single Particle Models (SPM) [122] are typical examples. These models rely on tens of physical and electrochemical parameters, which require ante-mortem characterization technics to extract them. Some parameters are simply adjusted to fit experimental data [120]. Besides the time consuming work needed to extract these parameters, running the model demands a considerable amount of time.

Multi-physics are initially designed to model a galvanostatic charge and discharge phenomena. Aging equation describing specific aging mechanisms are usually added to evaluate the loss of performance with time and with respect to the solicitation in question. Modeled phenomena include mainly the SEI growth, the Li-plating [79], [113], [123]. Few publications, reviewed in [86], include particle fracturing, electrode bulk cracking, pore clogging and dissolution of PE transition metals.

Accelerated aging tests are needed to adjust the degradation model parameters to fit the performance criteria loss [113].

5.4 Cumulative damage approach

The methodology for lifetime estimation of lithium ion batteries is based on the cumulative damage approach, also known as the Palmgren-Miner rule [124], [125]. The method proposes that damages of different amplitudes can be accumulated. The first hypothesis of this method suggests that the order of the stresses is independent of their damage. The second hypothesis considers that the approach is memoryless. In other words, the loss of performance for a new and old battery is the same. Different instances for using this approach can be given.

Calendar and cycle aging are most of the time tested independently. Models are parametrized for each, and then added up linearly to form a global model [89], [126]. In each of these models, the damage given by each stress is added up to model the decrease in performance. For example, in [127], a semi-empirical model was formed by adding the impact of the DOD (polynomial equation) to the impact of temperature (Arrhenius equation). In [126], the DOD and the cycle number are both modeled using an inverse power law and added to form a general polynomial describing the loss in performance.

The cumulative damage approach was tested for Li-ion batteries by Badey [124], during five months of tests. Badey [124] proposed to apply two different solicitations on the battery cell. The first (solicitation A) comprised the event 1 (cycling from SOC 25 to 75 %) followed by the event 2 (cycling from SOC 0 to 100 %). The second (solicitation B) comprised the event 2 followed by event 1. Both are done at 40 °C. The loss in capacity was studied.

The slope in the loss in capacity of event 1/solicitation A was two times bigger than the slope of event 1/solicitation B. This suggests that the order of the stresses has a role to play, and the memoryless property of the cumulative damage approach is not valid.

Badey [124] also proposed to examine the cumulative damage approach for calendar and cycling aging. He implemented two cycles, the first comprised 5 days of cycling and 15 days of calendar aging, and the second comprised 10 days of cycling and 30 days of calendar aging. The tests lasted five months.

The loss in capacity seemed to follow the same course for the two tests, suggesting that the cumulative damage approach is valid for the calendar/cycle aging, at least for five months.

Two recent publications [89], [126] employed semi-empirical modeling using the cumulative damage approach and the results were the following (Figure 8).

The conclusion made from Badey [124] (proposing that the cumulative damage approach can be valid for the first 5 months) is observed in the two cases of Figure 8. However, as soon as the 6 months mark is passed, the models deviates from the experimentally obtained results. This proposes that the cumulative damage

approach is problematic for long duration predictions. The fact that models are not reliable for long periods of time was also evoked by Korthauer in his book [14].

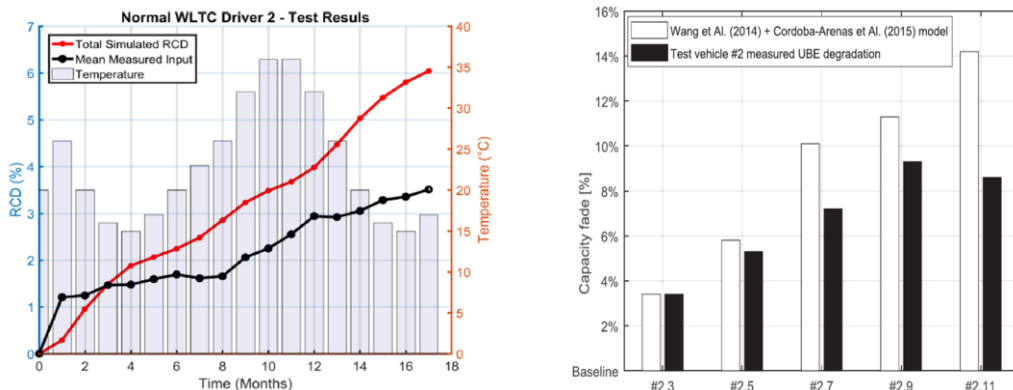


Figure 8. On the left: results from [126] comparing the model predictions to the outcomes of a normal drive cycle scenario with parking, driving, and a temperature variation. On the right: results from [89] comparing the model predictions to the outcome of a test vehicle on road where data points are obtained on a 6 months basis

5.5 Interdependence between calendar and cycle aging

As previously mentioned, considering a cumulative damage approach with calendar and cycle aging models is not valid. A certain interaction between calendar and cycle aging exists, and it is not linear. This non-linearity was examined a couple of times in literature.

Epding et al. [128] investigated the influence of rest periods on the capacity loss during cycle aging. To do so, they compared the evolution of the Usable Cell Capacity (UCC) of a cell that undergone cycling (2C charge and 1C discharge) without any rest period (green dots), a second that rested 2 days each 50 cycles (black dots) and a third that rested 2 days each 100 cycles (red dots). All three cells were aged at 10 °C (Figure 9).

Results suggest clearly that rest times has an impact to do on the evolution of the remaining cell capacity. The cell seems to regain capacity at each rest time, and the shape of the UCC evolution is different for the three cases.

For the parametrization of the models previously mentioned, rest times are neglected, especially for the cycling models. In real usage, rest times (calendar or parking times) constitute over 90 % of the battery lifetime. This starts to explain the erroneous interpretations of Figure 8.

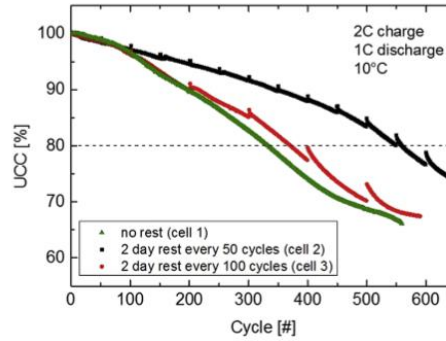


Figure 9. Plot of the evolution of the UCC in function of the cycle number for the three cells with different rest times frequency [128]

Redondo-Iglesias et al. [129] studied carefully the interaction between cycling and calendar aging, and reexamined the cumulative damage approach. They applied different profiles, in which the rest times varied from 24 to 3 hours.

They used the cumulative damage approach to separate the impact of calendar to cycle aging. They considered then that the calendar aging contribution (Q_{cal}) can be derived from calendar aging tests, and that the contribution of cycle aging (Q_{cyc}) is the subtraction of the obtained capacity from each profile (Q_{global}).

Their results suggest that cycle aging had in general a bigger impact when the calendar times were longer. They also concluded that increasing the Ah throughout does not always have a significant impact on the Q_{cyc} . They deduced that a non-linear interaction exists and shouldn't be neglected between calendar and cycle aging.

6. Observations

The methodology used nowadays for the lifetime estimation of Li-ion batteries is based on three main steps:

1. Accelerated aging tests
2. Parametrization of an performance/aging model
3. Lifetime estimation

The overstress technic is the dominant one, with the stress factors being the temperature, the power or current rate the SOC level and the DOD. Using overstress is successful in decreasing the performance level in a faster way. However, it engenders mechanisms that do not happen under normal stress conditions. Models, that have the purpose of predicting the performance loss of the battery under real conditions, are parametrized by experiments that do not replicate reliably the aging mechanism in question.

An SEI model (semi-empirical or multi-physical) should ideally be calibrated on an aging tests where the SEI is the dominant degradation mechanism. Most of the SEI models are nowadays calibrated on accelerated aging tests at 45 °C. In such

conditions, transition metals from the PE and gases formations happen, while the model considers only the SEI growth. This is a first source of error, explaining the discrepancy in the results found when comparing model to field measurements.

This being said, the first observation can be stated:

- Overstressing the battery leads to erroneous modeling interpretations

The cumulative damage approach isn't properly validated in terms of stress factors. It is, however, refuted for calendar and cycle aging.

- Linearly adding up aging models should be rejected

Up to the knowledge presented in this chapter, accelerated aging and lifetime estimation was never linked to the usage of batteries in real-world application. The third observation can then be introduced.

- Accelerated aging tests and models are decorrelated from the usage

During the 18th meeting of the UNECE sub-group Electric Vehicle and Environment (EVE) [130] the need of developing a methodology for the aging estimation of the battery under real-world usage conditions was mentioned. They also point out at the range decrease, and the ability to guarantee the customer with a minimum performance. That is where will lie the goal of the thesis.

7. Thesis goal and methodology

The goal of the thesis is to improve the current lifetime estimation approach by correlating the accelerated aging tests and modeling with the real-world usage of EV batteries. According to Nelson [87] and Carlsson [105], [131], an analysis of real-world usage is crucial prior to any lab testing. In order to guarantee the aging mechanisms consistency previously mentioned, lab tests should recreate the stress factors encountered during the application, and shouldn't surpass the application's domain. Which is where lies the importance of real-time data vis-à-vis the stress factors and the aging mechanisms of the battery [87], [131].

The main questions that rise here are the following: how are the batteries used in real-world applications? Can accelerated aging tests be representative of the real-world applications? Can they guarantee mechanisms consistency? Can the mechanisms be modeled and the lifetime estimated accurately?

In order to try and find an answer to these questions, the thesis proceeds as follows. First, an in-depth analysis of usage was elaborated. Usage data were gathered, assessed and analyzed from worldwide projects (Chapter 3). Results were complemented by a driving campaign on a monitored BMWi3 from CEA-Grenoble (Chapter 4). A usage representative accelerated aging protocol was designed and implemented on a Samsung PHEV 37 Ah cell, for PHEV applications (Chapter 5). Aging characterization technics were developed and used to identify the degradation mechanisms that occurred (Chapter 6). Finally, a multi-physical Newman P2D performance and aging model was parametrized and developed (Chapter 7).

Chapter 3 – Li-ion batteries' stress factors during electric vehicles' service lifetime

Highlights

- Assessed 228 million km and 7.8 million trips worth of data for over 37,000 EV
- Analyzed data for driving, charging and parking conditions
- Identified the most influential aging stress factors for the three types of EV
- Carried out a Risk Probabilistic Number analysis
- Established a framework for usage representative aging testing of Li-ion batteries

Having clear insights of the stress factors that the electric vehicle (EV) batteries encounter during their service lifetime is crucial for more reliable aging testing and modelling. Since the first deployment of Li-ion battery based EV, numerous driving campaigns with field data were published. The goal of this chapter is to gather, assess and analyze them in order to quantify the stress factors depending on the EV type. The targeted stress factors are the temperature of the cells, the discharging and charging rates, as well as the SOC ranges. A Risk Probabilistic Number (RPN) analysis was used to evaluate the stress factors with respect to their impact on the aging of Li-ion batteries.

1. Introduction

As mentioned in chapter 2, the accelerated aging testing are de-correlated from what really happens in the service lifetime of a battery. The goal of this chapter is to fill in this gap. To do so, numerous publications of EV field data are gathered and assessed from all-around the globe. The different operating and environmental conditions that EV batteries encounter during their lifetime are extracted, and the most critical ones are identified using a Risk Probabilistic Number (RPN) [105], [132] analysis.

The RPN analysis [105], [132] is the tool used to evaluate the stress factors encountered by the battery during its lifetime, accordingly to their impact on its aging. This will help conditioning future durability studies, as it will give an insight of what really happens in the service life of an EV battery. To the extent of our knowledge, in the field of LIB this tool was mentioned in a mere handful of publications [133]–[136]. However, it was used to evaluate the failure modes depending on some aging solicitations without referring to the vehicle usage. The novelty of this work lies in the identification of the frequency of occurrence of stress factors based on worldwide fleet data. Four main stress factors are covered:

- the cells' temperature (during driving, charging and parking conditions)
- the energy consumption (discharging power)
- the charging power
- the State Of Charge (SOC) and Depth Of Discharge (DOD)

The plan of the chapter goes as follows. After expressing the methodology and the source of the studies from which results were gathered, the analysis of usage is elaborated. For each stress factor, the field data are assessed and discussed, before identifying the associated degradation mechanisms. Finally, the Risk Probabilistic Number (RPN) analysis is elaborated, and recommendations for aging testing are given.

It should be noted that the chemistry of LIB cells is not much of an interest here. Their application in the EV, however, is. The three families of EVs are elaborated: the Battery Electric Vehicle (BEV), the Hybrid Electric Vehicle (HEV) and the Plug-in Hybrid Electric Vehicle (PHEV).

2. Methodology

In order to assess the stress factors that an LIB cell encounters in its service lifetime, numerous infield studies taken from literature are reviewed and analyzed (Table 1 and Table 3). Some data, exhibited in the form of graphs, were obtained using image processing based extraction [137]. As will be mentioned afterwards, certain data needed some harmonization to be compared with each other.

It can be seen from Table 3 that only one source gave some insights about the HEV application. This show the lack of interest towards this application. The most studied case was the BEV. The temperature of the cells was barely mentioned, even though

it is one of the most crucial factors in battery aging. It is well known that passenger vehicles spend most of their lifetime in parking conditions [138], [139]. Though, only five publications investigated this condition. The difficulty in accessing such information might be the reason.

Table 1. Cumulative volume of the studies analyzed

Targeted locations	Cumulative distance and number of trips	Cumulative duration	Total number of vehicles
Europe, North America, Asia (Far East) and Australia	228 million km and 7.8 million trips	3,108 days (approx. 8.5 years)	37,572 vehicles

A campaign done in CEA Grenoble with a monitored BMWi3 60 Ah (Table 2) can fill in this gap and complement the literature assessment [140]. The vehicle was equipped with over 70 thermocouples, but the focus was made only on the ones positioned on the top of the battery cells inside one of the modules (four thermocouples) and the ones positioned on the front and rear bumpers for the ambient temperature measurements (two thermocouples).

Temperature data were measured with 1 Hz frequency, whether the car is in motion, charging, or parked. This represents the major particularity of this vehicle, and the reason why it can complement the literature analysis. Other parameters such as the current, voltage and SOC of the pack, as well as the speed of the car were measured with a 10 Hz frequency. The study was done in 2018, where the vehicle was used by CEA agents for some work trips (1,000 km). Throughout the publication, it will be referred as “the CEA campaign”.

Table 2. Specification of the BMWi3 of the CEA campaign

Battery installed capacity (usable)	21.6 kWh (19)
Range	165 km
Battery pack thermal management	Active refrigerant system

Table 3. Detailed overview of the assessed studies

Source and Reference	Location	Size of the study	EV type	Driving (D) Charging (C) Parking (P)	T _{amb}	T _{cell}	SOC DOD	Energy Consumption	Charging
European Studies									
CEA campaign (2021) [140]	Grenoble, France	1 year and 1,000 km	BEV	D/C/P	✓	✓	✓	✓	✓
Aachen University (2021) [141]	Germany	123 days	BEV	D	✓	✓	✓	✓	-
KIT (2018) [142]	Germany	5,000 EV 4 years	BEV	D/P	✓	✓	✓	-	-
Ruhr-University Bochum (2015) [143]	Berlin, Germany	700,000 km	BEV	D	✓	-	✓	✓	-
Green e-motion (2015) [144]	Europe	413 EV	BEV-PHEV	D/C/P	✓	-	✓	✓	✓
NAF (2020) [145]	Norway	20 EV	BEV	D	✓	-	-	✓	-
AIT (2016) [26]	Vienna, Austria	945 trips	BEV	D	-	-	-	✓	-
TU Delft (2020) [146]	Netherlands	505 EV	BEV	D/C	-	-	✓	-	✓
Transport & Environment (2020) [147]	Europe (8 countries)	300 EV 250 days	BEV-PHEV	D/C	-	-	-	✓	✓
IFSTTAR (2016) [148]	Paris, France	36 EV 180 days	BEV	D/C	-	-	✓	-	✓
BMW Group and Vattenfall Europe (2013) [149]	Berlin, Germany	79 EV 180 days	BEV	D/C	-	-	✓	-	✓
EMEL (2012) [150]	Lisbon, Portugal	18,524 km 5 months	BEV	D/C	-	-	-	✓	✓
IWT (2015) [151]	Belgium	1,544,437 km	BEV-PHEV	D/C	-	-	-	✓	✓
MAHLE (2020) [152]	-	-	HEV		-	-	✓	-	-
UK 2000 TUS data (2013) [139]	UK	-	BEV	D/C/P	-	-	-	✓	✓

Aston University (2022) [153]	UK	15,194 km and 1,137 trips	BEV	D	✓	-	✓	✓	-
Green e-motion Ireland data (2016) [154]	Ireland	-	BEV- PHEV	D/C/P	-	-	✓	✓	✓
North American Studies									
NREL (2012) [155], [156]	AZ, LA and MN, United States	317 trips	BEV- PHEV	D	✓	✓	-	-	-
Stanford University (2017) [157]	Northern America	10,000 EV 2.5 million trips	BEV	D	✓	-	-	✓	-
FleetCarma (1) (2013) [158]	Northern America	11,418 trips	BEV- PHEV	C	✓	-	-	✓	✓
AAA (2019) [159]	United States	5 EV	BEV	D/C	✓	-	-	✓	✓
ABetterRoutePlanner (2018) [160]	United States	233 EV 70,000 km	BEV	D	-	-	-	✓	-
ABetterRoutePlanner (2018) [161]	United States	805 EV 350,000 km	BEV	D	✓	-	-	✓	-
UCLA (2016) [162]	Los Angeles, United States	17 EV 400 days	BEV- PHEV	C	-	-	-	✓	✓
FleetCarma (2) (2013) [163]	Toronto, Canada	52 EV	BEV- PHEV	D/C	✓	-	✓	✓	✓
U.S. Department of Energy(2015) [164]	United States (22 regions)	8,300 EV 201 million km	PHEV	D/C	-	-	-	✓	✓
National Household Travel Survey(NHTS) (2019) [165]	United States	392 EV	BEV	C	-	-	✓	-	✓
The EV Project (2012) [166]	United States (14 states)	3,823 EV 16,093,949 km	BEV- PHEV	D/C	-	-	✓	-	✓
Toyota Motor North America (2013) [167]	United States	125 EV 59,287 trips	PHEV	D/C	-	-	-	✓	✓
Asian Studies									
Tsinghua University (2020) [168]	Beijing, China	4,401,000 km	BEV	D	✓	-	-	✓	-
BEVMS (2016) [169]	Beijing, China	2550 EV	BEV	D/C	✓	✓	✓	✓	✓
(2020) [170]	Beijing, China	130 EV	BEV	D/C	✓	-	✓	-	✓
Nagoya University (2015) [171]	Japan	483 EV	BEV	C	-	-	✓	-	✓
Australian Studies									

Australian Energy Market Operator (AEMO) (2017) [172]	Australia	37 EV	BEV	C	-	-	✓	-	✓
University of Western Australia (2016) [173]	Australia	29,100 km	BEV	D	-	-	-	✓	-
The University of Western Australia (2013) [174]	Australia	67 EV	BEV	C	-	-	-	-	✓
Worldwide Studies									
CrossChasm (2015) [175]	Worldwide	4,000,000 km	BEV-PHEV	D	✓	-	-	✓	-
GEOTAB (2020) [176]	Worldwide	4,200 EV 5,200,000 trips	BEV	D	✓	-	-	✓	-
TOTAL			BEV: 35 PHEV: 12 HEV: 1	D: 31 C: 23 P: 5	18	5	18	26	23

3. Results and Discussion

3.1 Cell Temperature

3.1.1 Parking conditions

Field data. Parking events represents more than 90 % of the vehicles' lifetime [138], [139], and temperature is a major stress factor during the battery rest times. Investigating the temperature of the cells is therefore crucial. In the CEA Campaign, both the temperature of cells (T_{cells}) and the ambient temperature (T_{amb}) were measured during these events. T_{amb} was obtained by averaging the values from the two exterior thermocouples and T_{cells} was obtained by averaging the values from the four thermocouples positioned on the cells (Figure 10).

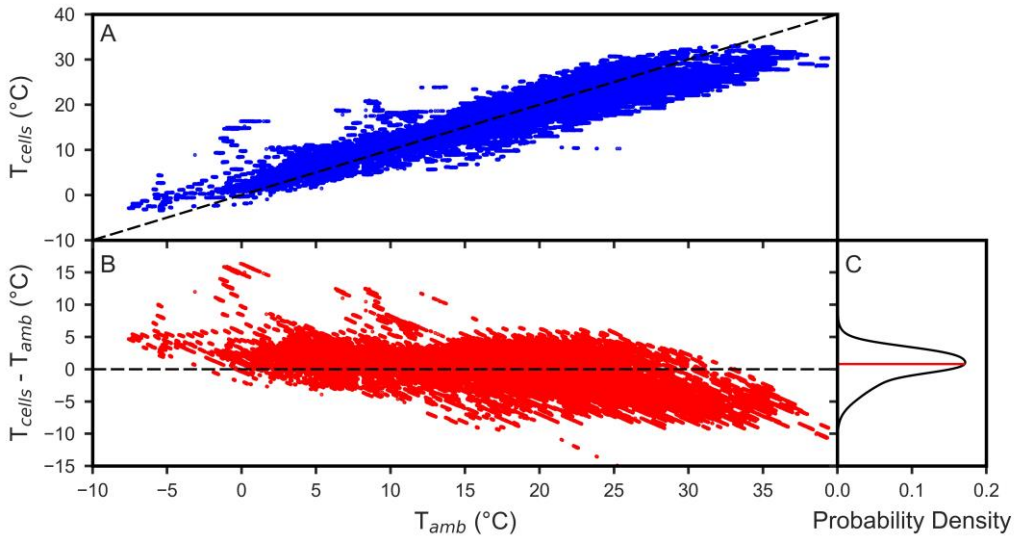


Figure 10. (A) Temperature of the cells in the battery pack plotted in function of the ambient temperature measured outside the vehicle. The black dashed line represents the identity function (B) The difference between the cells' and ambient temperatures plotted in function of the ambient temperature (C) The probability density diagram of the difference between the cells' and ambient temperatures, with the red line showing the median value

Overall, for the ambient and the cells' temperature respectively, the maximum value was 38.48°C and 33.14 °C, and the minimum value was -7.66 °C and -3.33 °C. Similar results were found in [142], where around 80 % of the battery pack temperatures values lied between 0 and 30 °C.

With the help of the identity function in Figure 10 (A), it can be seen that T_{cells} was higher than T_{amb} for cold weathers, while it was lower at warm weathers. In order to quantify this dissimilarity, Figure 10 (B) illustrates the difference between T_{amb} and T_{cells} in function of T_{amb} . It elevated mostly up to ± 5 °C and in rare cases beyond ± 5 °C. The probability density diagram of Figure 10 (C) shows a median value of 0.81 °C. With the distribution of the results being slightly skewed to the positive difference, it was concluded that it is somewhat more likely for T_{cells} to be greater than T_{amb} .

Discussion. It has been shown that the temperature of the cells is close to the ambient temperature at reasonable weather conditions. However, at extreme ambient conditions T_{cells} “bends” to the middle region (Figure 10).

This is due to two main reasons. First, the position of the battery pack in the BEV used, or in any EV, is in the underside of the car [177]–[179]. This is intended by car manufacturers to avoid the impact of solar irradiance. Second, the battery pack is thermally protected with, most commonly [180], [181], glass mineral wool (C_p (specific heat capacity) ≈ 900 J/(kg.K) [182]), aerogels ($C_p \approx 1,000$ J/(kg.K) [183]), silicone foams ($C_p \approx 1,260$ J/(kg.K) [184]) or polyurethane foams ($C_p \approx 2,700$ J/(kg.K) [185]). These insulating films induce a slow thermal inertia which keeps the battery from reaching the extreme values of T_{amb} .

Up to our knowledge, no additional studies were undergone to investigate the temperature of the battery in parking conditions. However, many of them monitored and studied the temperature of a fuel tank in ICE vehicles, and the position of the battery in an EV is close the position of the fuel tank in a conventional vehicle. It was found that the temperature of the fuel tank is quite close to the ambient temperature as well [186]–[188].

Associated Degradation Mechanisms. It is clear from literature that elevated temperatures (above 35 °C) at parking conditions accelerate SEI formation on the electrodes [34], [92], [94]. The cold weather does not seem to impact the aging of the cell at rest times [189]. With the results in hand, it can be concluded that the occurrence of those aging mechanisms on a cell level, as well as their kinetics, are not necessarily related to the ambient temperature values. T_{cells} values were rarely found above 30 °C and never above 35 °C, even if the maximum ambient temperature was 38.48 °C.

This statement, however, has some limitations. In this type of weathers, extreme temperatures (less than 0 °C and above 35 °C) rarely occurs. Additional studies should be undergone where extreme weather conditions happens at longer durations, in order to obtain a clearer answer about the correlation between aging mechanisms and ambient temperatures.

3.1.2 Driving conditions

Field data. The temperature of the cells during cycling conditions is quite impactful on both its performance and its aging [190]. Figure 11 illustrates this for four different long trips done in the CEA campaign, for the six thermocouples mentioned earlier. It can be seen in trips 1 and 4 that T_{cells} at the beginning of the trip was not equal to T_{amb} . This is in accordance with the discrepancy in temperatures at parking conditions found in Figure 10. In trip 2, while T_{amb} decreased with the trip length, T_{cells} remained above 17 °C. For most of the trip, while T_{amb} settled between 0 to 5 °C, T_{cells} ranged from 20 to 25 °C. In trip 3, T_{cells} was equal to T_{amb} (10 °C) in the first 20 min of the trip, and then it increased to 17 °C, before reaching 20 to 25 °C after an hour of driving. In all of the cases, the temperature of cell 4 was slightly below the temperature of the other cells. This difference increased with the trip duration. This cell was positioned on the side of the module, which itself was on the side the pack. Which means the closest possible to the body of the vehicle, and that explains its tendency to be closer to the ambient temperature values.

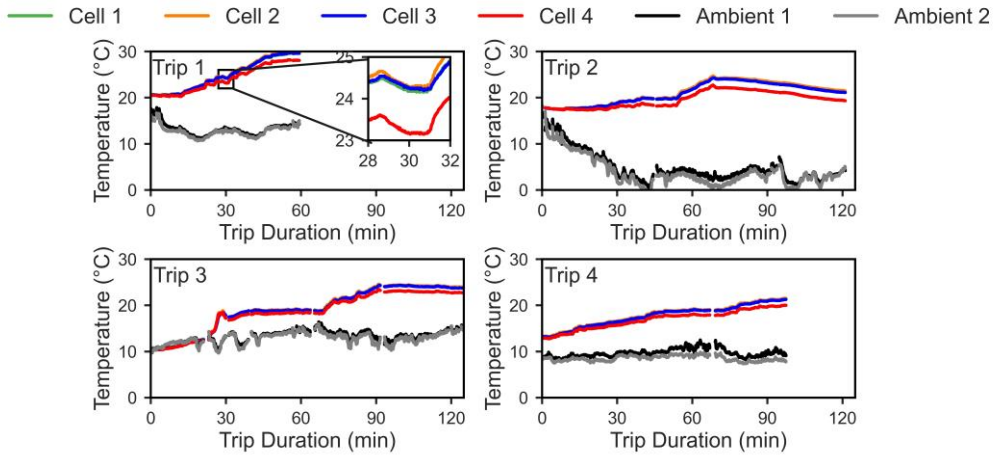


Figure 11. Temperatures of Cell 1, 2, 3 and 4 and ambient temperatures 1 and 2 in function of trip duration for four long trips

For the four examples mentioned, T_{cells} leans towards the 20 °C region as the vehicle is being driven. This is due to the active cooling/heating system. In order to examine relationship over the entire trips of the CEA campaign, the distributions of T_{amb} and T_{cells} are plotted in function of the trip duration in Figure 12.

As the trip duration increased, the distribution narrowed around 18 °C. The literature results are in accordance with the results obtained. It was shown by Schoch [142] that the cells' temperature was barely found to be above 30 °C with most of the temperatures between 10 °C and 25 °C.

Discussion. It was shown that there is a clear discrepancy between T_{cells} and T_{amb} , especially after 30 min of driving when the cells find themselves in their most optimal temperature range [191], [192]. This control over the temperature is mainly due to the Battery Thermal Management System (BTMS). In the case of the vehicle studied, the battery pack is integrated into a refrigerant circuit [142]. It has been shown that this type of BTMS can achieve a uniform temperature distribution within the battery pack [193]. However, the convergence of the temperature to their most optimal range requires some time after starting the vehicle. The temperature increase rate was measured to be around $0.84\text{ }^{\circ}\text{C}/\text{min}$ with a liquid cooling/heating system [194].

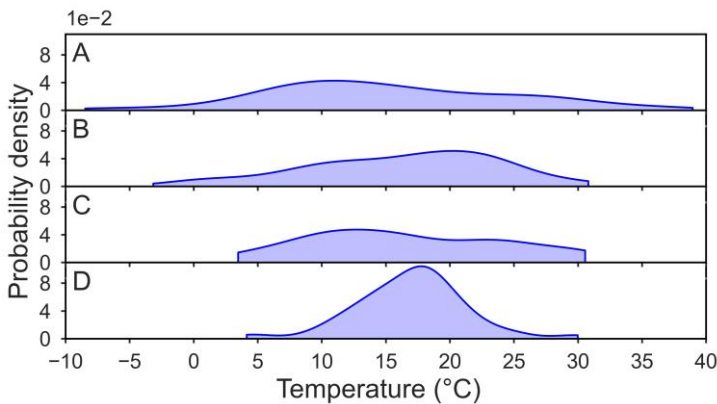


Figure 12. Probability density diagram of (A) the ambient temperature during driving times, (B) the cells' temperature for the first 15min of driving, (C) for the second 15 min of driving and (D) for more than 30 min of driving [140]

While the liquid and the refrigerant type systems aforementioned are known to be quite efficient, with the ability to guarantee a very low cell-to-cell temperature gradient within the pack [194]–[198], this might not be the case for air cooling/heating systems [195], [199]. Such systems are incompetent at extreme ambient temperatures [198], [200] due to their low heat transport capacity [201], an elevated time needed to heat up the pack [202] and a wider cell-to-cell variation ($>5\text{ }^{\circ}\text{C}$) [203]. Blömeke et al. [141] showed that in a 16 kWh Mitsubishi i-MiEV with a forced air type system [204], the temperature barely moves from its value at the beginning of the trip.

Associated Degradation Mechanisms. During driving, high temperatures (mainly above $35\text{ }^{\circ}\text{C}$ [159], [205]) do not only accelerated the SEI growth, but it can also lead to the dissolution of the active material of the positive electrode which will take part in the decomposition of the electrolyte and the formation of a passivating film on either electrodes [206]. Cold weather conditions will not only reduce the performance of the battery [207], but also induce particle fracturing on both

electrodes, due to the brittleness of the materials at low temperatures (mainly below 10 °C) [208]–[210]. This can lead to a formation of fresh SEI, a pulverization of the electrode material and a loss of contact with the current collector [41].

It has been shown that for battery packs with liquid and refrigerant type BTMS, the cases where the temperature of the cells exceed 30 °C or fall below 5 °C for a long duration are extremely rare [140], [155], [200], especially that the mentioned designs can afford a quite reasonable cell-to-cell variation. However, for short duration trips, the temperature of the cells might not reach the optimal range quickly, therefore inducing the aging mechanisms mentioned. In the case of the air cooling/heating system, these degradation mechanisms can happen much more frequently even for long trips, and damage the battery in a faster manner. Geotab concluded that aging rate of the Nissan leaf (air cooling/heating) is in average 4.2 % per year while the aging of the Tesla model S (liquid cooling/heating) is 2.3 % per year [35]. Even though the cooling/heating system is not the only factor that controls the degradation of the battery, it plays a reasonable role.

3.1.3 Charging conditions

Field data. The temperature of the cells is even more critical during charging sessions, due to both the harsh aging mechanisms [41], [68], [99] and the reduced charging efficiency [211]. The battery's useful energy decreases with decreasing temperature. This will impact the driving range and performance of the EV [190]. Furthermore, cells might experience a temperature increase during charging, which might cause other safety/aging issues [41], [212]. It is then important to monitor the evolution of T_{cells} during charging. The CEA campaign results are shown in Figure 13. No preheating of the pack was applied. The charging rates ranged between 1.5 kW (L1 charging – Level 1 corresponding to conventional residential settings) and 3 kW (slow charging).

Similarly to Figure 10 (A), the temperature of the cells is averaged (T_{cells}) and plotted in function of T_{amb} in Figure 13 (A). While the maximum T_{amb} captured during these charging session is 37.67 °C, the maximum T_{cells} was 33.11 °C. The minimum T_{amb} and T_{cells} values were respectively -5.87 °C and -3.49 °C. These results are quite similar to what was obtained during parking temperatures. In Figure 13 (B), it can be observed that, oppositely to Figure 10 (B), T_{cells} is much more likely to be superior to T_{amb} and can reach 15 °C more, especially in cold weather conditions. The probability distribution in Figure 13 (C) has a much different shape of the one obtained in Figure 10 (C). This one shows a much bigger probability of having a positive difference. The median value, represented by the red line, shows a value of 2.43 °C. Charging might induce some heating of the cells, which explains the higher median value when compared to parking conditions. This is especially true at cold weathers. Low ambient temperatures increases the resistance values and might therefore be the reason behind the abrupt T_{cells} elevations between -5 and 0 °C.

Otherwise, this difference does not seem to be very pronounced. T_{cells} was mostly affected by T_{amb} rather than the charging rates.

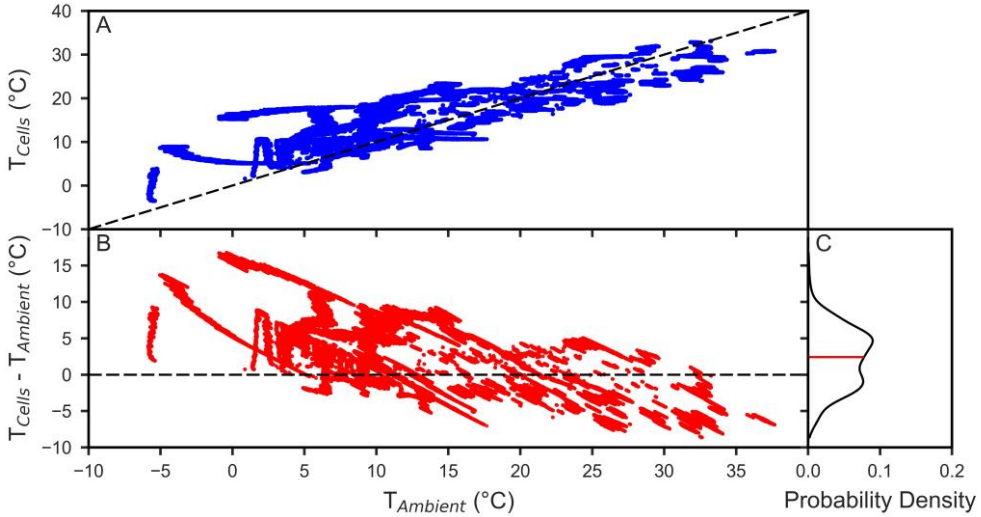


Figure 13. (A) Temperature of the cells in the battery pack plotted in function of the ambient temperature measured outside the vehicle during charging sessions. The black dashed line represents the identity function. (B) The difference between the cells' and ambient temperatures during charging sessions. (C) The probability density diagram of the difference between the cells' and ambient temperatures, with the red line showing the median value

Zou et al. [169] investigated the temperature of the cells with a charging platform that delivers an average of 5 kW. A temperature difference was noticed between the beginning of the charging session and the end, with the biggest difference (5 °C) being at low ambient temperature (10 °C) with respect to the lowest difference (3 °C) at 20 °C, which is in accordance with the results obtained in the CEA campaign.

Discussion. For low charging powers (L1 and slow), cells heating seems to be negligible. It is more pronounced at low ambient temperature though. Which means that cell heating is not an issue for this type of weather, and this type of charging stations. It is expected however, that for higher charging powers, a bigger temperature gain should happen. T_{cells} values falling below 0 °C are very rare. This is due, first, to the aforementioned heating, and second due to the thermal insulation of the battery pack. However, some charging cases were found around the 5 °C mark. It is worth then to examine what might happen in this case.

Associated Degradation Mechanisms. Low temperature conditions promotes slow lithium diffusion within the carbon-based electrodes (inducing a blocking of the diffusion paths) [68], minimal charge transfer kinetics and a smaller

conductivity in the electrolyte [213]. During charging, this activates lithium deposition, or plating, on the anode. Lithium plating is not only the result of a consumption of ions, but it can also transform into a potential safety risk as lithium dendrites growth become more prominent and can lead to short circuiting [68], [214]. Waldmann et al. [68] show that Li-deposition can be activated at 5 °C with a minimum constant current charging rate of C/2 (C-rate, with C being the nominal capacity of the battery cells) and a cut-off voltage of 4 V and above. Ge et al. [215] show that it can be triggered at -5 °C a C-rate of 0.65 C till a SOC of 100%, a C-rate of 1.3 C and a SOC of 97 % or even a C-rate of 2.6 C and a SOC of 22 %. In the case of the vehicle studied in the CEA campaign (21 kWh of installed battery capacity), a charging rate of 3 kW is equivalent to a C-rate of 0.13 C, which is not sufficient for the triggering of Li-plating. The 7 kW charger is equivalent to a C-rate of 0.3 C, which is still not sufficient, even at -5 °C. With the current charging practices (which will be further detailed in section 3.3), and the fact that the cells temperature is higher than the ambient temperature at cold weathers, low-temperature-Li-plating does not seem to be very alarming in weathers like this one.

3.2 Energy consumption

Expressed in Wh/km, it represents the energy delivered by the battery for the vehicle's functioning. It regroups the power needed for acceleration, as in the power to overcome air drag, rolling and elevation (grade) resistances. Furthermore, it includes the power needed for the 12 V devices, such as the cabin air conditioning, and more importantly the BTMS [26]. It was found, that it is dependent on four factors: the ambient temperature, the road type, the trip length and the vehicle weight.

3.2.1 Effect of ambient temperature on energy consumption

Field data. In order to visualize this relationship between the energy consumption and the ambient temperature, values from different studies were extracted and assessed in a single plot (Figure 14). For consistency purposes among the different studies, the increase in energy consumption with respect to its lowest value (%) was chosen to be the criteria to study. This is calculated using the equation (2) where E is the energy consumption (Wh/km) and E_{min} is the minimum energy consumption within the dataset.

$$\text{Increase in energy consumption (\%)} = \frac{E - E_{min}}{E_{min}} * 100 \quad (2)$$

Data issued from FleetCarma [158], [163] and Geotab [176], are in range rather than energy consumption. The inverse of the values was then taken in order to be included in the graph.

The black lines illustrate the second degree polynomial fit of the increase in energy consumption for the BEV (dashed line) and the PHEV (solid line). Calculating the fitting formula was done using SciPy libraries in Python [216]. The red square on the x-axis represents the temperature range where the minimum consumption values, identified on the x-axis by vertical lines, are located.

The trend seemed to be similar in all the cases, however at extreme the temperatures the energy consumption values were wider. This ended up in a funneling shape at the temperatures between 17.5 and 23.9 °C.

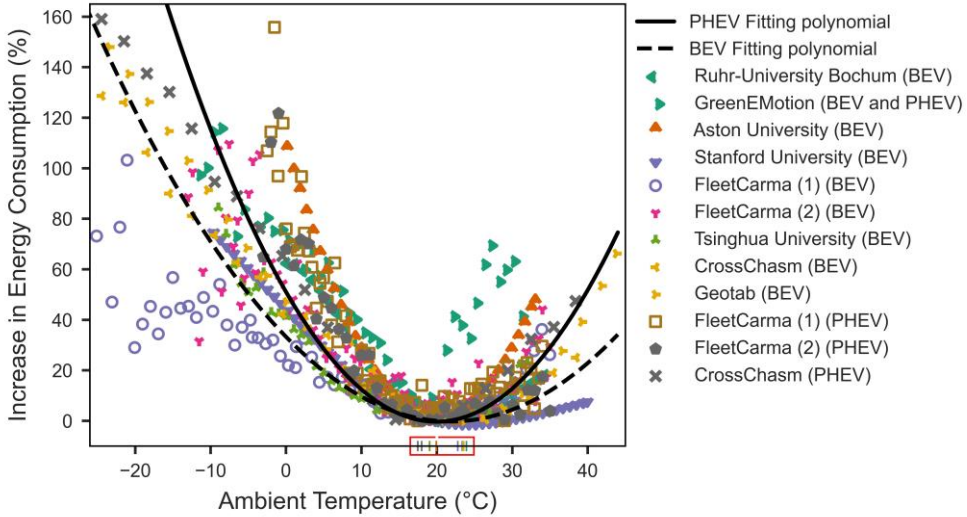


Figure 14. Increase in energy consumption (%) in function of ambient temperature issued from [143], [144], [153], [157], [158], [163], [168], [175], [176]. The legend refers to the “Source and Reference” of Table 3.

The PHEV and BEV second degree fitting polynomials are expressed in the following equations, where E_{BEV} and E_{PHEV} represent the energy consumption (Wh/km) in function of the ambient temperature and the lowest energy consumption value, E_{min} .

$$E_{BEV} = E_{min} \times [0.000702 T^2 - 0.0307 T + 1.3326] \quad (3)$$

$$E_{PHEV} = E_{min} \times [0.00129 T^2 - 0.0516 T + 1.5103] \quad (4)$$

It can be seen that data lack for the FleetCarma's PHEV (Chevrolet Volt) below -4 °C [158], [163]. In the case of some PHEV, the ICE solely alimnts the vehicle and heats up the battery, before it can be used.

As it impacts the energy consumption, ambient temperature influences indirectly the range of the vehicle too. The Norwegian Automobile Federation (NAF) tested the range of 20 best-selling electric cars in a cold and snowy Norway weather [145]. The ambient temperature varied from -6 to 3 °C. Results showed an average 18.5 % range

loss compared to the official WLTP (Worldwide harmonized Light vehicles Test Procedure) range, with a maximum value of 30 %, which is in agreement with the results shown in Figure 14. Similar results are found for Tesla vehicles' database [161], where the power demand is accentuated at extreme temperatures.

Discussion. The increase in energy consumption at low or high temperature, or the drop in range, is directly linked to the fact that the battery pack dedicates a big portion of its energy consumption to the pack and cabin warming or cooling [24], [27]. Thus energy is delivered to the heaters (resistance wires for example [202]), blowers, condenser and compressors etc. to supply the liquid and the refrigerant type systems. Air type systems demand less power from the pack, and passive cooling techniques (based on natural convection) require no power.

To illustrate this, the American Automobile Association (AAA) [159] calculated the driving range of a sample vehicle based on different drive cycles and by taking into consideration the influence of the BTMS. They concluded that the driving range decreases by 17 % and 41 % at 35 and -6 °C respectively, which is in accordance with Figure 14.

However, it should be noted that when the battery cell temperature is low, the loss of range is not only attributed to the increase in energy consumption, but also due to the loss of performance (lower diffusion, conductivity and reaction rates). When the temperature of the cell reaches its optimal operating conditions, the loss of range can then only be affected to the increase in energy consumption.

3.2.2 Effect of trip length on energy consumption

Field data. It was shown that the trip length can also affect the energy consumption, as illustrated in Figure 15 (the legend refers to the source in Table 3). Here, the increase in energy consumption (similarly to Figure 14) is plotted in function of the travelled distance. The energy consumption is inversely related to the length of the trip, with an abrupt decrease in the first 10 km of driving. Interestingly, this correlation is more pronounced at extremes temperatures [157]. The consumption increase obtained between 15 °C and 30 °C starts at around 190 % whereas at -15 °C it starts at around 330 %. This increase at extreme temperatures complements what is seen in the previous section.

Discussion. In the first miles of a trip, every vehicle is opposed to some fixed energy penalty linked to the start-up of the different electrical components. At lower or higher temperatures, the penalty is amplified due to both the cabin and the battery pack heating or cooling. It will take a while for the desired temperature in the cabin and in the battery pack to be reached, hence demanding more power from the pack during short trips. As the temperature might still be close to the ambient one, the increased power needed causes intensive stress on the battery cells. Over longer trips, this penalty is simplified, and the effect of the weather becomes less

pronounced as the target temperature of the pack and the cabin would be reached. Tesla Model S' user manual mentions “short trips” and “stop-and-go traffic” as an impact on the energy consumption [217].

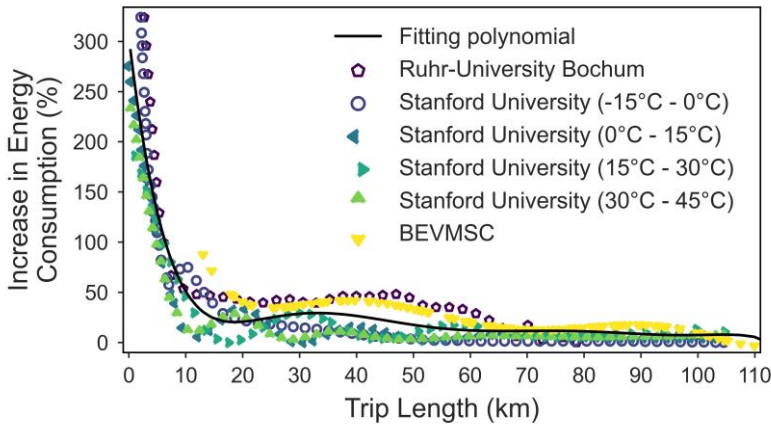


Figure 15. Energy consumption with respect to trip length issued from [143], [157], [169]. The legend refers to the “Source and Reference” of Table 3.

3.2.3 Effect of road type and vehicle mass on energy consumption

Beside ambient temperature and trip length, road type is also a main concern for the energy consumption. For a common ride, three main road types can be defined: urban roads, highway roads and a combination of both. According to EV-database, the energy consumption on highway is the highest [28]. It was found in [26] that the higher the speed of the vehicle is, the higher the air drag on the car is, causing the power demand to rise. Wager et al. [173] measures the energy consumption of a Nissan Leaf and a Mitsubishi i-MiEV on a highway. Their results weren't very different as they found that the energy consumption nearly doubles when the speed increase from 60 km/h to 110 km/h.

The WLTP is a driving profile that mimics the speed of the vehicle on four different road types levels: low, middle (urban), high and extra high (highway) [218]. It is used for electric vehicle range estimation, with a temperature range that varies from 14 to 23 °C, taking into account the auxiliaries' consumption. The table below shows the results of a WLTP parameterized for an average class 3b BEV with a weight of 1,800 kg and a width and height of 1.80 and 1.65 m respectively [28], [219]. The road resistances were set as advised by the official WLTP report [218]. A tank-to-wheel efficiency of 85 % was taken into account both for the delivered and the regenerative energies.

The results of the WLTP calculations are in accordance with the aforementioned studies. The higher the speed of the vehicle is, the higher the consumption is, to a certain extent that it doubles at highway routes.

Table 4. WLTP parameters assessment for an average BEV including the average energy consumption of the battery pack

	Duration (s)	Distance (m)	Maximum speed (km/h)	Average energy consumption (Wh/km)
Low	589	3,095	56.5	113.02
Middle	433	4,756	76.6	146.48
High	455	7,158	97.4	189.37
Extra-high	323	8,254	131.3	300.34
Total	1,800	23,262	-	-
Average	-	-	46.5	187.30

This relationship can be visualized too by plotting the power delivered and regenerated by the battery vs the speed of the vehicle, which could be done based on the raw data from the CEA campaign [140] (Figure 16). Here the P-rate was calculated by dividing the battery instantaneous power by the installed battery capacity in the vehicle. Positive values represent acceleration (discharging) and negative values represent regenerative braking power (charging). The histogram on the right represents the distribution of the different values encountered, and shows very few results above the 2 P mark or below the -1 P mark. The upper and lower limits for the P-rate during acceleration and regeneration can be visualized by the grey dotted lines. These limits are imposed by the drive train capabilities. Very similar results were also found in literature [160], [220].

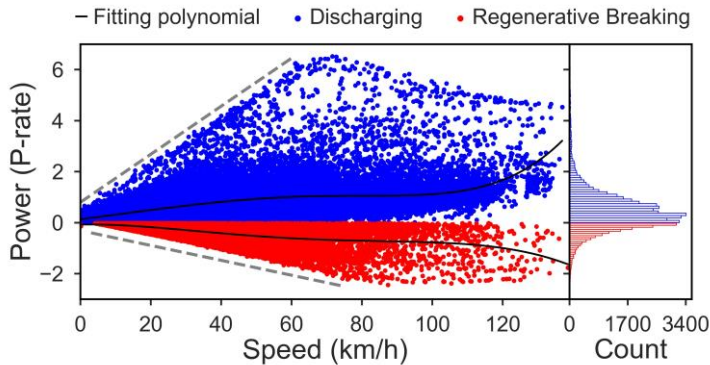


Figure 16. Power (P-rate) in function of the vehicle speed (CEA campaign)

Discussion. The energy consumption is impacted by the road type. For highway trips, the main barrier is the air drag [26], which explains the increasing trend of the energy consumption and power rate with the speed in the presented results.

The height difference between the point of departure and the destination is obviously a factor that should be taken into consideration, even though it wasn't mentioned. Asamer et al. [26] show that road grade becomes an issue when the destination altitude is 500 m higher.

3.2.4 Effect of vehicle mass on energy consumption

Field data. The mass of the vehicle impacts its consumption too. The heavier the vehicle gets, the bigger the power demand will be. In order to illustrate this, the WLTP energy consumption and the real energy consumption of 16 commercial BEVs are plotted in function of their weights. The data are taken from ev-database.com [28].

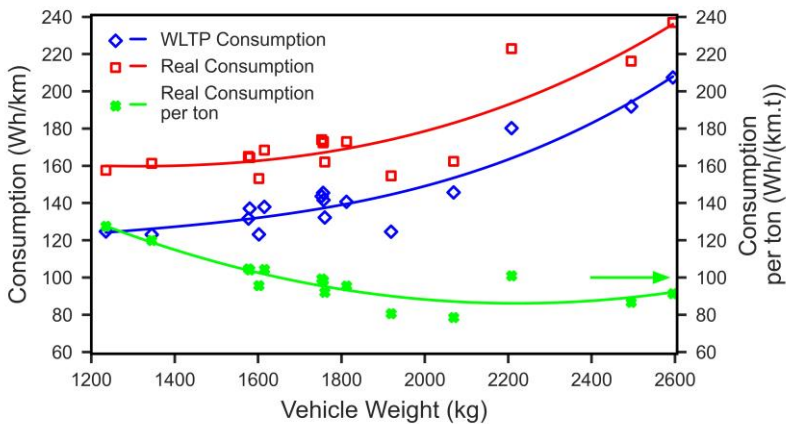


Figure 17. WLTP Consumption (corrected at 14 °C), Real Consumption (left axis) and Real Consumption per ton (right axis) plotted in function of the vehicle unladen weight

The real consumption seemed to be in average around 17.7 % higher than the WLTP consumption, which is not far from the results obtained with the NAF [145] (18.5 %) and from Rastani et al. [221] (21.6 %). This can be due to several reasons. First and foremost, the WLTP is based on specific road factors, e.g. a null gradient, fixed rolling and air resistances, which might not reflect the real conditions. Second, the charging losses are not taken into consideration in these WLTP measurement. Rastani et al. [221] show that charging losses can account for an additional 9.6 % of consumption for 1 phase 10 A charging (2.3 kW) compared to 3 phase 16 A charging (11 kW). Finally, the auxiliary consumption can have a share in this difference, even if the WLTP consumption is corrected at 14 °C.

Interestingly, the real consumption per ton alters around 100 Wh/(km.t) with an average of 98.6 Wh/(km.t).

Discussion. The vehicle mass impacts the consumption as a bigger power will be needed to propel the vehicle. The bigger the mass is, the bigger the consumption and the lower the range. This is even more pronounced at high speed profiles (Figure 18).

By taking the energy consumption of the overall WLTP profile and the one of the extra-high phase separately, the range of both was calculated in function of the installed battery capacity (from 2 kWh to 120 kWh) and the mass of the vehicle (from 1300 kg to 3000 kg) (Figure 18). The maximum value of a WLTP autonomy was around 780 km, while the extra-high (highway) maximum autonomy was around 460km (for a vehicle with a weight of 1,300 kg and a battery capacity of 124 kWh). Moreover, a vehicle with a weight bigger than 2,000 kg could barely reach a highway autonomy of 400 km, even with a battery capacity of 120 kWh.

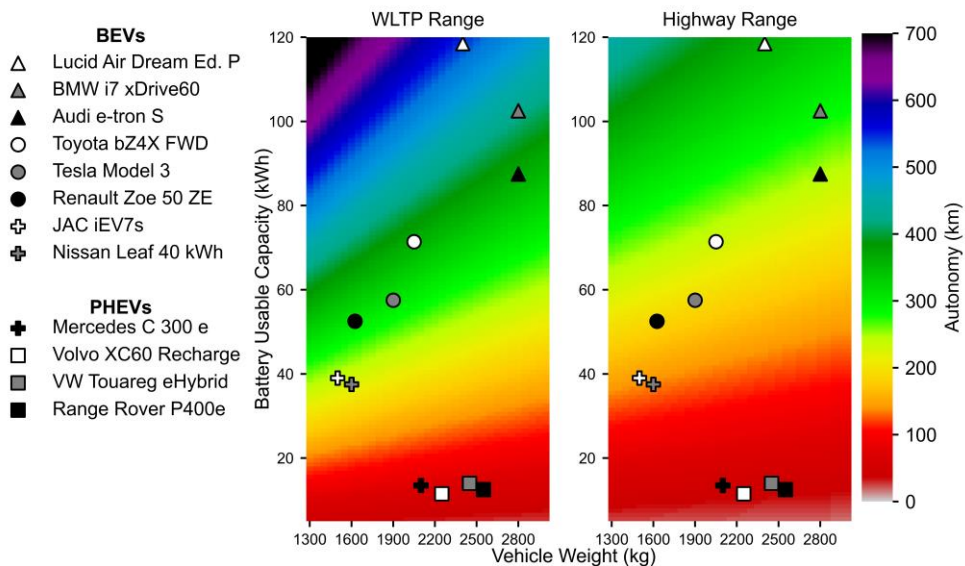


Figure 18. Impact of vehicle weight on its WLTP autonomy (left) and on its highway autonomy (right) in function of the battery installed usable capacity (kWh). The example of some vehicles are pointed out on the graph using the mass of the vehicle and the usable capacity of the battery from [28], [222]–[225]

The limitation of this results lies in the fact that a single frontal area (a width of 1.8 m and a height of 1.65 m) and a single tank-to-wheel efficiency (85 %) were taken into consideration for all the cases. While these two factors help in increasing the autonomy, their variation goes beyond the goals of the publications. The objective here is to have an idea of the importance of weight and road type on the performance of EVs.

Associated degradation mechanisms. An elevated discharge rate commonly induces particle fracturing due to the abrupt change in the electrodes' volume [99], [226], [227]. This can equally lead to the loss of contact between particles, loss of contact with the current collector and therefore a loss in both the active material and in lithium inventory [41]. These mechanisms are accentuated when the battery is at a cold temperatures due to the electrode material brittleness [208]–[210]. This tends to happen especially for short trips, where the BTMS cannot completely achieve its goal.

A high discharge rate induces also self-heating of the battery which will itself result in the previously mentioned phenomena, such as the SEI growth [41].

An elevated energy consumption is considered to be harmful to the battery cells when the equivalent discharge power rate, or P-rate, finds itself above 1 P [99], [226], [227]. Figure 19 shows the relation between the energy consumption, the battery pack installed capacity, the speed of propulsion and the P-rate, based on equation (5).

$$P_{rate} = \frac{Energy\ Consumption * Speed}{Battery\ Capacity} \quad (5)$$

In Europe [228], around 30 % of the average tip speed is between 50 and 100 km/h, and 10 % are above 100 km/h. For such values and for small battery capacities and elevated energy consumptions, high P-rates can be attained and can harm the battery. On the opposite, for battery capacities above 70 kWh, P-rates higher than 1 are rarely reached, even for high speed values. Increasing the battery capacity is thus a way to avoid this type of stress on the cells.

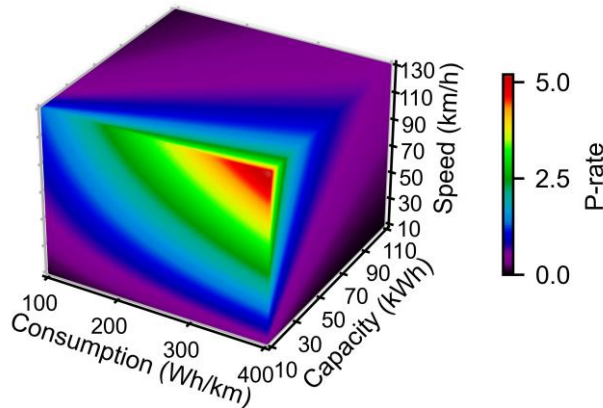


Figure 19. 3D heat map showing the evolution of P-rate with the energy consumption (Wh/kW), the speed of propulsion (km/h) and the battery installed capacity (kWh)

It should be noted however that dealing with the discharged power passing by the energy consumption gives an average view of the power demands. However, elevated peak power demands are required for acceleration purposes. This can be visualized in Figure 16. The trend in the acceleration power is less than 1 P for less than 70 km/h, and ranges between 1 and 2.5 P above 100 km/h. This is in accordance with the 3D-plot of Figure 19 for a battery capacity of 21.6 kWh. However, the full spectrum of power demands reaches values up to 6 P (Figure 16). The density diagram shows that values above 2 P occurred relatively rarely, as they correspond to the occasional acceleration demands.

The impact of constant current discharge is highly studied in literature, but additional studies should be done to investigate of occasional peak power demands.

3.3 Charging power

Charging impacts the aging of the battery depending on its frequency and its power rate. Thus the goal behind this section is to identify the different types of charging and to analyze the charging trends of EV users.

Field data. Different charging types exists nowadays [229]. The conductive charging, being the most common one, exists under three families.

First, the Level 1 (L1) charging. The charging power is between 1.4 and 1.9 kW (120 V – 12 to 16 A) [230]. For the average usable capacity of EVs (nowadays 61.7 kWh [28]), the L1 delivers, in terms of P-rate (h^{-1}), $1/37$ P. In other word, it needs 37 hours to fully charge an average EV. It is the most basic charging method as every EV comes with an adapter for an 120 V outlet, and simple residential charging is classified as L1 charging.

Second, the Level 2 (L2) charging. Its charging power range is very wide and dependent on the charging facility. It varies between 2.5 and 20 kW, typically 7 kW (208 or 240 V – 12 to 80 A) [230], [231]. For the average EV, it delivers anywhere from $1/25$ P to $1/3$ P, and typically $1/9$ P. It is the most common charging method. Lots of EV users install L2 charging facilities at home and it is found in public areas, shopping centers and workplaces.

Then comes the DC Fast Charging (DCFC). It can deliver from 50 kW up to 350 kW [230], [231]. For the average EV, this is equivalent to $1/1.2$ P and to 5.67 P, respectively. It is usually located in high-traffic spots or along highway corridors.

In the US, in Q4 of 2021, the L2 charging dominated the current trends of EV charging stations whether it is residential (86.2 % of charging units), public (80 %) or workplace (over 95%) [232]. Similar results were obtained by the Idaho National Laboratory (INL) [164]. In Europe [147], [233], in 2020, L2 3 kW facilities represented around 36 % of the total share, the chargers between 10 and 22 kW constituted around 45 %, the 22 kW to 50 kW chargers had a 15 % share.

According to [164], [234], in the US over 90% of charging is done either at home or at the workplace, and a large percentage is done at night [167], [235]. In a European study [147], it was shown that 60% of the charging were residential and around 15 % at work. A survey made in Paris, France, [148] showed that 94 % of the EV users prefer to charge at home. Other surveys done in Portugal [150], Japan [171] and Australia [174], showed very similar results.

Discussion. In Europe as in the US, the L2 charging is leading [236]. So charging power is most commonly around 7 kW, or 1/9 P and maximum 20 kW, or 1/3 P, for today's average capacity.

It was shown too that for a big portion of the EV market all-over the world, charging is done quite frequently, at home or at work, when the opportunity offers itself. This abundant charging reflects what is known as "range anxiety". This behavior towards the EV technology can simply be explained as the fear of running out of energy before reaching another charging station [237].

Associated degradation mechanisms. The two main degradation mechanisms that might occur at strong charging power rates are the particle cracking, similarly to the discharging rates [210], and the Li metal deposition at the carbon based negative electrodes. At high charging rates, the transport of ions from the positive to the negative electrode is faster than usual. This can lead to a blockage of the diffusion paths inside the negative electrode and an accumulation of lithium on the electrode/electrolyte interphase. An electrode potential lower than 0 V vs Li/Li⁺ favors the formation of metallic lithium. This will mainly consume usable lithium or even hinder some intercalation sites, hence reducing the accessible capacity [68].

A low cell temperature favors the potential of the negative electrode to get below 0 V vs Li/Li⁺. A charging rate above 1 P and a cell temperature below -5 °C favors this mechanism to occur [68], [215]. This last one is especially true if the charging is made up to elevated SOC levels, which will be further discussed in the following section. Thus, two conditions should be present to induce this mechanism: a low cell temperature and a power rate above 1 P.

An elevated P rate can occur for vehicles with a usable battery capacity which is equal to power rate. As the most common charging method is the L2, the harmed EVs are then the ones with usable capacities of between 2.5 and 20 kWh. The average usable battery capacity for BEVs is around 61.7 kWh [28] so the vehicles with less than 20 kWh are mostly old models. However, this might impact PHEV batteries, which are typically between 10 kWh to 30 kWh, especially if they are not equipped with a pre heating option.

It should be noted that publications found in literature mostly deal with constant current experiments whereas in real application the charging is always delivered in terms of power. Furthermore, for rapid chargers the power rate is also rarely constant from the beginning till the end of charge. It follows a decreasing trend when

the SOC surpasses the 50 % mark, and this is to reduce the occurrence of Li-plating [238], [239]. Lab experiments should be more representative of real charging scenarios in order to have a clearer view of the degradation mechanisms.

3.4 State of Charge (SOC) and Depth of Discharge (DOD)

The SOC is another main factors that impacts the aging of the battery. Before looking at field data, it is important to differentiate the absolute (or real) SOC from the user SOC, and the different operational strategies depending on the EV type.

The user SOC is the value that the driver notices on the board of the vehicle. For a BEV, the user SOC is expressed in percentage of the remaining range or allowed battery capacity. The real (absolute) SOC, however, is the one that reflects the average SOC of the battery cells. It ranges from around 90 % to 20 % during normal usage, preventing the upper and lower regions of being reached both for aging and safety reasons [35], [240], [241]. As shown in [242], an absolute SOC 100 can cause a very harmful stress on the battery when compared to SOC 90 during calendar aging. This discrepancy between the real and user SOC is illustrated in Figure 20 [140]. In the case of HEV, the battery operates in CS mode in a mid-range SOC, commonly between 70 and 30 % [29], [152]. For PHEV batteries the CD mode operates roughly between SOC 90 and 30 %, whether the CS mode operates between 40 and 20 % [29], [240], [243]–[245]. The field studies that will be mentioned later deals with the user SOC rather than the real SOC, as the data are gathered from the electric board of the vehicle.

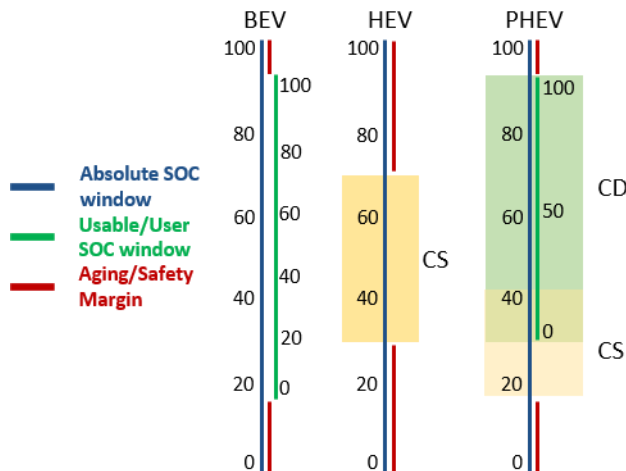


Figure 20. Absolute and usable SOC values depending on the vehicle type

Field data. The cell average voltage in function of the user SOC is illustrated in Figure 21, using the field data obtained in the CEA campaign [140]. Here the cells'

voltage is obtained via the voltage of the pack considering a perfect homogeneity in the pack (Figure 11). The safety and aging margins can be seen with the help of the black and red dashed lines illustrating the operational limits (absolute SOC) of the battery [246].

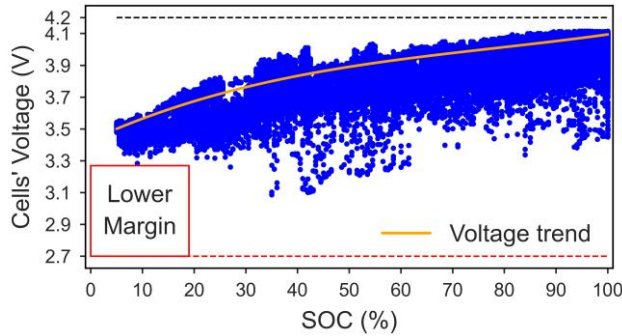


Figure 21. Average cell voltage versus user SOC from the CEA campaign [140]

The SOC at the beginning of charging events and end of charging events have been widely studied in literature. The following figure illustrates the results extracted from different studies, published in the form of histograms [139], [144], [166], [169], [172]. Each point represents the mid-point of the bins, and the width of each horizontal bar represents the range of the bins. The legend refers as well to the country where the studies were undergone. The results from Green e-Motion cover BEV and PHEV data whereas the others cover only BEV.

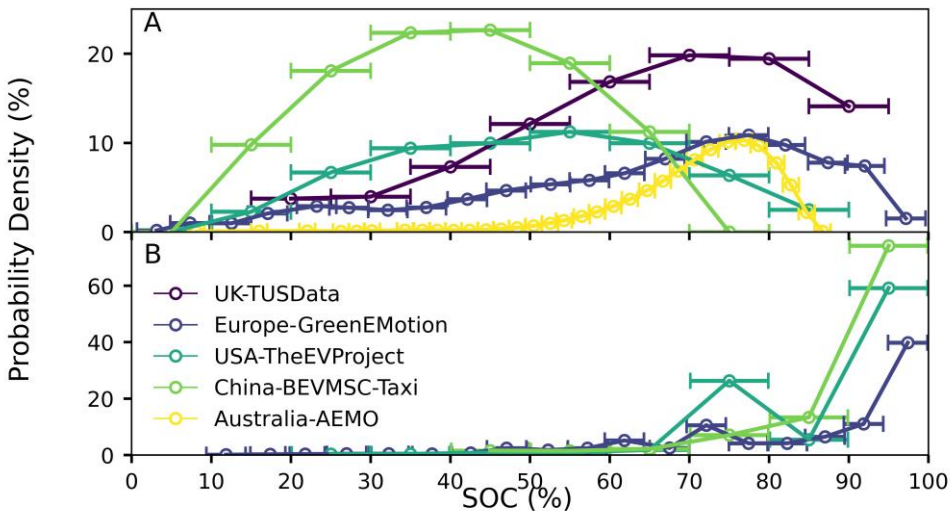


Figure 22. SOC at the beginning (A) and end (B) of charging events [139], [144], [166], [169], [172]. The legend refers to the country of the study, and the “Source and References” from Table 3.

These results are in accordance with other literature findings made in different countries such as Canada [163] (average SOC before charging of 65 %), the Netherlands [146] (50% of plug-ins with SOC above 60%), Japan [171] (average SOC before charging of 70 %) and UK [153] (65% of the trips started with a SOC of 70 % or higher). These were not included in the previous figure as the information wasn't explicitly exhibited.

A very similar result was shown in a study done by “Transport Canada” [89], [247], where two BEV were driven on predefined roads. With a daily distance of 100 km, which is much higher than the average daily driving range in Canada or even in the US (around 64 km [248], [249]), and with a charging frequency of twice a day (mid-day and overnight), the minimum SOC reached was most frequently between 40 and 50 %. Which means that with realistic driving distances, the SOC will barely reach such values, which is in agreement with Figure 22. Schoch [142] showed that the most occurred DOD values are between 20 and 40 on the upper SOC range, above 65, for a BEV. It was also concluded that 80 % of the time the SOC in calendar conditions was above 55 %, and values below 50 % were attained less than 15 % of the time.

Discussion. SOC at beginning of charge. Charging tends to start above the 50 % mark for private users. In the US, the results seemed to be spread over the entire range, with the average skewed to the 50 percent mark [166]. This is due to the elevated average trip length when compared to European countries (in average 17.90 km vs 11.97 km respectively [228], [248]). Furthermore, short trips (less than 10 km) are very common in European countries (60 to 80 % of the trips [228], [250]). Whereas in the US [251], less than 60 % of the trips were short, and 31 % were between 10 and 32 km.

The distance travelled is not only dependent on the country, but also on the type of vehicle used. FleetCarma [163] showed that the daily travelled distance with a Nissan Leaf (BEV) is 32.1 km while it is 80.8 km with a Chevrolet Volt (PHEV). The problem of range isn't much of an issue with the PHEV. This proves that the charge depleting mode of a PHEV is more prone to be completely used, especially that the battery of a PHEV can make in average between 30 and 90 km.

The previously mentioned studies [147], [148], [150], [167], [171], [174], [234], [235], illustrated the abundance of opportunity charging, which is mainly due to the users' range anxiety. Adding this to the plenitude of short trips, the occurrence of elevated SOC levels during the life of a battery is now comprehended.

For taxis, however, the trend seems to be skewed to the 40 % mark, as they are prone to drive for very long durations before charging.

SOC at end of charge. As charging mostly starts at high SOC marks, and is done for long durations, it will end most of the time at the maximum SOC (Figure 22 (B)). A tiny peak appears around the 70 % mark for private users and not for taxis. This is another instance of abundance charging, in which private users will start charging at the presented opportunity. For taxi drivers, the SOC should be at its maximum before the start of a working day.

Associated degradation mechanisms. Making the battery cycle at elevated mid-SOC regions induces SEI formation [252] due to the low potential on the negative electrode. Li deposition on the carbon-based negative electrode tends to be formed when the charging is stopped at cell voltage of 4.2V (with conventional lamellar cathodes) [68]. However, the user SOC of 100 % corresponds to an absolute SOC of 90%, which means a voltage between 4.07 and 4.10. Furthermore, the charging rates tends to be at their minimum at high SOC levels. Li deposition is therefore not considered to be alarming, unless the cell-to-cell voltage variation is very wide, or the temperature regulation during charging is not applicable and the cell temperatures is less than -5°C [215].

4. Risk Probability Number (RPN) analysis

In the previous section, the factors of stress were assessed in EV usage conditions. An RPN analysis can now be done in order to evaluate their impact on the aging of LIB cells [105].

As mentioned in literature [105], [133]–[136], the RPN is the product of three elements ranked over 10: the severity (S) rating of the stress [253], its probability of occurrence (P) rating, and its ease of detection (D) rating. The higher the S rating is, the harsher the stress is on the battery. The higher the P rating is, the bigger its probability of occurrence. Finally, a high D rating means that the impact of the stress factor on the battery is hardly detected, while a low rating indicates the opposite.

It has been shown that to detect a certain failure mechanisms in the battery, ex-situ or complex in-situ techniques are needed [40], [54], [134]. Detecting them during the usage without the need of post-mortem analysis or in-depth electrical characterization is somehow difficult to be done nowadays. Therefore, the D element is omitted in this RPN analysis.

The electrical stresses (charging and discharging regimes, SOC and DOD) do not induce the same stress over the entire temperature spectrum [254]. So a new factor is introduced: the P_T , and it represents the probability of occurrence of the given temperature.

Furthermore, these stresses are different from an EV application to another. So the P factor introduced earlier on, will now be written P_x where x =BEV, HEV or PHEV.

Hence, we introduce the “adapted RPN” analysis, expressed as the following.

$$RPN = S * P_T * P_x \quad (6)$$

The higher the RPN is, the more care should be given to this stress factor. In other words, the stress factors with the highest RPN should be the ones used during accelerated aging tests to obtain usage representative results [105], [255].

In this case study, the P_x values were assigned qualitatively by referring to the aforementioned results and discussions. The P_T values are based on probability of occurrence calculations obtained in the CEA campaign.

The S level is evaluated using equation (7).

$$S = \left(1 - \frac{Ideal\ Rate}{Rate}\right) * 10 \quad (7)$$

The capacity “rate” loss for each stress factor (% of capacity fade/cycle or % of capacity fade/month) was obtained from [34], [42], [118], [226], [242], [253], [254], [256]–[260]. Whereas the “ideal rate” loss was obtained from [47], [261]. For calendar aging conditions, an LIB should hold for 10 years before reaching its End Of Life (EOL) [47]. The EOL is considered to be 80 % of the initial capacity. Which means that the ideal rate of calendar aging is 0.17 %/month. For a 10-year life, it is mentioned in [261] that the battery should hold for 5000 full cycles before reaching its EOL. The ideal mean rate is then 0.0040 %/cycle over the lifetime of the battery. For simplicity reasons, only NMC/Graphite cell chemistry will be focused on, as it is the actual dominant technology.

The RPN analysis is presented in

Table 5, where score above 200 (>200) are considered harmful and are colored in red, scores between 100 and 200 (>100 and ≤200) are less harmful and colored in orange, while the rest are considered not harmful at all.

4.1 Breakdown and Discussion of the RPN analysis

4.1.1 The BEV batteries

The most important stresses found in a BEV battery was cycling at high mid-SOC regions at mild and low temperatures, and parking at high SOC levels. The “range anxiety” behavior is the reason behind this stress.

The discharge power in a BEV is not much of a concern at mild temperatures. However, it is at low temperatures, as the battery delivers a big portion of its power to the pack thermal management, especially with active cooling/heating systems. This is especially true for short distance trips where the battery temperature is still

low. The coexistence of these two stresses (low temperature and high discharge power) is therefore highlighted.

4.1.2 The HEV batteries

HEV batteries (power type) operate at central mid-SOC regions. So everything related to high SOC stresses do not happen in the life of a power type battery in EV applications. The two most common stresses are cycling, in a CS mode, with high rates at mild and low temperature regions. This is the only factor that can harm the battery in real usage conditions, as it induces particle fracturing, especially at low temperatures.

Table 5. RPN analysis of LIB for automobile application for a central European weather

Driving/Charging Conditions				BEV		HEV		PHEV	
Cell Temperature	P _T	Stress Factor	S	P _x	RPN	P _x	RPN	P _x	RPN
High (>35 °C)	1	High mid-SOC	6	9	54	0	0	7	42
		Wide DOD	9	2	18	0	0	8	72
		Discharge power	8	5	40	10	80	6	48
		Charge power	8	2	16	0	0	2	24
Mild	6	High mid-SOC	5	9	270	0	0	7	210
		Wide DOD	7	2	84	0	0	8	336
		Discharge power	7	2	84	10	420	4	168
		Charge power	8	2	96	0	0	4	192
Low (<10 °C)	3	High mid-SOC	5	9	135	0	0	7	105
		Wide DOD	9	2	54	0	0	8	216
		Discharge power	8	7	168	10	240	8	192
		Charge power	9	2	54	0	0	2	53

Parking conditions

Cell Temperature	P _T	Stress Factor	S	P _x	RPN	P _x	RPN	P _x	RPN
High (>35 °C)	1	High SOC	8	9	72	0	0	7	56
Mild	5		5	9	225	0	0	7	175
Low (<10 °C)	4		0	9	0	0	0	7	0

4.1.3 The PHEV batteries

For PHEV batteries (energy/power type), the high mid-SOC region and the high SOC parking are less impactful than in a BEV case as consumers tend to drive longer.

However, a wide DOD spectrum is more prone to happen, explaining why this factor is considered harmful both at mild and low ambient conditions. Even though range anxiety seems less pronounced with the PHEV technology, opportunity charging was still found in the consumer behavior, explaining the high RPN level for elevated SOC stress.

Oppositely to a BEV, the discharged power is considered a harmful stress at mild temperatures. This is due to the low installed battery capacity (Figure 19). This stress is more pronounced at low temperatures. It should be noted however that for some PHEV, low temperature operation ($< 0\text{ }^{\circ}\text{C}$) is avoided. Furthermore, during the CS phase, similarly to an HEV, high power cycling is also considered as a stress at lower SOC regions.

4.1.4 Limitation of the RPN analysis

One of the major limitations of the RPN analysis is the discussion around range anxiety inducing high SOC stresses. Different strategies are currently being adopted to alleviate this behavior such as increasing the pack capacity, applying battery swap, implementing more DCFC infrastructures, or even battery in route charging technics [236]. If range anxiety is strongly present with today's usage, it can potentially disappear with the deployment of the mentioned, or other, solutions. Therefore the RPN analysis should be re-evaluated with time.

The location where the RPN analysis is done is another issue. As mentioned earlier, the P_T evaluation was based on the weather of Grenoble, which can be very similar to central European or central western USA weathers. Things will probably differ if the location is different, for example southern Europe, where the P_T at high temperatures can reach values above 3. In the current case, none of the stresses was considered impactful at high temperatures ($> 35^{\circ}\text{C}$).

Another limitation is in the evaluation of the factor of stress and the rate loss calculation. In order to be consistent among all publications, the capacity in Ah was here chosen to be the performance criterion. However, the energy capacity calculation and the increase in internal resistance are two other criteria that are mentioned in some standards [45], [47]. In the EV industry, the WLTP range is the criterion that defines the EOL. These mentioned criteria can evaluate differently the S value.

The EOL level is chosen to be at 80 % of the initial capacity. This custom is very common in the field of LIB and it was firstly announced by USABC in 1996 for Nickel Metal Hydride (NiMH) batteries [262]. It should be noted that the NiMH batteries specific energy is about half of LIB' [11], [263], and therefore using the same EOL value might not be very representative. Saxena et al. [264] simulate vehicles from the U.S. National Household Travel Survey (NTHS) and prove that up to 40% of usable capacity, the battery can still serve the travel need of more than 65% of U.S.

drivers. Further investigation should be done to find a better EOL level for EV applications.

Finally, it should be noted that most of the literature focuses on the aging single battery cells. Studying the aging of the entire pack together should bring more consistency in the results.

5. Conclusion and perspective on battery testing

The impact of the usage of EVs on the occurrence of stress factors on the battery cells was investigated throughout this review. Data issued from studies all around the globe were assessed, along with some raw data analysis from a BMWi3 driven in Grenoble, France. Operational differences were highlighted concerning the different types of EVs, and the most significant stress factors were underlined.

It was found that the temperature of the cells is not directly correlated to the ambient temperatures when the car is parked and this due to the thermal insulation of the pack. During driving, two stresses coexist for short trips: elevated discharged power and low/high temperatures. This is especially true for EVs with active pack thermal regulation. For long trips, the battery temperature reaches its optimal range, removing the impact of the temperature. It was shown that the smaller the pack capacity is, the bigger the discharge stress. For EVs with passive pack thermal regulation, the impact of the temperature is present over the whole trip. Charging temperatures are not very critical from an aging perspective, as the charging methods applied nowadays don't necessarily induce the very unwanted Li-plating. Elevated SOC ranges are very common for BEVs and PHEVs and this is due to the "range anxiety". For BEVs, the DOD is usually quite low for European countries as most of the trips are less than 10 km, which is not the case for Northern American countries. For PHEVs, higher DODs are more prone to happen as their battery capacity is in average around half of the BEVs' battery capacity. HEVs operate at middle SOC regions so these stresses are inexistent.

The key takeaway of the study is the RPN analysis made in section 4. The stress factors depend highly on the application, and durability tests should be done differently. For energy type cells, accelerated aging can be done by using the high SOC as an accelerating stress factor for calendar aging, and narrow DOD cycling in high SOC regions, along with high discharge power rate at low cell temperatures. For power type cells (HEV), high power cycling is the main stress factor within the middle SOC region both at mild and low temperatures. To finish, energy/power types cells dedicated for PHEV applications can be accelerated by high discharge or charge power rates over a wider DOD window (from SOC 90 to 30 %), both at mild and low temperatures. For calendar aging, high SOC levels can be used as an accelerating stress factor.

It should be noted that, depending on the EV technology, time and space, the RPN analysis should be re-evaluated as customer behavior can differ. The same is true for the temperature probabilities of occurrence.

Accelerating the aging of an energy type battery by cycling over a full DOD is what happens frequently in literature. But it can be seen in the RPN analysis that a full DOD rarely occurs in real life situations. Another example is the distinction between the absolute and user SOC. Lots of examples can be given from literature where the batteries are tested over their entire absolute SOC region, e.g. from 2.7 V to 4.2 V. Whereas it can clearly be seen from Figure 21 that these values are never reached in real conditions. In the newest versions of the USABC standard for battery testing [47], [90], this distinction is made.

The RPN analysis helps in identifying the most influential stress factors in the service life of an EV battery, and serves as a guide for parametrizing and designing reliable accelerated aging testing.

Chapter 4 – Battery Electric Vehicle driving campaign

Highlights

- Launched an 11 months driving campaign using a fully monitored BMWi3 60 Ah vehicle
- 24 drivers volunteered to use the vehicle for their home-to-work trips
- Thermocouples were positioned on the cells inside the pack
- Measurements were done during driving, charging and parking conditions

It was shown in chapter 3 that literature data don't always give access to some important information, such as the temperature of the cells during operation. The mentioned BMWi3 in chapter 3 was fully monitored to provide such information, but the data issued from few work trips. The vehicle wasn't used daily, so reliable data analysis and solid conclusions about driving and charging couldn't be drawn. The goal behind this chapter is to use the same vehicle in an experiment where it will be used daily by volunteers from CEA for typical home-to-work driving.

1. Introduction

The instrumented BMWi3 mentioned and elaborated in the previous chapter was used here to carry out a daily usage study. The goal is to benefit from the accuracy and richness of the data that can be exploited in the instrumented BMWi3, and carry out a representative usage experimentation. The obtained information can then complement the results of the RPN matrix deduced from Chapter 3, in the purpose of a better understanding of the BEV batteries stress factors.

In this chapter, first, the methodology and the experimental protocol are detailed. Second, the results are illustrated and discussed. The underlined features are the range variations of the vehicle, the SOC levels, the charging and discharging data and the temperature of the cells. Finally, results will be discussed and compared to the results obtained earlier on.

2. Methodology

The driving campaign experimentation started on the 20th of September 2021 and ended on the 20th of August 2022. It happened in the Grenoble-Alpes metropole, in France. The following subparts elaborate the instrumentation of the vehicle, the data harnessing and processing, as well as the campaign protocol.

2.1 Vehicle instrumentation and data harnessing

The vehicle consists of an all-electric BMWi3 60 Ah (Figure 23), bought by CEA in 2016 in the framework of a project. Since then, it was parked most of the time fully charged, and travelled 5,000 km.

During this project, it was instrumented as explained in the previous chapter. Briefly, the vehicle was equipped with over 70 thermocouples from the entire architecture of the battery pack to the vehicle level. In the purpose of this study, data from the thermocouples that were implemented on the cells (4 thermocouples) and the ones that measured the external temperature (2 thermocouples) were extracted and studied. The goal is to capture the stress factor in question, which is the temperature of the cells.

Temperature measurements were done on a 1 Hz frequency, while other electrical and GPS measurements were done on a 10 Hz frequency, using a data logger device.

Raw data were sent daily to the cloud in a CAN file format (.mf4), before being converted to “.csv” files. Next, in the framework of this study, Python scripts were developed to pre-process and clean the data (e.g. removing erroneous values) using the “pandas” module [265]. Additional Python scripts were developed for data post-processing using the “numpy” module [266], for data representation using “matplotlib” [267] and “seaborn” [268], and for mapping representation using “plotly” [269].

Due to some issues related to the data logger, temperature measurements during driving couldn't be retrieved effectively during the first part of the driving campaign, i.e. the months of September till December of 2021. The data logger was replaced by another newer version in the beginning of January 2022.



Figure 23. The BMWi3 during the driving campaign. On the left: During a charging session with a 2 kW L1 charger. On the right: During the dawn of a cold winter day in the Alps

2.2 Experimental protocol

It was shown in chapter 3 (Figure 15), that the stress factors can be dependent on the travelled distance. Three home-to-work distances categories were identified by the French INSEE (Institut National de la Statistique et des Etudes Economiques) [270]: the short (< 10 km), the medium (10 to 20 km) and the long (20 to 40 km).

For this reason, an invitation for the participation in the study was sent to the CEA's department of electricity and hydrogen for transportation (DEHT). 24 persons volunteered to participate in the study. They were categorized accordingly to the mentioned distances:

- Category A, short distance (<10km);
- Category B, medium distance (10 to 20km);
- Category C, long (20 to 40km);

Participants used the vehicle for two weeks each, to come to work in the morning and return home at night. Two weeks were considered sufficient to fulfil results reproducibility. Participants were allowed to make stops between their home-to-work travels, but not to use the vehicle on weekends. The goal is to capture the most common daily driving scenarios.

In order to obtain data about similar environmental conditions for every category, drivers from the three categories succeeded each other in the following manner : 2

weeks for Category A, the next 2 weeks for Category B and the following 2 weeks for Category C.

A 3 kW (L2) charging was provided to the participants at CEA. Unfortunately, it wasn't always available and therefore a replacement 2 kW residential charging (L1) was provided. Participants were also allowed to charge the vehicle at their house with a 2 kW residential (L1), if accessible. The participants were given the choice to charge whenever they feel the need. This was done to study the range anxiety factor.

The protocol is illustrated in the Figure 24.

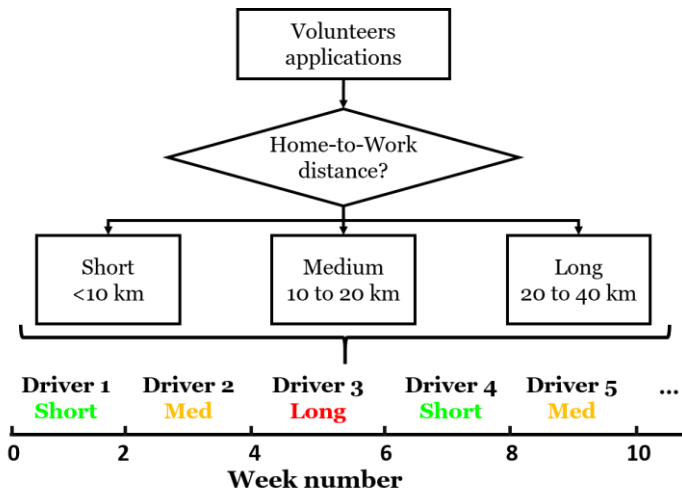


Figure 24. Protocol of the BMWi3 campaign

3. Results and discussion

Before tackling the results analysis, the main numbers of the experimentation are illustrated in Table 6. One “trip” is defined by a minimum travelled distance of 0.5 km after the vehicle start. One “home-work trip” is defined by the trip made either from home to work or from work to home, without taking into consideration the number of stops in between.

The number of trips exceeded by 1.9 times the number of home-work trips. In other words, in average, 1.9 stops/per home-to-work distance were made. That includes mainly bringing and picking up kids to school, as well as grocery stops. It sums up to an average of 10.3 km/trip.

Table 6. Driving campaign numbers

CEA Volunteers	24
Cumulative distance travelled (km)	8,642
Number of trips	838
Number of home-work trips	442
Maximum altitude reached (m)	1,160
Maximum speed reached (km/h)	152
Size of the generated data (Gb)	35
Greenhouse gases (kg)	0

It can be seen that different types of roads were visited, ranging from the highways to the mountains. In order to illustrate this clearly, the GPS data issued from the vehicle are plotted on the map of Grenoble in Figure 25. On the panel A of Figure 25, an isodistance map illustrates the three home-to-work distance categories, with the CEA of Grenoble being in the center of the map. GPS data are plotted on the maps of Panel B and C. On panel B the color code refers to the altitude, whereas on panel C, the color code refers to the speed value.

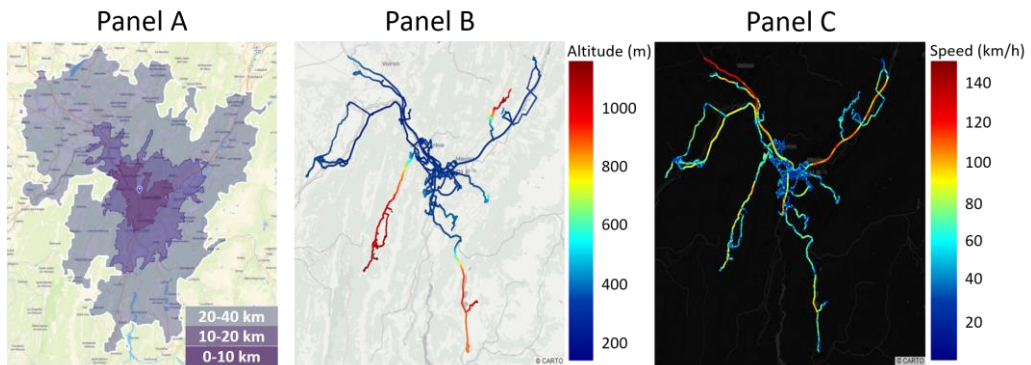


Figure 25. Panel A: isodistance map showing the three categories of home-to-work distances; Panel B: GPS data displayed with a color indicating the altitude level; Panel C: GPS data displayed with a color indicating the speed value

3.1 Range in function of temperature

The range of the vehicle given by the BMS is directly linked to the electrical consumption of the battery pack. At extreme temperatures, the consumption increases, as energy is delivered to the thermal management system. To visualize this impact, the range can be studied in function of the ambient temperature (Figure

26). The range was obtained by taking the totality of the range values given by the BMS at SOC 100 %. The orange line represents the second degree polynomial fit.

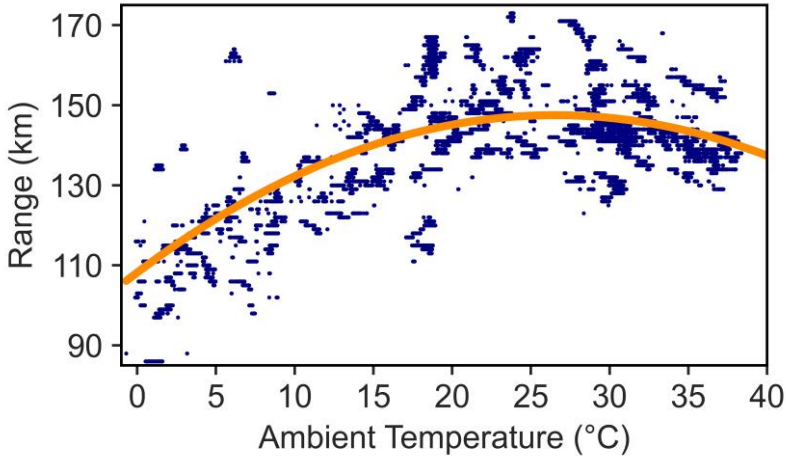


Figure 26. Range values in function of the ambient temperature

The maximum range value was 173 km at 23.7 °C, while the lowest was 86 km at 0.5 °C, proposing a span of 87 km. In other words, the energy consumption can double at 0 °C when compared to its minimum. This in agreement with what was seen in chapter 3. The spread in the values comes from the method used by the BMS for the estimations of the range. The methods found in literature are quite numerous [271], and the one used by the actual BMS is unknown.

3.2 SOC

As the study contained equally short, medium and long distances, the SOC at the start of charging can be revealing. Figure 27 illustrates the probability density of the SOC at the beginning (top graph) and end (bottom graph) of charging sessions.

The mean SOC value was found to be at 55 % SOC. The peak in density between SOC 80 and 90 % is revealing of the range anxiety. Drivers that tend to do short trips are usually prone to charge when opportunity presents itself. The next peak that appears between 40 and 50 % reveals the limit at which the users tend to charge their vehicle.

It can be telling to identify the association between the travelled distance between two charging sessions, and the SOC at the beginning of charge. To do so, a 2D density plot of the SOC at the start of charge in function of the travelled distance before the charge is illustrated in Figure 28.

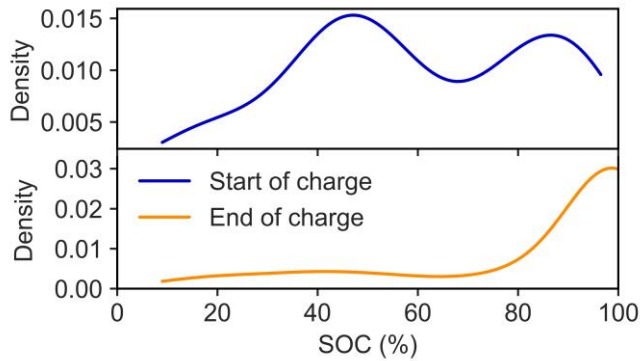


Figure 27. Distribution of the SOC at the beginning of charge

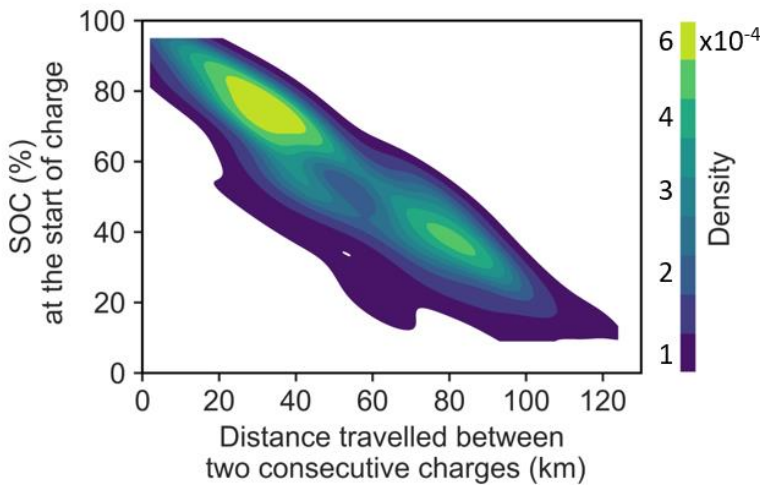


Figure 28. 2D density plot of the SOC at the start of charge and the distance travelled between two consecutive charges

It can be noticed that the largest and highest density region can be found between a travelled distance of 22 and 43 km, for a SOC region of 84 to 69 %. This is another instance of the range anxiety. The second dense area can be found between 74 and 87 km, for a SOC region of 42 and 34 %. This represents mainly the drivers that could charge their vehicle only after a long home-to-work roundtrip (category C of users living between 20 and 40 km far from CEA).

For a same travelled distance value, the SOC at the start of charge can vary quite significantly. This is a consequence of the energy consumption, which is very dependent on the ambient temperature, as well as the road type. For example, participants that travelled 40 km at cold weather using highway routes will find the vehicle at a SOC of 40 %, while others that drove the same distance in urban roads at mild temperatures will find it above 80 %.

3.3 Charging data

3.3.1 The two types of charging

As mentioned in the method section, two charging types were used during this driving campaign. The method of charging can impact the aging behavior of the battery, so extracting this data can be enlightening.

The charging power is obtained by multiplying the current throughput of the battery by its voltage value. The result is plotted in function of the SOC in Figure 29.

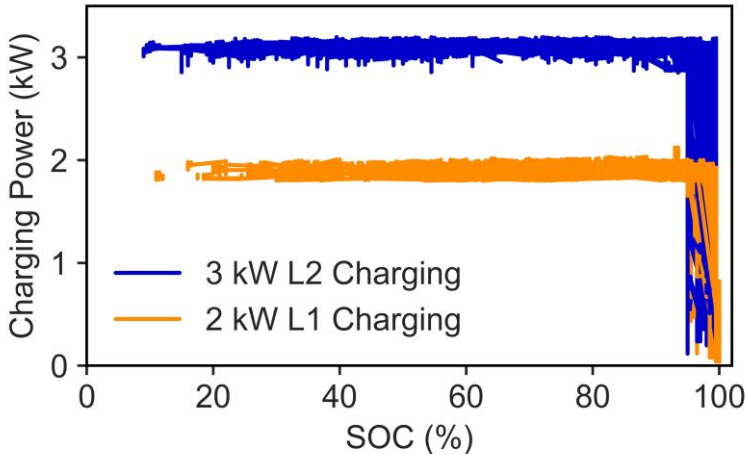


Figure 29. Illustrating the power (kW) of the two charging types

The noise found for both power values is a combination of the grid's perturbations and the sensibility of the measurement. Results suggest that the charging type follows a constant power (CP) trend with a floating (CV) at the final SOC levels. 3 kW and 2 kW charging are equivalent to a P/7 and a P/11 rate respectively.

The CV is identified by the decrease in the power value. As illustrated, the floating does not start at the same SOC level for every charge. Floating depends on the voltage value. As seen in chapter 3 (Figure 21), voltage limitations are imposed on the battery pack. When the maximum voltage is reached, if the charging capacity is not at its maximum level, a CV is then applied. At low temperatures, the resistance of the cell is higher, the voltage reaches its limit much faster and for this reason the floating will start at a lower SOC value.

At this charging power, lithium plating is usually avoided, which is why a simple CP-CV is chosen.

3.3.2 Charging energy

The charged energy in function of the starting SOC is another feature of interest. It gives insights on the used energy, hence the depth of charge (DOC) value. In Figure

30, the charged energy (in Wh) is plotted versus the starting SOC. The black and red dashed lines reveal the installed and usable energy capacity, respectively, given by the manufacturer. The usable/installed energy ratio is equivalent to 87 %.

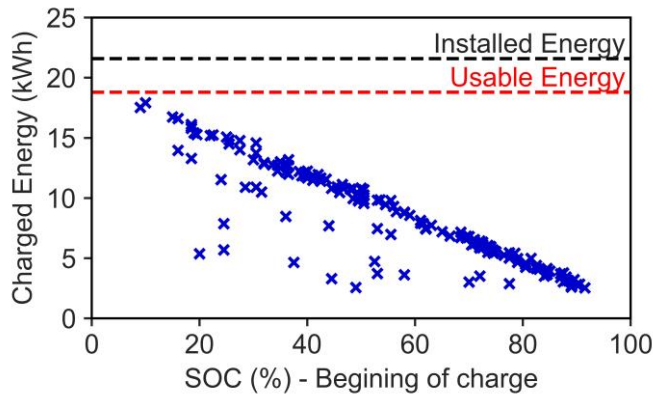


Figure 30. Charged energy in function of the SOC at the beginning of charge

The outcomes of Figure 30 suggest that the maximum charged energy is 17.9 kWh, while the usable capacity is 18.8 kWh, indicating a DOC of 95 %.

However, the starting SOC was 9 % and the final SOC (not illustrated Figure 30) was found to be 100 %, revealing a DOC of 91 %.

This difference implies either that the SOC desynchronized with aging, or that the battery was operating outside its aging margins. Yet, a total of 18 % (13 % + 5 %) of its capacity remained unused.

3.4 Discharge

It was concluded from Chapter 3 and from Figure 26, that the energy consumption is greater at extreme temperatures. It was also mentioned that the energy consumption increases with the vehicle speed. The increase in energy consumption, exhaustively elaborated in Chapter 3, is only a consequence of the increase in the discharged power. The discharged power is one crucial stress factor abundantly mentioned in the battery aging literature.

The purpose then is to illustrate the relationship between the discharged power and both the ambient temperature and the vehicle speed. The power is obtained by multiplying the instantaneous current of the battery pack by its voltage. The result is then divided by the installed battery capacity (21.6 kWh) and expressed in P-rate (h^{-1}). The reason behind this conversion is purely illustrative. A P-rate value is more telling, and more significant as it is equivalent to the P-rate of a single cell. The P-rate is then plotted in function of the vehicle speed, for different temperature ranges: cold ($T \leq 5 \text{ }^\circ\text{C}$), chilly ($5 \text{ }^\circ\text{C} < T \leq 15 \text{ }^\circ\text{C}$), mild ($15 \text{ }^\circ\text{C} < T \leq 25 \text{ }^\circ\text{C}$) and hot ($T > 25 \text{ }^\circ\text{C}$).

To visualize the region of interest, the median and the 75th percentile of the P-rate values are plotted together (Figure 31).

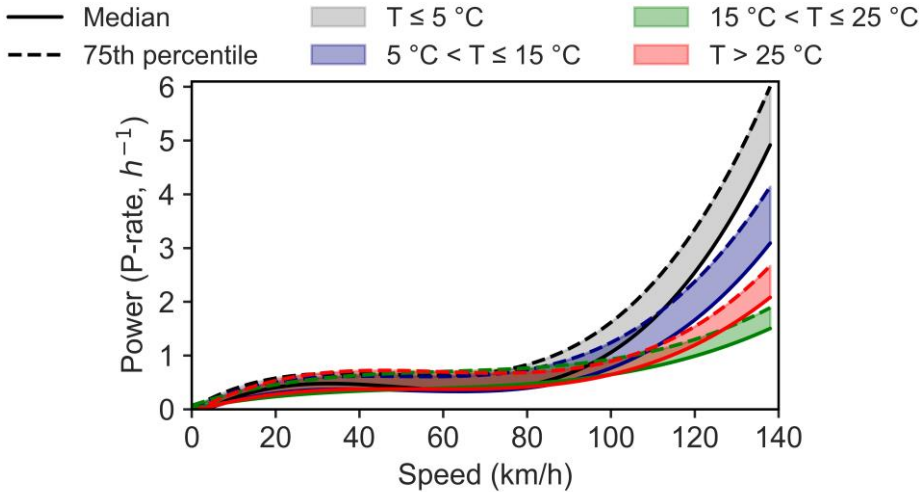


Figure 31. Discharge power expressed in P-rate (h^{-1}) versus the vehicle speed with respect to the ambient temperature

Results of Figure 31 suggest that below 80 km/h, the difference in the power demand was not affected by the ambient temperature. Passing beyond this limit, the difference tended to increase. The exponential increase in power demand was the highest for the cold temperatures, reaching up to 6 P above 130 km/h. The second highest increase was for chilly weathers, where the discharged power reached up to 4 P. The lowest the temperature, the highest the need to heat (both the pack and the cabin), the bigger the power demand.

The smallest increase, where the 2 P was not even attained, was during mild weathers. In these kind of weathers, the battery finds itself naturally at its optimal operative condition, as no additional heating or cooling is required. Finally, above 25 °C, cooling becomes needed. The power started increasing again and surpassed the 2 P rate at high speeds.

This tendency can be visualized too in Figure 26. However, the key point here is the power value, and the speed level at which the differences start to appear. For urban trips, where the speed does not surpass 60 km/h, it is expected that the discharge power will not play an additional role, neither in the available range, nor in the battery aging. It starts having an influence above 80 km/h, especially for highway roads.

3.5 Cell temperature in function of trip length

A lot has been said about the battery thermal management system. The previous subparts elaborated its impact on the range and the discharged power. In this part,

the temperature of the cells are studied. It has been shown in Chapter 3 (Figure 15) that, depending on the travelled distance and the thermal management time, the cells reach their optimal operating range.

In order to examine this, the measurements of the four thermocouples that were positioned on top of the battery cells were averaged (denoted as T_{cells}) and plotted in function of the ambient temperature. The ambient temperature is the average of the measurements of the two external thermocouples (denoted as $T_{ambient}$). Data are illustrated as a 2D density plot (Figure 32). The identify function (red line) helps in determining whether T_{cells} is higher than $T_{ambient}$ (left-hand side of the red line), or not (right-hand side of the red line).

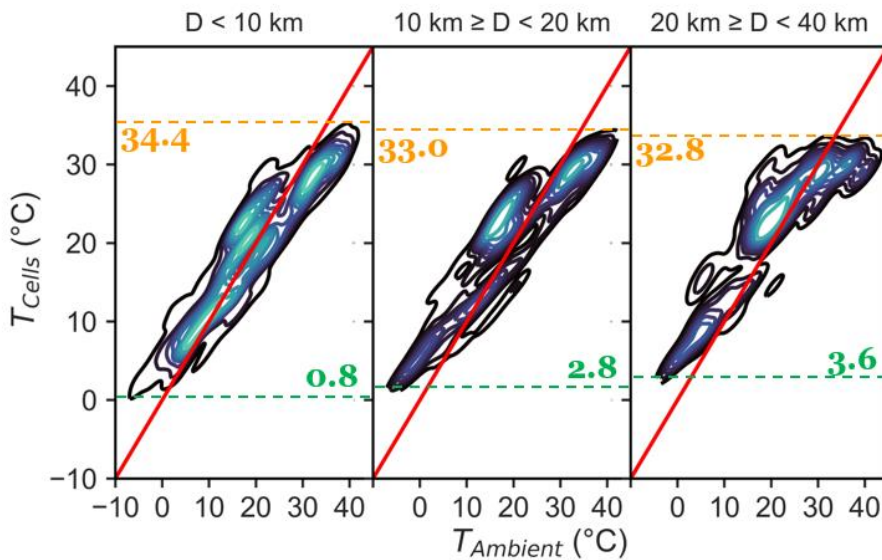


Figure 32. 2D density diagram of the cells' temperature with respect to the ambient temperature, and to the distance travelled (D)

At first glance, it can be noticed that the temperature of the cells did not fall below 0 °C, even when the ambient temperature was -8.2 °C. On the other hand, the maximum cell temperature did not surpass the 34.4 °C mark, even when the ambient temperature passed the 41.9 °C. This illustrates both the efficiency of the pack thermal insulation and the quick reactivity of the thermal management.

However, this conclusion does not omit the fact that if the vehicle was parked for a longer duration of time at -8.2 °C, for example, lower temperatures could have been reached by the cells. A daily usage of the vehicle can then limit the impact of the external temperature.

For ambient temperatures below 25 °C, it can be noticed that as the driving distance increased, the distribution of the cells' temperatures migrated to the left-hand side of the red line, indicating that the thermal management was heating up the cells. For

temperatures above the 25 °C mark, the distribution densified around 28 °C, keeping the temperatures at the right-hand side of the red line. Here the cooling seemed to be very efficient.

A slight narrowing of the temperature range window with the travelled distance can be seen, putting in evidence the impact of the thermal management.

4. General discussion

The vehicle used for the driving campaign was bought in 2016, while the experimentation was done between 2021 and 2022. Before starting the study, the batteries suffered from 5 years of calendar aging (at mostly high SOC) and 5,000 km of driving (work trips). The aging effects were seen in the calculation of the charged energy in function of the usable capacity. As the majority of literature studies are made on newly bought vehicles, this one has the particularity of using an aged vehicle. The vehicle was still able to fulfill the need of all the drivers, even the ones that lived at elevated altitudes, and 40 km far from the work location.

The ambient temperature was identified to have an impact on the energy consumption and the discharged power. The range estimations of the vehicle reduced at extreme temperatures as the energy consumption increased, indicating a general increase in the discharged power. The discharged power seemed to be significantly impacted when the speed of the vehicle surpassed 80 km/h. This increase in the discharged power is a consequence of the battery thermal management system.

In cold weathers, for short trips, the thermal management did not seem to be quick enough to heat up the cells. For longer trips, the temperature of the cells increased, but was still found to be between 5 and 10 °C, showing the limitations of the thermal management. This contradicts what has been deduced from chapter 3. It could either be associated to the deterioration of the thermal management itself (as the vehicle was bought five years before the campaign was launched), or its inefficiency in dealing with temperatures of 0 °C. Some other reasons might exist though, and further investigations are needed.

Low temperatures and the high discharge rates can then coexist, even at longer trips, which ages the battery in a much faster rate. The associated aging mechanisms include the fracturing of the SEI and the active material particles, or even material loosening, causing both a loss in capacity and increase in the cells' resistance [41].

The thermal management proved to be quite efficient for high temperatures and long trips, maintaining most of the cells' temperature below 30 °C.

3 kW L2 charging and 2 kW L1 residential charging are both done using a CP-CV profile, and don't seem to induce any lithium plating due to their low relative P-rate. However, as these two charging types are very slow (P/7 for the L2 and P/11 for the L1), the drivers felt the need to recharge the vehicle quite often. A significant amount

of drivers plugged in the vehicle after 22 to 43 km of driving, hinting at what is commonly referred to as “range anxiety”. This keeps the battery at elevated SOC regions (found to be between 100 and 77 %, in average). At these levels, it is known that the SEI growth is accelerated and NMC degradation is triggered [41].

5. Conclusion, limitations and perspectives

The driving campaign elaborated in this chapter, was done using a monitored BMWi3, and a design of experiment was planned and executed to capture typical daily home-to-work travels. Three categories of home-to-work distances were studied: short, medium and long. The main results suggested that the low temperature, high discharge rates and elevated SOC window due to range anxiety, are three stress factors that coexist abundantly. Oppositely to what was deduced in the previous part, for some cases, the low temperature can still be considered a stress even at long trips. The ambient temperature impact on the discharged energy was quantified. It was found to have a significant impact above 80 km/h.

The limitations of the study includes the following. First, some participants consisted of experts in the field of electric mobility and Li-ion batteries. Their use of the EV differs from the population’s totality. For example, a considerable amount of drivers started charging the vehicle from a very low SOC and that might include people on which the “range anxiety” has no effects. To reduce the effect of range anxiety on the population, policies aim at increasing drastically the density of charging stations. However, in this study, the charging was located mainly in the work place and were very slow (3 kW). This hints at the fact that range anxiety can be omitted simply by making the public more familiar with the technology, and not necessarily by increasing the amount of charging stations. This idea was also evoked by Noel et al. [272].

Second, one factor wasn’t considered here and it is the altitude increase of the vehicle. Such regions can increase the discharged power value, hence increase the stress level. Third, the size of the study is limited to only one vehicle. Ideally, different vehicles should be monitored and studied to end up with more solid conclusions.

In terms of perspectives, a lot can be made with the generated data. The BMWi3 aging campaign was implemented with 70 thermocouples over the entire architecture of the battery pack. Only six of them were needed for this study. Using the entire range of thermocouples, 3D thermal maps of the pack architecture can be drawn with respect to the travelled distance. Additionally, by using the charging data, incremental capacity analysis can be made to identify the degradation mode that occurred during the study.

Chapter 5 – Accelerated aging protocol and performance loss

Highlights

- Designed a novel accelerated aging protocol
- Applied the protocol on Samsung PHEV 37 Ah cells
- Downscaled stress factors identified on a PHEV pack level
- Studied the interdependence between cycle and calendar aging
- Developed a new way of defining the SOH using a WLTP cycle

The literature review evoked the interdependence of aging mechanisms, which are linked to a series of stress factors. Field data chapter 3 and 4 suggested that stress factors are interdependent too. The most impactful ones in the lifetime of an EV battery are parking at high SOC, low cell temperatures and high discharge rates, especially for vehicles with a small battery pack (such as the PHEVs). The ambition behind this chapter is to design and implement an accelerated aging protocol by taking into consideration these observations on commercial EV batteries.

1. Introduction

Following the identification of the most critical (severity and frequency) stress factors that happen during the lifetime of an EV, the purpose of this chapter is to detail the design and implement an accelerated aging protocol. Its drive is to take into consideration the observations made, without neglecting the interplay of cycling and calendar aging on the aging of the cell. The protocol is applied on an commercial PHEV battery. The loss of performance is illustrated in the final subparts, with an interpretation of the results.

2. Methodology

In this part, the details of the methodology used for the accelerated aging campaign are elaborated. It contains an appropriate description of the patented accelerated aging protocol [273], the parametrization of the protocol depending on the cell and its usage, and finally the checkup processes that are used to monitor the decrease in performance.

2.1 Accelerated aging protocol: a general idea

Prior to implementing the accelerated aging protocol, the usage and the application should be clearly defined. To be reliable and representative of this usage, the first step of this protocol is to rely on an in-depth field analysis, such as the one made in chapter 3 and 4.

Then, the goal is to derive aging phases (p) and classify them depending on their severity and their occurrence (by referring to the RPN matrix). If n phases are identified to be impactful during the lifetime of a battery, the first phase level, p_1 , is the most critical one, and p_n is the less critical one.

The second step is to apply these phases on the battery cells following a concentric approach (Figure 33). In other words, the protocol will comprise n levels, were each level contains the previous phases and the n^{th} one. For example, phase m (p_m), comprises $p_1 + p_2 + \dots + p_{m-1} + p_m$. The phases are applied by taking into consideration their amplitude and their duration, depending on their occurrence in usage. For each level, a model is derived, allowing the parametrization of a complete model, irrespectively of the model type.

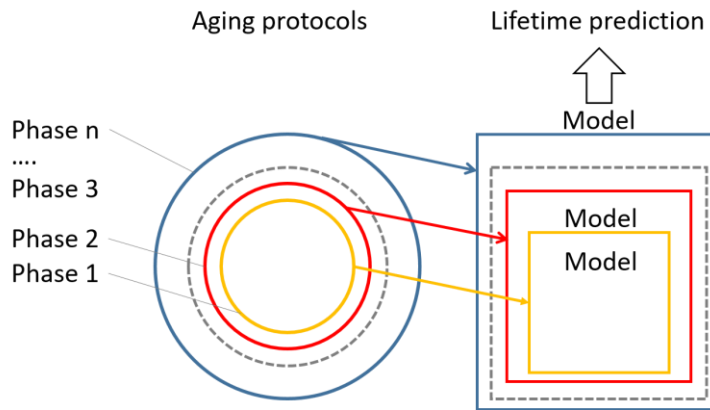


Figure 33. Accelerated aging protocol schematic [273]

2.2 Cell identity and application

The protocol in question can be applied on any type of cell for any application. The initial goal of the thesis was to apply it on cells for the three automotive applications (BEV, HEV and PHEV). Due to time and material constraints, the focus was then put on one cell type. The PHEV cells were chosen for two reasons. First, their capacity was small enough to suit the safety criteria of the testing platform at CEA, oppositely to the BEV cells. Second, a sufficient number of cells were provided, oppositely to the HEV cells.

The cell in question is a 37 Ah prismatic Samsung SDI PHEV [274]. As it will be discussed in the ante-mortem analyses of chapter 6 and 7, the positive electrode of the cell is made of NMC 111, its negative electrode is made of graphite, and its electrolyte is based on LiPF_6 salt in a mixture of organic carbonates. As described by its datasheet, the cell's nominal capacity is of 37 Ah. The nominal capacity is used as a reference to calculate the current values (for example, $C/20$ is equal to 1.85 A). Its maximum voltage limit is 4.2 V, its minimum voltage limit is 3.0 V, and its nominal voltage is of 3.66 V. The maximum possible applied current is 180 A.

Designed for PHEV applications, this cell was recovered from the battery pack of a commercial PHEV vehicle with a range of 41 km and a usable battery capacity of 14.7 kWh. This vehicle has a rated power of (105 kW) and a curb weight (2,539 kg), and a maximum speed of 220 km/h. Its pack has a total number of 108 Samsung PHEV cells.

2.3 Protocol parametrization

2.3.1 Identification of phases

The usage of batteries in PHEVs was covered in Chapter 3. Three main phases can be identified. The first is the parking phase, which represents over 90 % of a vehicle lifetime [44], [138]. This comprises the “inactive” periods, where the vehicle is parked before the first trip of the day (over 70 % of the vehicle lifetime [138]), and the “active” periods, where the vehicle is parked between two trips. The parking times induces what is commonly referred to as calendar aging. For this reason, this first phase is going to be referred to as the “Cal” phase.

The second is the driving, which constitutes less than 10 % of the vehicle’s lifetime [44], [138]. “Short Trips” (ST) made in vehicles ranges around 8 km [275], [276] and constitutes a big portion of today’s usage. It has been shown that in Europe, over 70 % of the trips were less than 10 km [228], and 34 % of French commuters live less than 10 km away from their job. Otherwise, it has been shown that 30% live between 10 and 20 km [270]. The additional 10 km is then considered to be distance of the “Long Trips” (LT). The ST and LT are then the other two phases.

For PHEVs, two kinds of operating conditions were identified in chapter 3, the Charge Depletion mode (CD) (SOC 90 to 30 %) and the Charge Sustaining (CS) (SOC 20 ↓ 40 %) modes (illustrated in Figure 34). The previously mentioned ST and LT fill in the CD mode of the battery. The CS mode, will constitute another type of trips which will be described as “Hybrid Trip” (HT). Chapter 3 suggested that the range anxiety is less pronounce with PHEV users as they tend to drive for longer trips because of this hybrid functionality. For this reason HT for long durations will be a separate phase.

The mentioned phases are illustrated in Figure 34.

Concerning the charging protocol, the most common charging method nowadays is the L2, with an average charging power of 7 kW (as shown in chapter 3 part 3.3). With respect to the vehicle in question, this represents a charging power rate of $P/2$ (as a reminder the power rate (P-rate) is the power throughput (W) divided by the total energy of the battery (Wh)). Charging is then not very critical in today’s usage, it will not be considered as another phase.

It should be noted that when the common charging powers reaches higher values and the charging rate surpasses the $P/1$ mark, it could then be considered as another stress, hence another aging phase.

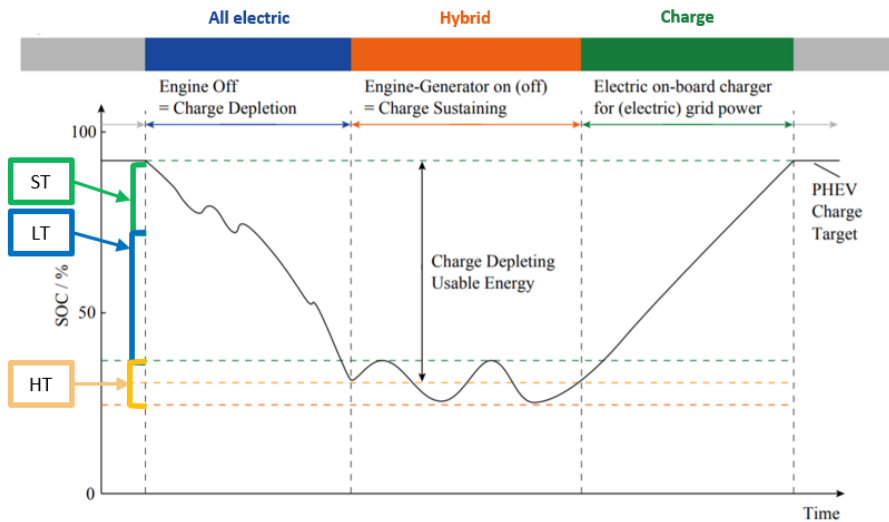


Figure 34. PHEV operating conditions [277] with the ST (Short Trip), LT (Long Trip) and HT (Hybrid Trip) phases highlighted. The “All electric” mode is referred to as Charge Depletion (CD) and the “Hybrid” mode is referred to as Charge Sustaining (CS)

To conclude on the phases’ identification, the four aging types are the following:

- Cal SOC 90 %, SOC 60 % and SOC 30 %
- Cal SOC 90 % + ST (referred to in the text as Cal + ST)
- Cal SOC 90 % + ST +LT (referred to in the text as Cal + ST + LT)
- Cal SOC 30 % + HT (referred to in the text as Cal + HT)

2.3.2 Phases parametrization

The phases parametrization refers to the identification of the stress factors, as in the SOC, for the Cal phase, the power discharge rates and durations for the ST and LT phases. The temperature is considered as an environmental condition and not a stress. This procedure requires a top-down approach. In other words, results from chapter 3 are used to determine the stress factors on the battery pack level, which will then be downgraded to the cell level.

The usage analysis of chapter 3 suggested that SOC 90 % is the most common value for parking times for PHEVs in their CD phase. Additionally, SOC 30 % is commonly observed as it is the mid-SOC of the CS phase. SOC 60 % is chosen as a median value.

To estimate the discharge power values from the cells with respect to the ST and LT, the procedure will be based on the energy consumption (Wh/km) values. It was shown that the energy consumption is primarily based on two variables:

- The ambient temperature (Mild or Extreme)

- The road type (Urban, (U); Highway ,(H) or Combined, (C))

The increase in energy consumption is then quantified using the following approach. A reference energy consumption value is identified, and multipliers of this value are assigned to each road type (U, C and H) under each climate, by referring the chapter 3.

The energy consumption of the vehicle given by the manufacture, 261 Wh/km. It is obtained by testing the vehicle following a WLTP (World Harmonized Light Vehicle Test Procedure) procedure [218]. The WLTP procedure is tested at the optimal cell temperature, it simulates urban and highway roads, and travels 23.26 km. It represents then a 25 °C LT (C) (Long Trip – Combined road type). This value is then assigned as the reference energy consumption (underlined in Table 7)

The ST comprises the vehicle start-up and the travelled distance, which is usually located in urban areas [275], so only one road type (U) is assumed for ST. As shown in chapter 3, at the vehicle start-up, some extra “energy penalty” is consumed, when compared to the rest of the trip. Along with this, under extreme temperatures (less than 5 °C or more than 35 °C) a considerable amount of the energy is delivered to the thermal management system. This seemed to be more critical for low ambient temperatures.

For these reasons, a multiplier of 1.5 (accounting for the “energy penalty”) is used for the ST at 25 °C (i.e. $261 \text{ Wh/km} \times 1.5 = 407 \text{ Wh/km}$), a multiplier of 2 and 2.5 are applied for the ST at 45 °C and 0 °C respectively (accounting for the thermal management demands). These are based on the results obtained in Figure 14 of chapter 3.

The LT, on the other hand, constitutes the three types of roads. At urban trips (U), the battery consumes the less. The higher the speed, the higher the energy consumption. At 25 °C, a multiplier of 0.8 is assigned for the LT (U) (the vehicle consumes less than the reference value) and a multiplier of 1.5 is given for the LT (H) phase (considering that the highway trips increase by 1.5 the consumption value).

The energy consumption value at the LT phase is also dependent on the ambient temperature (as illustrated too in chapter 4). For LT phases, no distinctions will be made for the 45 and 0 °C, they will be both categorized as “extreme temperatures”. At extreme temperatures, the energy consumption is assumed to be 1.3 times bigger than the values at 25 °C.

The estimated values for the energy consumptions are multiplied by the average speed of each road type to obtain an equivalent power value (equation (8)). The average speed for urban areas is considered to be 40 km/h, for highway trips it is 120 km/h, and finally for the combined case it is 80 km/h.

$$P(W) = \text{Consumption (Wh/km)} * \text{Speed (km/h)} \quad (8)$$

Finally, this power value is divided by the number of cells in the pack (108 cells) to obtain the discharged power per cell. The duration of each solicitation is obtained by dividing the range (8 km for ST and 10 km for LT) by the speed value.

Table 7 illustrates the power value per cell in function of the phase (ST and LT), the temperature and the road type. The power is given both in W and P-rate (obtained by dividing the power (W) by the energy of the cell, found in the following parts to be 147Wh).

Table 7. Parametrization of the aging protocol depending on the usage for the CD phase. U = Urban, C = Combined and H = Highway.

	T °C	Road type	Multiplier	Consumption (Wh/km)	Speed (km/h)	Duration (min)	Power/cell (W)	P-rate (h ⁻¹)
ST	25 °C	U	1.5	407	40	12	150	1
	0 °C		2.5	680			250	1.7
	45 °C		2	545			200	1.4
LT	25 °C	U	0.8	210	40	12	80	0.5
		C	1	<u>261 (WLTP)</u>	80	7.5	195	1.3
		H	1.5	392	120	5	435	3
	0 °C or 45 °C	U	1.05	270	40	12	100	0.7
		C	1.3	340	80	7.5	250	1.7
		H	2	510	120	5	570	3.9

The interdependence of stress factors is effectively taken into consideration, similarly to usage. For extreme temperatures the discharged power increases. For long duration trips (i.e. DOD), the power is variable depending on the road type.

For the HT, the procedure is much simpler. During these trips, the power charged and discharged from the battery pack looks like the one described by USABC [278] for the CS mode of a PHEV. Three types of PHEVs are proposed: the 20, 40 and 60 miles. The studied batteries are used in a 41 km (25.5 miles). The PHEV-20 miles is then chosen. The typical power demand is described in Table 8. Here the CS is described for a duration of 1 min 30 s. The protocol is repeated 14 times to make up for a long duration trip (21 min).

Table 8. CS phase parametrization based on [278]

Time increment (s)	Cumulative time (s)	Pack power (W)	Cumulative energy (Wh)	Cell Power (W/cell)	P-rate (h ⁻¹)
36	36	3,000	30	28	0.19
4	40	18,000	50	167	1.1
48	88	-3,130	8.3	29	0.19
2	90	-15,000	-0.1	139	0.93

2.3.3 Aging protocol cycle

Now that the phases are identified and parametrized, the next step requires to cycle them, as shown in Figure 35. Hereunder are illustrated the Cal, Cal + ST, Cal + ST + LT and Cal + HT phases.

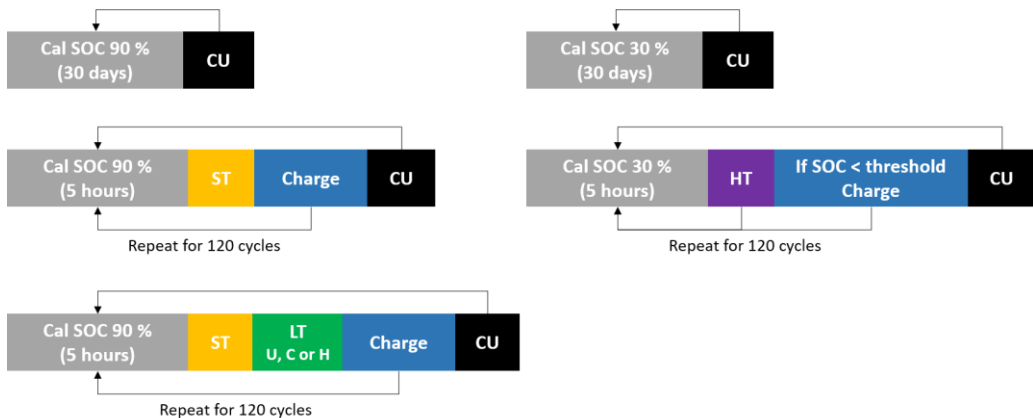


Figure 35. Schematic showing the succession of the aging phases during the accelerated aging protocol where CU is the acronym for checkup

Driving to Parking ratio. Choosing a calendar (parking) duration of 5 hours is done with respect the percentage of Cal time found in usage (above 90 %). In other terms, an ST of 12 min (Table 7) and a Cal time of 5 hours (Figure 35) represent a Parking time of 96 %. An ST + LT of 24 min with the same Cal time represent a parking time of 92 %.

SOC definition. The SOC is defined based on its thermodynamic description [54], [279]–[281], as illustrated in equation (9).

$$SOC = \frac{\text{Remaining exchangeable Li}^+ \text{ ions}}{\text{Total exchangeable Li}^+ \text{ ions}} = \frac{\text{Residual capacity at low rate}}{\text{Maximum capacity at low rate}} \quad (9)$$

In this way, the SOC is associated to a voltage value, obtained via voltage vs SOC curves at low charging/discharging rate. Here, the SOC is attained using a charging procedure (Figure 35), so the C/20 charging curve is used for the voltage vs SOC assimilation. This process was considered to be sufficiently accurate, combining precision to time efficiency [60], [280], [281]. The SOC, as defined here, differ with aging. For this reason, a C/20 charge process is comprised within the monthly checkup protocol, as explained in the following subparts, and the voltage vs SOC curve is updated for each cell after each month of aging.

For example, in the beginning of life (BOL), the SOC 90 % was assigned to a voltage of 4.066 +/- 0.0023 V, the SOC 60 % to a voltage of 3.759 +/- 0.0015 V and the SOC 30 % to a voltage of 3.601 +/- 0.00098 V. The standard deviation of each value refers to the cell-to-cell variation.

Charging. As explained earlier, the most common charging procedure nowadays is the L2 (7 kW). On a cell level, this is equivalent 65 W (7,000 W / 108 cells in the pack). The chosen charging method is then the same for all the cases and it is a constant power (CP) at 65 W. A constant voltage (CV) is applied then on the targeted voltage. The CV current cutoff is 1.85 A (C/20).

For the HT phase, charging is not needed. In theory, Table 8 suggests a final cumulative energy of -0.1 Wh. This indicates that a cycle induces a slight loss in voltage. During calendar aging, the voltage might decrease too (auto-discharge). For this reason, a threshold value of 3.55 V is assigned. If the voltage decreases below this value, a slow Constant Charging (CC) procedure of C/10 is applied along with a CV at 3.6 V with a cutoff current of C/50.

Cycle definition and checkup frequency. A checkup is done on a monthly basis for the Cal phase. For the Cal + ST, LT and HT processes, a monthly checkup should be similarly done on the cell for consistent comparison purposes. A “cycle” starts from the Cal phase and ends at the charging phase. It simulates then a usual trip that starts when the vehicle is parked, drove for a certain period of time and then plugged in for charging. Around 4 cycles are done per day, so 120 cycles per month. Checkups are then made each 120 cycles.

Number of cells per condition. Three cells per condition were used for the Cal phase, while two cells per condition were used for the other cases, for reproducibility reasons.

2.4 Checkup protocol

The checkup protocol, mentioned in Figure 35, is made in the Beginning of Life (BOL) of each cell before the launching of the protocol, and each month (or 120

cycles). Its main objective is to determine the performance loss of the cell, align the diagnostic tools of chapter 5 (parts 2 and 3), and serve as a validation of the performance and degradation models of chapter 7.

Before proceeding with the checkup procedure, it is important to determine the performance criteria that need to be traced with aging.

2.4.1 Performance criteria

Choosing the performance criteria is crucial for an accurate representation of the battery State Of Health (SOH). From a general perspective, the SOH is given by:

$$SOH(\%) = \frac{P_t}{P_i} \times 100 \quad (10)$$

where

P_t is the value of the performance criteria at time t

P_i is the initial value of the performance criteria

The performance criteria are used to assess whether the product has reached its End of Life (EOL). The choice of the performance criteria is the very crucial, and the reason behind choosing it is often nebulous in literature.

Background. As mentioned in chapter 3, assigning the capacity (obtained at a constant current discharge) as a performance criterion is very common in the field of batteries. The EOL is usually at 80 % of the initial capacity, or 130 % of the initial internal resistance [89], [126].

The first issue with these methods, is that they are based on constant currents, e.g. C/3 discharged rate [282]. During normal driving sessions, the current is adapted accordingly to the voltage of the cells, in the goal of delivering the requested power for the EV. For the same power demand, as voltage decreases, the current increases and therefore is never constant.

Second, setting 80 % of initial capacity is inspired by the Ni-MH batteries testing field [262]. Ni-MH batteries have about half the specific energy of Li-ion batteries [11], [263], explaining why this custom is problematic.

These methods are based on an “electrochemical” perspective and are far from the application reality, as proved by Saxena et al. [264].

End-user perspective. Setting the performance criteria should rather be based on practical and economical perspectives. As explained by Carlsson [105], [131], the practice consists of specifying the purpose of the component and service lifetime requirement from an end-user and product point of view. This, accompanied by the economic impact of aging, will help establishing the minimum performance expectations that must be maintained for the targeted service lifetime [255]. If the performance criterion is not based on such analysis, it might lead to erroneous interpretations, such as premature EOL, or too tardy EOL, leading to safety issues.

This concept started to appear in the USABC updated standards explaining that the performance criteria and the acceptable margin loss should be determined by the EV manufacturer depending on the application [47]. No further details were given though.

Application. As a reminder, the studied battery is used for PHEV applications. So from an end-user and manufacturer's perception, the first aim of PHEVs lies in achieving the initial all-electric range (in km) specified by the constructor.

From a physics perspective, the range is the energy capacity (Wh) of the cells, which is revealing of both the Ah capacity and the internal resistance [283]. The energy is obtained using equation (11).

$$E_{Discharged} = \int_{t_i}^{t_f} U * I dt \quad (11)$$

where

U is the voltage (V)

I is the current (A)

t_i is the time at the beginning of the discharge

t_f is the time at the end of the discharge

The method used to discharge the battery and measure the energy is crucial. As mentioned previously, fixing the current is definitely far from the field reality. Fixing the power is more illustrative of the battery operation, but yet, not very representative.

Manufacturers measure the range of an EV using a standardized driving cycle for comparison purposes. Nowadays, the common standard is the WLTP (World Harmonized Light Vehicle Test Procedure) [218], evoked in chapter 3.

Ideally, the discharged energy should then be obtained by applying a downscaled (to the cell level) WLTP drive cycle within the operating SOC values. This will not only give an energy value, but also a range (in km). This measure of performance can then be directly assimilated to the application.

Two ways of evaluating the SOH are then proposed: the first is the energy measurement at a constant discharged power, and the second is the WLTP range. Thus, two types of CU are implemented: the primary checkup, and the secondary checkup.

2.4.2 Primary checkup

This monthly checkup follows the steps shown in Table 9.

The protocol starts by a residual CC discharge at C/2 before applying three C/2 cycles, i.e. CC-CV charge (cutoff current of C/20) and CC discharge, within the

voltage limits of the cell (3 to 4.2 V). The objective of this first step is to balance the cell and to have a same starting point for the performance characterization.

The following step is to apply a CP-CV charge (cutoff current of C/20) and CP discharge, with a power value of 65 W. The reason behind this is to obtain the energy value (in Wh) of the cell, which is the first performance criterion elaborated in part 2.4.1.

The final step of the primary checkup procedure is the C/20 cycle. A residual C/20 CC discharge is made before launching this step, to ensure that the full voltage range (3 to 4.2 V) is covered (as seen in Figure 36), and to avoid any missing data due abrupt voltage relaxation. The C/20 CC charging process is followed by a CV with a cutoff current of C/50, before the CC discharge process.

This C/20 process is of utmost importance as it serves as a pillar for battery diagnostics (that will be elaborated in chapter 6) and for the voltage vs SOC curve that needs to be updated each month.

Table 9. Monthly checkup procedure

Step	Solicitation	Number of cycles	Purpose
1	C/2 Residual discharge to 3 V	1	Deduce the residual capacity for a proper capacity measurement
2	C/2 charge (CC-CV at 4.2 V) C/2 discharge (CC till 3 V)	3	Cell electrical balance and capacity measurement at the last cycle
3	P/2 charge (CP-CV at 4.2 V) P/2 discharge (CP till 3 V)	1	Obtain the energy capacity of the cell
4	C/20 residual discharge to 3V	1	To avoid voltage relaxation
5	C/20 charge-discharge	1	For battery diagnostics and for the OCV vs SOC curve

Figure 36 illustrates the steps 2 (labeled as CC), 3 (labeled as CP) and 5 (labeled as C/20). The voltage during these steps is plotted in function of the testing time.

Using the discharge curve of the CP phase (step 3), the energy value (calculated using equation (11)) was measured. The energy retention is then calculated using equation (12).

$$\text{Energy retention (\%)} = \frac{E_t}{E_i} \times 100 \quad (12)$$

where

E_t is the value of the energy (Wh) at time t

E_i is the initial value of the energy (Wh)

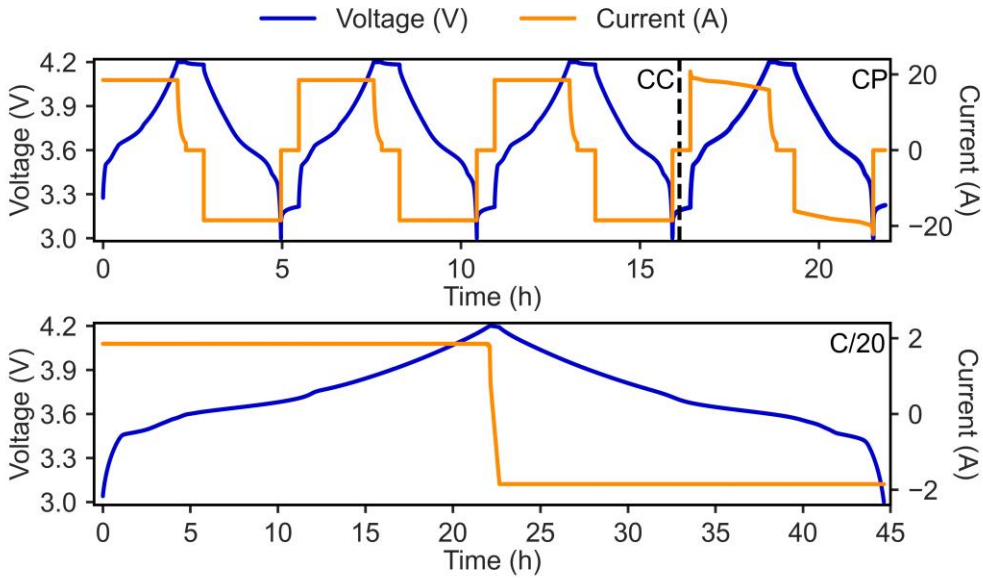


Figure 36. Monthly checkup protocol showing the CC, CP and C/20 phases, as in steps 2, 3 and 5 from Table 9

2.4.3 Secondary checkup

The secondary checkup goal is to determine the range that the battery cell can provide when upscaled to a pack level. As explained previously, this requires the establishment of a power profile based on the WLTP report [218].

WLTP profile. In this report [218], three different speed profiles are given depending on the class of the vehicle. In this case, the vehicle has a rated power (105 kW) to curb weight (2,539 kg) ratio of 41 and a maximum speed of 220 km/h, so assigned as a class 3b vehicle. After choosing the corresponding speed profile (summarized in Table 10), the procedure requires transposing it to a power per cell profile.

Table 10. Summarizing the different phases of the WLTP speed profile for a Class 3b vehicle

WLTP phase	Duration (s)	Stop duration (s)	Stop percentage (%)	Distance (km)	Max Speed (km/h)
Low	589	156	26.5	3.10	56.5
Medium	433	48	11.1	4.76	76.6
High	455	31	6.8	7.16	97.4
Extra High	323	7	2.2	8.25	131.3

TOTAL	1,800	242	11.65	23,26	90.45
--------------	--------------	------------	--------------	--------------	--------------

Equation (13) describes the transition from the instantaneous speed value (S_i) to the instantaneous power value of the electric motor ($P_{EM,i}$). $P_{EM,i}$ should then be enough to reach that speed, transport the mass of the vehicle (M_V), and overcome the potential road resistances (R_i) [26]. R_i is expressed in equation (13) with $i = [rolling, gradient, air]$.

$$P_{EM} = \{[(R_{rolling}) + (R_{gradient} \times S_i) + (R_{air} \times S_i^2)] + R_D \times M_V \times a_i\} \times S_i \quad (13)$$

Here $R_{rolling}$ stands for the rolling resistance, and is mainly dependent on the nature of the road and the tires. The value recommended by the WLTP report [218] is 0.14 N/kg, which is typical of ordinary car tires on asphalt [284]. $R_{gradient}$ stands for the gradient resistance, and is reliant on the steepness of the road. The WLTP profile is undergone on a flat road so this resistance is nil. R_{air} represents the wind resistance, and relies on the frontal surface of the vehicle. Its detailed expression is given in equation (14) [218], where R_{air} is expressed in $N/(km.h^{-1})^2$, w is the width of the vehicle (without the mirrors) and h is its height. The given numbers are based on the assumption taken in a wind tunnel (where the vehicle range is tested).

$$R_{air} = (2.8 * 10^{-6} \times M_V) + (0.0170 \times w \times h) \quad (14)$$

In equation (13), R_D is a factor that denotes the internal resistance of the drivetrain during acceleration, and its value is 1.03, as proposed by [218]. Finally, a_i is the instantaneous acceleration.

After obtaining the P_{EM} , the tank-to-wheel (T2W) efficiency loss should be taken into consideration to obtain the power that should be delivered by the battery pack (P_{BP}). A T2W of 85 % is taken into consideration for acceleration values ($P_{EM} \geq 0$), which is quite common in for an EV [285]. For deceleration ($P_{EM} < 0$), a wheel-to-tank (W2T) efficiency is assumed to have the same value as the T2W efficiency (equation (15)).

$$P_{BP} = \begin{cases} \frac{P_{EM}}{T2W}, & P_{EM} \geq 0 \\ P_{EM} \times W2T, & P_{EM} < 0 \end{cases} \quad (15)$$

Finally, P_{BP} is divided by the number of cells in the pack to obtain the power of a battery cell P_{BC} .

$$P_{BC} = \frac{P_{BP}}{\text{Number of cells in the pack}} \quad (16)$$

The schematic of Figure 37 summarizes this procedure.

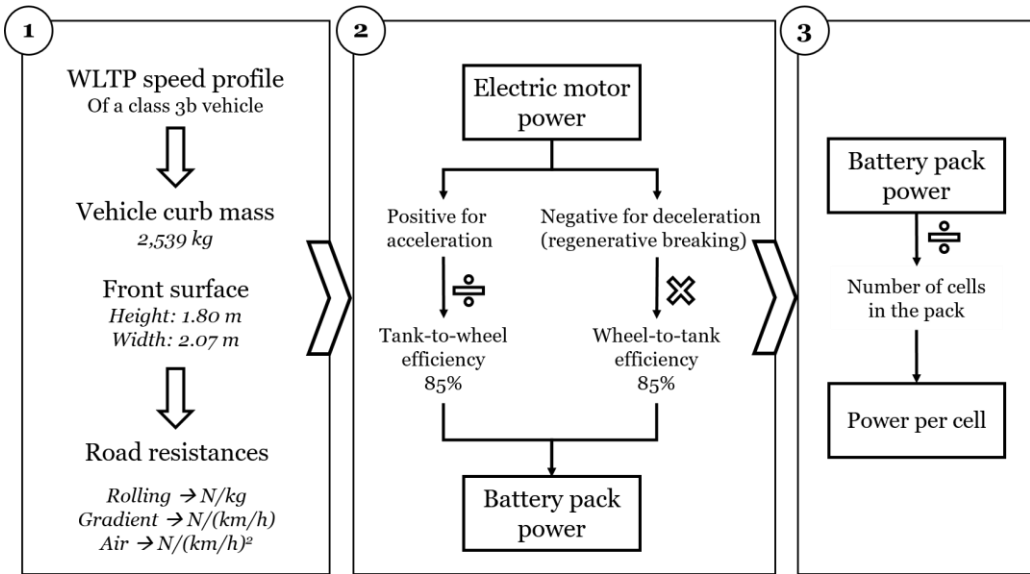


Figure 37. Schematic describing the transposition from the WLTP official speed profile to a power per cell profile

Additionally, the current limitation of the battery (max 180 A in discharge, imposed by the cell manufacturer) should be taken into consideration. Therefore any power value that makes the current surpass 180 A should be “shaved”, or leveled, and labeled as “downgraded” in Figure 38. In this case, in a normal PHEV, the Internal Combustion Engine (ICE) assists the battery to reach the required level.

Figure 38 illustrates the speed profile of a WLTP (first plot), the corresponding cell power and its downgraded version taking into consideration the 180 A limit (second plot), and the cumulative travelled distance (third plot). The cumulative distance is obtained by calculating the travelled distance per time step knowing the speed value. The low, middle, high and extra high phases of the WLTP are highlighted.

SOC measurement. As previously mentioned, the range of the PHEV is measured between SOC 90 and 30 %. In other words, evaluating the upscaled range of the battery cell requires cycling the WLTP profile within this SOC region. It is therefore needed to measure the SOC loss while cycling and stop the cycle at a SOC of 30 %.

In order to do so, the Coulomb counting method is used, based on equation (17) [286].

$$SOC_t = SOC_{t-1} + \frac{I_t}{Q_I} \Delta t \quad (17)$$

where

SOC_t is the obtained SOC at time step t

SOC_{t-1} is the obtained SOC at the pervious time step

I_t is the current at time step t

Q_I is the total rated charge/discharge capacity under a charge/discharge current of I

Δt is the difference between time step $t-1$ and t

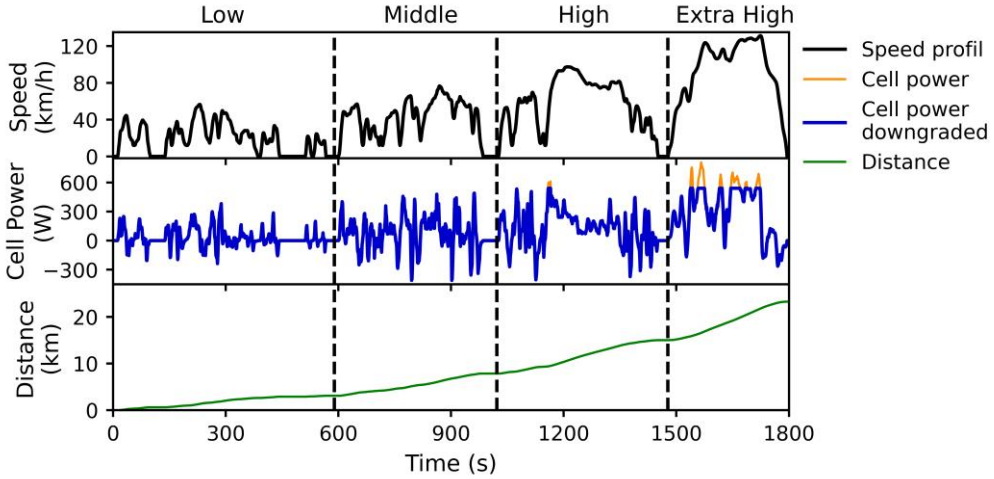


Figure 38. WLTP protocol scaled on a 37 Ah Samsung PHEV cell

Theoretically, for every possible charge/discharge current I , the charge/discharge capacity Q_I should be obtained and used accordingly with respect to the current level. For simplification purposes, the average power of a WLTP cycle (152 W, around a P-rate of P/1) is applied on the battery prior to the WLTP procedure (CP-CV charge till 4.2 V with a cutoff current of $C/20$, and a CP discharge till 3.0 V). This is done to measure the capacities both for charge and discharge, and this same capacity is used for the entire WLTP cycle. As WLTP profile frequency is 1 Hz, the Δt is always set to 1. So for every step of the profile, the SOC is measured as in equation (18).

$$SOC_t = \begin{cases} SOC_{t-1} - \frac{I_t}{Q_{dis(152W)}}, & P_{BC} \geq 0 \\ SOC_{t-1} + \frac{I_t}{Q_{cha(152W)}}, & P_{BC} < 0 \end{cases} \quad (18)$$

where $Q_{dis(152W)}$ is the capacity obtained with a discharge of 152 W and $Q_{cha(152W)}$ is the capacity obtained with a charge (CP-CV) of 152 W.

From equation (18), it can be noticed that the decrease in SOC, hence in available range, is based on two factors. First, the current value at time t . It is dependent on the power demand (fixed) and the voltage value, and is referred to as the resistive

factor. The lower the voltage at time t , the higher the current. The higher the current, the faster the loss in SOC.

Second, the discharged or charged capacities. They are referred to as the capacitive factors. The lower Q_{dis} , the faster the loss in SOC. The lower Q_{cha} , the slower the increase in SOC (regenerative braking).

When the SOC reaches 30 %, the WLTP test is stopped, and the obtained range (i.e. cumulative distance obtained by calculating the travelled distance per time step knowing the speed value) is extracted.

2.4.4 Frequency and condition of checkups

Frequency of checkups. The primary checkup is made monthly (or each 120 cycles) for all the cells, except one cell of each Cal condition. As mentioned previously, three cells were used per Cal condition. One of them was checked up only at BOL and at the end of test. By comparing the loss of performance and the diagnosis (Chapter 6) of the cells that were checked up monthly and the cells that were checked up only twice, the impact of the checkups can be identified.

The secondary checkup was supposed to be made at least in the BOL and EOL of all conditions. Due to time constraints, it couldn't be done as desired. It was applied on all the cells at BOL though. It was applied additionally on the following conditions, which were judged to be the most critical:

- Calendar aging SOC 90 % 25 °C (BOL and EOL)
- Calendar aging SOC 90 % 45 °C (BOL and EOL)
- Cal + ST + LT (C) aging 25 °C (monthly)
- Cal + ST + LT (H) aging 25 °C (monthly)
- Cal + ST + LT (H) aging 45 °C (BOL and EOL)

The reason behind this is that this checkup required some special care. Only few available benches allowed for its elevated currents and its dynamic behavior. However, this was enough to draw conclusions on the relation between the loss in capacity obtained when the power is constant and the loss in WLTP range.

Checkup conditions. Calendar aging cells were stored unconnected to test benches (Figure 39). To undergo the checkup procedure, cells were disassembled from their setup and were connected individually (single setup) to the test benches and were compressed accordingly. Cells that undergone the other aging procedures were kept in their setup and were checked up together (double setup).

3. Experimental setup

3.1 Cell compression

When the cells were implemented in their pack, they were slightly mechanically compressed. No specific information of the compression value were provided. In order to mimic their application environment, isolated metallic plates were used to compress the cells that were confronted to the same aging condition. A pressure of $0.5 \text{ N}\cdot\text{m}$ was used on each corner of the plates, as illustrated in Figure 39.

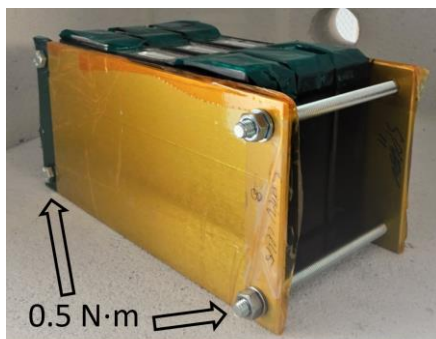


Figure 39. Typical setup of calendar aging with three cells per condition

3.2 Cell holder design.

A cell holder was designed (Figure 40) in order to:

- adapt the benches' cables to the flat battery terminals
- withstand the elevated power and current discharges (up to 570 W and 180 A)
- guarantee a good air circulation under the cells
- compress up to three cells with each other to mimic the pack environment

The cells are to be tested independently. They are mechanically assembled together, but not electrically.

The numbers in the following paragraph (❶, ❷...) below refer to Figure 40.

The terminals of the studied cell are flat (as shown in Figure 39), and are not adapted to match the nut-and-bolt design of the benches' cables. For this reason, battery connectors ❶, designed for 200 A current load, were procured. The particularity of such connectors is that a probe, passing through the length of the connector, was used for voltage measurement, allowing four-terminal sensing. Copper based contact fingers were designed to link the cables to these connectors both for the current load ❷ and the voltage ❸ measurements.

To guarantee a good enough air circulation under the cells, the Bakelite lower support was crosshatched ④. Finally, the same compression system ⑤ showed in Figure 39 was used.

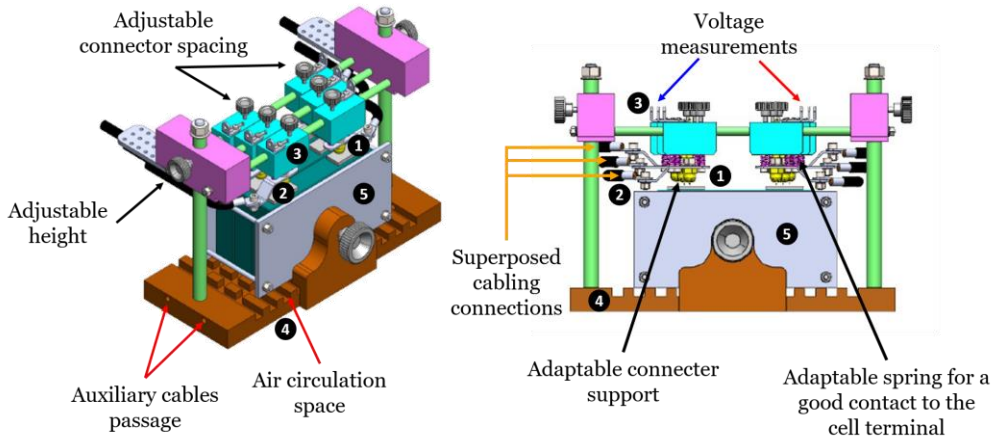


Figure 40. Cell holder design with numbers refereeing to the main components, elaborated in the paragraph above

3.3 Test benches and climatic chambers

The protocol in question is applied on a PEC SBT benches (50 A, and 250 A channels) as well as Biologic VMP benches (200 A), which is adapted for dynamic driving profiles.

For temperature control cells were stored in Binder KBF-S 1020 for the 25 °C conditions. ESPEC ARG-1100-10 for the 45 °C conditions. These chambers are equipped with air venting to ensure a better temperature control. They can then be assimilated to air cooling strategies for EV battery packs. Before each test, the a thermalization duration of 2 hours is imposed, to make sure the temperature at the level of the cells is at the desired level.

Images of the connected cells are shown in Figure 41 and Figure 42.

3.4 Data sampling and processing

Correctly sampling the data is of crucial importance. High frequency sampling generates inconvenient big files and low frequency sampling might hinder some information. According to the battery testing perspective of Dubarry et al. [287], a perfect frequency sampling should allow for around 2,000 points per step. For this reason, a sampling frequency of 1/3 Hz was taken for C/2 and P/2 cycling (2,400 points/step), and a 1 Hz frequency for the WLTP profile (minimum 1,800 points/step).

C/20 cycling required some specific care. The reason behind this cycling is to extract peak information for further battery diagnostics (as will be explained in chapter 5, parts 2 and 3). For this reason, sampling was done at a frequency of 1/10 Hz (7,200 points/step), unless the voltage varied for more than 2 mV.

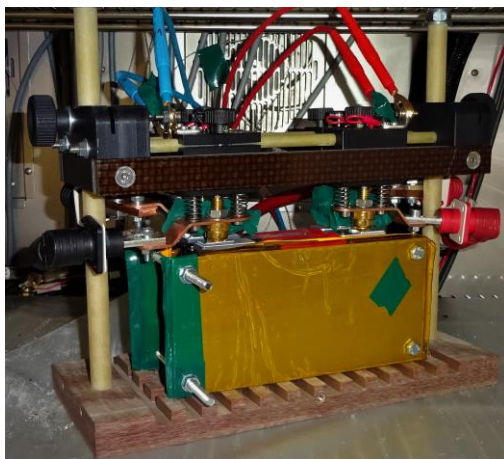


Figure 41. Experimental setup illustrating two cells of a same condition connected to Biologic benches inside a Binder climatic chamber

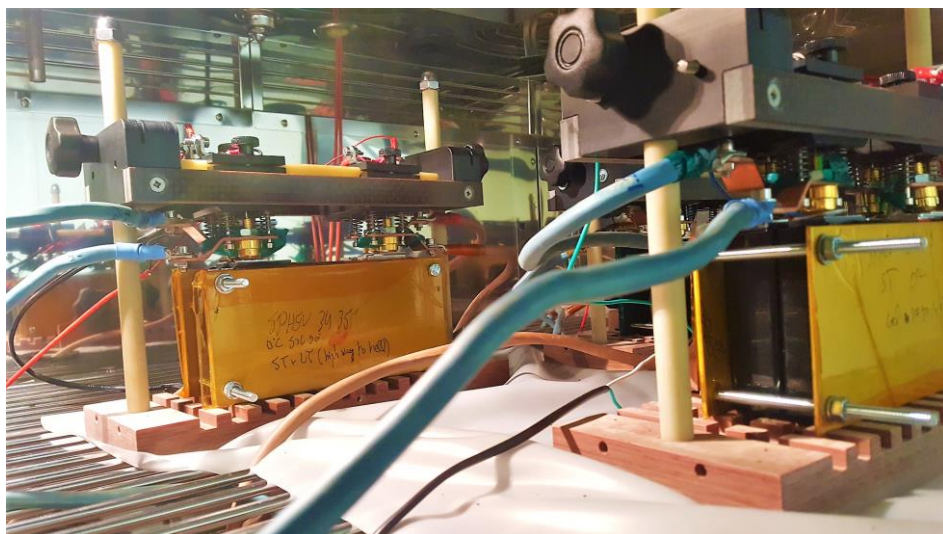


Figure 42. Inside the ESPEC climatic chamber, cells connected to PEC benches

Data were stored on the PC that is connected to the testing benches using file formats specific to the testing benches. Additional programming using the Python coding language was done to process these files. Python scripts were developed using the “pandas” module [265], the “numpy” module [266], and, for data representation, the “matplotlib” module [267].

4. Results and Discussion: cell-to-cell variation

Measuring the cell-to-cell variation at BOL helps in identifying the spread in the cells' performance values and examining their initial dispersion. This step is crucial before launching the accelerated aging protocol to make sure the homogeneity in the lot is sufficiently acceptable for comparison, and to exclude the outlier samples.

Performance variation. The method proposed by Dubarry et al. [287] consists of measuring and comparing three criteria of the battery cell to determine the spread: the capacity ration (Ah.SOC⁻¹) at C/5, the rate capability (ratio of the capacities at C/2 and C/5) and the resistance (mOhm) (using the voltage drop of C/2 and C/5 discharge rate).

The major limitation of this method is that it is reliant on the harnessing of two discharge curves (C/2 and C/5) and don't really show different facets of the battery's capabilities. The other limitation, is that it is based on constant current discharges, far from the application reality.

To overcome these limitation, three main criteria were taken into consideration, all three taken from a single setup (individually tested cells):

- the two performance criteria evoked in the earlier subparts
 - the discharged energy with a P/2 rate
 - the WLTP range
- the voltage of the cells at SOC 90 %

The first criteria represents the energy capacity of the battery, the second represents its range (including its energy and power capabilities), and the third is one of the main indicators of consistency within a battery pack [23]. In this way, usage-representative criteria are chosen, showing different facets of the battery's capabilities.

Representing the data within a 3D cube (Figure 43) is inspired by Dubarry et al. [287]. In Figure 43, the dimensions of the cube represent three times the inter-percentile range (which is the range between the 25th percentile and the 75th percentile) for the three attributes. This method is known to detect outliers [288]–[290].

No outliers were found in this lot. The median of the WLTP range was 36.41 km (with a standard deviation of $\sigma = 0.17$ km, or 0.47 %), the median of the energy was 146.56 Wh ($\sigma = 0.56$ Wh, or 0.38 %) and the median of the voltage at SOC 90 % was 4.066 V ($\sigma = 0.0023$ V, or 0.06 %).

The lot is then concluded to be homogenous enough and samples are then comparable.

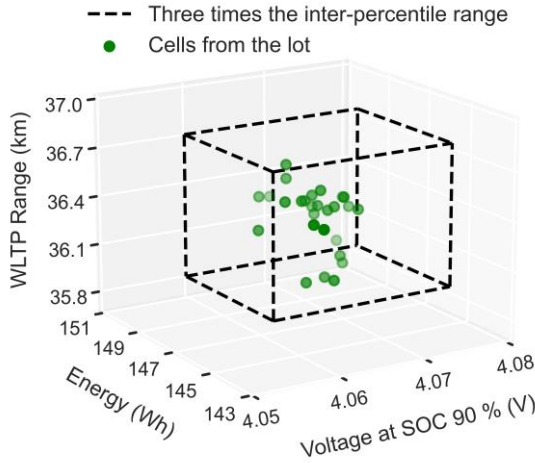


Figure 43. Cell-to-cell variation of the lot in question. The darker the color of the scatter, the nearer to the point of vision.

Electrochemical variation. To go deeper into the analysis of the cell-to-cell variation, the investigation of the incremental capacity (IC) of the entire lot was done. It consists of using the C/20 charge curve to calculate the derivative of capacity with respect to the voltage (dQ/dV , where Q is the capacity (Ah) and V is the voltage (V)). For simplification purposes, $\Delta Q/\Delta V$ is rather considered, with a constant ΔV of 5 mV.

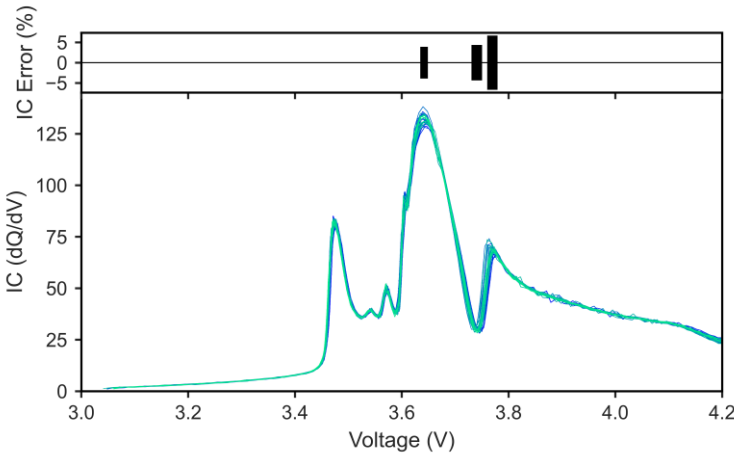


Figure 44. Investigating cell-to-cell variation of the lot in question using IC curves for a C/20 charging (lower plot). The upper plot illustrates the spread of the IC peaks and valleys: on the vertical axis the relative spread (%) (length of the sticks), on the horizontal axis the spread of the peaks' positions (V) (width of the sticks)

Here the intensity and the positional spread of the peaks are examined. The peaks that are found below the 3.6 V mark are quite similar for all the cells, with a very negligible spread, not visible on the upper plot of Figure 44. The peak at 3.643 V showed a quite considerable spread. The relative range of its intensity is 7.82 % while its positional spread is 14.4 mV. The valley at 3.741 V showed a relative intensity spread of 8.74 % and a voltage spread of 19.8 mV. Finally the last peak (3.770 V) had the highest intensity spread (13.39 %) and a voltage spread of 19.2 mV.

The last valley and peaks are very illustrative of the “electrochemical” cell-to-cell variation found in the cells. According to the ‘alawa tool (that will be elaborated in details in chapter 5 part 3) this difference is assimilated to a slight difference in the lithium inventory from a cell to another. Similar conclusion can be concluded from [34].

Discussion. Overall, the cell-to-cell variation is very negligible. As mentioned in the methodology and equipment section, the cells in question were recovered from a commercial PHEV pack. This explains the very close similarity in the performance attributes.

A slight discrepancy was found in the last valley and two peaks of the slow charging process. This is very illustrative of the “electrochemical” cell-to-cell variation. According to the ‘alawa tool (chapter 6) this difference is assimilated to a slight difference in the lithium inventory from a cell to another. Similar conclusion can be concluded from [34].

A loss of lithium inventory can be due to some calendar aging might have occurred between the day cells were made up to the day of the test. The cells were recovered from the PHEV battery pack in early 2020, therefore, at least 1.5 years of calendar aging happened before the cell-to-cell variation testing. It can also be linked to some heterogeneities within the cell, which can be generated from different sources [291]–[295].

5. Results and discussion: accelerated aging

The aging experiment went as expected for all the cells, with the exception of the cells that undergone the Cal + ST + LT (H) condition at 45 °C. Around the 200th cycle for the two cells, the Ohmic resistance increased to a certain extent that the voltage reached rapidly its lower limit during the LT (H) phase. The LT (H) phases lasted barely few seconds, instead of 5 min. This huge increase in internal resistance for this condition will be mentioned in the results analyses.

5.1 Energy evolution

In this subsection, the energy retention (equation (12)) of a discharge at constant power is monitored and studied.

5.1.1 Cal conditions

The energy retention of the Cal condition are examined in this subpart. As a reminder, three SOC levels were tested (SOC 90, 60 and 30) under two temperatures. Three cells per conditions were used, where one cell wasn't checked up (unless in the beginning of life (BOL) and at the end of test). In Figure 45, the energy retention is plotted in function of the aging month.

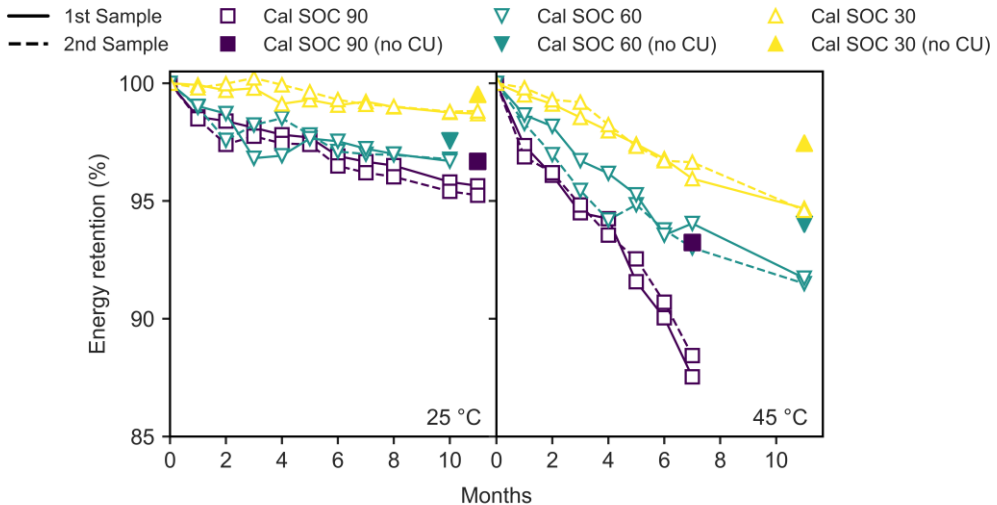


Figure 45. Calendar aging conditions energy loss plot showing the first and second sample of each condition (solid and dashed lines) as well as the third sample which undergone no checkups (no CU, filled points) (experimental error is $\pm 0.1\%$ which is here the size of each point)

25 °C. For all the cases, the first and second samples seemed to follow the same trend, except for the SOC 60 conditions during the third and fourth month. Concerning the cells that were checked up, the average energy retention of the SOC 90 condition seemed to be the lowest with an average of 95.42 % at the 11th month. It showed a rate loss of 0.014 %/day. The energy retention average of the SOC 60 condition is 96.72 % at the 10th month, with a rate loss of 0.011 %/day, which is very comparable to the SOC 90 condition. Finally, the SOC 30 condition had a final energy retention of 98.75 % showing a minor rate loss of 0.0037 %/day.

It can be noticed that for all three conditions, the no-checkup cells suffered the least. By subtracting the energy retention of the cells that did not undergo checkups by their equivalent with checkups, the impact the checkups had on the energy loss (%/CU) can be estimated. For the SOC 90 condition, 0.138 %/CU represents the energy loss caused by the checkups. This value is lower for the SOC 60 (0.103 %/CU) and SOC 30 (0.0955 %/CU) conditions. Thus the checkups impact the capacity of the cell differently for each condition.

45 °C. Similarly to the 25 °C condition, the samples of SOC 60 conditions were kind of dispersed, oppositely to SOC 90 and 30 cells. Starting with the cells that were checked up, the SOC 90 cells passed the 90 % energy retention mark to reach an average value of 87.98 %, and a rate loss of 0.057 %/day. The experiment stopped here for this condition due to the huge inflation of the cells (which will be further discussed in Chapter 6). SOC 60 cells reached an average of 91.61 % (0.0349 %/day) and SOC 30 cells reached an average of 94.64 % (0.0223 %/day).

The same method previously mentioned is used to calculate the impact of the checkups. 0.875 %/CU is the impact of the checkup on the SOC 90 aging, which is around 6 times the impact of checkups at 25 °C. It was less pronounced for SOC 60 (0.35 %/CU) and SOC 30 conditions (0.40 %/CU).

5.1.2 Cal + ST + LT Conditions

Here in Figure 46, the energy retention of the Cal SOC 90 % with checkup is plotted along with the Cal + ST and Cal + ST + LT conditions. As a reminder the Cal phase of the Cal + ST and Cal + ST + LT was carried out at SOC 90 %. The goal is to identify the impact of the energy loss induced by the ST and LT on the Cal condition. The letter in brackets next to the Cal + ST + LT refers to the road type: (U) is urban, (C) is combined and (H) is highway. The energy retention is plotted in function of the month of aging (upper horizontal axis) and the cycles (lower horizontal axis). Energy measurements were done every 120 days, which is equivalent to 30 days, so that the comparison can be made.

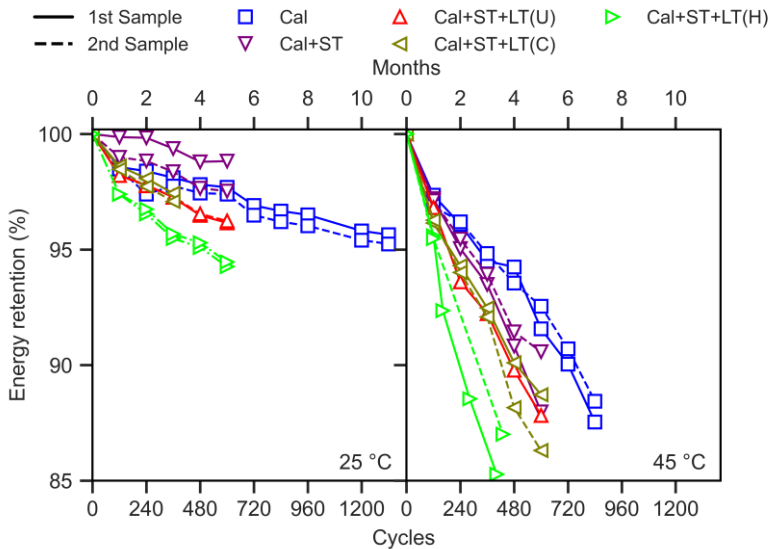


Figure 46. Loss of Energy with respect to the number of cycles and months of aging for the 25 °C and 45 °C conditions (experimental error is +/- 0.1 % which is here the size of each point)

25 °C. Starting with the 25 °C aging, results suggest that Cal + ST cells aged either similarly or less than the Cal cells, making for an average rate loss of 0.012 %/day (vs the Cal condition of 0.014 %/day). This indicates that the ST impacts very slightly the Cal conditions. The two cells of the CAL + ST varied quite differently, but the reason behind this discrepancy couldn't be clarified.

Cal + ST + LT (U) (0.025 %/day) and (C) (0.023 %/day) conditions impacted slightly the energy value of the Cal, and followed together the same trend. The mentioned conditions followed all of them a square root shape decrease.

A significant difference started to appear with the Cal + ST + LT (H) condition, which in this case followed a steeper continuous loss in energy, showing a total of 0.038 %/day.

45 °C. Oppositely to the 25 °C condition, here the Cal + ST had a significant impact on the Cal phase, following the same linear trend, and a rate loss of 0.072 %/day (vs the Cal condition of 0.057 %/day). Cal + ST + LT (U) (0.081 %/day) and (C) (0.083 %/day) phases induced a further decrease in the energy retention, but no clear differences were identified between the two conditions. Finally, the LT (H) (0.14 %/day) condition showed a steeper linear decrease, as the trend differs significantly from the other conditions.

5.1.3 Cal + HT Conditions

Finally, the Cal + HT condition is compared to the Cal SOC 30 % condition (Figure 47), in the purpose of illustrating the impact of the HT on the Cal aging of the cells. As a reminder the Cal phase of the Cal + HT was carried out at SOC 30 %.

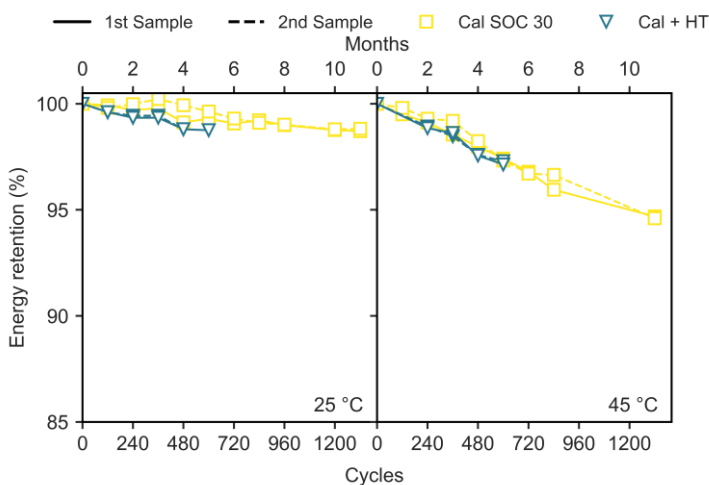


Figure 47. Energy loss of the Cal SOC 30 and Cal + HT aging condition loss, showing the first and second sample of each condition (solid and dashed lines) (experimental error is +/- 0.1 % which is here the size of each point)

The rate loss of the Cal + HT is 0.0083 %/day at 25 °C (vs 0.0037 %/day for the Cal SOC 30) and 0.0185 %/day at 45 °C (vs 0.0162 %/day for the Cal SOC 30).

It is very difficult to say if the HT had a significant impact on the Cal aging condition in this case. It can simply be concluded that the energy loss trend of the Cal + HT seems to be slightly below the trend of the Cal condition, both at 25 and 45 °C.

5.1.4 A note on the difference in the coulomb capacity (Ah) and the energy value (Wh)

As seen in the previous subparts, the energy value (Wh) of the cells was processed and compared. The energy value, as in the area under a discharge curve, takes into consideration the loss in both the coulomb capacity (Ah) and the drop in voltage, or resistance (equation (11)). In literature and standards, the coulomb capacity (Ah) is usually solely focused on. Figure 48 examines the difference between these two parameters for the same discharge curve at constant power. The energy retention is plotted in function of the capacity retention. An identity function is plotted as a grey dashed line. Values above this function indicates that the energy loss was higher than capacity loss.

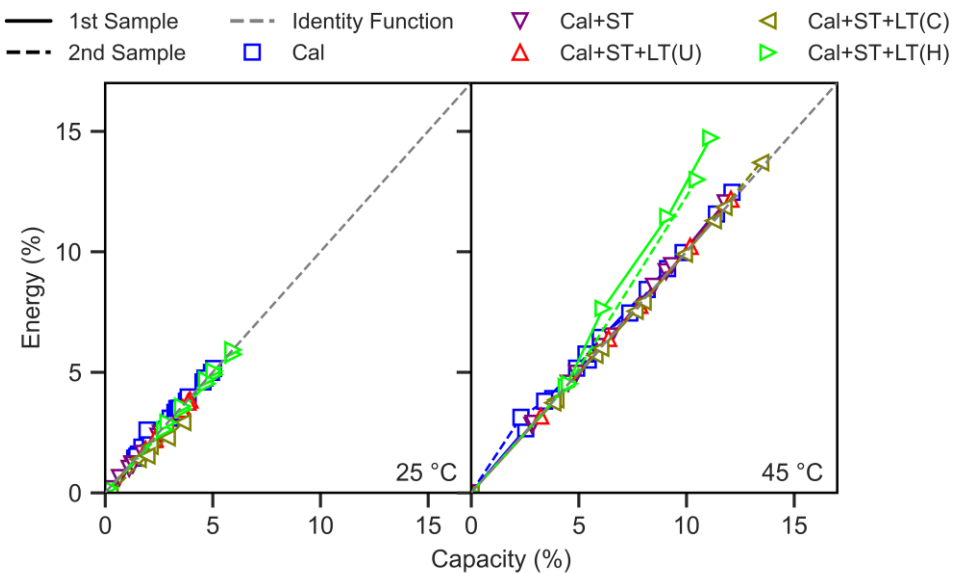


Figure 48. Relative energy loss in function of relative capacity loss

As seen, the results vary most of the time linearly. However, the energy value of the Cal + ST + LT (H) at 45 °C phase tend to increase faster than the capacity value. The final average 13.9 % value of the energy is while the capacity is 10.81 %. This shows that both values are not always comparable. The difference, as mentioned previously, is that the energy value takes into consideration the loss in internal

resistance. This proves that the internal resistance of the Cal + ST + LT (H) cells increased considerably. As mentioned previously, the LT phase couldn't be completed properly after the 200th cycle as the drop in voltage was very significant. The reasons behind this increase in internal resistance will be studied in chapter 6.

5.2 WLTP Range evolution

5.2.1 WLTP range value in function of the setup

As mentioned previously, checkups were done both on a single setups for Cal conditions, and on a double setup for the remaining conditions. It was also mentioned that the WLTP cycle was applied at BOL for all the cells. It was found out that the obtained range is not similar for the two setups.

It was noticed that when the cells were assembled, the obtained range value was higher. In other words, cells gained in range when gathered in a double setup. Figure 49 illustrates the probability density of the obtained range for the single and double setup cells.

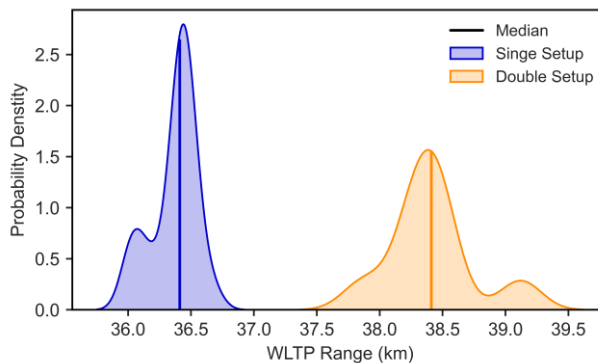


Figure 49. Probability density distribution of the range value of cells when tested individually (single setup) or assembled (double setup)

To try and explain this discrepancy, temperature measurements were made in the center side of the cell both for both setups. Figure 50 illustrates the temperature measurement in the first plot, the decrease in SOC in the second plot and the range in the third plot. Results are plotted in function of the time during a WLTP profile from SOC 90 to 30 %, for the two types of setups. The test was carried out in a 25 °C climatic chamber.

Results suggests that when tested individually, the cells heated up to a temperature of 29.2 °C, with an average of 27.0 °C. When assembled, the temperature reached a maximum of 40.5 °C, with an average of 33.3 °C. The larger increase in temperature occurs in the extra high phase of the WLTP in both cases. This is where the vehicle speed and the discharged power are at their maximum level. A high temperature

condition increases the available capacity of a cell, as it favors a smooth kinetic behavior [296].

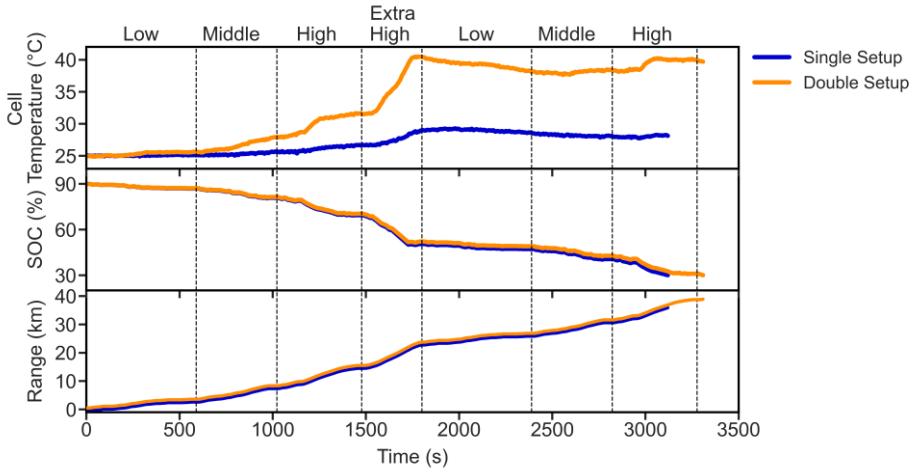


Figure 50. Illustrating the temperature (taken from the center side of the cell), the SOC evolution and the range of a cell in a single and double setup during WLTP cycling

A better kinetic behavior also decreases the internal resistance of the cell. This explains the reason behind the minor increase in temperature during the second WLTP cycle of the double setup, after 1,800 s.

The evolution of the SOC level illustrates the result of this. The SOC 30 mark, announcing the end of charge depleting (CD) mode of a PHEV, is reached faster by individually-tested cells, yielding then a lower a range.

The range proposed by the EV manufacture for the PHEV that uses this cell is 41 km at BOL, which is closer to the value obtained when cells were in a double setup. Using a bigger number of cells assembled together might increase the obtained result and reach 41 km.

However, a note should be made on the cooling. It was shown in chapter 4 that cooling can be quite efficient in a battery pack where refrigerant thermal management is used. In this climatic chamber, the temperature of the cells were hardly maintained.

The obtained results reveals the impact the testing setup has on the obtained results. As a reminder, cells that undergone Cal + ST + LT (C) and (H) at 25 °C were tested together in a double setup, so thermal interaction did impact the results obtained. The remaining conditions were tested in a single setup.

5.2.2 WLTP range loss

As previously seen the range value obtained differ with respect to the setup. For this reason, the same setup is used for each cell during its entire aging process, and the comparison is made with respect to the initial value. Figure 51 illustrates the lost in range (km) depending on each aging scenario.

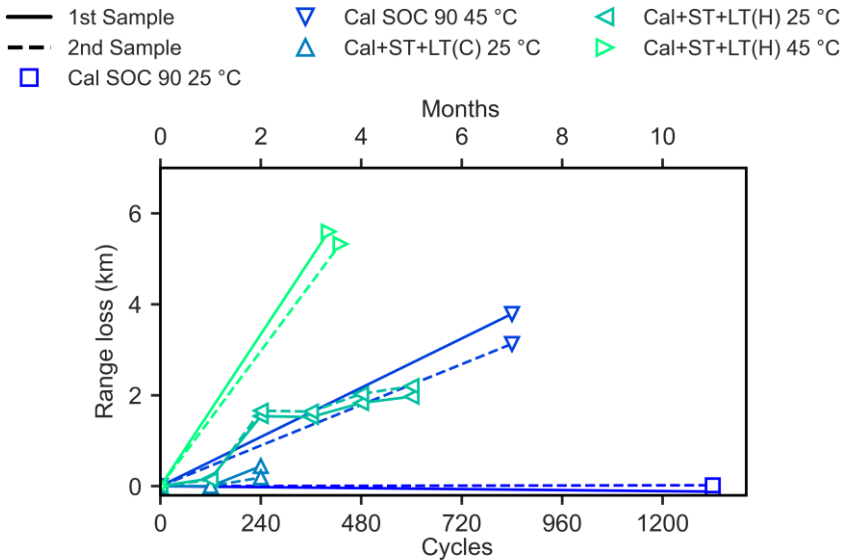


Figure 51. Range loss in function of five different aging scenarios (error in range is ± 0.0416 km, equivalent to the size of each point)

The Cal SOC 90 25 °C condition cell did not suffer any loss in range. The Cal + ST + LT (C) started to lose some significant kilometers at cycle number 240. The (H) condition on the other hand suffered significantly on cycle 240, after this the value increased slightly to reach a total loss of 2.1 km. The Cal SOC 90 45 °C suffered an average of 3.4 km loss after 7 months. Finally, the Cal + ST + LT (H) at 45 °C lost the most with an average of 6.1 km after 400 cycles, and around 3.5 months of aging.

5.2.3 WLTP range loss compared to the energy loss

In order to examine the difference between the two SOH criteria, (energy value with a constant power discharge and the WLTP range), Figure 52 confronts them in one plot.

The identity function helps in identifying the discrepancy of both values. It can be noticed that for the Cal SOC 90 25 °C condition, the energy lost an average of 4.9 % of its initial value, while its range lost nil. For the ST + LT conditions at 25 °C, the range loss started to be visible after 3 % in energy loss, where it followed the identify function trend.

Concerning the 45 °C conditions, the energy loss of the Cal scenario showed an average of 11.9 % in energy loss with a range loss of 9.5 %. The ST + LT (H) scenario results suggest that the trend the range loss (15.6 %) is bigger than the energy loss (13.7 %).

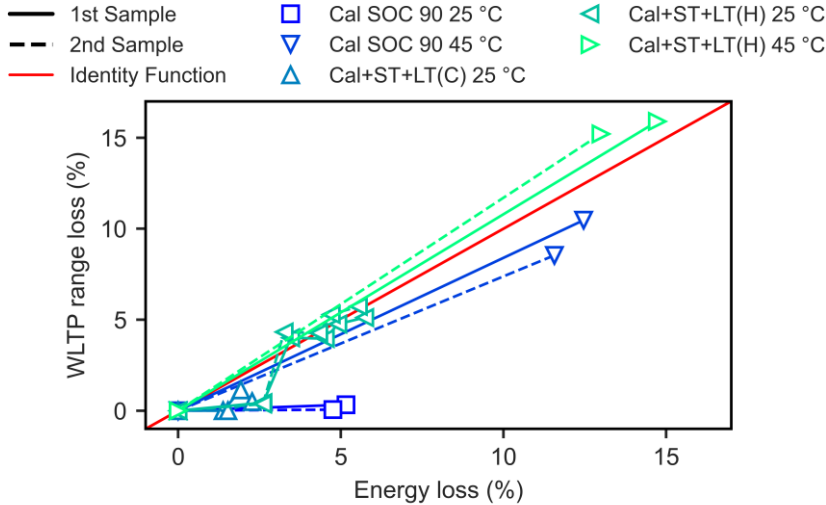


Figure 52. WLTP range loss in function of the energy loss obtained with a constant power discharge

These results prove that the loss in energy, as measured here or in standards [45]–[47], is not always correlated to the loss in range. As seen previously, the loss in range is not only based on a capacitive factor but also on a resistive one factor. And this resistive factor has a major role to play.

5.2.4 Impact of the resistive behavior on the WLTP profile

In order to visualize the resistive behavior during a WLTP, the extra high phase of the profile (1475 to 1800 s of the plot of Figure 50) was focused on, as it contains the highest power demand. Three parameters were monitored: the current, the voltage and the SOC.

Temperature has a direct impact on the resistive behavior. For this reason, cells that were tested in a single setup are separated from the ones tested in a double setup.

Single setup cells results. As a reminder, cells tested in a single setup are the Cal SOC 90 % 25 °C (energy loss around 4.9 %), Cal SOC 90 % 45 °C (energy loss around 11.9 %) and the Cal + ST + LT (H) 45 °C (energy loss around 13.7 %).

The figure below illustrates the voltage (first plot), the current (second plot) and the SOC (third plot) in function of the time during the extra-high phase of the WLTP profile.

Results of Figure 53 suggest that the Cal SOC 90 25 °C condition did not suffer much in terms of resistance increase, as the current and voltage values coincided very well. The Cal SOC 90 45 °C suffered more seriously as the voltage dropped significantly. The minimum voltage reached is 3.36 V (vs 3.47 V in the BOL). As a consequence, the current was around 5.0 A more than the BOL current. The Cal + ST + LT (H) suffered the most, as its voltage reached a minimum of 3.28 V, and its current reached an average of 164 .6 A, as it was 10 A more than the BOL current.

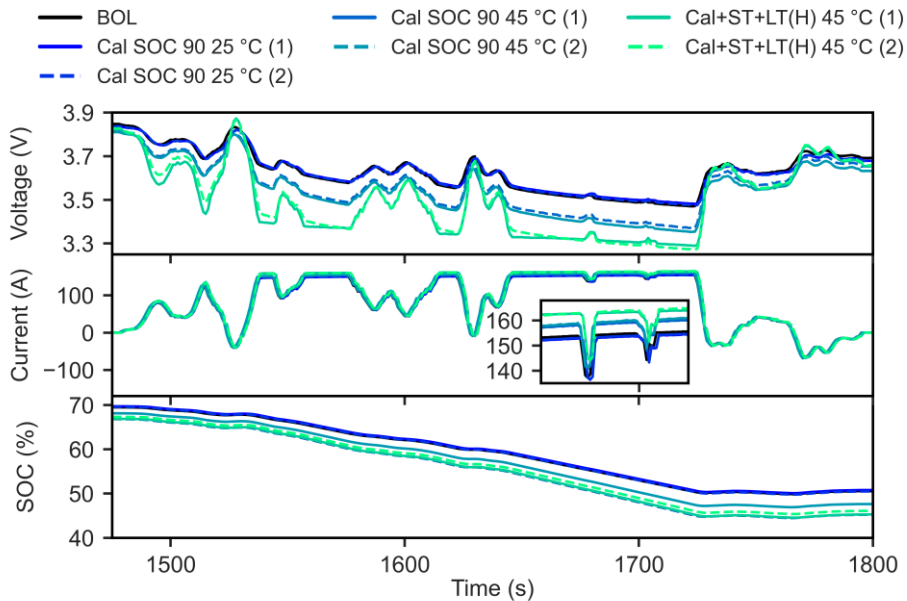


Figure 53. Resistive behavior of the aged cells in the extra high phase of the WLTP for the single cell setup

The resistance increase started to appear then for cells that suffered more than 10 % in energy loss.

As a result, a decrease of the SOC curve was noticed. The SOC in general nearly loses 20 % during this phase, and 20 % for all the previous phases (knowing that it started at SOC 90 %). This shows that the highway phases usually impact the most the remaining range. Furthermore, the difference in SOC between the BOL and the mostly aged cells nearly doubles between the beginning (2.6 %) and the end (5 %) of this phase. These results suggest that the impact of aging can be seriously noticed during the driving profiles that look like the extra high phase of a WLTP.

Double setup cells results. The targeted cells here are the Cal + ST + LT (C) 25 °C (energy loss around 2.5 %) and the Cal + ST + LT (H) 25 °C (energy loss around 6 %).

Results of Figure 54 suggest that there is a very few visible loss in internal resistance. A slight difference is seen in the SOC decrease curve, as a consequence of the loss in capacity.

The minor loss in internal resistance could be due to the double setup. When together, the temperature of the cells reach up to 40 °C, as seen in Figure 50. At such temperatures, the kinetic behavior of the cell is enhanced and the internal resistance becomes low enough to lose significance.

However, this conclusion cannot be confirmed, as the energy loss of the cells did not surpass 6 %.

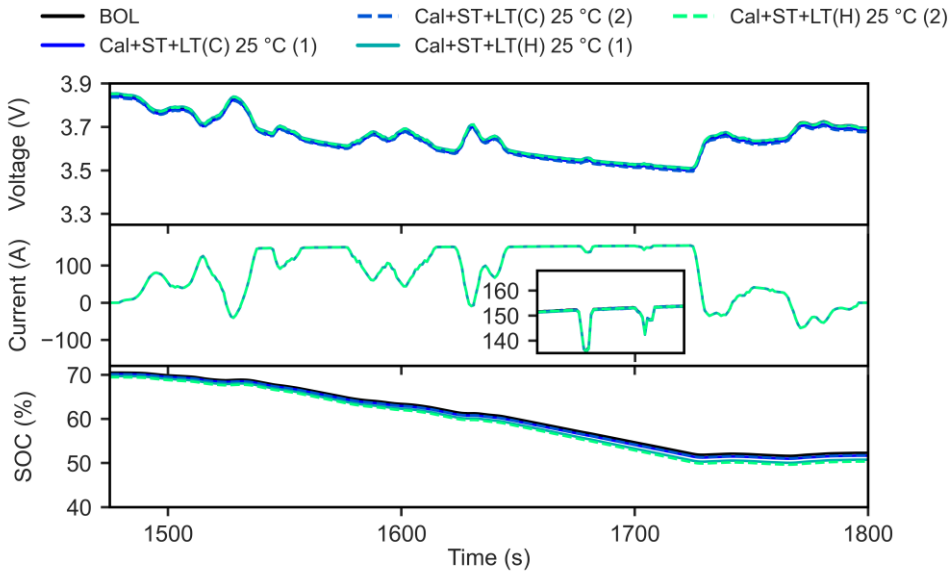


Figure 54. Resistive behavior of the aged cells in the extra high phase of the WLTP for the double cell setup

5.2.5 Outcomes of the WLTP results and perspective

The WLTP checkup procedure represents a new method to measure the SOH of the battery. As seen, it consists of measuring the “range” of the battery, hence the performance loss is expressed in km, rather than Ah or Wh.

Results suggest that the range is not necessarily related to the loss of energy. In some cases the battery lost more energy than range, as the resistance increase was very negligible. In other cases the battery lost more range than energy, and that is due to a huge increase in the battery resistance. This being said, using the area under a discharge curve of a constant power solicitation (i.e. the energy) does not reflect accurately a loss in range.

The extra high phase of a WLTP, or any highway phase, represents an opportunity to visualize this drop in internal resistance. Both the discharged current and the voltage helps in picturing this increase.

It was also found that the cell setup impact the end result. In individually tested cells, the temperature rises up to 32 °C while with a double setup, it goes beyond 40 °C. The impact of the internal resistance is then hidden.

During operating conditions, cells are stuck one to another. In other words, the temperature increase might be very similar to EV battery packs with air cooling strategies. If the pack is equipped with efficient cooling strategies, results are not comparable.

The WLTP range measurement was demonstrated to be a useful tool that can deliver information on the increase in internal resistance and the loss in energy capacity, together summarized in a single criterion, which is the range. However, the results of such experiments depend on the available benches, the temperature control of the chamber and finally the setup of the cells. Additional work need to be done in this area to try and de-correlate properly the energy loss and internal resistance increase to the range of the cell.

6. Conclusion and perspectives

In this chapter, a novel way of testing Li-ion batteries for EV applications was elaborated. It consists of referring to the usage of batteries both to identify the different phases of usage, and to parametrize the testing parameters (such as the SOC and the discharge power). This patented protocol takes into consideration the interdependence of the stress factors, such as the temperature and the road type effects on the discharged power. It also provides a way to study the impact of each phase on the previous ones, such as the impact of the cycle and the calendar phases, while maintaining the same frequency of each phase found in usage (i.e. over 90 % of calendar aging and less than 10 % of cycle aging).

The identified aging phases Cal, ST, LT and (separately) HT, are added up together in a concentric approach to study their interdependence. A cycle starts with a Cal of 5 hours, a discharge that mimics real case scenarios on different road types and temperatures, and the most common charging method until reaching a SOC of 90.

It was shown that at 25 °C, the ST did not seem to impact much the aging course of the battery at Cal conditions. When the discharge duration time increased, the impact started to gain significance, and when the highway power rates were applied the energy loss was steeper. If the SEI growth was the main mechanism at Cal conditions [41], longer cycling introduces a new aging mechanism that interacted with the SEI growth. The next chapter targets more precisely this issue.

At 45 °C, ST impacted the aging course of the battery, and the higher the cycling intensity (duration and rate), the faster the loss in energy. The shape of the curve was somehow kept the same, until the highway rate was applied. This suggests that, similarly to the 45 °C condition, the highway rate induced a new aging mechanism.

At both temperatures, the HT phase did not seem to impact significantly the course of Cal aging at SOC 30 %. At SOC levels alternating between SOC 40 % and SOC 20 %, and P-rates not surpassing the 1.1 P mark, aging seemed to be negligible, at least for the duration of the test.

It was also shown that checkups affected the course of aging. By applying the primary checkup monthly, the battery aged more rapidly. This impact is accentuated both at higher SOC and higher temperatures. It seems that checkups initiate a new aging mechanism that is further affected by the SOC and temperature levels. This issue will be further discussed in the following chapters.

The chapter also provides a novel way of testing the SOH of the battery by applying a downscaled WLTP cycle. The loss of performance is expressed in km, rather than Ah or Wh. It was shown that both values (loss in energy and loss in range) are not necessarily related. The loss in range combines both the increase in resistance and the loss in capacity. With this in hand, a WLTP range measurement can be the only checkup made for future aging studies. The entire protocol lasts less than an hour, it provides a usage representative value, and combine the two most studies criteria found in literature (capacity and internal resistance).

As mentioned, the accelerated aging protocol couldn't be done at low temperatures, although this was found to be very frequent with usage. It can be interesting to apply it at 0 °C. Furthermore, it can be applied on other type of cells such as BEV and HEV cells.

Chapter 6 – Identification of the degradation mechanisms

Highlights

- Developed the Electrode Balancing and Diagnosis (EBD) tool
- Used the 'alawa tool to identify the aging modes
- Carried out post-mortem analyses on three aged cells
- Decoupled the aging mechanisms triggered by each driving scenario

In the previous chapters, an accelerated aging protocol was derived from an exhaustive usage analysis, and was carried out on Samsung 37 Ah PHEV cells. Three different aging scenarios were tested for two different temperatures (25 and 45 °C): calendar, calendar + short trip, calendar + short trip + long trip. The purpose of this chapter is to decouple the aging caused by idle times and the one caused by the trips, through an investigation of the degradation mechanisms triggered by each scenario. This step is crucial as it will explain the different losses in performance observed in the previous chapter. It will also serve as a pillar for the following chapter where degradation mechanisms are modelled.

1. General methodology

The identification of the aging mechanisms is done on two levels: the macro level, which underlines the aging modes, and the micro level, which shed a light on the aging mechanisms.

The macro level is based on the voltage response of the cell from a C/20 charge/discharge current. Through diagnostic tools, such as the Electrode Balancing and Diagnosis (EBD) and the ‘alawa tool [58], the Loss of Lithium Inventory (LLI) and the Loss of Active Material (LAM) of each electrode are derived. This methodology is often referred to as the “mechanistic method”.

The micro level goes beyond the cell voltage response. Post-mortem analyses are done and they include the opening of the cell, a visual inspection of the electrodes physical condition, surface microscopy observations, and an investigation of their electrochemical state via half-cell experiments.

2. The Electrode Balancing and Diagnosis (EBD) tool

The EBD tool was developed in the framework of the thesis. It aims at identifying the electrodes’ balancing evolution with aging, from a cell charging curve, with the goal of determining the aging modes. Its general principles were already evoked several times in literature [61], [62], [297].

The general idea is to find the State of Lithiation (SOL) parameters of the electrodes (y , for the positive electrode; x , for the negative electrode) for which their corresponding potential (U_p and U_n) matches the voltage of the cell (V_{cell}). The relationship between V_{cell} and the electrodes potential is illustrated in equation (8). The batter resistance, R , is combination of both the ohmic and polarization resistances.

$$V_{cell} = U_p(y) - U_n(x) + IR \quad (19)$$

where

U_p is the potential of the PE

U_n is the potential of the NE

I is the imposed current

R is the battery resistance

With aging, V_{cell} varies due to loss of the electrodes’ accessible capacity (LAM) and the loss of lithium inventory (LLI), which “unbalance” the stoichiometry. In this way, identifying the stoichiometry disturbance of the electrodes highlights the aging modes.

Before proceeding, the main assumptions of using his method are the following:

Assumption 1: The half-cell potential of the electrodes in function of the lithium stoichiometry, i.e. the voltage curve shape, does not fluctuate with aging.

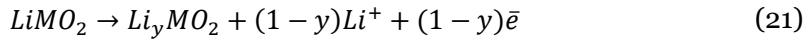
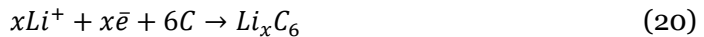
Assumption 2: A C/20 current both for the full cell and the electrode potential is considered to be low enough for the identification of the peak and to assume a semi-quasi equilibrium state.

Assumption 3: A charge scenario is favored over a discharge scenario or an “average” one. During real life usage, SOH estimations of the battery pack are usually done during charging processes where the current is controlled.

2.1 EBD principals

The idea is to describe mathematically the relationship between the voltage response of a charging cell and the electrode parameters such as their accessible capacity and their SOL.

Equation (20) and (21) illustrate the intercalation and de-intercalation reactions that happen on the two electrodes of the Samsung PHEV 37 Ah, during a charging process. The active material of the negative electrode, NE, is the graphite, $6C$. The active material of the positive electrode, PE, is illustrated by a lithium transition metal oxide, $LiMO_2$, where the M in this case is $Ni_{0.33}Mn_{0.33}Co_{0.33}$ or NMC 111.



Here x and y are normalized Li contributions, as in $x=1$ denotes a fully lithiated graphite and $y=0$ denotes a fully de-lithiated NMC. They are also referred to as the SOL parameters.

It should be noted that the lithiation here is limited to the “cyclable” lithium within the active material potential boundaries, which are 2.7 to 4.3 V vs Li/Li⁺ for the NMC 111, and 0.01 to 1.0 V vs Li/Li⁺ for the graphite. Within these boundaries, x and y vary between 0 and 1. For example, $y=0$ refers to an NMC 111 potential of 4.3 V.

A subscript of x and y that varies between 0 and 100 refers to the SOC of the full cell. In other words:

$$V_{max} = 4.2 \text{ V} = U_p(y_{100}) - U_n(x_{100}) \quad (22)$$

$$V_{min} = 3 \text{ V} = U_p(y_0) - U_n(x_0) \quad (23)$$

The normalized capacity of the cell is equal to the amount of cyclable lithium that can be intercalated in each electrode’s active material within the SOC limitations.

This being said, the capacity can then be written in function of the SOL parameters and the capacities of the electrodes, as illustrated in equation (24).

$$C = C_n * (x_{100} - x_0) = C_p * (y_0 - y_{100}) \quad (24)$$

where

C is the capacity of the cell

C_n is the NE capacity

C_p is the PE capacity

The normalized capacity of the electrodes can be then expressed with the following equations (25) and (26).

$$C_n = \frac{C}{x_{100} - x_0} \quad (25)$$

$$C_p = \frac{C}{y_0 - y_{100}} \quad (26)$$

During a charging process, the normalized charging capacity of the cell (Q_{ch}) can be expressed in function of the SOL factors, as in equation (27). The variables y and x illustrate the SOL of each electrode during charging.

$$\frac{Q_{ch}}{C} = \frac{y_0 - y}{y_0 - y_{100}} = \frac{x - x_0}{x_{100} - x_0} \quad (27)$$

By plugging in equation (25) in (27), x can be expressed in function of the charging capacity, the capacity of the NE and the initial SOL (equation (28)).

$$x = \frac{Q_{ch}}{C_n} + x_0 \quad (28)$$

By plugging in equations (26) and (28) in (27), y can be expressed in function of the capacity of both electrodes, their initial SOL, and x (equation (29)).

$$y = \frac{y_0 * C_p + x_0 * C_n}{C_p} + \frac{C_n * x}{C_p} \quad (29)$$

Here, the numerator of the first element represents the total amount of cyclable lithium, which is defined by the total amount of lithium inside each electrode at a certain SOC. Equation (29) can then be written as in equation (30), where C_{Li} represents the total amount of lithium present in the cell.

$$y = \frac{C_{Li}}{C_p} + \frac{C_n * x}{C_p} \quad (30)$$

Equation (30) expresses y with respect to the total amount of cyclable lithium, the capacity of both the PE and the NE active material, and the charging SOL of the negative electrode.

Equation (31) can then be written in function of θ , where θ is the set of parameters $[C_{Li}, C_n, C_p, x_0, R]$.

$$V_{EBD}(\theta) = U_p \left(\frac{C_{Li}}{C_p} + \frac{C_n * x}{C_p} \right) - U_n \left(\frac{Q_{ch}}{C_n} + x_0 \right) + IR \quad (31)$$

Equation (31) expresses mathematically the voltage response of a cell in function of the cell parameters, θ . It will be used to reconstruct the voltage of the “real” cell during a C/20 charging scenario. The parameters will then be optimized for an accurate reconstruction of the experimental curve. Reconstructing the voltage response of the “aged” cells will result in a new set of parameters θ . The evolution of the parameters θ will hint at the aging modes.

The aging modes refer to the Loss of Lithium Inventory (LLI), the Loss of Active Material of both the negative electrode (LAM_{ne}) and the positive electrode (LAM_{pe}). The following expressions describe these concepts mathematically, where the upper scripts i and a refers to initial and aged, respectively.

$$LLI = 1 - \frac{C_{Li}^i}{C_{Li}^a} \quad (32)$$

$$LAM_n = 1 - \frac{C_n^i}{C_n^a} \quad (33)$$

$$LAM_p = 1 - \frac{C_p^i}{C_p^a} \quad (34)$$

2.2 EBD algorithm and usage methodology

The main input to the algorithm is the potential vs Li/Li⁺ of the electrodes in function of their SOL that ranges from 0 to 1 ($U_p=f(x)$ and $U_n=f(y)$). Following “Assumption 1” stated in the introduction of this part, this input was taken from the unaged electrodes and will not vary during the aging of the cell. To do so, electrode samples were taken from the full cell, following the procedure explained in the section 5.1 of this chapter.

Since the experimental voltage curve is a C/20 charge, then, for consistency purposes, the potential of the PE was obtained for a C/20 de-lithiation (0.220 mA, considering the capacity of the electrode at C/10) and the potential of the NE is obtained for a C/20 lithiation (0.207 mA, considering the capacity of the electrode at C/10).

The second input is the experimental C/20 charging voltage curve of the cell (V_{exp}). The imposed current was 1.85 A, considering the nominal capacity of the cell (37 Ah).

The idea is then to optimize the θ parameters to solve for equation (35), where the tolerance, ε in Figure 55, is 0.5×10^{-3} . This tolerance is considered to be sufficient for an accurate enough reconstruction of the voltage curve.

$$\min_{\theta} |V_{EBD} - V_{exp}|^2 \quad (35)$$

where

V_{EBD} is the voltage output of the EBD tool

V_{exp} is the experimental voltage of a C/20 charge

The algorithm is illustrated by the flowchart of Figure 55.

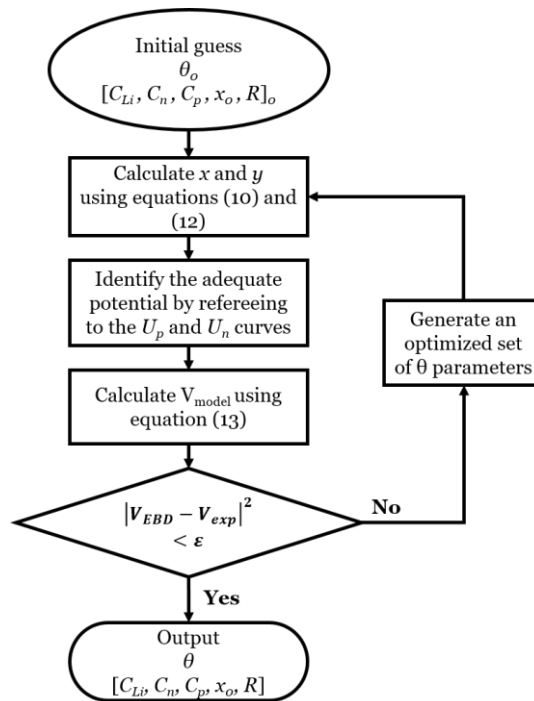


Figure 55. Flowchart for the EBD tool

During the accelerated aging tests, C/20 checkup procedures were carried out monthly, as explained in chapter 5. After each checkup, a new C/20 voltage curve (a new V_{exp}) was entered in the tool for the estimation of a new set of parameters.

2.3 EBD calibration at BOL

Calibrating the tool and making sure that its outputs are valid is necessary before its application. To do so, the C/20 charging voltage curve at BOL was used as a calibration. The output of the model and its Incremental Capacity (IC) (dQ/dV) were

compared to the experimental outcome. IC verification is used to assertively confirm that the tool is able to replicate the phases transitions of the material.

In Figure 56 (A), the C/20 experimental voltage curve is plotted along with the voltage output of the EBD tool. The absolute voltage error of the two curves is plotted in Figure 56 (A'). The IC of the two outcomes are compare in Figure 56 (B). The error of the IC peaks and valleys are illustrated in Figure 56 (B') by sticks. The width of the sticks (vertical axis) represents the peak's positional error (V) on the voltage axis, and the length of the sticks (horizontal axis) represents the relative difference (%) between the peaks' intensities (when positive, the experimental is higher than the EBD outcome).

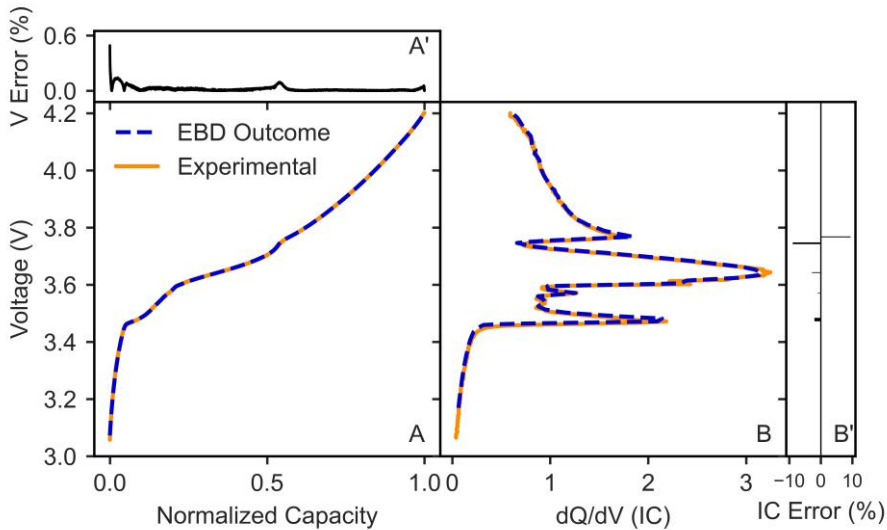


Figure 56. Calibration of the EBD tool at BOL. (A) Experimental C/20 charge voltage curve along with the EBD tool results. (A') EBD tool outcome vs Experimental voltage absolute error. (B) IC curve of the experimental C/20 charge along with the IC curve of the simulated C/20 charge. (B') Experimental vs simulation IC peaks error

The voltage error was nearly 0 % for the entire C/20 charging process. The positional error was negligible for all peaks (< 1 mV), except the one that stands around the 3.5 V, with an error of 9.90 mV. The valley around 3.75 V has a positional error of 3.74 mV. Concerning the intensity of the peaks, it was overall inferior to 10 %. The highest errors occurred on the valley at 3.74 V and the peak at 3.77 V, having values of 8.91 % and 9.48 %, respectively. It should be noted that in the cell-to-cell variation verification in Figure 44 of chapter 5, it was noticed that the same valley and peak showed a spread of 8.74 % and 13.39 %. This explains the wide difference observed here. With this in hand, the EBD tool was considered to be valid at BOL and then well calibrated.

The outcomes are given in Table 11. The Loading Ratio (LR) represents the ratio of the negative to the positive capacity (N/P ratio). The “offset”, as stated by [58], represents the amount of lithium consumed on the negative electrode through parasitic reactions such as the formation and growth of the SEI. To obtain this values, the capacity of the PE (C_p) is subtracted by the total amount of lithium present at BOL (C_{Li}). This is done under the assumption that between the formation and the post-mortem process, no additional SEI was formed.

Table 11. Outputs of the EBD tool for the BOL (normalized values)

C_p	C_n	C_{Li}	LR	x_0/x_{100}	y_0/y_{100}	<i>Offset</i> (% of C_n)
1.087	1.057	1.024	0.972	0.00556/0.952	0.937/0.0169	5.94

The capacity of the PE is slightly higher than the NE one, hence yielding an LR ratio of 0.972. Experimentally, the areal capacity of the half-cell electrodes gives a value of 0.946 ± 0.0170 . The EBD tool outcome has a relative difference then of 2.45 %.

The outputs of the calibration and electrode balancing can be visualized in Figure 57.

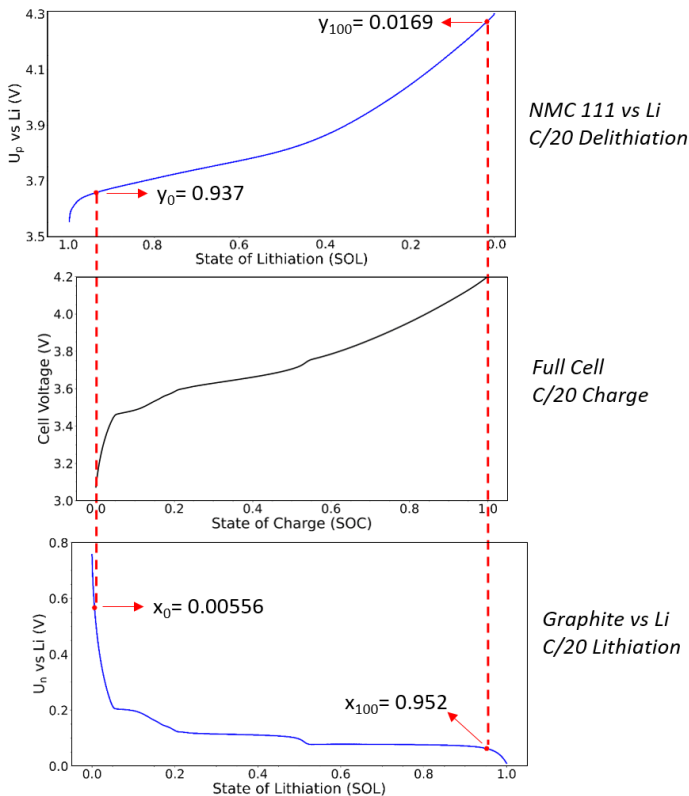


Figure 57. Electrode balancing results from the EBD tool

2.4 Application and Results

In order to identify the C_{Li} , C_n and C_p evolution of each cell with aging, the C/20 charging curves of the full cell, obtained during the monthly checkups, were entered in the EBD tool and new parameters were extracted. Results of chapter 5 suggested that the trend in the performance loss evolution was reproducible enough. For this reason, only one cell per condition is analyzed using the EBD tool.

The EBD tool was applied on the following aging conditions:

- Calendar SOC 90 % (Cal)
- Calendar SOC 90 % without checkups (Cal (no CU))
- Calendar SOC 90 % + Short Trip (Cal + ST)
- Calendar SOC 90 % + Short Trip + Long Trip (Cal + ST + LT) for the Urban (U), Highway (H) and Combined (C)

This choice was done for the sake of decoupling the impact of cycling (ST and ST + LT scenarios) on the calendar aging of the cells, and quantifying the impact of the checkups. It was shown in Chapter 5 that the checkups tended to degrade the performance of the battery.

The evolution of these parameters are plotted in Figure 58 (25 °C) and Figure 59 (45 °C), using equations (32) to (34).

The plots are separated into three parts, where the first illustrates the evolution of the LLI, the second the LAM_{pe} and the third the LAM_{ne} . The values are plotted in function of the cycle number (on the lower horizontal axis) and the month (on the upper horizontal axis). Checkups are done each month for all conditions. ST and LT conditions undergone 120 cycles per month.

LLI. The LLI evolution of the Cal condition at 25 °C (Figure 58) seemed to increase in a square root fashion. It showed an LLI value of 3.92 %, while the Cal-NoCU condition showed an LLI of 3.53 %. While this remain in the error margin (+/- 0.55 %), it might hint at the reason why the Cal condition aged more than the Cal (no CU) (chapter 5).

Results suggest that the Cal + ST showed an almost similar evolution to the Cal scenario, with a lower elevation.

The Cal + ST + LT scenarios, on the other hand, had a considerable impact. The more intense the cycling (discharge duration and rate), the higher the LLI, while maintaining a square root evolution.

Concerning the (H) scenario, the LLI increased brusquely in the first month of aging, and steadied for the next two months of cycling, hence keeping the square root shape but with a higher amplitude. After this, the LLI value increased exponentially, hinting very probably at the activation of an additional aging mechanism.

2.4.1 Aging at 25 °C

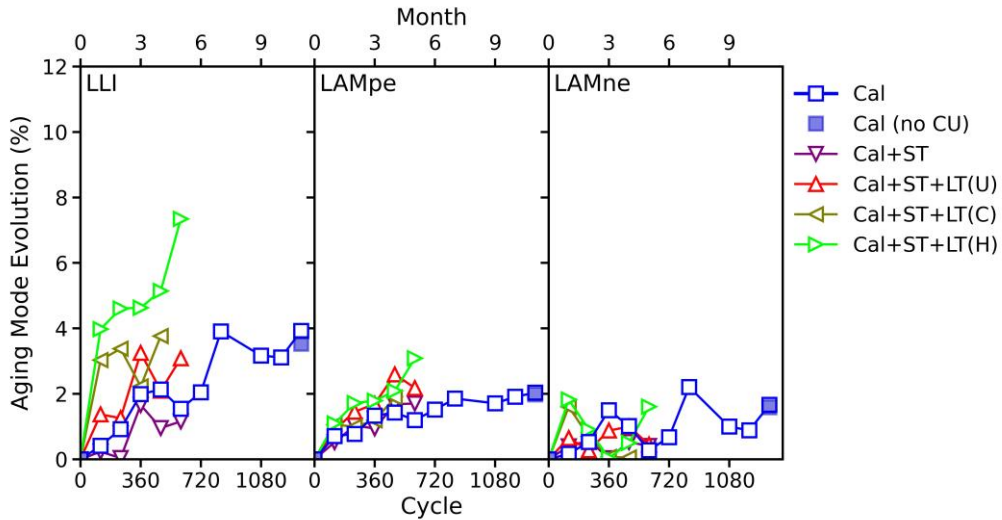


Figure 58. Aging modes evolution at 25 °C (error = +/- 0.55 %)

LAM_{pe}. During Cal conditions, the first points of the LAM_{pe} had a higher amplitude than the LLI. LAM_{pe} increased in a square root shape, reaching a relatively steady phase after the 8th month. The Cal (no CU) condition showed a very value at the last checkup, proposing that the checkups do not to have a significant impact on the LAM_{pe}.

The plot suggests that Cal + ST and Cal + ST + LT (U) and (C) did not seem to impact significantly the LAM_{pe}.

The (H) condition values increased at a slightly faster rate, showing certain changes in the shape of the curve at the last checkup.

LAM_{ne}. Lastly, LAM_{ne} values fluctuated between 0 and 2 % for all conditions. A minor increasing trend can be identified, especially for the Cal condition. The Cal (no CU) condition showed again a very similar result to the Cal condition, proposing that the checkups might not have a clear impact on the LAM_{ne}.

2.4.2 Aging at 45 °C

LLI. In general, the LLI seemed more significant than the results obtained at 25 °C (Figure 59). In the Cal scenario, its evolution starts with a linear increase in the first two months, seems to stabilize in the following two months, before increasing linearly for the remaining months. The Cal (no CU) condition showed a significant difference when compared to the Cal values (8.57 % vs 11.33 % respectively).

Cal + ST induced very comparable LLI levels with the Cal aging for the first 2 months, but LLI carried on with a slightly higher rate, before stabilizing and increasing again.

Increasing the discharged duration with long trips, ST + LT (U) and (C) amplified further the LLI rate with comparable results, maintaining the same shape.

Lastly, the Cal + ST + LT (H) scenario showed a very steep increase in the LLI before the 240 cycles mark. After this, the rate of growth decreased. As seen previously, after the 200th cycle, the resistance of the cell increased to a certain extent that, consequently, the LT phase lasted very few seconds, instead of 5 min, as the voltage used to reach rapidly its lower limit. This means that the impact of the LT phase was very negligible after the 240th cycle, which explains the reason behind the lower growth.

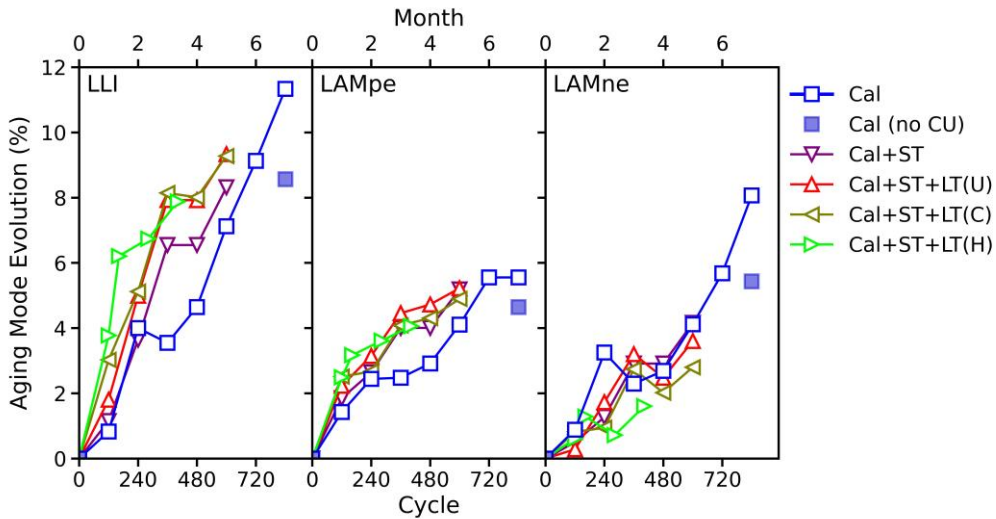


Figure 59. Aging modes evolution at 45 °C (error = +/- 0.55 %)

LAM_{pe}. For the Cal condition, the LAM_{pe} seemed to be very intense in the first stages of aging, with values higher than the LLI. For the second and third month, the level seemed to stabilize, before increasing again after the fourth month to form two square root shape curves. This can be assimilated to two stages of aging. The result of the Cal (no CU) condition suggests a reduced LAM_{pe} than the Cal condition (4.64 vs 5.56 %), suggesting that the checkups had a significant impact on the LAM_{pe}.

While ST and LT scenarios seemed to increase slightly the rate of LAM_{pe}, it is difficult to quantify this. The difference between Cal, ST and LT remains within the error bars in the first two months of aging. After this, while the LAM_{pe} stabilized with the Cal scenario, it kept on increasing with the ST and LT scenarios, following a single square root shape.

LAM_{ne}. For the Cal condition, the LAM_{ne} curve showed a significant increase, especially after the fourth month. The Cal (no CU) condition proposes a significant difference in the obtained LAM_{ne} value (5.43 vs 8.07 %). The plot suggests that the Cal + ST and Cal + ST + LT scenarios followed a similar trend.

2.5 Discussion

The analysis of these results is made on two levels. The first underlines the aging mechanisms consistency between the aging at 25 °C and the one at 45 °C by focusing on the calendar condition. The second will highlight the impact of each driving scenario on the calendar aging.

2.5.1 Aging mechanism consistency

In order to evaluate the aging mechanisms consistency between the 25 and 45 °C aging, the EBD obtained results for the Cal and Cal (no CU) conditions are plotted in. Similarly to the previous parts, the three panels represents, from left to right, the LLI, LAM_{pe} and LAM_{ne} evolutions.

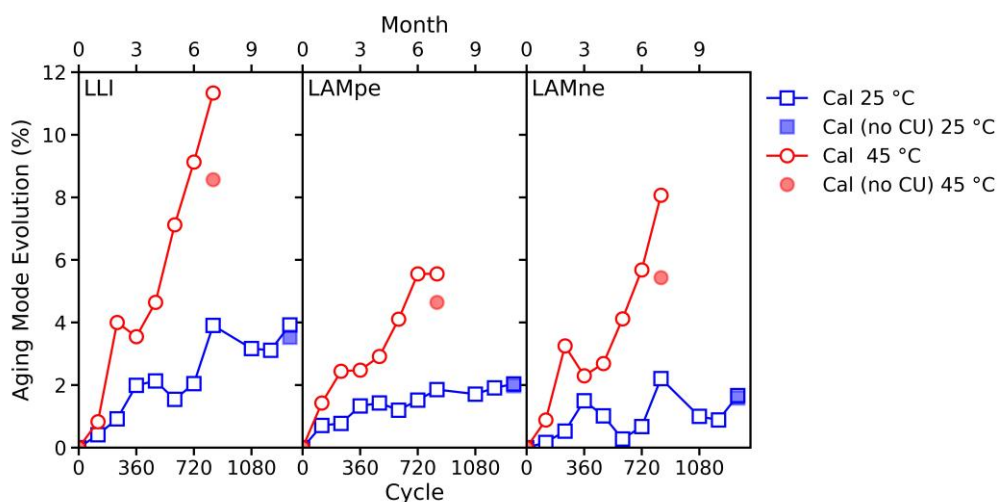


Figure 60. EBD outcomes of the Cal and the Cal (no CU) conditions of both temperatures (error = +/- 0.55 %)

At 25 °C the LLI value increased in a square root shape, while at 45 °C, the shape was mostly linear with a steep slope. This indicates that the origin of the growth, or its nature, are not the same. The square root shape at 25 °C can be assimilated to the SEI growth [94]. At 45 °C, other mechanisms might have assisted this growth.

The evolution of the LAM_{pe} at 45 °C is quite steep, suggesting the hypothesis of the dissolution of transition metal, which is accelerated at high temperatures [75], [77], [298]. Such mechanism isn't surprising here as the cell spent most of the time at SOC 90 %, where the PE active material is found at a low state of lithiation. It has been proposed in literature [76] that the dissolved transition metals can pollute the SEI layer and increase its growth rate. This can explain the steeper increase in the LLI, which coincided with the increase in LAM_{pe}. At 25 °C, the LAM_{pe} followed a square root shape at 25 °C. Suggesting that the dissolution of transition metals at 25 °C can be limited to the beginning of aging.

The LAM_{ne} increased also very steeply at 45 °C, when compared to its homologue at 25 °C, which had no significant rise. The increase coincides very well with the increase in LLI, proposing that the accelerated growth of SEI might have caused some pore clogging.

As a conclusion, the aging mechanisms consistency for both temperatures is very questionable here. The evolution of the aging modes and the possible origins of the mechanisms do not coincide between the two temperatures.

2.5.2 The impact of the ST and LT on the Cal aging

In order to study the impact of the ST and LT, the discussion below will refer to Figure 58 (25 °C) and Figure 59 (45 °C)

25 °C. Results suggest that the ST phase did not have any significant impact on the rate of LLI. This indicates that the corresponding aging mechanisms might be the same, at least for the first five months of aging.

The Cal + ST + LT (U) phase did increase slightly the LLI, and the (C) amplified it more significantly. Both managed to share a common square root shape, similarly to the Cal phase.

Up to this level, the suggested mechanisms behind this phenomena can be the cracking of the SEI surface due to cycling, which increases the contact surface and accelerates its growth. ST + LT scenarios are the reason behind the cracking of the SEI, and the Cal phase is the reason behind its growth, hence keeping the square root shape. As the cycling gets more intense (discharge duration and rate), the SEI cracks further, and lithium is further consumed, which could explain this rise in LLI when ST + LT is applied. This is known as the breakdown and repair process [38], [66].

For the ST + LT (H) phase, the LLI followed a similar evolution in the first three months, but with a higher amplitude, due to the reason mentioned above. Starting with the fourth month, the LLI value increased exponentially. This suggests that a new phase in the aging process was triggered. At such elevated currents, the cracking of the particles can happen alongside the cracking of the SEI. This opens up new areas for the formation of a new SEI layer, and the intensive further consumption of lithium [38], [50], [66].

It is hard to conclude the ST and LT had an impact on the LAM_{pe} and LAM_{ne} . It seems to be in general controlled by the Cal phase. For the (H) phase, however, a start in the increase of the LAM_{pe} was noticed at the last checkup, and coincided very well with the increase in LLI. If the LLI is assumed to be mostly done on the NE, the electrodes potential become imbalanced to each other. This pushed the PE potential to higher values, and can excessively de-lithiate it, hence accelerating its degradation [41].

45 °C. The LLI shape was quite remarkable, and followed these stages, for all conditions:

1. Linear increase
2. Stabilization
3. Linear increase

Even if the shape was the same for all aging conditions, the amplitude of the stabilization phase wasn't. For the Cal condition, the stabilization came at an amplitude of 4 % LLI. For the other conditions, it was reliant on the cycling intensity, i.e. discharge duration or discharge rate. The Cal + ST increased the level of the "stabilization" phase by a significant amount. A simple discharge was enough to increase the level of LLI, and that is due to the SEI surface cracking, which could be intensified at high temperatures [41].

In the Cal + ST + LT (U) scenario, the only factor that adds up here is the discharge duration. Only that was enough to increase even more the stabilization phase. A larger DOD was known to induce further cracking and accelerate the SEI growth [299].

In the Cal + ST + LT (C), the discharge duration was the same as in the previously mentioned scenario, but the factor that added up is the discharged rate. This wasn't enough to increase the stabilization phase, it only increased the amplitude of the initial LLI rise (further SEI cracking).

For the ST and ST + LT cases mentioned, the LLI value suffered from another increase after the 480th cycle. This suggests particle cracking, opening up new areas for the formation and growth of a new SEI layer. At high temperatures, particle cracking is favored, and that might be the reason why at 25 °C, this phenomena is not observed [41].

The most reliable information to deduce from the Cal + ST + LT (H) is that it induced a very steep LLI in the first two stages of aging. This can be attributed to the SEI and/or particle cracking due to excessively high current densities, which causes a considerable mechanical stress on the electrodes. This explains the increase in the internal resistance after the 240th cycle mark, where the LT phase couldn't be completed.

The LAM_{pe} shape was different for the Cal and for the cycled cells. While the Cal induced two square root curves, the other induced only one. The LAM_{pe} for the ST and ST + LT phases suggests that the PE suffered more due to the instability and unbalancing of the PE electrode. The potential of the PE gained higher values due to the LLI at the NE, as explained previously [41].

The LAM_{ne} seemed to be controlled by the Cal phase for the ST and ST + LT (U and C) scenarios. For the (H) scenario, it seemed to be lower than the other cases.

2.6 The key take-away points

Hereunder, the key points of the analysis to take away, with some possible aging mechanisms reasons.

- Cal at 25 °C seems to be dominated by LLI, due to the SEI growth identified by the square root shape curve, and LAM_{pe} , due to the dissolution of positive transition metals at high positive electrode potentials.
- Cal at 45 °C seems to be dominated by LLI, due to a much steeper growth of SEI, LAM_{pe} , due to a harsher dissolution of transition metals, and LAM_{ne} , which can result from thickening of the SEI layer leading to pore clogging.
- At 25 and 45 °C, the LAM_{pe} in the first stage of aging had a value that is greater than the LLI. This implies that LAM_{pe} starts at a higher rate in the beginning of aging, and this is associated to the instability of the PE due to high SOC levels.
- Increasing the rate of discharge will cause SEI cracking and growth, hence, further LLI consumption, and that is especially true at high temperatures, where the cracking is favored.
- Increasing the discharge duration without increasing the discharge rate (Cal + ST + LT (U and C)) amplifies the intensity of LLI, without changing the shape of the curve. The discharge duration hence adds up the SEI growth rate due to its further cracking.
- The Cal + ST + LT (H) 25 °C scenario induced two stages of aging for the LLI. The first looks like a square root shape with the highest intensity, as the discharge depth and rate are the highest. The second looks like a sudden exponential increase, and can be assimilated to the particle cracking at high discharge rates, which can lead to the formation of a fresh SEI, hence a harsher consumption of LLI.
- The LAM_{pe} and LAM_{ne} seemed to be controlled by the calendar phase at 25 °C, while at 45 °C, the LAM_{pe} increased as cycling was applied. This is due to the consumption of lithium at the NE and the unbalancing of the electrodes' potential.

3. Application of the 'alawa toolbox

The 'alawa diagnostic tool can also help in identifying the degradation modes. It has been provided to us by Dr. Matthieu Dubarry from the Hawai'i Natural Energy Institute (HNEI). Its development details and principles are explained in [58].

In a nutshell, it has the ability to reconstruct the voltage curve of the full cell under specific charging rates, by using the half-cell electrodes potential. Aging modes can be plugged in by the user, and the evolution of the IC curve's peaks and valleys of the full cell can be tracked. It will be used as another way of identifying the aging modes.

In the following section, its calibration is going to be elaborated.

3.1 Calibration of the ‘alawa tool

Very similarly to the EBD tool, a main component of its calibration is the half-cell potential of the electrodes under different charging rates. The goal here is to reconstruct accurately the voltage curve of the full cell. Half-cell experiments were done using the protocol explained in section 5.1. The LR ratio found experimentally (0.946 %) and the offset value obtained from the EBD tool (5.94 %) were plugged in. The outcome is validated experimentally in Figure 61. In Figure 61 (A), the IC curve of both the cell and the ‘alawa outcome are plotted in function of the voltage for a C/20 charge. In Figure 61 (B), the error sticks of the peaks and valley are plotted. The length of the sticks represent the intensity error of the peaks, while their width represents the positional error.

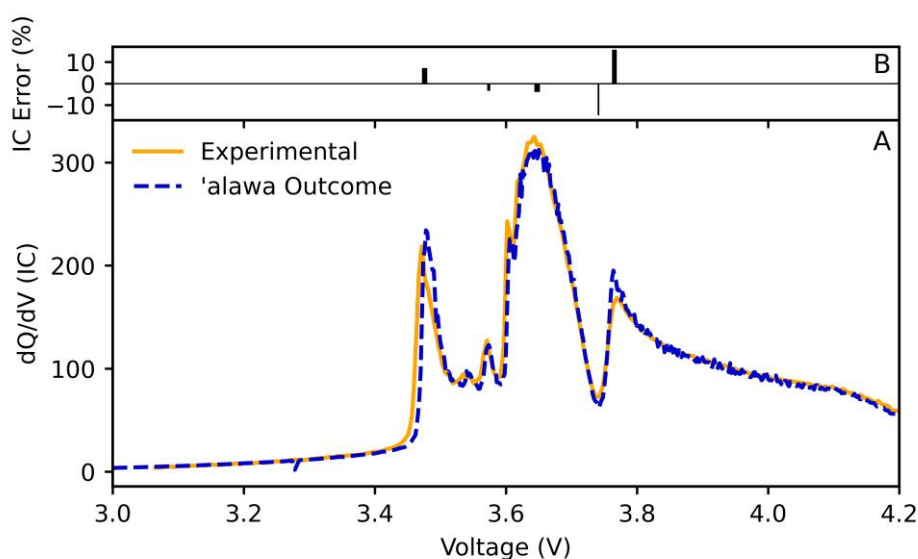


Figure 61. Calibration of the ‘alawa model at BOL. (A) Experimental C/20 charge voltage curve along with the ‘alawa tool results. (B) Experimental vs simulation IC peaks error: on the vertical axis the relative difference (%) between the peaks’ intensities (length of the sticks), on the horizontal axis the difference between the peaks’ positions (V) (width of the sticks)

The peaks positional error ranges between 2.60 mV to 6.40 mV, and the only valley (at 3.74 V) error is less than 1 mV. The intensity relative error is usually less than 10% except for the peak at 3.77 V and valley at 3.74 V, with 15.72 % and 14.70 % respectively. These same peak and valley were found to have the highest intensity error in the EBD tool. The reason, as explained earlier, comes from the cell-to-cell variation (Figure 44 of chapter 5).

3.2 Identification of the Features Of Interest (FOI)

The 'alawa tool helps in simulating the evolution of the IC curve under different aging modes. The FOIs, as explained in [300], [301], are used to track the core information of the IC curve. They can represent the intensity of certain peaks and valleys, their position on the voltage axis, the area under certain regions or even the slope of certain peaks. The goal is to correlate the evolution of the FOIs with the aging modes via 'alawa, and compare them to the evolution of the experimental FOIs.

Hereunder (Figure 62), four simulations were done on the calibrated 'alawa tool for this cell: LLI, LLI + LAM_{pe}, LLI + LAM_{ne}, LLI + LAM_{pe} + LAM_{ne}. The goal was to choose the most revealing FOIs for an efficient comparison with the experimental data.

It is possible in 'alawa to differentiate two kinds of LAM [58]: the LAM_{li} and the LAM_{deli}. The first refers to the LAM when the electrode was lithiated and the second refers to the LAM when the electrode was de-lithiated. The LAM_{li} involves some LLI. So to eliminate any confusion, the only LAM that was taken into consideration was the LAM_{deli}.

LAM_{ne} and LAM_{pe} were not entered in the 'alawa without LLI here. It was assumed that LLI always occurred at such conditions and LAM never took place alone.

Simulating these on 'alawa required to plug in a certain "evolution rate" expressed in % per cycle (or per day) for each mode. So when modes were combined, equal shares were assumed for every mode. This assumption was taken here for the purpose of studying the trends of the FOIs, and should be kept in mind for further interpretations.

The peak that stands at 3.47 V (FOI 1), the one that locates at 3.63 V (FOI 2) and the one that situates at 3.78 V (FOI 3), at SOH 100 %, were chosen as FOIs. Both their position on the voltage axis and their intensity varied considerably under all aging scenarios. Additionally, the area under the curve between 4.0 and 4.1 V (FOI 4) suggests a LAM_{pe}. The four FOIs are illustrated in Figure 63 on an IC curve at BOL in function of the voltage.

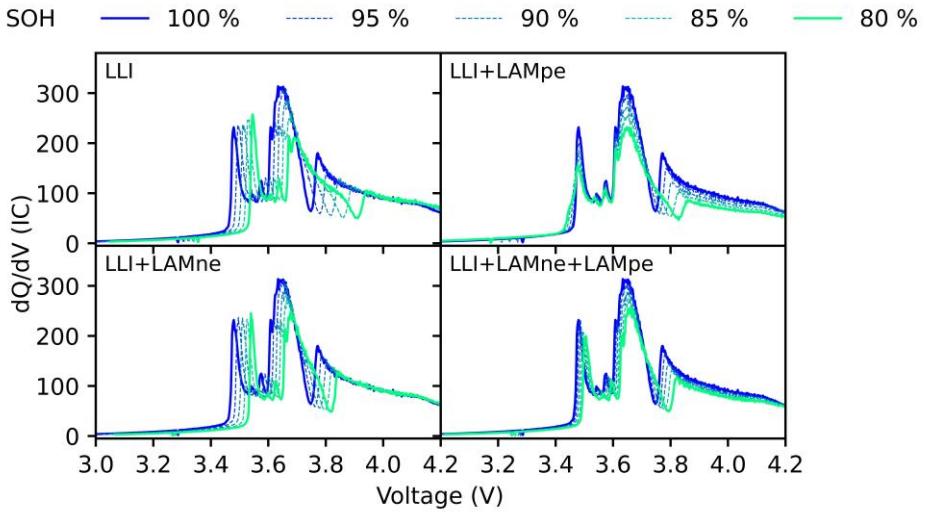


Figure 62. Simulation of the IC curve under different aging scenarios

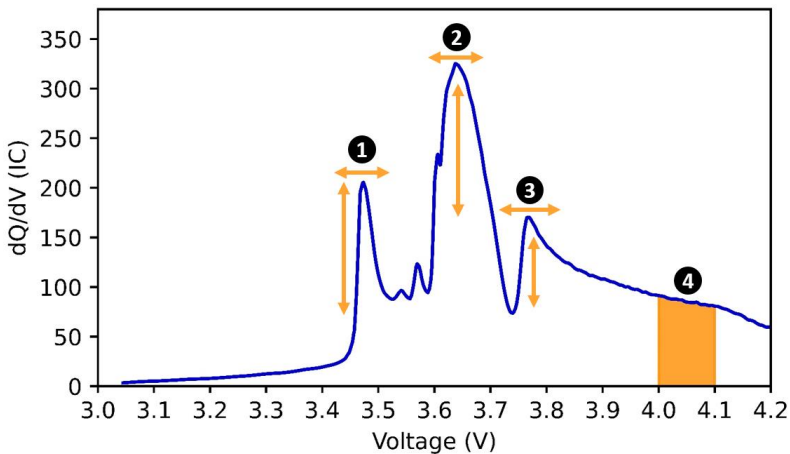


Figure 63. FOIs selection. The numbers refer to the FOI identity, the orange indications refer to the region of their evolution: vertical arrows refer to the peak intensity shift, the horizontal ones refer to the voltage shift, and the orange zone refer to the area evolution

3.3 Aging modes identification

In order to identify the degradation modes that happened during aging, the evolution of the FOIs issued from the experimental results will be compared to the FOIs' evolution obtained by simulations from 'alawa.

To try and correlate the effect the cycling has on calendar aging, the experimental data points that will be plotted hereunder are the following for 25 and 45 °C.

- Calendar SOC 90 % Aging (Cal)
- Calendar SOC 90 % + Short Trip Aging (Cal+ST)
- Calendar SOC 90 % + Short Trip + Long Trip (Cal+ST+LT) for the Urban (U), Highway (H) and Combined (C)

The intensity and voltage shift of FOIs 1, 2, 3 and 4 are plotted in Figure 64, Figure 65, Figure 66 and Figure 67 respectively. The FOIs of the four degradation modes (LLI, LLI + LAM_{pe}, LLI + LAM_{ne}, LLI + LAM_{pe} + LAM_{ne}) are plotted as lines, and the FOIs of the experimental IC curves are plotted as markers. In this manner, the assimilation between the markers and the lines can be made, making it possible to identify the aging modes. FOIs are plotted in function of the SOH. Here, the SOH represented the capacity of the battery at a C/20 charging rate.

3.3.1 FOI 1 – 3.47 V – Intensity and Voltage shift

The FOI 1 evolution of both the experimental IC curves (markers) and the 'alawa simulation (lines) are plotted in Figure 64.

At 25 °C, concerning the intensity of the peak, all conditions followed the trend of LLI + LAM_{pe}. It should be noted however that the more intense the cycling is, the faster the SOH decreased, but the highlighted mechanism was the same. Overall, and especially for the first points of the Calendar condition, the points were slightly below the LLI + LAM_{pe} line. This indicates that the share of LAM_{pe} was slightly higher than the one simulated in 'alawa.

The voltage shift, at 25 °C, showed a trend of LLI or LLI + LAM_{ne}. The differentiation is impossible as with both conditions the peak shifted to higher voltage values at the same rate. However, with aging the LLI was more and more highlighted. The Cal and the Cal + ST + LT(H) condition showed a very clear trend of LLI after an SOH of 97 %, but with a much higher rate than the one simulated in 'alawa.

At 45 °C, the trend of the peak intensity was the same for all conditions, similarly to the 25 °C aging. Oppositely to the 25 °C condition, the points here were found to be higher than the LLI + LAM_{pe} line, which means that the LLI share was this time slightly higher. Concerning the voltage shift, the Cal, Cal + ST, Cal + ST + LT (U) and (C) showed somehow the same trend. The aging mode altered between LLI and LLI + LAM_{pe} + LAM_{ne}. However, the voltage shift of Cal + ST + LT (H) evolved as an LLI mode.

Thus, this peak does not allow any clear decoupling between the calendar and calendar + cycling conditions, except for the highway scenario at 45 °C. In general FOI 1 seems very dependent on the calendar phase, and show that the LLI + LAM_{pe} was the dominating aging mode.

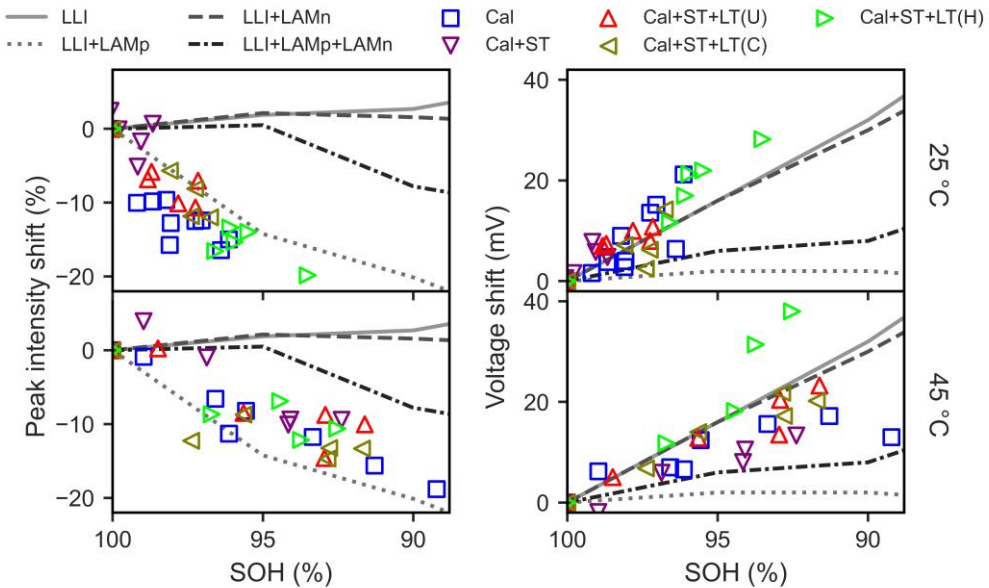


Figure 64. FOI 1 – peak at 3.47 V at BOL – relative peak intensity shift (left) and voltage shift in mV (right) for 25 °C (first row) and 45 °C (second row). Lines represent the ‘alawa simulations outcomes while the markers represent the experimental outcomes. For clarity, LAMP refers to LAM_{pe} and LAMn refers to LAM_{ne}

3.3.2 FOI 2 – 3.63 V – Intensity and Voltage shift

The FOI 2 evolution of both the experimental IC curves (markers) and the ‘alawa simulation (lines) are plotted in Figure 65.

At 25 °C, the intensity of FOI 2 seemed not to alter around 0 +/- 5 % for all the cases, which reveals an LLI or an LLI + LAM_{ne} mode. The last point of the Cal + ST + LT(H) condition underline hints at LLI + LAM_{ne} . The voltage shift of this peak tends to follow the trend of all the modes except LLI. This underlines the fact that LLI wasn’t present on its own, and was always accompanied by an LAM.

At 45 °C, the intensity of the peak seems very informative, oppositely to its voltage shift where values did not differ much. The intensity of the Cal condition seemed to follow an LLI or an LLI + LAM_{pe} + LAM_{ne} mode. Cycling at low DOD (Cal + ST) revealed more closely an LLI mode with a slightly higher intensity shift value. Higher DOD values (Cal + ST + LT) were much closer to LLI + LAM_{ne} .

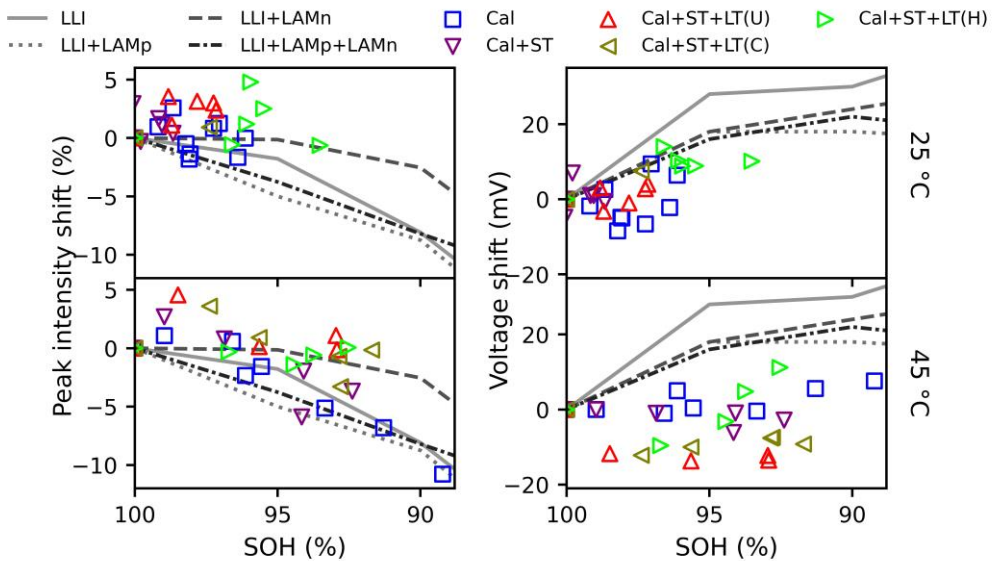


Figure 65. FOI 2 – peak at 3.63 V at BOL – relative peak intensity shift (left) and voltage shift in mV (right) for 25 °C (first row) and 45 °C (second row). Lines represent the ‘alawa simulations outcomes while the markers represent the experimental outcomes. For clarity, LAMP refers to LAM_{pe} and LAMn refers to LAM_{ne}

Overall, the extracted information from this shift revealed that cycling a higher DOD induces LAM_{ne} , and this is more accentuated at high temperatures.

3.3.3 FOI 3 – 3.78 V – Intensity and Voltage shift

The FOI 3 evolution of both the experimental IC curves (markers) and the ‘alawa simulation (lines) are plotted in Figure 66.

Very similarly to FOI 1, FOI 3’s peak intensity reveals $LLI + LAM_{pe}$ and LLI for all conditions at 25 °C. The highway conditions suffered from a more intensive LLI loss. The voltage shift reveals also a clear LLI loss for all conditions, and a more severe one for the highway condition. At 45 °C, the peak intensity discloses clearly a LLI for all conditions. The voltage shift tells a different story. For most of the conditions, $LLI + LAM_{pe}$ and $LLI + LAM_{ne}$ are clearly plotted. For the highway condition, the first part of aging is $LLI + LAM_{ne} + LAM_{pe}$, while starting from SOH 95 %, the dominant aging mode is LLI .

Thus, this FOI reveals the LLI and $LLI + LAM_{pe}$ nature of the aging a 25 °C, without a clear distinction between aging scenarios, except for the highway scenario where LLI becomes sever. At 45 °C the intensity of this peak reveal its LLI side for all aging conditions. Its voltage shift reveals a change of aging modes for the highway scenario.

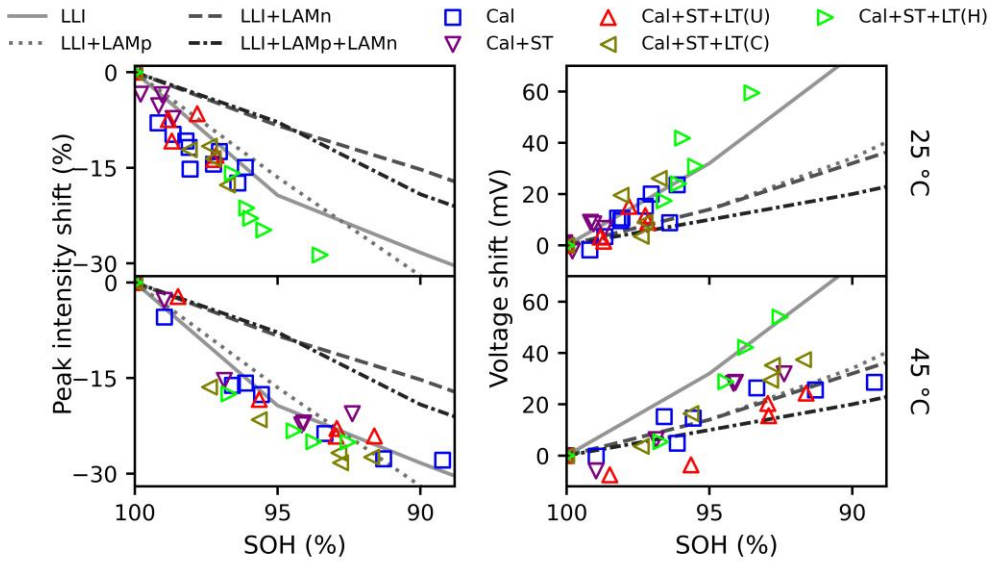


Figure 66. FOI 3 – peak at 3.78 V at BOL – relative peak intensity shift (left) and voltage shift in mV (right) for 25 °C (first row) and 45 °C (second row). Lines represent the ‘alawa simulations outcomes while the markers represent the experimental outcomes. For clarity, LAMP refers to LAM_{pe} and LAMn refers to LAM_{ne}

3.3.4 FOI 4 – 4.0 to 4.1 V – Area evolution

The FOI 4 evolution of both the experimental IC curves (markers) and the ‘alawa simulation (lines) are plotted in Figure 67.

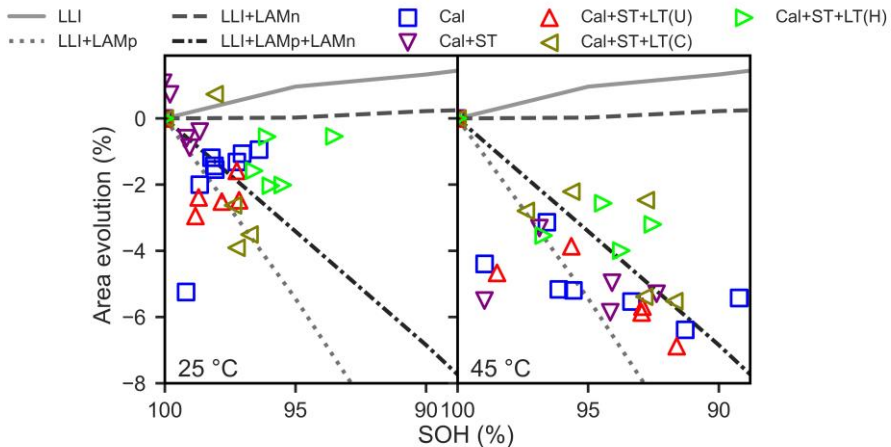


Figure 67. FOI 4 – area below 4.0 to 4.1 V – for 25 °C (left) and 45 °C (right). Lines represent the ‘alawa simulations outcomes while the markers represent the experimental outcomes. For clarity, LAMP refers to LAM_{pe} and LAMn refers to LAM_{ne}

FOI 4 particularity is that it reflects a contribution of LAM_{pe} . At 25 °C, Cal and Cal + ST conditions tend to follow the $LLI + LAM_{pe}$ or $LLI + LAM_{pe} + LAM_{ne}$ trends. For the Cal condition, the loss of positive material seems to start heavily at the first stage of aging but then seems to stabilize, revealing LLI. The Cal + ST + LT (U) and (C) tend to follow more closely $LLI + LAM_{pe}$. The tendency of the (H) condition lies between $LLI + LAM_{pe} + LAM_{ne}$, and seems to stabilize for the last point, hinting at LLI.

At 45 °C, the initial drop of area is more considerable than the previous conditions. This proves that the LAM_{pe} is proportional to the ambient temperature. However, after the first 5 % of SOH loss, the points tend to follow the $LLI + LAM_{pe} + LAM_{ne}$ trend.

Overall, this means that the effect of LAM_{pe} tends to be more visible in the first stages of aging, and after this, LLI and/or LAM_{ne} losses seems to be more impactful.

3.4 Discussion and confrontation with the EBD

The FOI 1 revealed the $LLI + LAM_{pe}$ nature of the aging. Its intensity seemed to be controlled by the calendar condition and did not show any distinction when cycling was applied. Its voltage shift was only different for the highway trips, showing the LLI harsh impact. This result suggests that the FOI 1 is mostly controlled by the calendar aging.

FOI 4 underlined the fact that LAM_{pe} happened at all conditions irrespectively of the scenario. It showed a high LAM_{pe} in the beginning of aging, and a certain stabilization, especially for the Cal at 25 °C. The same seems to happen at 45 °C but with a higher amplitude. Interestingly, after an SOH of 95, the rate of $LLI + LAM_{pe}$ seems to stabilize and to follow a $LLI + LAM_{pe} + LAM_{ne}$ trend, for all conditions.

These observations are in agreement with the results obtained with the EBD tool. LLI and LAM_{pe} were present regardless of the aging scenario. LAM_{pe} was seen to be proportional to the temperature. At 45 °C, the LLI shows a steep increase, which is seen here with FOI 1.

Oppositely to FOI 1, FOI 2 isn't controlled solely by the calendar aging. Its evolution suggested that $LLI + LAM_{ne}$ might have happened at high discharge rates, especially at 45 °C. It also reveals that calendar condition at 45 °C suffers from $LLI + LAM_{pe} + LAM_{ne}$. FOI 3 highlighted the LLI, which increases both with temperature and with cycling intensity.

The fact that LLI is proportional to both the cycling intensity and the temperature, and the loss of both LAM_{pe} and LAM_{ne} during calendar aging at 45 °C has also been identified and quantified with the EBD tool. However, the presence of LAM_{ne} when Cal + ST + LT (H) are applied at 45 °C wasn't very clear in the EBD tool outcomes. Post-mortem analysis will validate whether the LAM_{ne} did occur.

4. The limitations of the EBD and the ‘alawa methods

The aforementioned tools rely on some hypotheses that limit their accuracy. First of all, they are based on the assumption, stated in the introduction of 2, that the half-cell potential of the electrodes in function of the lithium stoichiometry do not change throughout the aging of the cell. While some literature counter this hypothesis, especially for NMC electrodes [61], and others support it [58], [302], it remains questionable and experimental validations are needed.

Second, these tools illustrates a general view of the cell performance. In other words, it reflects the average LAM and LLI, and overshadows local changes in the electrodes’ capacity/structure.

Third, the outcome of these tools reflects most of the time the dominant aging mode and not all of them. So the result might eclipse other aging mechanisms that happened on a lower rate, or other mechanisms that do not impact the capacity at C/20.

This introduces the fourth limitation. These tools omit kinetic changes as they are primarily based on a C/20 charge rate. An LAM caused by electrode particle cracking, particle exfoliation or a loss of electric contact, to name a few, can reflect a potential loss in the electrode insertion resistance. The same is true for an elevated LLI, which can potentially come from an intensive growth and densification of the SEI layer [39], [41]. However, these tools does not provide the relationship between their outcomes and the increase in internal resistance.

Finally, the LAM value obtained from these tools reflects that some part of the electrode material are no more accessible or usable. This surely includes the damaging of the electrode internal structure, but not only. A gas bubble due to the change in the internal structure of the PE, or some electrolyte consumption can hinder a certain accessible surface. A thick SEI layer can be formed and can clog some of the electrode pores. These phenomena are included in the LAM value. Therefore, the LAM value just reflects that some part of the electrode material are not accessible or usable, and not necessarily that the particles cracked.

While these methods are very useful for some applications where quick and effective information about the cell health are needed, they should be used qualitatively rather than quantitatively, and post-mortem validation is always needed.

5. Post-mortem: a crucial validation

In order to overcome the limitations of the mechanistic method, post-mortem studies are needed. While post-mortem can refer to a huge amount of work, very straightforward experiments can be sufficient to complement the mechanistic approach and validate the results.

1. A visual inspection can reveal mechanical/structural changes (LAM) (i.e. tearing off the coating from the collector to the separator during the physical

separation of the components) or even Lithium deposition (LLI), which can be identified on the negative electrode and on the separator as white spots. This can also be helpful in identifying whether gas bubbles were formed and eclipse some electrode surface, hence limiting their availability (LAM).

2. The recovery of the electrodes material is another important aspect for coin cell experiments. Electrode samples are cut in a circular shape and included in a half-cell (vs Li-metal) where electrochemical tests are done, as will be detailed hereunder. Capacity measurements at C/20 can reveal the amount of remaining active material. Resistance measurement trough HPPC (Hybrid Power Pulse Characterization) tests can reveal the structural changes inside the electrode.
3. Electrode surface analysis by the SEM (Scanning Electron Microscopy) technique can reveal the presence of lithium plating and electrode surface cracking

The post-mortem analysis was carried out on an unaged cell, and on the cells that aged at 45 °C as their SOH fell much faster than the 25 °C cells. The chosen cells were:

- SPHEV 11 – Calendar at 45 °C and SOC 90 % with monthly checkup
- SPHEV 12 – Calendar at 45 °C and SOC 90 % without monthly checkups
- SPHEV 54 – Calendar SOC 90 % + Short + Long Trip at 45 °C with checkups

5.1 Post-Mortem methodology

5.1.1 Battery dismantling and visual inspection

Before launching the post-mortem procedure, cells were carefully put in condition. Fully discharging them was done for safety reasons [34], [40]. A C/20 discharge and a floating at 3.0 V (SOC 0 %) for 30 min were succeeded twice, as illustrated in Figure 68.

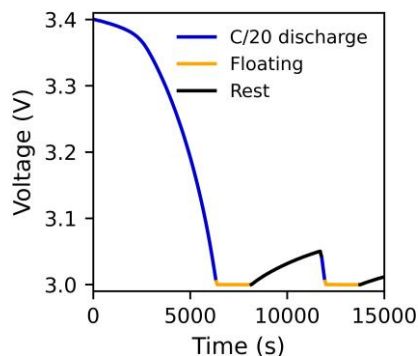


Figure 68. Procedure for the post-mortem conditioning of the cell

After introducing the discharged cell in the Argon glove box, it was dismantled using adequate tools and cell elements were separated. A visual inspection was then made and pictures were taken.

5.1.2 Electrode surface analyses by SEM

Surfaces of interest of both electrodes were sampled and used from SEM analysis. SEM was done using Bruker equipment.

5.1.3 Coin-cell experiments

One type of coin cell was needed: the half-cell, i.e. active material vs Li-metal. Its setup is illustrated in Figure 69.

As will be discussed in Chapter 7, the electrodes of this cell are two sided. Therefore removing one side is needed to have only one active material side. It was done using N-Methyl-2-pyrrolidone (NMP) solvent (and scrapping with a ceramic scalpel when needed for the NE) as described in [34]. Electrodes were cut in circular shape samples with a diameter of 14 mm. The separator, cut in the same manner but with a 16 mm diameter, was taken from the unaged cell to satisfy the need of these experiments. A small portion of the electrolyte from the unaged cell was recovered and studied to conclude that it was made of Ethylcarbonate (EC) – Dimethylcarbonate (DMC) – Ethylmethylcarbonate (EMC) at 1:1:2 weight percent proportions, using the GC-MS technic. A similar solution was synthesized and used for the half-cell experiments. Further details of the electrolyte and the separator will be exposed in Chapter 7. The same electrolyte and separator are taken for consistency purposes, to ensure that the coin-cell experiments reflects the operation in a full cell.

Coin-cells were prepared (Figure 69), and then connected to Biologic BCS-800 benches before launching electrochemical tests, which are described in Table 12.

The value of the current is expressed in C-rate. For the C/10 and the C/1 currents the C is considered to be, theoretically, 4.2 mAh for the PE and 4.4 mAh for the NE. For the C/20 procedure, the capacity was corrected by taking the average of the capacity obtained during the last C/10 cycle. This is done in order to be as accurate as possible concerning the C/20 procedure.

The current values remained the same for the new and the aged samples for coherent comparisons.

Steps 4 and 6 of Table 12 require to perform the HPPC on for every 5 % of capacity (SOL of 5 and 10 %, or 90 and 95 %). The reason behind this practice is to try to have a clear value of the resistance at the most critical phases of the electrode state: when it is nearly fully occupied or unoccupied. For the SOL between 10 and 90 %, a 10 % increment was taken, as illustrated by step 5.

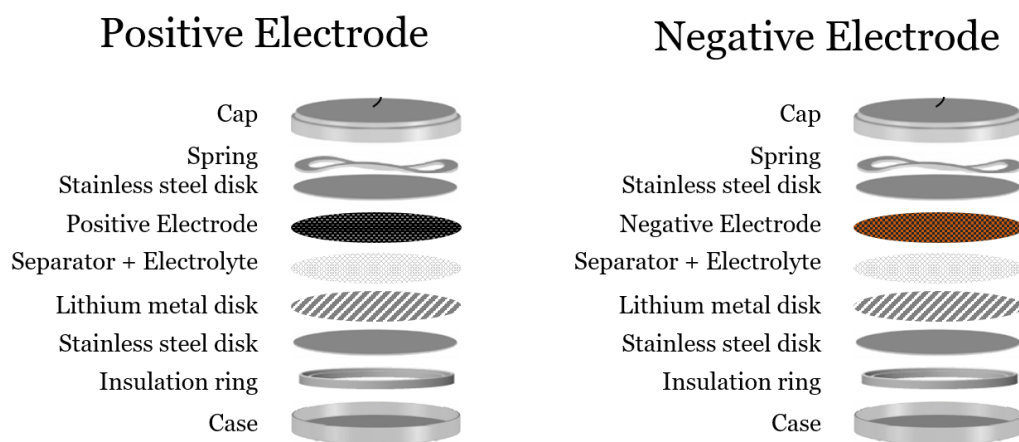


Figure 69. Half-cell design for the positive and the negative electrode active material

Table 12. Electrochemical test carried out on the half-cells

Step	Solicitation	Number of cycles	Purpose
1	OCV for 1 min	-	Potential measurement
2	C/10 charge-discharge	3	Cell electrical balance and capacity measurement at the last cycle
3	C/20 charge-discharge	1	For ESS and 'alawa initialization and validation with aging
4	1 C pulse for 30 s and C/10 charge for 5 % of the electrode capacity	2	HPPC tests for the illustration of the kinetic behavior of the electrode during lithiation and delithiation.
5	1 C pulse for 30 s and C/10 charge for 10 % of the electrode capacity	8	
6	1 C pulse for 30 s and C/10 charge for 5 % of the electrode capacity	2	
7	C/10 charge-discharge	1	Verification of the state of the electrodes after the test, to ensure that the electrodes did not suffer much
8	Repeat steps 5, 6 and 7 for discharge	1	
9	C/10 charge-discharge	1	

5.2 Visual inspection

5.2.1 Cell thickness evolution

The SPHEV 11 (Cal 45 °C SOC 90 % with checkups) and the SPHEV 12 (without checkups) inflated significantly, to a certain extent that they couldn't fit inside their setup no more. The thickness of the battery cells was measured and compared to the thickness of an unaged cell. Measurements were taken using a caliper, along the length of the cell on the center line, each 20 mm and each 10 mm for mid points. The thickness values are plotted in function of the measurement position (mm) in Figure 70.

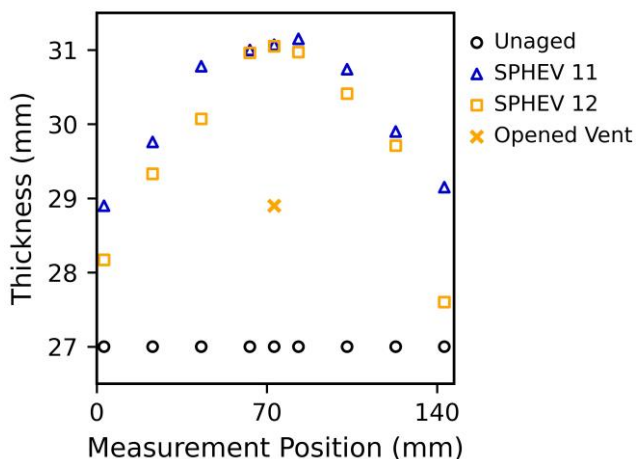


Figure 70. Thickness of the cells along their length. The thickness of each point is equivalent to the measurement error of the caliper (+/- 0.05 mm).

Results suggest that either gas formation or electrode inflation occurred with aging. As soon as the gas vent was opened during the dismantling procedure, the cell shape flattened and its thickness decreased by 2 mm (measured for the SPHEV 12). The casing of the cell is made of aluminum, which is known for a relatively high malleability. This denotes that the inflation was due to some gas formation and not electrode inflation, and explains the quick change of shape when the gas was dissipated.

The gas formed within the SPHEV 11 and the SPHEV 12 induced a very similar trend in the shape of the cell, with overlapping values in the center. However, on the sides of the cell the thickness of the SPHEV 12 seemed to be lower. This can hint at the amount of gas produced by each cell.

This could be a consequence of the phase change of the PE [41] (from layered to spinel and rock salt phases hence releasing O₂ [303]) which is very common for this

aging scenario (SOC 90 %) [304]. This is in agreement with the LAM_{pe} obtained in both the EBD and 'alawa tools.




Released O_2 can potentially react with the EC found in the electrolyte to produce CO_2 and CO. Other gases might result from the decomposition of the electrolyte components at high potential. Gas can also be emitted when SEI grows, or when a secondary SEI is formed.

The SPHEV 54 did not show a noticeable inflation.

5.2.2 The physical state of the electrodes

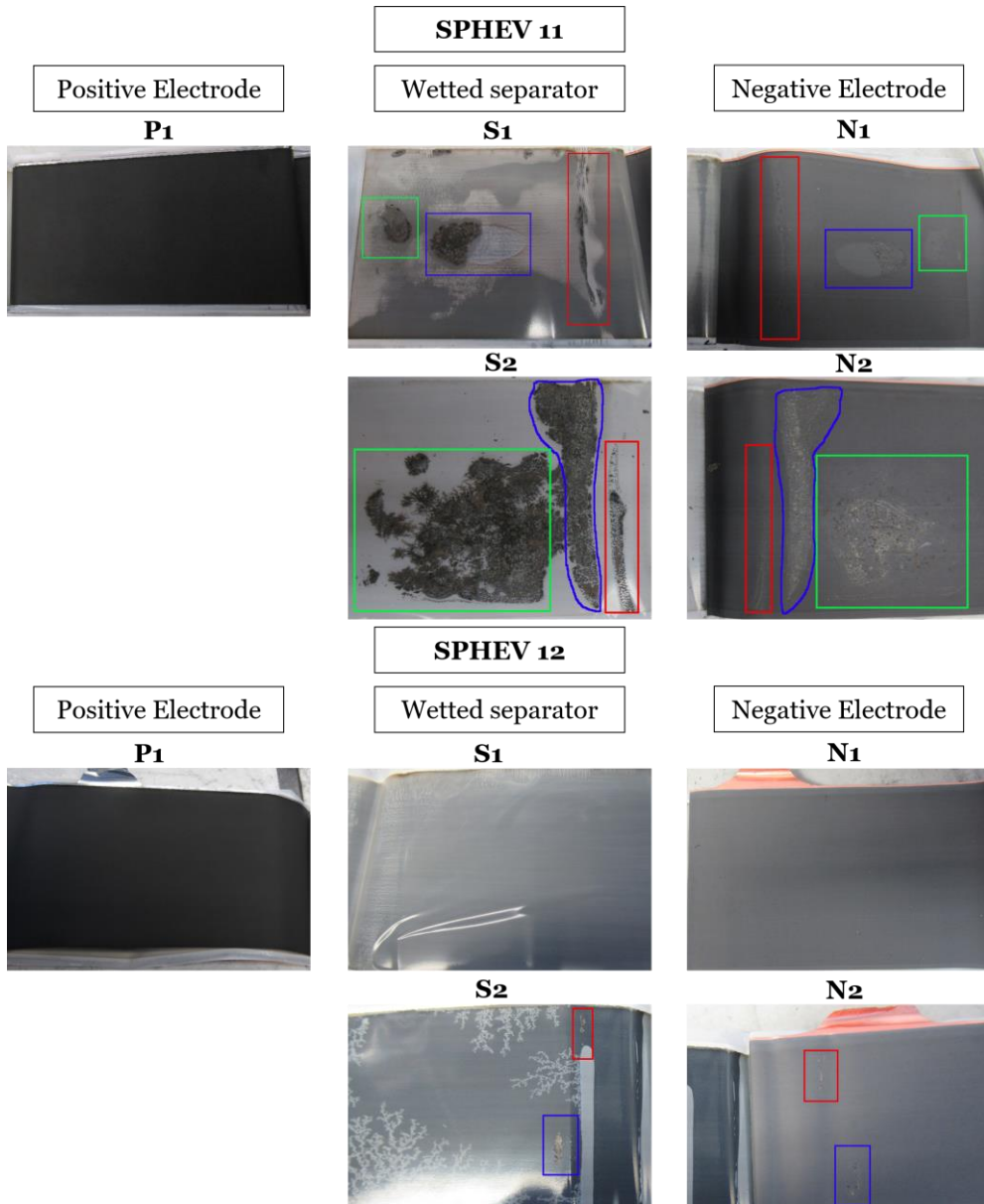
Starting with the unaged cell, samples from the electrodes and the separator are shown in Table 13. No defects are visible and the components are well impregnated by electrolyte (like shown by the translucent aspect of the separator which whitens progressively when the most volatile solvents are evaporated).

Table 13. Visual inspection of the battery internal components of an unaged SPHEV cell

Positive	Wet Separator	Negative
		

For the SPHEV 11 and SPHEV 12, noticeable electrode aging deformations were found after the first turns in the roll. In Table 14, images found on the same line corresponds to the surfaces that face each other. The PE did not suffer from any physical noticeable or severe change, so only one picture is shown. The light is shed on the defects found on the facing electrodes. Nearly every mechanical defect that happened on the negative electrode was found on the separator. They were outlined in order to help the reader to puzzle them up. The letter and number above each image (e.g. P1) refers to the element (P = positive electrode, S = Separator, N = Negative electrode) and are referred to in the text after the table.

Table 14. Post-mortem visual inspection of SPHEV 11 and 12

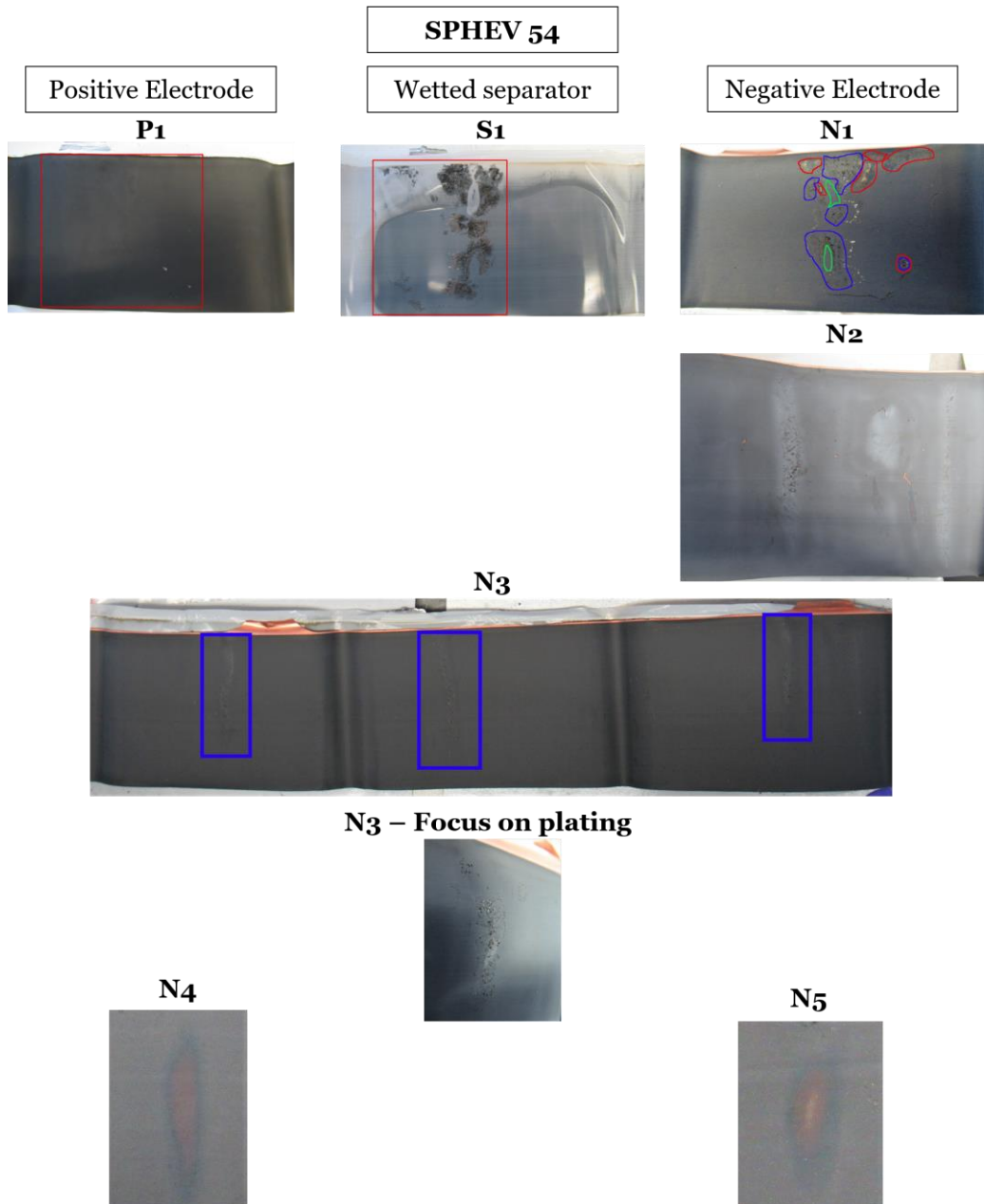


SPHEV 11. It can be clearly seen, from a first glance, that the negative electrode and the separator of the SPHEV 11 suffered major visible defects due to metallic deposition (SPHEV 11 – S1, N1, S2 and N2). Gas bubble traces were found abundantly on the separator and the NE. The SPHEV 12, on the other hand, suffered from very minor noticeable physical changes. Some of them were found near the folds (SPHEV 12 – S2 and N2), but nothing as severe as the defects found on the SPHEV 11. Gas bubble traces weren't noticeable in SPHEV 12.

The only difference between these two cells is the checkups, which seems then to be the reason behind the observed phenomena. This discrepancy in the electrodes' states are in harmony with also the difference in the capacity evolution of both cells shown in chapter 5 and the difference in the aging modes evolution.

Table 15 shows the images of SPHEV 54, with a focus on the NE.

Table 15. Post-mortem visual inspection of SPHEV 54



SPHEV 54. The physical state of the SPHEV 54 electrodes seemed to be more impacted than the SPHEV 11 electrodes. The image SPHEV 54 – S1 and N1 suggests a mixture between electrode material loosening (red contour), metallic deposition illustrated as white dots (blue contour) and gas bubble formation (green contour). On the separator, metallic deposition can be seen behind every contour besides the gas formation one.

Aging defects, especially metallic deposition, were seen to be repeating on a periodical basis, as seen in SPHEV 54 – N3. The propagation of the defects is not the focus of this thesis, but remains a noteworthy point. The more the defects repeat themselves, the more they weigh.

Finally, some areas such as the ones seen in SPHEV 54 – N4 and N5 were identified all around the electrode. This color palette – golden yellow to dark grey or black – refers to the different lithiation state of the graphite [305], [306]. Golden yellow indicates the presence of fully lithiated graphite (LiC_6) – Stage 1. Dark red indicates the presence of partially lithiated graphite (LiC_{12}) – Stage 2. Blue and dark blue refers to the third stage of de-lithiation (LiC_{18}) – Stage 3. And finally dark grey or black refers to the “dilute” stage – Stage 4.

The presence of these areas indicates that some of the lithium got stuck inside the loosened graphite. As it stopped working, the lithium remained inside the graphite and did not re-homogenized with the electrode bulk. In this way, both active material and lithium inventory are lost. Similar results were obtained in [307].

It should be noted that during the electrode preparation for coin cell testing, a soft NMP spread was enough for the removal of one side of the graphite. For the unaged and the SPHEV 11 cells, NMP barely softened the region while a hasher scrapping was needed. This indicates that the graphite started to loosen of the copper current collector surface.

5.2.3 The nature of the metallic deposition

A verification procedure is done to verify that the observed white spots are formed of metallic lithium. A quick method consist of putting the separator, or the metallic debris taken from the separator, under a hood, and rinsing it with some drops of water. The reaction between Li and water is very exothermic and leads to sparks. The appearance of sparks serves as an indicator of the presence of lithium (de-lithiated graphite does not react with water under these conditions).

Of course, a few graphite particles, disconnected from the bulk but in contact with the deposited lithium, were present within the separator debris. It cannot be confirmed whether the these graphite particles contained, or not, some re-lithiated lithium. This could contribute in a minor way in the formation of sparks.

Figure 71 illustrates the experiment done on the separator debris of the SPHEV 11 (first row) and the SPHEV 54 (second row). Sparks appeared significantly, suggesting that the white spots are indeed constituted of metallic lithium.

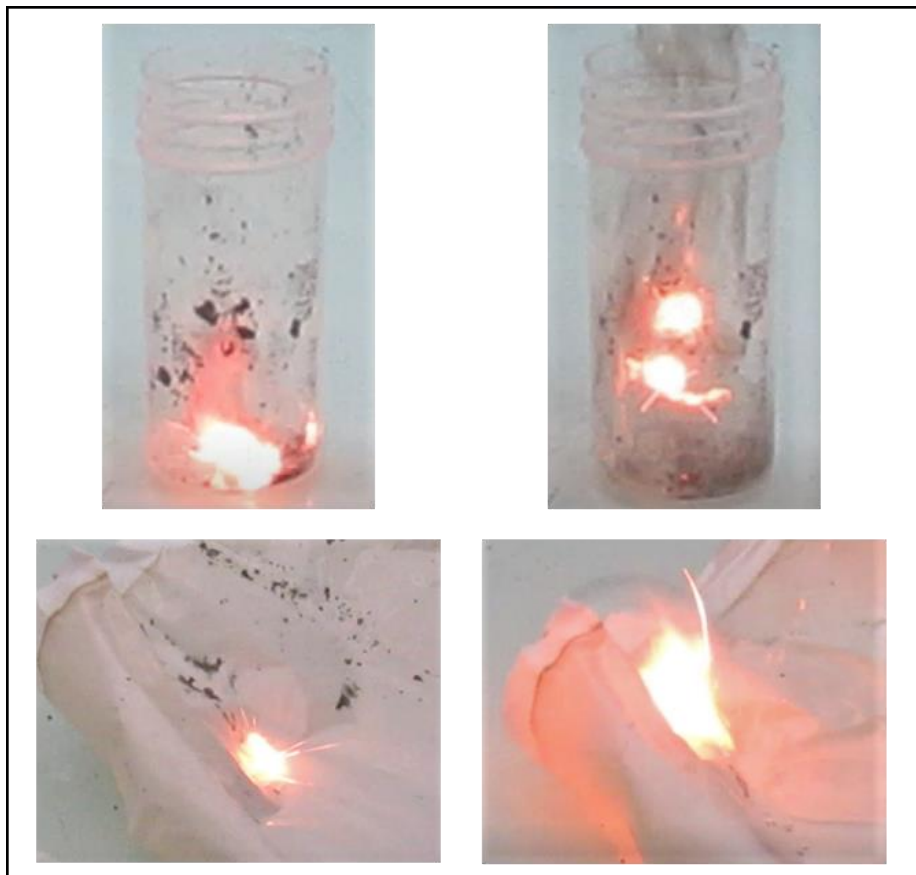


Figure 71. Sparks' appearance on the separator (first row, SPHEV 11) and on the debris taken from the separator (second row, SPHEV 54), as an indicator of the presence of Lithium

5.3 SEM analyses

The water-separator experiment proposed that some metallic lithium was formed during the aging processes of the SPHEV 11 (Calendar at 45 °C and SOC 90 % with monthly checkup) and the SPHEV 54 (Calendar SOC 90 % + Short + Long Trip (Highway) at 45 °C with checkups). It was also figured out that the graphite was very loose on the copper current collector.

In order to investigate closely the surface conditions of the electrodes of these two cells (SPHEV 11 and SPHEV 54), SEM analyses are done. The NE regions containing metallic lithium (white spots), and regions with no noticeable changes, were

sampled. PE regions were also sampled. Results are compared to the SEM outcome of the fresh cell.

As stated previously, and as will be detailed in chapter 7, an alumina (Al_2O_3) coating is present on the graphite surface. A gentle scrapping with a ceramic scalpel was applied on the NE surface that suffered from no noticeable changes. On the white spots, no scrapping was applied.

SEM images were taken using different magnitudes in the range of 10 μm , 5 μm and 1 μm , with an Electron High Tension (EHT) value of 15 kV.

5.3.1 Scrapped vs non-scrapped region

Figure 72 illustrates the difference between a scrapped and non-scrapped region of a fresh cell's NE.

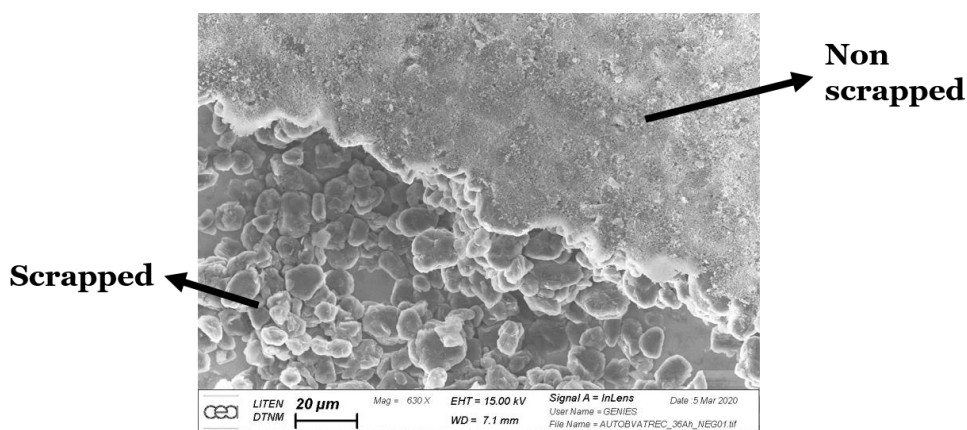


Figure 72. SEM image showing a scrapped and a non-scrapped region of a fresh cell's NE

The non-scrapped region looks very much like a white homogenous surface, hiding the graphite particles. In order to make the graphite particle visible, scrapping was needed.

5.3.2 Negative electrode of the SPHEV 11

Figure 73 illustrates the SEM images taken for the NE of the SPHEV 11 (second and third column, C – H), compared to the SEM images of the NE of a fresh cell (first column, A – B). No defects regions are depicted as (ND) and regions with white dots are depicted as (WD).

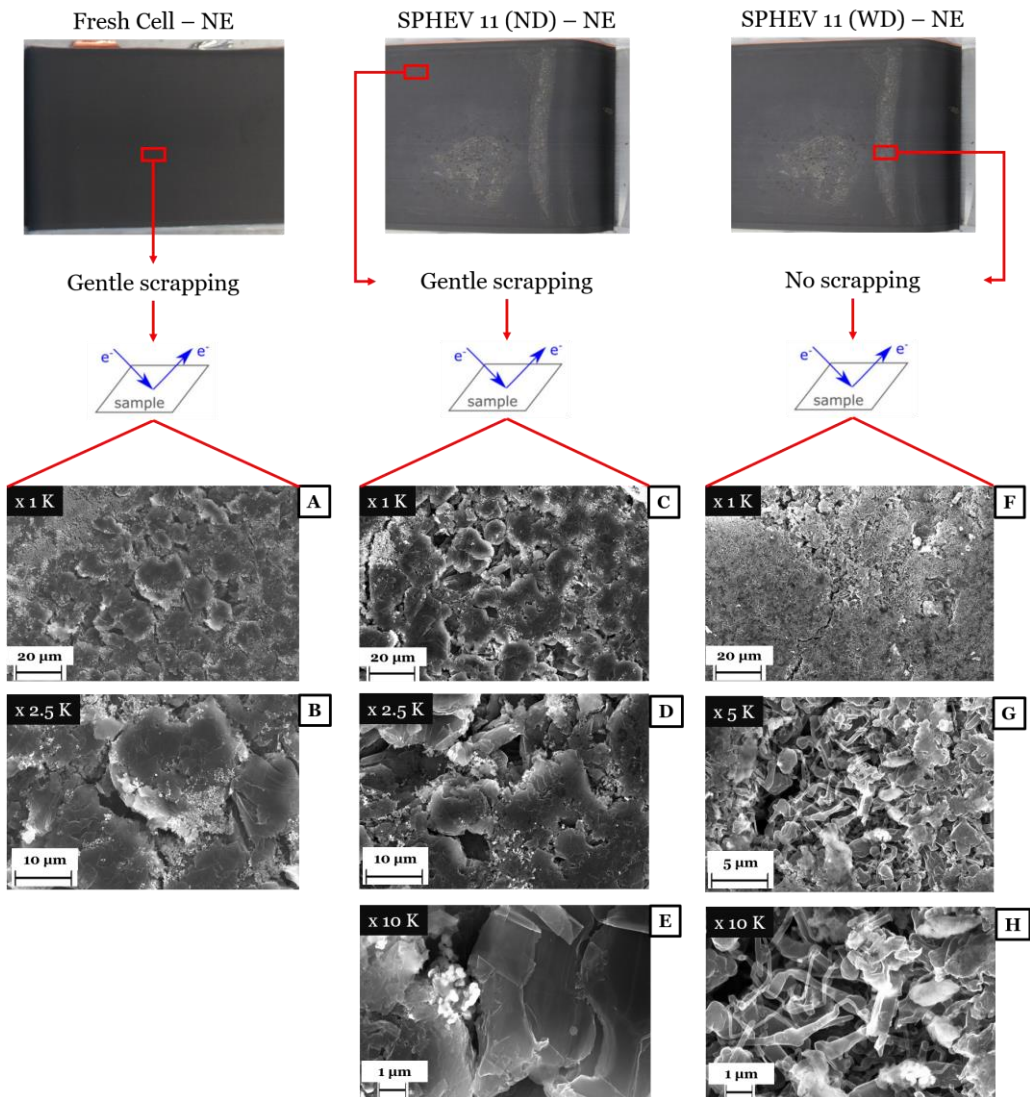


Figure 73. SEM images of the fresh (first column, A – B) and the NE of the SPHEV 11. The second column (C – E) represents the surfaces with no defects (depicted as ND) and the third column (F – H) represents the surface of white dots (depicted as WD).

No major differences can be found on the graphite particles of the region with no defects, when compared to the fresh cell. This suggests that the aging mechanisms that happened did not impact the electrode particles at this level.

The alumina coating can be identified in Figure 73 F by a white surface. Yet, accumulation of metallic lithium and the formation of dendrites was easily visualized in Figure 73 G and H. This indicates that the metallic lithium formed, and passed through the alumina coating.

5.3.3 Negative electrode SPHEV 54

Concerning the SEM analysis of the SPHEV 54, the first differences noticed on the alumina surface of the non-scraped regions. Figure 74 shows a comparison of the fresh and the SPHEC 54 NE.

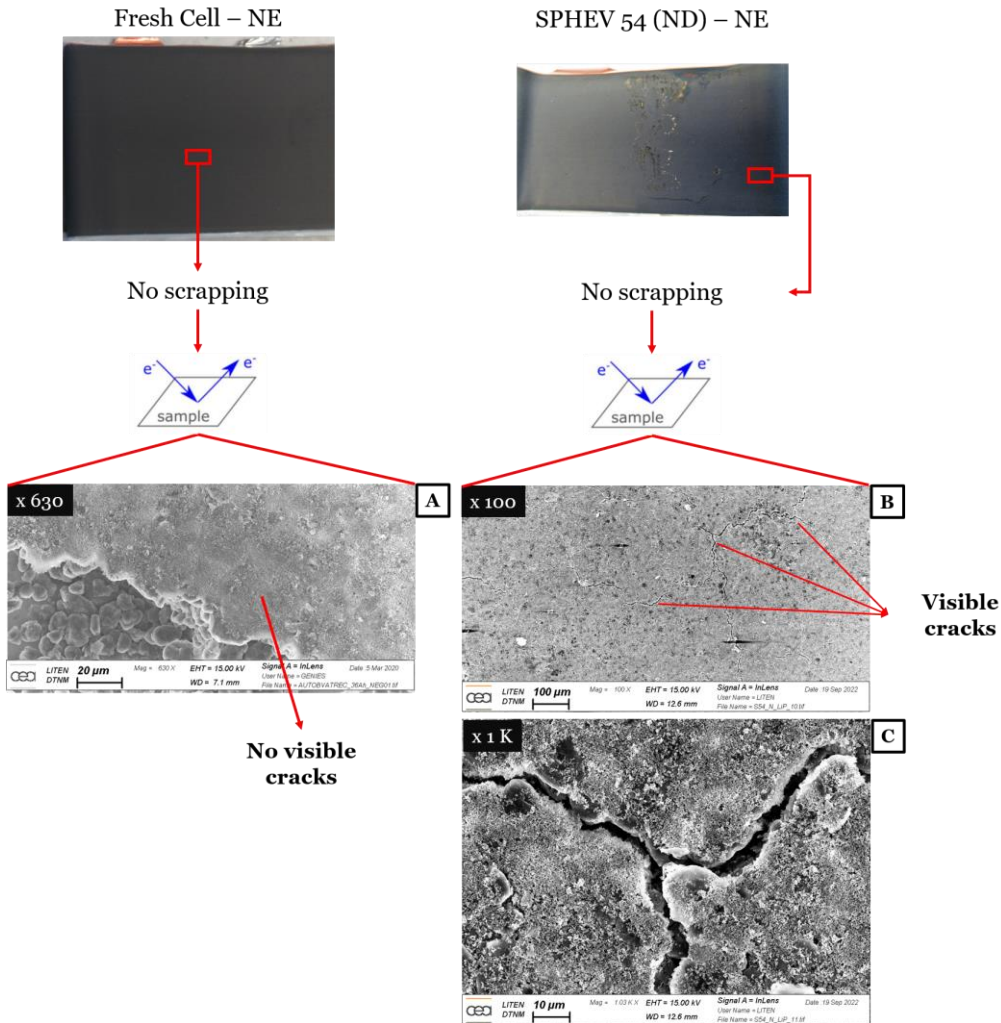


Figure 74. SEM images of the alumina non-scraped surface of the NE of the fresh cell (A) and the SPHEV 54 cell (B – C)

For on a magnitude of $\times 630$, cracks were not visible on the fresh NE (Figure 74 A). However, at a magnitude of $\times 100$, cracks were visible on the NE of the SPHEV 54 (Figure 74 B). Figure 74 C shows a closer look at the cracks of the SPHEV 54 NE.

Figure 75 illustrates the SEM images of the white dots found on the NE of SPHEV 54.

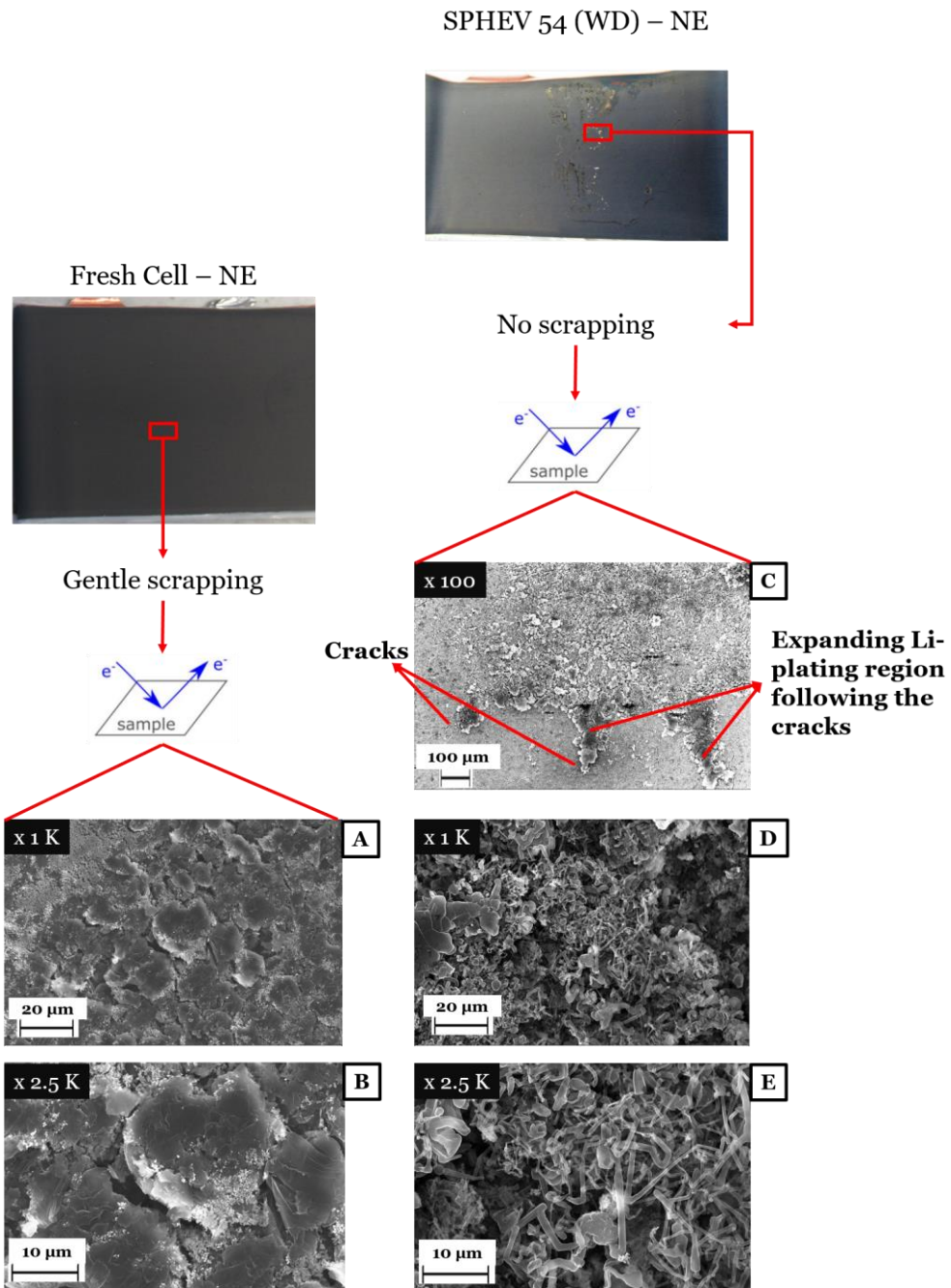


Figure 75. SEM images of the fresh (first column, A – B) and the NE of the SPHEV 54. The second column (C – E) represents the surface of white dots (depicted as WD).

Results of Figure 75 suggest that the white dots were indeed formed of metallic lithium which grew in a dendritic shape (Figure 75 E). Figure 75 D proposes that the metallic lithium surface expanded following the cracks.

5.3.4 Positive electrodes of the SPHEV 11 and the SPHEV 54

The PE surface was analyzed using SEM imagery, and results are exposed in Figure 76.

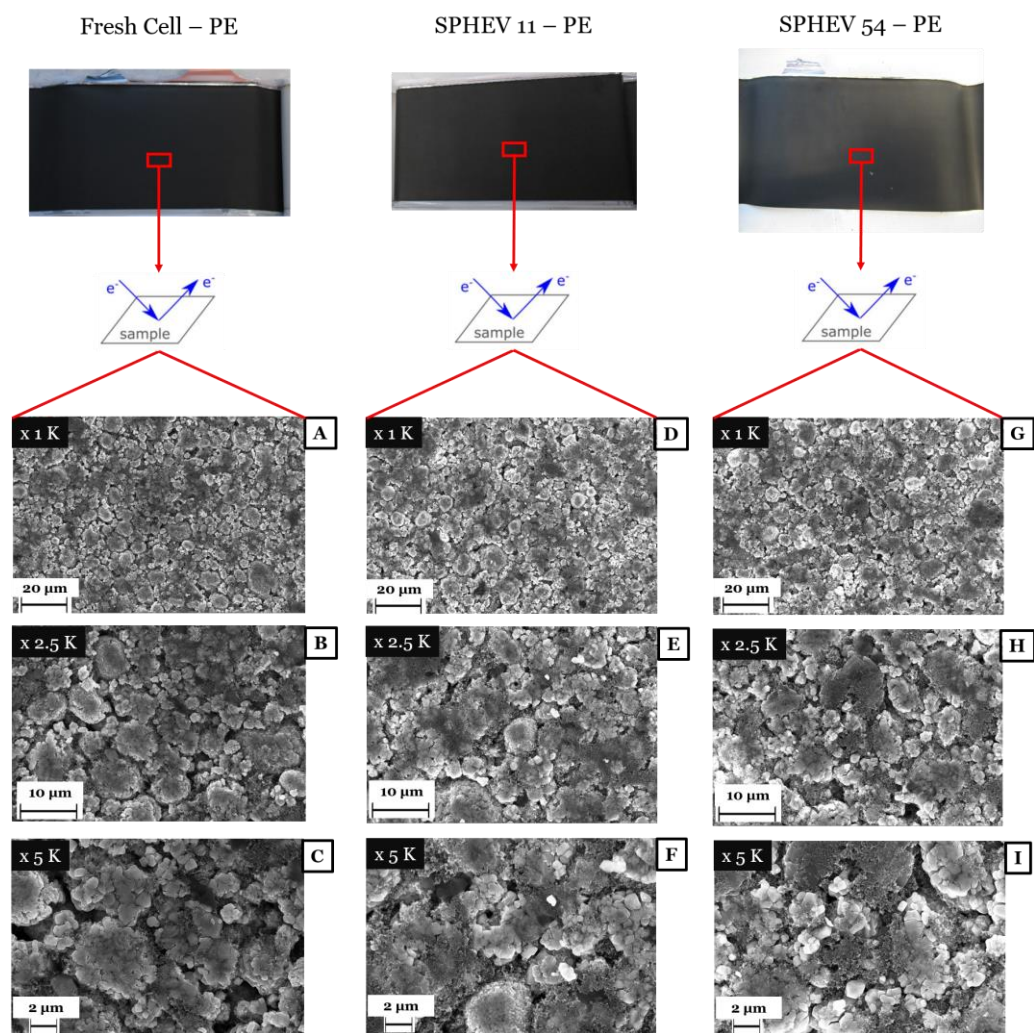


Figure 76. SEM images of the fresh cells' PE (first column, A – C), the SPHEV 11's PE (second column, D – F) and SPHEV 54's PE (third column, G – I)

Results of Figure 76 suggests that the PE did not suffer any noticeable change after its aging.

5.3.5 SEM outcomes

Highway cycles (SHEV 54, Calendar SOC 90 % + Short + Long Trip (Highway) at 45 °C with checkups) were seen to be at the origin of cracks in the electrode bulk. This is at the origin of the active material loosening evoked earlier when the active material was easily removed. Li-plating was also detected, and found to follow the paths formed by cracks. Li-plating might originate then from the checkups, but the formation of cracks, decreasing the local area capacity, could have aggravated the Li-plating formation.

The PE of both SPHEV 11 and SPHEV 54 did not show any noticeable change.

5.4 Discussion on the results obtained by the visual inspection and the SEM

SPHEV 11. This cell aged at 45 °C at SOC 90 % with monthly checkups. While the growth of the SEI is natural and known at such aging conditions, the deposition of metallic lithium seems counter intuitive. With a N/P ratio of 0.94 %, the checkups seemed to be the reason behind this deposition.

The cell that did not undergo checkups (SPHEV 12) did not show any white dot or metallic deposition. SEM analyses proved that NE surface of the SPHEV 11 with no defects or white dots (assumed to be similar to the NE surface of the SPHEV 12) showed no dendrites or whiskers formation. On the other hand, SEM images and the separator-water experiment, proved that the white dots found on the NE surface of the SPHEV 11 were made of metallic lithium.

Another observation can be made on the Li-plating positioning. It commonly appears on the folds of the rolls and around gas bubbles.

Folds lead to mechanical stress on the electrode damaging its structure, during the cell assembly process. In the literature review of chapter 2, it was shown that the electrodes are folded in a prismatic cell. Which means that the areal capacities can be locally much lower than the total average, hence exposing this part of the electrode to higher current densities [308]–[310]. Elevated current densities will quickly reduce the potential of the negative electrode below 0.0 V vs Li during charging, favoring the deposition of solid lithium, even at normal charging rates (C/2 for example).

Gas bubbles, having a null Li-ion diffusivity, eclipse the functioning of a certain surface of the electrode. This means that the current density around the gas bubble is much higher than the average one, creating a heterogeneous current gradient [310]. This will brusquely reduce the local potential below 0.0 V vs Li.

It should be noted that during EV usage (chapter 3), the safety margins are imposed by the BMS and a full SOC is never reached. So in order to avoid the impact of Li deposition, checkups should be done in the operational voltage/SOC limits, hence

between SOC 20 and 90 %. This is also advised in the newest versions of the USABC standard for battery testing [47], [90].

SPHEV 54. This cell undergone the following aging: Cal + ST + LT (H) 45 °C with monthly checkups. Highway cycles were seen to be at the origin of cracks in the electrode bulk. This is at the origin of the active material loosening evoked earlier when the active material was easily removed.

Metallic lithium also deposited on the NE, as proved by the SEM images and the separator-water experiment. It was not only found around bubbles, but also locally around regions where graphite was totally unstuck. Furthermore, SEM images show a certain propagation of the Li-plating region, following the cracks found in the electrode bulk.

In these regions, the areal capacity of the electrode was altered, and induced, as explained above:

1. Increase in the local current density of the NE
2. Reduction the local potential of the NE
3. Deposition of metallic lithium on the NE

Li-plating might have happened due to the checkups as explained earlier, and was aggravated and expanded because of the cracks formed by the highway cycles. During the aging protocol, charging was done till SOC 90 % at C/2. However, with the cracks being formed, such “calm” charging could have induced further Li-plating too.

5.5 Coin-cell sampling

This first glance into the aged cells highlighted the occurrence of heterogeneities of aging. Local defects can occur either due to an initial imperfection (e.g. variation in electrode mass loading, imperfect slurry dispersion etc.) and/or due to harsh aging mechanisms, and can propagate on the entire electrodes.

For coin-cell experiments to be representative, numerous samples should be taken, to capture the behavior of the different surface types identified.

For this reason, for the SPHEV 11's NE, four samples were taken from visually damaged, or “ragged” regions, while four others were taken from “smooth” regions. The PEs that faced these regions were sampled too. So a PE sample labeled as “ragged” means that it was in front of a NE ragged surface.

As the SPHEV 11 and the SPHEV 12 undergone the same aging scenario, only the first was chosen for coin-cell sampling. Samples that are labeled as “smooth” are considered to have undergone a similar evolution as the SPHEV 12, which was found to be quasi entirely “smooth”.

For the SPHEV 54, two samples were taken from the surfaces that suffered from “Li deposition”, two others were taken from “bright areas” and finally two others were taken from the “smooth areas”.

5.5.1 Electrodes' capacity evolution: results and discussion

The electrodes' capacity at C/20 was chosen to be the first criteria to analyze as the diagnostic tools (elaborated in the previous parts) are based on a C/20 charge. To be consistent, a de-lithiation of the PE and a lithiation of the NE were highlighted to represent a full cell charging set-up. This will give an insight of the remaining active material capacity since a C/20 capacity does not include the kinetic losses.

SPHEV 11 – Cal at 45 ° C and SOC 90 %. The C/20 capacity is plotted for each electrode sample. Blue circles refer to the ragged area and orange triangles refer to the smooth area. The error bar is solely related to the measurement error. Density plots facing these illustrate the spread of the results (Figure 77).

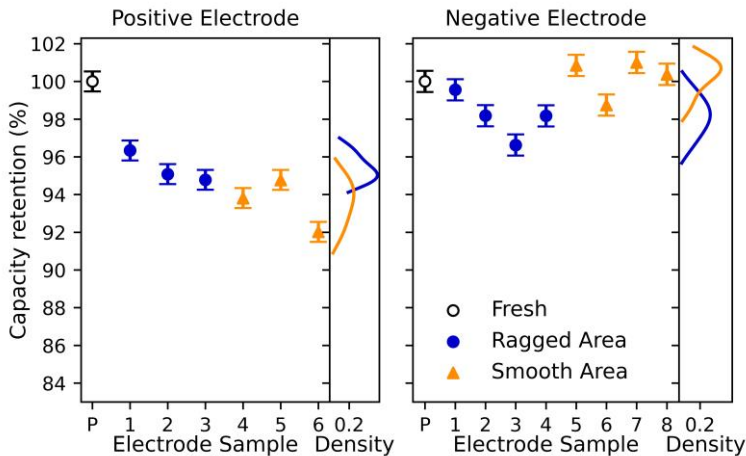


Figure 77. Electrodes' capacity retention for a C/20 charging set-up after Cal at 45 °C and SOC 90 %. The nature of the area describes the state of the NE.

The PE clearly suffered much more than the NE in terms of available capacity. Positive capacity retention values ranged from 92.0 to 96.3 % with an average of 94.7 %, hence a total loss of 5.3 %. The PE surface that faced the ragged area aged less (in average 4.6 %) than the one that faced the smooth area (in average 6.5 %). This indicates that, as the surfaces were not properly interacting due to surface defects on the NE, their aging stopped or slowed down.

Negative capacity retention values reached a minimum of 96.6 %, with a total average of 99.2 %. In this case, ragged areas mainly contained Li deposition. Under these conditions, deposited metallic lithium can undergo side reactions with the electrolyte to form additional SEI [79] and clog the pores, hence reducing the available capacity [311]. Smooth areas, on the other hand, suffered barely.

Considering the hypothesis that the smooth areas of the SPHEV 11's NE aged similarly to the entire NE of the SPHEV 12, which did not have any ragged area, calendar aging at 45 °C and SOC 90 % did not impact significantly the available capacity of the NE. Oppositely, it did impact the available capacity of the PE. Thus, in an aging scenario where checkups do not occur, the PE ages in average more and the NE ages less.

SPHEV 54 – Cal + ST + LT (H) at 45 ° C. The C/20 capacity for the PE and the NE of the SPHEV 54 was plotted in Figure 78 for each sample. Blue circles refer to the Li deposition areas, green squares refer to the bright areas, and orange triangles refer to the smooth area. The error bar is solely related to the measurement error. Density plots facing these graphs illustrate the spread of the results.

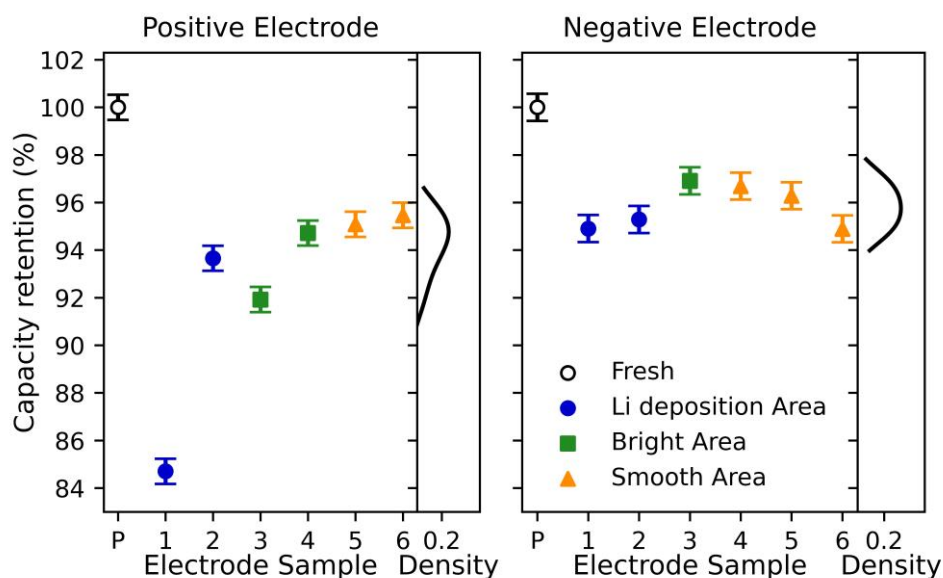


Figure 78. Electrodes' capacity retention for a C/20 charging set-up after Cal + ST + LT (Highway) at 45 °C. The nature of the area describes the state of the NE.

The PE capacity retention average in general is 92.59 %, which is lower than the one from the previous condition (94.7 %). The capacity of the PE that faced the smooth area seemed to be the highest (95.27 %), followed by the capacity of the PE surface that faced bright areas (93.32 %). Surfaces that faced the Li deposition area showed one value at 93.65 % and the other at 84.70 %. This proves that the impact of heterogeneities can be quite harsh. The reason behind this huge drop in capacity can be the following. As solid lithium deposited on the NE surface, it engendered additional SEI formation, hence consuming more lithium. This, in turn, led to an excessive de-lithiation of the PE due to the potential unbalancing of both electrodes [59], [312]. This means that the local potential of this PE surface was in the higher region most of the time, hence making it degrade faster than the other surfaces.

The NE suffered much more (95.83 % in average) than the precious condition (99.20 %), showing a narrow spread. The results seem to be independent of the nature of the surface.

The obtained outcomes prove that the drop in the average capacity in the NE is solely due to the ST + LT (H) phases. The reason behind this drop in the electrode capacity could be referred to the electrode surface cracking noticed during SEM characterization.

It could be also assigned to the electrode particle cracking. As the electrode faces elevated currents during discharge, its particles crack, and fresh SEI layer grows inside the cracks. With the crack propagation, graphite particles exfoliate, causing what is referred to as “island formation” [41]. Particle cracking couldn't be proved, and remains a hypothesis. Further post-mortem analyses are needed. However the electrode surface cracking was noticed in the SEM characterization.

Both reasons causes some parts of the electrode to be inactive, leading to a loss in the electrode capacity, triggering in turn an increase in the local current density. The consequence of an increase in the local current density is nothing but an increase in the concentration gradient, hence an increase in the mechanical stress, and further particle or surface cracking.

5.5.2 HPPC resistance calculation: results and discussion

The internal kinetic state of the electrodes is as important as their “accessibility” state. To illustrate its evolution during aging, pulse tests are done at 1C over the entire lithiation stoichiometry range of the electrodes, both during charge and discharge. The resistance values illustrated in Figure 79 are measured simply by dividing the voltage difference between the beginning of the pulse and at its end, by the imposed current ($\Delta V/\Delta I$), after 30 s. This resistance, referred to as pulse resistance, comprises contributions from the electronic resistance of the cell, its charge transfer resistance (electrode/electrolyte) and its polarization resistance which involves the ionic diffusion in the solid state [54].

SPHEV 11 – Cal at 45 ° C and SOC 90 %. The obtained resistance values are plotted in Figure 79 for the electrodes of the SPHEV 11. The first and second column represents the lithiation and de-lithiation of the active material, respectively. The first and second row represents the NE and the PE results, respectively. Black and white circles refer to the fresh cells. Blues markers represent the resistance of the NE ragged areas, and the resistance of the PE that faced these areas. Orange markers represent the resistance of the NE smooth areas, and the resistance of the PE that faced these areas.

NE. During the lithiation of the NE, the resistance of the fresh and aged electrodes seems to be generally overlapping. The resistance of the ragged areas 2 and 3 are higher and this can simply be related to the pore clogging phenomenon due to the

deposition of metallic lithium followed by further SEI formation, explained earlier on.

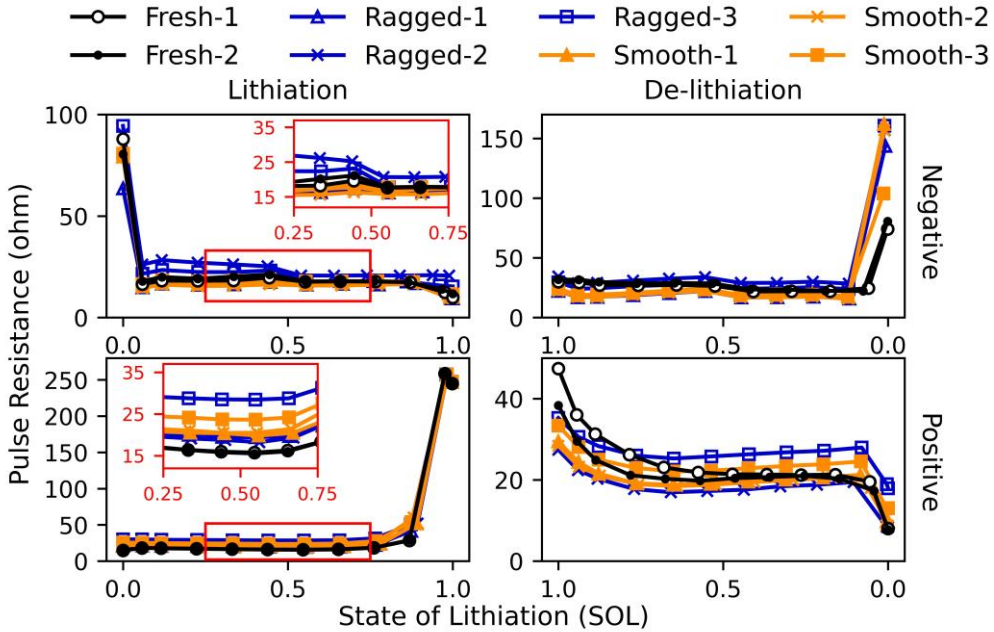


Figure 79. Kinetic state of the electrodes illustrated by the 30 s pulse resistance via HPPC test on half-cells: First row, Negative Electrode results; Second row, PE results; First column, Lithiation; Second column, Delithiation.

For the delithiation process, values overlap for the entire lithiation stoichiometry range before reaching the final de-lithiation state (SOL of nearly 0), where the resistance of the aged cell were found to be nearly two times higher than the unaged cell. This phenomenon could be associated to the increase and the densification of the SEI layer associated to this aging scenario. The dissolution of the transition metals from the PE, unstable at elevated SOC regions [41], accelerates the SEI growth [76], [313].

PE. On the other hand, the pulse resistance of the PE considerably increased during lithiation. The dissolution of transition metal explains very well this increase, which was also obtained in [314]. By losing a TM (most commonly Mn [41]), the positive active material will also lose contact with the additive conductive particles, hence weakening the kinetics of the electrode [314].

During de-lithiation, another interesting phenomena is identified and that is the reduction of resistance in the beginning of de-lithiation. The reason behind this is the initial voltage value before the first pulse. Between the lithiation and delithiation pulses, i.e. step 7 in Table 12, the cell is reinitialized by a charge/discharge cycle. At the end of this step, the voltage relaxed more than it did in the BOL, due to the

increase in the resistance. The higher the initial voltage is, the lower its increase after a 30 s current pulse. This reduces then the value of the resistance.

SPHEV 54 – Cal + ST + LT (H) at 45 ° C. The obtained resistance values of the electrode of SPHEV 54 are plotted in Figure 80. The first and second column represents the lithiation and de-lithiation of the active material, respectively. The first and second row represents the NE and the PE results, respectively. Black and white circles refer to the fresh cells. Blues markers represent the resistance of the NE lithium deposition areas, depicted as LiDA, and the resistance of the PE that faced these areas. Green markers represent the resistance of the NE bright areas, depicted as BA, and the resistance of the PE that faced these areas. Orange markers represent the resistance of the NE smooth areas, and the resistance of the PE that faced these areas.

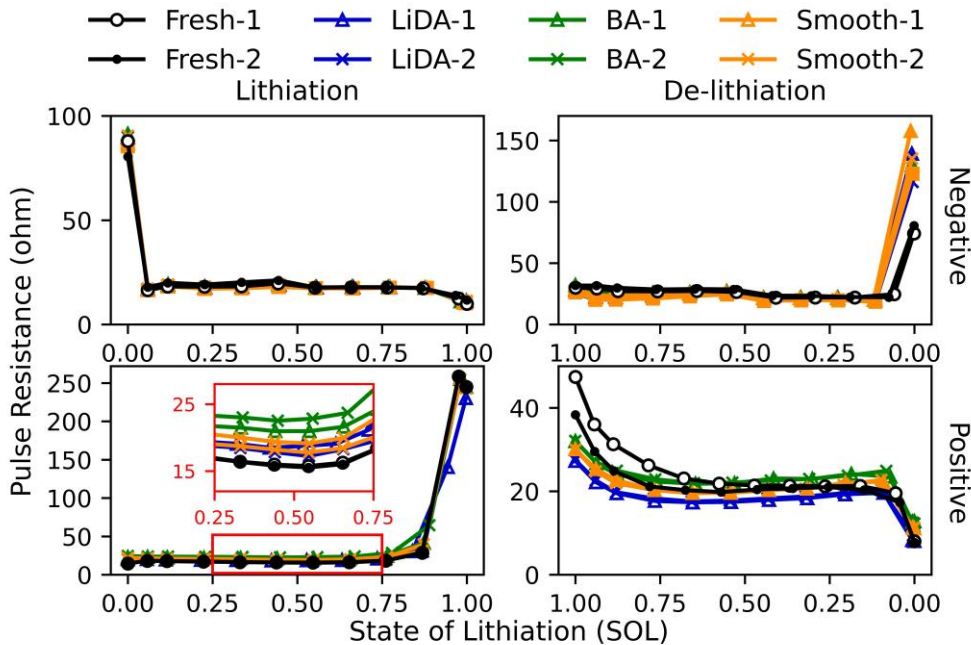


Figure 80. Kinetic state of the SPHEV 54 electrodes illustrated by the 30 s pulse resistance via HPPC test on half-cells: First row, Negative Electrode results; Second row, PE results; First column, Lithiation; Second column, Delithiation. LiDA stands for Li Deposition Area, BA stands for Bright Area.

NE. The resistance of the NE during lithiation is indifferent to the aging state. During de-lithiation, it seems to differ at the last SOL levels. The resistance values in this region showed an average of (133.5 ohm), slightly lower than the SPHEV 11 case (147.2 ohm).

The impact of aging on the internal resistance seems to be dependent on the aging duration rather than on the solicitation. In other words, the calendar phase controls

the increase of the electrodes resistance. The time spent in calendar (4 months) aging wasn't long enough to cause pore clogging and densify the SEI layer as seen in the previous case scenario (7 months).

The limitation of this conclusion resides in the fact that it is qualitative rather than quantitative. The duration spent in calendar aging is not the same, for this reason, the conclusion cannot be totally confirmed. It remains, though, a solid hypothesis.

PE. Concerning the PE lithiation, the resistance showed very similar trends to the SPHEV 11, but with a slightly lower tendency, as value did not surpass the 25 ohm mark. During de-lithiation, the same tendency is observed but, again, with a lower amplitude.

The increase in the PE resistance could come directly from the time spent at high potential values. As SEI grew at a high rate due to the ST + LT (H) phases, the PE potential increased, as explained earlier. This clarifies why the resistance values had relatively the same level when compared to the SPHEV 11 case, even though less time was spent in calendar mode.

5.5.3 Positive electrode initial potential: a significant information

The potential of PE after cell opening can report indirectly on the trapped lithium ions in the NE (due either to SEI growth or Li plating).

As a reminder, the full cell was completely discharged (Figure 68) before its opening. This means that the PE must have been in its state of maximum lithiation (of cyclable lithium, within its SOL operational boundaries). If it is not, then parasitic reactions occurred on the NE and the cyclable lithium inventory was not fully accessible.

The potential of the PE hints at its SOL. If it is low enough, then it was fully lithiated and no cyclable lithium was consumed. Oppositely, if it is higher and its SOL is not at its maximum level, then the lithium inventory was consumed. This is very well explained by Dubarry et al. [58] and illustrated by Matadi et al. [315].

In order to identify the amount of trapped lithium in front of every PE surface used for coin cell experiments, the method used is the following (Figure 81):

1. Measure the potential of the PE versus Lithium just after coin cell assembly
2. Measure the average capacity of the electrode below this potential using the C/20 lithiation/de-lithiation curve, to match the potential value to an SOL
3. Deduce from this value the average SOL of the PE at SOC 0 % at BOL obtained from the EBD tool for a discharge and charge curve (5.93 %)
4. Upscale this value to a full cell level by taking into consideration the ratio of surfaces between the coin cell to the surface of the full cell electrode
5. Normalize using the cell capacity at BOL (40.8 Ah)

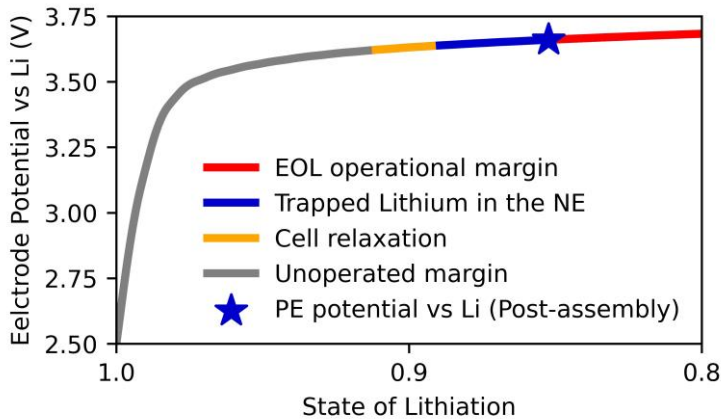


Figure 81. Method for the calculation of the amount of trapped Lithium in the NE using the PE potential vs Li

When applying discharged protocol (Figure 68) was applied, the voltage of a fresh cell relaxed till 3.07 V, before cell opening. Even if the same protocol was applied on the SPHEV 11, its voltage managed to relax till 3.30 V, before cell opening. Which means that the cell wasn't completely discharged. A 3.30 V value is equivalent to an average SOC of 2.18 % (calculated using the C/20 charge and discharge voltage curves at EOL). So 2.18 % should be reduced from the obtained value. Concerning the SPHEV 54, its voltage relaxed till 3.21 V before opening, equivalent to a SOC of 1.25 %. This value is then taken into consideration.

The obtained results are illustrated in Figure 82 for SPHEV 11 and 54. The measured amount of trapped lithium for each type of area that the PE faced, are plotted below. The left panel is dedicated for the SPHEV 11 cell (Cal 45 °C and SOC 90 %) and the right panel is dedicated for the SPHEV 54 cell (Cal + ST + LT (H) 45 °C).

SPHEV 11. For the first case, the average of the trapped lithium is 8.69 % and 4.30 % on the smooth and the ragged surfaces, respectively, and a total average of 6.50 %. It can be seen that the smooth surface trapped more lithium than the ragged surface. The smooth surface produced “more efficiently” SEI products, as it was completely operational. This is harmony with the idea evoked earlier concerning the loss of capacity of the PE. The electrode sample 3 (ragged) had a very low initial potential, hence nearly no lithium were trapped in the negative electrode. This could be due a stopped interaction between the two surfaces. It might be due, for example, to the presence of gas bubbles that completely blocked the accessibility of these electrode faces, hence preventing the growth of SEI.

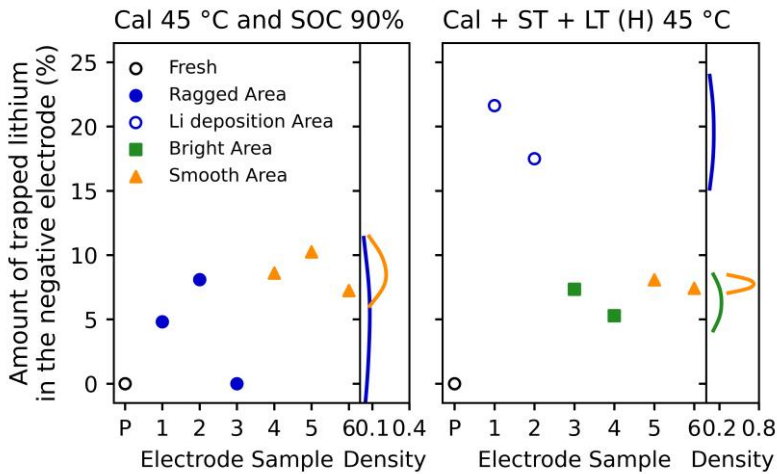


Figure 82. Amount of trapped Lithium in the NE in front of every PE surface for SPHEV 11 (left) and SPHEV 54 (right) (the size of each point represents the error, $\pm 0.57\%$)

SPHEV 54. On the other hand, the quantity of trapped Lithium was in general higher for the SPHEV 54 with an average of 11.21 %. Li deposition area seemed to have the highest value (with an average of 19.56 %). As Li deposited on the NE, it triggered the formation of a “secondary SEI” on the accumulated solid lithium, which further consumes cyclable lithium [80]. A high discharge rate caused the further breakdown of both the “primary” and “secondary” SEI, making new surfaces accessible for a “fresh” SEI, hence consuming and trapping further Li [41].

The PE surfaces facing bright areas showed an average value of 6.31 %, which is very comparable to the SPHEV 11 ragged cases (6.46 %, without taking into consideration the third sample). At some point of the aging process, gas bubbles were formed and stopped the further formation of SEI. This phenomena happened for both condition, and is therefore controlled by the calendar phase and not impacted by the cycling.

The PE surfaces that faced smooth areas had showed an average value of 7.75 %, which is slightly lower than the average of the SPHEV 11 condition (8.69 %). Thus, cycling does not have a direct significant impact on these areas, which seems to be controlled by the calendar condition.

6. Conclusion, discussion and perspectives

The main degradation mechanism that appeared in these different scenarios is the formation and growth of the SEI on the NE. However, it occurred in different ways and accompanied by other phenomena for each scenario.

For the Cal condition at 25 °C and SOC 90 %, the EBD and the ‘alawa tool results suggest that the SEI took the form of a simple growth, triggered by the potential of the NE. In this case, which represents a big percentage of the usage, the dissolution

of the PE transition metals could contaminate this layer and potentially accelerate its growth. Overall, the LLI due to this mechanism took the appearance of a square root shape curve.

For the same scenario at 45 °C (SPHEV 11), the SEI did seem to occur but in a different manner. In the first months of aging, the increase in LLI had the shape of a square root curve. Which indicates that the mechanism could have been the same as in the 25 °C scenario, but with a higher rate. After these two months, the LLI increased linearly indicating that the mechanisms changed. As shown by both the EBD and the 'alawa tool, LAM_{pe} occurred more intensely, which means that transition metals from the PE could have contaminated the SEI more densely and accelerated its growth. The post mortem analyses validated the fact that SEI happened quite severely (6.5 % of the lithium stuck in the NE). However, the Li deposition on the NE has been noticed during by SEM images, indicating that this could be the reason behind the steep increase of LLI, and also the reason behind the formation of more SEI (secondary SEI on the metallic lithium). Li deposition happened to be around gas bubbles, which might had not appear at 25 °C.

Looking at the condition of the calendar aging at 45 °C SOC 90 % without checkups, (no bubbles formed, no Li deposition, and a trapped Lithium of 4.3 % (smooth area of SPHEV 11)), it can be concluded that the checkups had a dirty role to play in the degradation of this cell.

At 25 °C, the first impact on the aging of the cells was seen for ST and LT trips and the main reason behind this was assumed to be the SEI breakdown and repair process. The SEI cracks before the particle does, as it has a different Young's moduli and fracture toughness [41]. Further particle micro-cracks was assumed to occur [38], [50], [66] when highway was applied, opening up extra area for the formation and growth of a fresh SEI, leading to an exponential increase of the LLI (observed in the EBD results).

At 45 °C, SEI fracturing was supposed to have started with ST scenarios. As the aging stages advanced, the LLI seemed to stabilize before re-increasing again steeply. This was associated to particle micro-cracks, which seems to be favored at high temperatures [41]. For Highway scenario (SPHEV 54) the steep LLI was observed directly in the beginning, suggesting that particle micro-cracks might have started in the early stages of aging. SEM analyses of the NE suggest that the electrode bulk was fractured. The capacity of the NE decreased by an average of around 4.2 %. This proves that particle micro-cracks might not be the only reason behind the quick decrease of capacity (or increase of LLI). This indicates that Highway scenarios induced some mechanical stress on the electrode structure, and some "islands" formed. The "islands" of lithiated graphite were identified during the visual inspection (golden yellow spots), similarly to what was obtained in [307].

"Island" formation and the de-cohesion of the NE material leads to a decrease in the local capacity, increasing the current density. This, in turn, leads to the deposition

of metallic lithium at each charge (even if stopped at SOC 90 %) and a further LLI. Lithium deposition can lead to secondary SEI formation, clogging the pores of the graphite and inducing a decrease in the local capacity. This leads to high local discharge and charge rates and to further material de-cohesion. And the cycle goes on (Figure 83).

LAM_{pe} then did occur at all conditions as the SOC was found to be at 90 % in calendar condition. Results suggest that LAM_{pe} was not only dependent on the temperature and the SOC, but also on the LLI, especially when this one occurred on the NE. The higher the LLI, the higher the potential of the PE. This was validated too with post-mortem analysis, where the quantity of trapped lithium was correlated to the potential of the PE.

Figure 83 assesses the interdependence of the degradation mechanisms with respect to the aging solicitation. The impact of the aging solicitations is represented by a blue arrow indicating the solicitation type: Charge, Cal SOC 90 % and ST + LT. An aging defect on the NE (e.g. imperfect slurry dispersion on the folds of the electrodes) causes a decrease in the local areal capacity and an increase in the current density. When a charge is applied, the potential of the NE drops rapidly below 0 V vs Li, leading to metallic lithium deposition (proved by SEM images). Metallic lithium deposition causes further LLI and a secondary SEI formation. Both leads to high PE potential and possible de-lithiation. This causes the dissolution of transition metals (or rock salt formation) leading to an LAM_{pe}. Transition metals dissolution can pollute the SEI and assist in accelerating its growth (relationship between LLI and LAM_{pe} identified in the EBD tool). Dissolution of transition metal and accelerated SEI growth can also be a consequence of calendar aging and SOC 90 % (most common parking practice), even if aging defects are non-existent. The SEI growth leads to further LLI and the cycle goes on. When cycling is applied for low intensities (ST) SEI cracks. When the cycling intensity increases (ST + LT) particle micro-cracks (assumed by the LLI curve change of shape and by referring to [38], [50], [66]) and electrode surface fracturing occurs (validated by SEM images). SEI cracking and particle micro-cracks leads to further SEI formation and growth (secondary and fresh SEIs) leading to possible pore clogging, inducing a new defect on the NE. Electrode surface fracturing causes material de-cohesion and a possible LAM_{ne}. It also created further variations in the electrode areal capacity, and the cycle goes on.

Interestingly, for cases when LAM_{ne} does not occur, LAM_{pe} causes the N/P ratio to shift and reach higher values. This happens when parking is done at high SOC, which represent a big portion of the EV life. Li deposition is less favored when the N/P ratio increases. On the opposite, when the NE degrades faster than the PE, Li plating is more favorable [316]. However, such phenomena was unlikely to happen in the studied scenarios, as parking was always done at high SOC and at mild or high temperatures. In this way, the N/P will either increase (Figure 77), or stay at the same level (Figure 78).

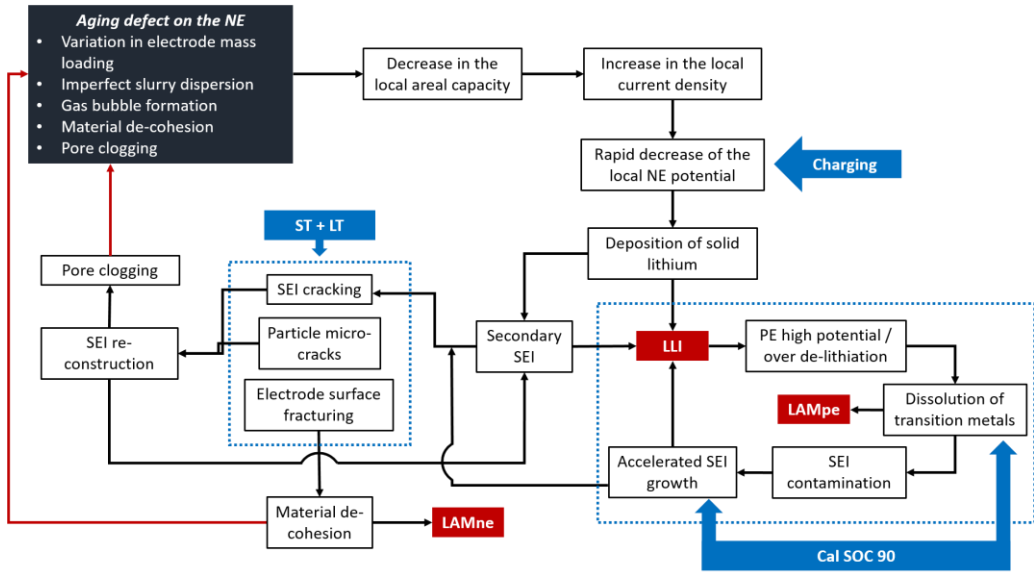


Figure 83. Aging cycle showing the interdependence of the mechanisms and the aging modes with respect to a general Cal + ST + LT scenario

In cases where the EV is parked at low temperatures and high SOC, the aging is expected to slow down. This suggests that, with ST + LT (H) scenarios where the NE is expected to lose some capacity, the N/P can potentially go into the direction of favoring Li deposition. Unfortunately, this condition (testing at low temperatures) couldn't be achieved. It remains though an interesting perspective, as the battery temperature was found to be in the low region during usage, especially in European weathers.

Chapter 7 – Performance and Aging Modeling

Highlights

- Parametrized a Newman P2D model for the Samsung 37 Ah PHEV cell
- Identified experimentally 73 % of the model parameters
- Validated the performance model with IC curves and L2 charging
- Implemented the SEI and LAM models
- Modeled the particle exchange surface increase

A usage representative testing protocol was designed and implemented on Samsung 37 Ah PHEV cells, in the framework of the previous chapters. In chapter 6, diagnosis tools and post-mortem analyses were done to identify two main degradation mechanisms that assist in the growth of SEI: the LAM_{pe} , LAM_{ne} , and the increase in the particle exchange surface (SEI fracturing, particle micro-cracks and deposition of metallic lithium). The purpose of this chapter is to try and model these phenomena using both a literature based SEI model with a variable exchange surface, and a mechanistic approach. A Newman P2D performance model was parametrized for the cell in question, and aging models were added to it.

1. Introduction

In order to have access to the physical state of the Samsung 37 Ah PHEV cells, modeling its performance and aging is done using a Newman P2D approach. The purpose of this chapter is to elaborate briefly the leading principles of the Newman P2D performance model, i.e. the “unaged” model. The boundary conditions of the main parameters are underlined, as well as their contribution in the governing equations. The next purpose is to elucidate the methods used to measure the electrochemical and physical parameters of the model. Then, the performance (non-aged) model is calibrated and compared to the experimental data of the cells in the Beginning Of Life (BOL). The following part of the chapter covers the implementation of aging models and equations in the Newman P2D model. Finally, results are compared to the aged experimental data, and conclusions are drawn.

2. Model development

2.1 The continuum approach

The Newman P2D (Pseudo 2D) model, first introduced by Doyle, Fuller and Newman in the 1990s [121], consists of a continuum description of the battery “sandwich” internal design. The “sandwich” conception represents the negative electrode (NE), the separator, and the positive electrode (PE), next to each other on the horizontal axis. These three compartments are all porous and filled with the electrolyte. So each layer is treated as a superposition of two continua. One of them represents the electrolyte and the other represents the solid matrix (which is also known as the porous electrode theory) [113].

In other words, at each point in the geometry of an electrode, the two phases coexist quantitatively, depending on their corresponding volume fraction [120]. Additionally, to each point is associated a suitable active material particle, filling a volume fraction of the solid matrix. It is in contact with the electrolyte to intercalate and de-intercalate ions, i.e. current exchange (Figure 84).

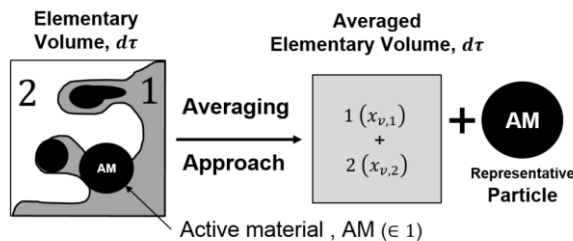


Figure 84. Representation of the continuum approach [120] where x_v represents the volume fraction of each continuum and the subscripts 1 and 2 represent the solid and liquid phases respectively

The same goes for the separator phase, however, it is not associated to any active material, and its solid phase is electrically insulated.

In each continuum, electrochemical properties are averaged over a representative elementary volume of the electrode, small enough compared to the compartment, and large enough compared to the dimensions of the pores [113].

The idea behind this approach is to account for the necessary features of each compartment without going into the detailed micro-structure geometry. This introduces one of the main assumptions of the model: the described battery domain is a macro-homogenous phase. Micro-irregularities (e.g. the particle size distribution, shape irregularities etc.) are ignored (e.g. the electrode is assumed to be made of perfectly homogenous spheres).

Figure 85 illustrates a general view on the sandwich approach showing the liquid and the solid continua.

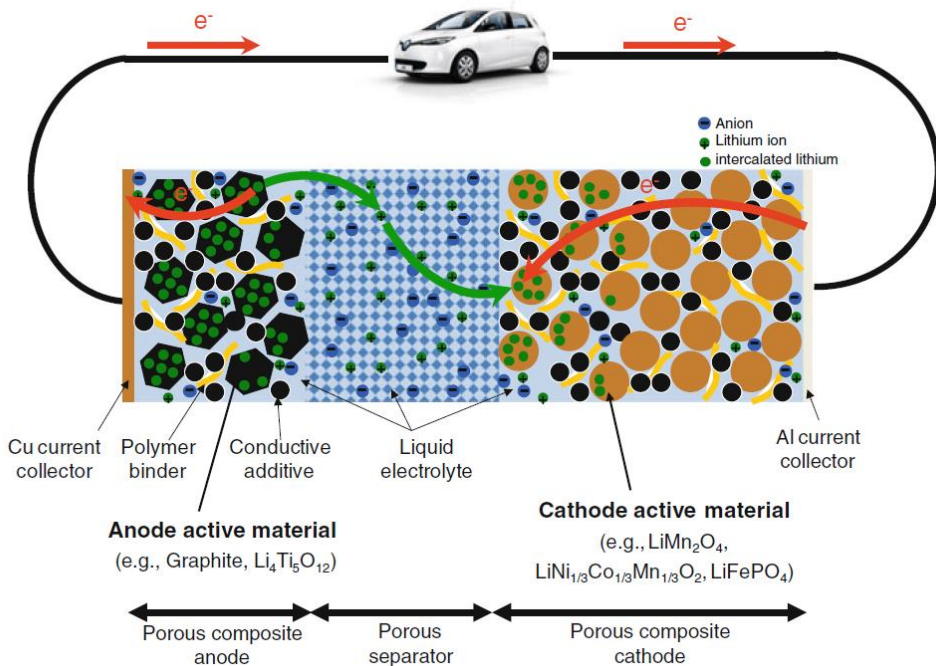


Figure 85. Illustration of the battery "sandwich" approach as modeled by the Newman P2D [113]

During a discharge, Li-ion migrates from the porous anode (NE), to the porous cathode (PE), passing by the wetted separator. It is assumed that this migration happens on a horizontal axis (first dimension), perpendicular to the "sandwich". This domain of exchange is referred to as the "macro" domain [113]. The second dimension is the electrode particle radius, considered spherical and isotropic. The ions are assumed to diffuse inside the solid phase in a radial dimension, which is referred to as the "micro" domain [113].

The model is treated as 1-D problem (horizontal axis), and the pseudo second dimension is related to the diffusion inside the particle, hence its name “Pseudo 2D”. In other words, the transport phenomena happen only on the dimension perpendicular to the electrode surface. Transport that happens on the y direction parallel to the electrode surface, are neglected.

2.2 Governing principles

Before describing the governing equations, it is important to define the geometry attributes. The three compartments are illustrated in Figure 86. The x dimension of this figure will be used as a reference when explaining the boundary conditions. For example $x=L_n$ refers to negative electrode/separator interphase. The pseudo second dimension of the model is illustrated by the red radius (with the red r mark) in the active material spherical particle.

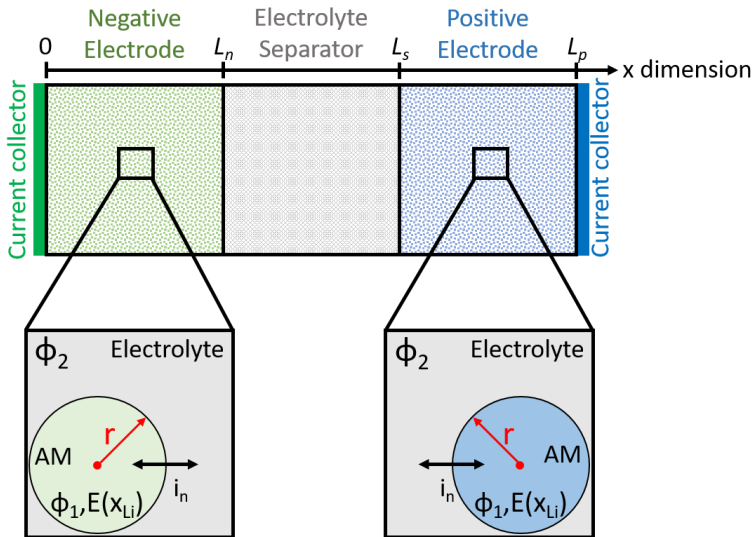


Figure 86. Illustration of the governing equations and the boundary conditions of the Newman P2D model [120] (AM = Active Material). Φ_2 is the electric potential of the liquid phase (V); Φ_1 is the electric potential of the solid phase (V); $E(x_{Li})$ is the equilibrium potential of the active material vs Li (V); i_n is the intercalation current density ($A/(m^2)$).

During a charge/discharge process, currents are provided from a displacement of electrons in the solid phase and ions in the liquid phase. It can then be considered that there is an electronic current density, i_1 , circulating across the solid phase, and an ionic current density, i_2 , circulating across the liquid phase. Flowing through the horizontal dimension, the sum of these two current densities is assumed to be uniform across the electrode. An increase of one is compensated by a decrease of the other.

$$\nabla \cdot i_1 + \nabla \cdot i_2 = 0 \quad (36)$$

The ionic current density (i_2) value at the current collector of both electrodes is nil (i.e. at $x=0$ and $x=L_p$), whereas the electronic current density (i_1) is nil at the electrode/separators interface (i.e. at $x=L_n$ and $x=L_s$). This means that, across the separator, the current is solely carried by ions.

The driving force of the electrons' displacement in the solid phase is the electric potential (Φ_1). i_1 is then expressed by the Ohm's law (equation (37)).

$$i_1 = -\sigma_1^{eff} \nabla \Phi_1 \quad (37)$$

where

σ_1^{eff} is the Electronic conductivity of the solid phase (S / m)

The driving forces of the ions displacement in the electrolyte are assumed to be the gradient concentration (i.e. diffusion) and the gradient of ionic potential (i.e. migration). By relying on the binary electrolyte approach (the solvent and the ions/cations of the salt) and the concentrated solution theory (proposing that interactions exist between charged species), i_2 can be written as follows.

$$i_2 = -\kappa^{eff} \nabla \Phi_2 + 2\kappa^{eff} \frac{RT}{F} (1 - t_+^0) \left(1 + \frac{d \ln f_{\pm}}{d \ln c_2} \right) \nabla \ln c_2 \quad (38)$$

where

κ^{eff} is the effective ionic conductivity of the electrolyte (S/m)

Φ_2 is the electric potential of the liquid phase (V)

t_+^0 is the transference number of lithium in electrolyte

f_{\pm} is the mean molar activity coefficient of the electrolyte

c_2 is the concentration of lithium in the electrolyte (mol/m³)

When a current is applied, a charge transfer between the solid phase (active material) and the liquid phase, along their surface of contact is done. And that is equal the divergence of the ionic current density and to the negative divergence of the electronic current density.

$$\nabla \cdot i_2 = -\nabla \cdot i_1 = aFj_n = ai_n \quad (39)$$

where

a is the area of the active material/electrolyte interface (m²/m³ of the electrode)

F is the Faraday's constant (96,485 C/mol)

j_n is the pore wall flux of lithium (mol/(m².s))

i_n is the intercalation current density (A/(m²))

It is assumed that the charge transfer happening on the surface of the active material, i.e. lithium intercalation/de-intercalation, follows a Butler-Volmer kinetics. The intercalation current density is then expressed as follows.

$$i_n = i_0 \left[\exp\left(\frac{\alpha F \eta}{RT}\right) - \exp\left(-\frac{(1-\alpha)F \eta}{RT}\right) \right] \quad (40)$$

where

α is the symmetry factor

i_0 is the exchange current density (A/m²)

R is the ideal gas constant J/(mol K)

T is the absolute temperature (K)

η is the overvoltage (V)

F is the Faraday's constant (96,487 C/mol)

The value of i_n is nil at the electrolyte/separator domain ($L_n < x < L_s$). The overvoltage is expressed as the difference between the electrode potential ($\phi_1 - \phi_2$) and its equilibrium potential ($E(x_{Li})$), measured vs Li.

$$\eta = \phi_1 - \phi_2 - E(x_{Li}) \quad (41)$$

where

Φ_1 is the electric potential of the solid phase (V)

Φ_2 is the electric potential of the liquid phase (V)

$E(x_{Li})$ is the equilibrium potential of the electrode vs Li (V)

x_{Li} is the lithium stoichiometry

It can be noticed that there's a dependence on the equilibrium potential of the electrode, which itself is dependent on the lithium stoichiometry.

The exchange current density (i_0) is reliant on the concentration of the species implicated in the charge transfer process. It can then be written in function of the intercalated lithium (x_{Li}), the fraction of vacancy sites in the host material ($1 - x_{Li}$), the concentration of lithium ions at the interface of the active material (c_2), normalized by dividing over the maximum concentration (c_2^0), and the charge transfer rate (k_i).

$$i_0 = F k_i (1 - x_{Li})^{(1-\alpha)} (x_{Li})^\alpha \left(\frac{c_2}{c_2^0}\right)^{(1-\alpha)} \quad (42)$$

where

k_i is the charge transfer rate (mol/(m².s))

c_2 is the concentration of lithium ions in the electrolyte at the interface (mol/m³)

c_2^0 is the reference concentration of lithium ion in the electrolyte (mol/m³)

x_{Li} is the Lithium stoichiometry

Now that the transport phenomena, the kinetics principles, and the geometrical aspects are set, a mass balance is done on the elementary volume of a liquid phase, present in the entire domain as a continuum.

$$\frac{\varepsilon \partial c_2}{\partial t} = -\nabla \cdot N_{Li} \quad (43)$$

where

ε is the volume fraction of the liquid phase

N_{Li} is the flux of the lithium ions

The flux is expressed in function of the effective diffusion coefficient of the salt (D_2^{eff}), the concentration gradient ($\partial c_2 / \partial x$), the transference number (t_+^0) and intercalation current density (i_n).

$$N_{Li} = -D_2^{eff} \frac{\partial c_2}{\partial x} - (1 - t_+^0) \frac{ai_n}{F} \quad (44)$$

where

D_2^{eff} is the effective diffusion coefficient of the salt (m^2/s)

The flux is nil both at $x=0$ and $x=L_p$.

The transport phenomena inside the active material particle (i.e. the pseudo second dimension) is described through the active material mass balance (equation (45)).

$$\frac{\partial c_s}{\partial t} = \frac{1}{r^2} \frac{\partial}{\partial r} \left(D_1 r^2 \frac{\partial c_1}{\partial r} \right) \quad (45)$$

where

D_1 is the lithium diffusion coefficient inside the active material (m^2/s)

c_1 is the lithium concentration in the active material (mol/m^3)

r is the radius of the active material (m)

At $r=0$ (i.e. in the center of the active particle) the radial concentration divergence ($\partial c_1 / \partial r$) is nil, and at the surface interphase, $D_1 \partial c_1 / \partial r$ is equal to the pore wall flux (j_n).

A summary of the described phenomena is done in Table 16.

2.3 Assumptions and limitations

The described model takes into assumption some major points, limiting its reliability and domain of validity.

First of all, thermal effects are neglected. In other terms, the model is isothermal, and takes the temperature as an initial fixed parameter.

Second, the parameters that tend to vary at different temperatures follow an Arrhenius behavior. Finding the Arrhenius equation parameters is done by assimilation (fitting) to experimental data.

Third, as the transport phenomena happened on the 1D axis, the only mechanical changes are done normal to the electrode planes (thickness increase of the SEI for

example). Particle fracturing and material de-cohesion happening in the 3D dimensions are neglected.

Table 16. Summerizing the P2D Newman phenomena depending on the cell sandwich domain

Phenomena	Mathematical representation	Boundary conditions
Porous electrode region		
Transport phenomena in the electrolyte	$\frac{\varepsilon \partial c_2}{\partial t} = -\nabla \cdot N_{Li} = \nabla \cdot D_2^{eff} \frac{\partial c_2}{\partial x} - (1 - t_+^0) \frac{ai_n}{F}$	$N_{Li} = 0$ at $x = 0$ & $x = L_p$
Ionic displacement in the liquid phase	$\vec{i}_2 = -\kappa^{eff} \nabla \Phi_2 + 2\kappa^{eff} \frac{RT}{F} (1 - t_+^0) \left(1 + \frac{d \ln f_{\pm}}{d \ln c_2} \right) \nabla \ln c_2$	
Current displacement in the solid phase	$\vec{i}_1 = -\sigma_1^{eff} \nabla \Phi_1$	$\vec{i}_1 = 0$ at $L_n < x < L_s$
Kinetics (Butler-Volmer equation)	$i_n = i_0 \left[\exp\left(\frac{\alpha F \eta}{RT}\right) - \exp\left(-\frac{(1 - \alpha) F \eta}{RT}\right) \right]$	$i_n = 0$ at $L_n < x < L_s$
Particle domain		
Diffusion of Li in the spherical particles	$\frac{\partial c_s}{\partial t} = \frac{1}{r^2} \frac{\partial}{\partial r} \left(D_1 r^2 \frac{\partial c_1}{\partial r} \right)$	$D_1 \frac{\partial c_1}{\partial r} = 0$ at $r = 0$ $D_1 \frac{\partial c_1}{\partial r} = \frac{i_n}{F}$ at the surface of the particle
Separator domain		
Ionic displacement in the liquid phase	$\vec{i}_2 = -\kappa^{eff} \nabla \Phi_2 + 2\kappa^{eff} \frac{RT}{F} (1 - t_+^0) \left(1 + \frac{d \ln f_{\pm}}{d \ln c} \right) \nabla \ln c$	
Transport phenomena in the electrolyte	$\frac{\varepsilon \partial c_2}{\partial t} = \nabla \cdot D_2^{eff} \frac{\partial c_2}{\partial x}$	$N_{Li} = 0$ at $x = 0$ & $x = L_p$

Fourth, the effective transport parameters of the electrode layer are approximated. Measuring the parameters values experimentally is usually done in the bulk phase of the medium. However, their value in the porous electrode (referred to as “effective”) is needed. An common approximation of the effective value of transport parameters is the following [317].

$$P^{eff} = P \frac{\epsilon}{\tau} \quad (46)$$

where

P represents a transport parameter

P^{eff} represents its effective homologue

ϵ is the porosity of the electrode

τ is the tortuosity of the electrode

In this model, the transport parameters that were subject to this rule are the salt diffusion in the electrolyte (D_2^{eff}) and the ionic conductivity (κ^{eff}).

2.4 Problem resolution and validation

2.4.1 Solution and expected outcomes

The equations listed in Table 16 are expressed in Cartesian coordinates of two axis where the first represents the x dimension that passes through the cell sandwich conception, and the second represents the radial dimension of the particle.

The problem then solves for the variables of the equations: the concentration of lithium both in the electrolyte (c_2) and the electrodes (c_1), the current density in both the electrolyte (i_2) and the electrodes (i_1), the intercalation current density of the active materials (i_n), and the potential of the electrolyte and the electrodes (Φ_1 and Φ_2).

The cell voltage (U) is then readable by subtracting the solid phase potential of the negative current collector (i.e. Φ_1 at $x = 0$) by the solid phase potential of the positive current collector (i.e. Φ_1 at $x = L_p$).

$$U = \Phi_1(x = L_p) - \Phi_1(x = 0) \quad (47)$$

The Newman P2D model is used to represent the behavior of the cell during galvanostatic operations within voltage operating conditions. The applied current is then entered as a second-type (Neumann) boundary condition, imposed on equation (39) at the current collector/electrodes domains. The voltage is then extracted as shown in equation (47). Imposing the voltage as a limit is applied as a Dirichlet condition.

Imposing a constant power (CP) application is done by imposing a variable current that depends on the specified power, as a boundary condition.

The capacity (Ah) is then calculated by integrating the current value over time within the voltage limitations. The energy (Wh) is calculated by integrating the voltage curve over the capacity within the voltage limitations.

$$I(t) = \frac{P_{imposed}(W)}{U(t)} \quad (48)$$

where

$I(t)$ is the variable current in A at time t

$P_{imposed}$ is the required imposed power in W

$U(t)$ is the voltage of the cell in V at time t

2.4.2 Operating process and tools

The operating process goes as illustrated in Figure 87. The aforementioned equations were taken from the CEA library of models, already implemented before the start of the thesis. The parameters needed for the equations were either extracted experimentally, or assumed from literature (as will be elaborated in the further subparts). They were added to the CEA's database of parameters. A Matlab 2020b script was used to retrieve both the needed equations and parameters, in order to build the Newman P2D model. The script contained also initial state information (e.g. starting stoichiometry of both active material), the operating conditions (e.g. C-rate and temperature), and the limitations of one event (e.g. cutoff voltage and floating conditions). This was sufficient to initialize and calibrate the model.

The script also executed the resolution of the mentioned parameters and equations in COMSOL 5.5. The resulting COMSOL file contained the implemented parameters and equations, as well as the solution of the model (e.g. voltage curve).

The implementation of equation (48), the development of aging mechanisms, and the cycling procedure of the cell (as will be elaborated in the further subparts), were done in this resulting COMSOL file. Next, the newly developed equations were added to the CEA library.

Finally, results were post processed using python tools. Here, the voltage curves were illustrated, derived for incremental capacity (IC) analysis, and compared to experimental data.

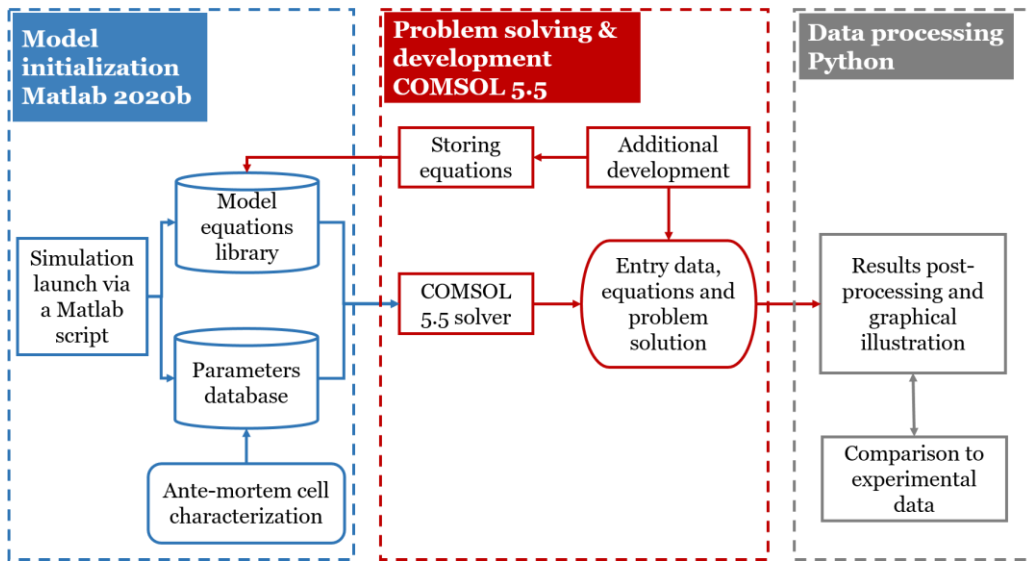


Figure 87. Flowchart showing the methodology and numerical tools used to implement and run the Newman P2D model

2.4.3 Validation strategy

The model was considered valid if its outcome and predictions were confirmed by the experimental observations. Concretely, if the voltage curve under a certain solicitation, predicted by the P2D Newman model, corresponded to the response obtained experimentally by the same solicitation, then the model was considered valid.

Two different strategies were used to validate the model.

The first, consists of comparing the IC curves of a C/20 (1.85 A) charging process. Comparing the peaks/valleys position and intensity reveals whether the representation of the active material intercalation phase change is satisfactory. This is also important for evaluating the aging simulation outcomes. Chapter 6 showed that the peaks/valleys movement can hint quite accurately at the loss in the lithium inventory (LLI) or the loss in active material (LAM). Making sure that the IC curve of the P2D model yields the same the variation in peaks, hence, the same LLI and LAM of the experimental, is needed for a complete validation.

The second consists of comparing simulated charging curves. The most common charging methods found in today's usage (chapter 3, part 3.3) are the L2 chargers. A typical L2 consists of a 7 kW charging, and a faster charging technics found in today's usage is the Tesla 16.5 kW charging [318]. For the PHEV vehicle that employs this battery, the 7 kW and 16.5 kW are equivalent to 65 W and 152 W for the cell, respectively. The model should therefore describe precisely these types of charging powers.

2.5 Parameters extraction

As previously noticed, the equations of the model are reliant on a long list of known parameters. These parameters needed to be extracted from the cell in question (Samsung SPHEV 37 Ah), so that the model could represent accurately its behavior. Some parameters demanded extra time to be measured, and are therefore either assumed, or taken from literature. Publications that used identical or very similar materials were then chosen. A summary of all the parameters is presented at the end of this subpart.

The battery dismantling procedure was undergone as described in chapter 6.

2.5.1 Geometrical parameters

Dismantling the cell revealed that two identical rolls were connected in parallel inside the solid casing.



Figure 88. Illustration of the Samsung PHEV 37 Ah and its connected rolls found inside

The dimensions of the electrodes are listed in Table 17. It was found that the electrodes were two sided. The thicknesses of one side were of interest, and were measured using a digital micrometer. The total surface was obtained by multiplying the dimensions of one roll by 2, as the electrodes were two sided, and again by 2, to account for the second roll.

Table 17. Dimensions of the Samsung PHEV electrodes

NE Coating thickness (μm)	PE Coating thickness (μm)	NE dimensions (one roll) L(mm) \times l(mm)	PE dimensions (one roll) L(mm) \times l(mm)	Total NE surface (m^2)	Total PE surface (m^2)
59	57	5,438 \times 80	5,260 \times 75	1.578	1.74

The measurement of the electrodes (without the current collector) loading yielded values of 8.5 mg/cm²/side for the negative electrode, and 18.2 mg/cm²/side.

2.5.2 Electrolyte related parameters

The data sheet of the cells mentions that the electrolyte is made out of “LiPF₆ + organic carbonates”. The goal is to identify the nature of these organic carbonates. As mentioned in chapter 6, a very small portion of the electrolyte was recovered. This was enough to characterize it via the GC-MS technique [319] and the results inferred that the electrolyte is mainly made out of EC:DMC:EMC with 1:1:2 %w. For further characterization, a solution with the same composition was synthesized. The reference concentration of lithium in the electrolyte was assumed to be $c_2^0 = 1M$. So 1M of LiPF₆ was added to the solution to form an electrolyte of EC:DMC:EMC 1:1:2 + 1 M LiPF₆. The same electrolyte was used for all the coin-cell characterizations.

Ionic conductivity (κ) and activation energy (Ea_κ). The conductivity of the electrolyte is one of its major parameters. To measure it, the electrolyte was first sandwiched in a coin-cell with two blocking electrodes made out of stainless steel, 0.5 mm thick and 16 mm wide (Figure 89). A spacer of known dimensions was used to set a space between the two stainless steel disks. The coin-cell setup was connected to a Biologic VMP 3 bench for Electrochemical Impedance Spectroscopy (EIS). A 0.8 mA perturbation was applied from 200 kHz to 1 Hz at the open circuit potential. The same experiment was undergone at a temperature from -30 to 60 °C, with an interval of 10 °C from -30 to 10 °C, an interval of 5 °C from -10 to 45 °C, and a final measurement at 60 °C. The temperatures of interest lie within the -10 to the 45 °C, and that is the reason why a smaller increment was chosen for this region.

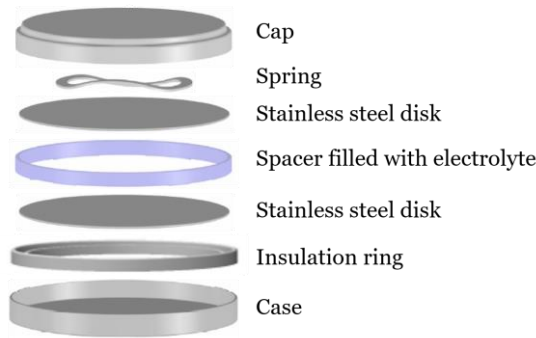


Figure 89. Coin cell design for electrolyte conductivity measurement

To obtain the conductivity, the following formula was applied [320].

$$\kappa = \frac{l}{R_{el}A} \quad (49)$$

where

κ is the conductivity of the electrolyte expressed in mS/cm

l is the thickness of the spacer between the two stainless steel disks

R_{el} is the bulk resistance of the EIS spectrum

A is the surface covered by the electrolyte

The bulk resistance (R_{el}) was obtained by taking the intersection of the EIS spectrum with the horizontal axis of the Nyquist plot. The thickness of the spacer (l) was measured with a digital micrometer, and A is the surface area of the spacer.

In Figure 90 (A), the ionic conductivity is plotted in function of the testing temperature of the cell for both samples (1 and 2). Figure 90 (B) illustrates the relationship between the logarithm of conductivity times the temperature ($\ln(\kappa T)$) in function of the inverse of temperature ($1/T$). This underlines the Eyring relationship, described in equation (50) [321]. The slope of $\ln(\kappa T)$ in function of $1/T$ yields the activation energy Ea_{κ} .

$$\kappa = \frac{A_{\kappa}}{T} e^{\left(\frac{-Ea_{\kappa}}{RT}\right)} \quad (50)$$

where

κ is the conductivity of the electrolyte (mS/cm)

A_{κ} is the pre-exponential factor

T is the absolute temperature (K)

Ea_{κ} is the apparent activation energy (J/mol)

R is the gas constant (J/(K.mol))

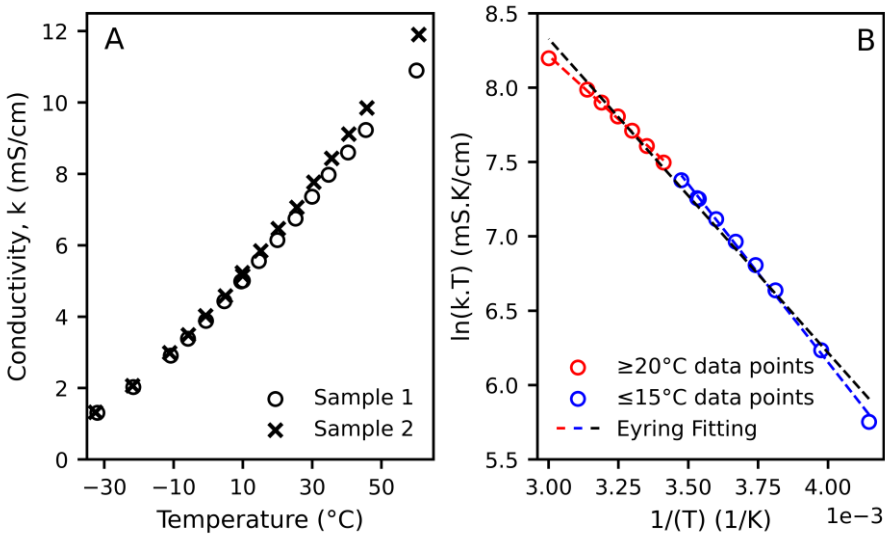


Figure 90. (A) Conductivity of the electrolyte samples expressed in mS/cm in function of the temperature of the test in °C; (B) the logarithm of the conductivity (of sample 1) times the temperature in function of the inverse of the temperature (here in K). The black dashed lines represents the general linear fitting of the data, while the red and blue dashed lines fit the points above 20 °C and below 15 °C respectively.

Results of Figure 90 (A) suggest that the spread in the ionic conductivity values between the two samples was very tiny for temperature less than 25 °C, with a relative difference smaller than 5.0 %. This value increased starting from 30 °C, and reached a relative difference of 6.3 % at 45 °C, and 8.5 % at 60 °C.

For modeling purposes, this should be kept in mind. A single ionic conductivity value can represent the global electrolyte around 25 °C or less. However, this approach seems to be less acceptable for higher temperatures, especially at 60 °C.

Results of Figure 90 (B) suggest that a general fitting (black dashed line) of the data describes poorly the behavior of the conductivity for the entire range of temperatures ($Ea_{\kappa} = 17.56 \text{ kJ}/(\text{mol.K})$). As illustrated, temperatures above or equal to 20 °C follow a common trend ($Ea_{\kappa} = 14.22 \text{ kJ}/(\text{mol.K})$), and temperatures strictly below 20 °C tend to follow a different trend ($Ea_{\kappa} = 19.91 \text{ kJ}/(\text{mol.K})$).

In the framework of this work, the choice of activation energy was then adapted to the application. The desired temperatures are 25 and 45 °C, so the activation energy of the temperatures above 20 °C was chosen. The values from Sample 1 (Figure 90 (B)) and Sample 2 were average to lead an activation energy value of $Ea_{\kappa} = 14.56 \text{ kJ}/(\text{mol.K})$.

The conductivity of the electrolyte does not only vary with temperature, but also with the concentration of Lithium ions. Ecker et al. [213] measured this variation and showed that it follows a very similar trend for different temperatures. Ecker et al. worked on an EC-EMC mixture with 1M LiPF₆ electrolyte, and it is assumed that the electrolyte of this cell follows the same trend.

Equation (51) adapts the relation obtained by Ecker et al.. The idea is to multiply the entire equation by the ratio of conductivity obtained at 25 °C in Figure 90 (A) (6.90 mS/cm) to the conductivity obtained by Ecker et al. (9.60 mS/cm) at this same temperature. The whole is coupled to the Eyring equation to yield relation between the conductivity, the concentration of ions and the temperature.

$$\kappa = \left(\frac{6.90}{9.60}\right) \times (1.73 + 17.92 c_2 - 12.98 c_2^2 + 2.667 * c_2^3) \times \left(\frac{298.15}{T}\right) \quad (51)$$

$$\times \exp\left(\left(-\frac{14560}{8.314}\right) \times \left(\frac{1}{T} - \frac{1}{298.15}\right)\right)$$

Diffusion coefficient (D_2). The salt diffusion of the ions ($D_2 \text{ (m}^2/\text{s)}$) in the electrolyte is assumed using the Einstein law [213], described in equation (52).

$$D_2 = \frac{\kappa \times k_B \times T}{e \times N_A \times c_2^0} \quad (52)$$

where

κ is the conductivity of the electrolyte (mS/cm)

k_B is the Boltzmann constant (J/K)

T is the absolute temperature (K)

e is the elementary charge (C)

N_A is the Avogadro's number (1/mol)

c_2^0 is the reference lithium concentration in the electrolyte (mol/m³)

This law was designed for dilute solutions, so its utilization in this case, where the concentrated solution is assumed, is only an approximation. It was found in literature that this approximation can still be valid enough in the case of electrolytes similar to the actual one [213]. In this case, it holds the value of $1.84 \times 10^{-10} \text{ m}^2/\text{s}$ at 25 °C, and $2.36 \times 10^{-10} \text{ m}^2/\text{s}$ at 45 °C.

Transference number (t_+^0) and molar activity coefficient (f_{\pm}). The transference number was assumed to have the same value (0.363) of the electrolyte EC:EMC:DMC 1:1:1 with 1M LiPF₆, and the mean molar activity coefficient of the electrolyte was assumed to be nil [120].

2.5.3 Separator related parameters

Thickness (l_s). During the dismantling procedure, the separator was recovered and samples were taken for characterization. The thickness of the separator was measured using a digital micrometer. 20 samples were taken from different position of the separator and the obtained average value was $20.75 \mu\text{m} \pm 0.19 \mu\text{m}$.

Porosity (ϵ_s). Its porosity was measured using He pycnometry (AccuPyc II 1340). Six separator sheets of known dimensions ($50 \times 2.5 \times 0.0021 \text{ cm}$) were inserted into the testing chamber of the pycnometer. The measured, or skeletal, volume is then 1.575 cm^3 , and its mass was 0,83 g. In a nutshell, the He pycnometry procedure consists of measuring the difference between the volume of the gas in an empty chamber and its volume when the chamber is filled with the separator. This yield the volume of He that is present within the separator, also known as the effective volume. The porosity is then calculated using equation (53).

$$\epsilon_s = 1 - \frac{d^{eff}}{d} = 1 - \frac{V}{V_{eff}} \quad (53)$$

where

ϵ_s is the porosity of the separator

d is the density of the separator

d_{eff} is its effective density

V is the volume of the separator

V_{eff} is its effective volume

50 filling cycles were enough for the stabilization of the value, and the porosity was calculated to be 0.434 %.

Effective ionic conductivity (κ^{eff}) and MacMullin number (N_{Mu}). To measure the effective conductivity, a very similar approach to the one mentioned in the electrolyte section was used. EIS measurement were done similarly, but with a larger temperature increment. The coin cell setup resembled much to the setup of Figure 89, but the spacer was replaced with a separator sample of adequate diameter.

The MacMullin number concept is introduced hereunder as the ratio of the electrolyte conductivity to the effective conductivity.

$$N_{Mu} = \frac{\kappa}{\kappa^{eff}} \quad (54)$$

where

N_{Mu} is the MacMullin number

κ is the ionic conductivity of the electrolyte

κ^{eff} is its effective conductivity

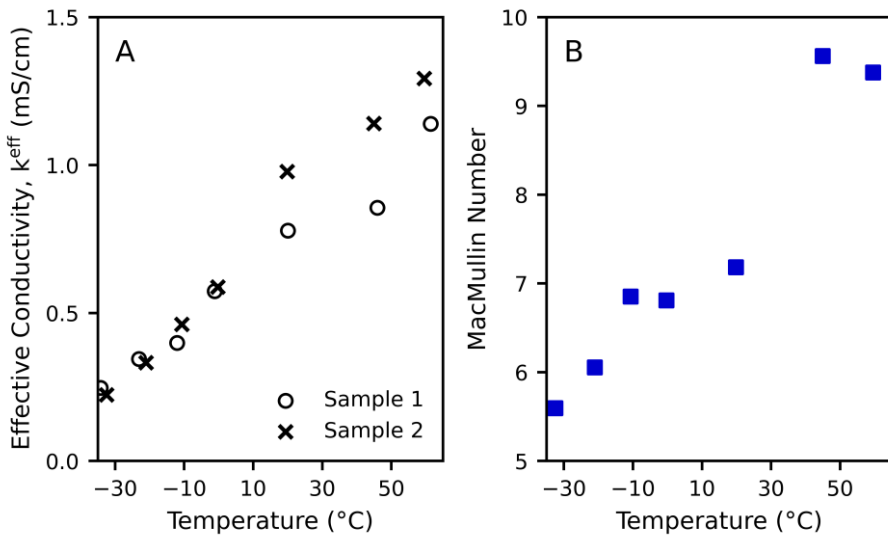


Figure 91. (A) Effective conductivity measured at temperatures ranging from -30 to 60 $^{\circ}$ C; (B) The MacMullin number obtained by dividing the average conductivity of the two electrolytes samples by the average effective conductivity

Figure 91 (A) illustrates the effective conductivity in function of the temperature. It can be seen that at temperatures below 0 $^{\circ}$ C, the spread in values was very narrow, similarly to the bulk conductivity (Figure 90 (A)). Above the 20 $^{\circ}$ C mark, values showed a relatively wide spread.

For simplicity purposes, the values were averaged, and they were divided by the average values obtained from the bulk conductivity (Figure 90 (A)) to obtain the MacMullin number, illustrated in Figure 91 (B) in function of the temperature.

The MacMullin number increased with temperature. In other words, the difference between the bulk conductivity and the effective one increases with temperature. The ratio seems to be stable between -10 and 30 °C, with a value of 6.95, and increases up to 9.47 between 45 and 60 °C.

2.5.4 Electrodes related parameters

Nature of the electrode and particle diameter. The data sheet of the cells mentioned that the PE is made of Lithium Nickel Manganese Cobalt, and the NE is made of Graphite. In order to have a more detailed vision on these active materials, SEM-EDX analyses were done. It was concluded that the NE active material was made of graphite, coated with alumina ceramics (Al_2O_3). Such coating is used for a better cycling stability and an improved safety [322]. To visualize the graphite particles, a very soft and careful scrapping was applied with ceramic tools. The particle size was found to be between 2 and 10 μm .

The PE active material was mostly made of NMC 111. Its particle size was found to be between 10 and 20 μm . A minor amount of NCA was also found in the electrode. It was shown that the addition of NCA can help in increasing the energy density of the material [323].

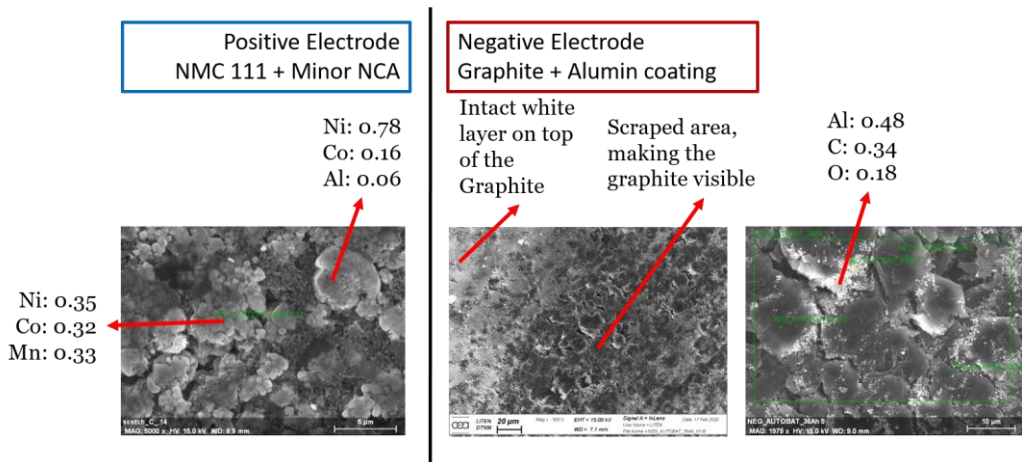


Figure 92. SEM images of the active material of both electrodes, and EDX point analysis identified by the red arrow

Fraction of active material (ϵ). In order to identify the fraction of active material, half-cell experiments were undergone using the same methodology explained in chapter 6 part 5.1.3. As the NCA was found in a very minor fraction, and the only mentioned chemistry in the data sheet was NMC, NMC 111 will only be considered. The theoretical capacity of NMC 111 is 278 mAh/g, and its designed to

operate within a stoichiometry range of 0.4 to 1. If the stoichiometry of lithium goes below 0.4, the material becomes unstable [324], [325]. This means that the theoretical “achievable” capacity is 167 mAh/g. Experimentally, the capacity obtained (by averaging a C/10 CC-CV charge and a C/10 CC discharge as explained in chapter 6 part 5.1.3) was 157 mAh/g, indicating that the mass fraction of NMC 111 is 0.94.

The graphite “achievable” capacity is found in literature to be 330 mAh/g [326], and the measured capacity was 316 mAh/g; The mass fraction of the graphite is then 0.96.

Porosity (ϵ). The porosity of the material is another crucial parameter for the model. Unfortunately, it is couldn't be done using He pycnometry. The following method, based on the differences in theoretical and practical density, is used.

First, it is assumed that the remaining 4 % constituting the negative electrode is made of a commonly used binder, the SBR. The density of the SBR is 940 kg/m³ [327] and the one of the graphite is 2,270 kg/m³ [328], which adds up then a total density of 2,145 kg/m³. The practical density of the active material is measured and gives 1,441 kg/m³. Plugging in those values in equation (55) yields a porosity value of 32.82 %.

$$\epsilon = \frac{\rho_{practical}}{\rho_{theoretical}} \quad (55)$$

where

ϵ is the porosity of the desired electrode material

$\rho_{practical}$ is the practical density of the material

$\rho_{theoretical}$ is the theoretical density of the material

The same procedure is repeated for the positive electrode material. It is considered then that the remaining 6 % of the electrode material is equally distributed between two common binders the C65 (1,600 kg/m³ [329]) and the PVDF (1,780 kg/m³ [330]). Considering an NMC111 density of 4,770 kg/m³ [331], the obtained porosity is 25.03 %.

OCV. As explained earlier, the validation is done on a charging profile. Therefore, for consistency reasons, the OCV vs SOL profile of the lithiation of the graphite and the delithiation of the NMC is included in the model. It was shown in [332] that a significant hysteresis between the lithiation and delithiation OCV profiles is found, and for this reason the average between the two profiles isn't considered here.

The chosen method for identification of the OCV vs SOL is the so called “pseudo-OCV” method [332]. In other words, a C/20 current is applied to either de-lithiate or lithiate totally the material (extra details about the current values are given in Chapter 6). Such applied current is low enough to consider a quasi-steady-state,

hence including the term “pseudo”. The pseudo-OCV method guarantees a clear identification of the phases transition in the material.

The other commonly chosen method is the Galvanostatic Intermittent Titration Technique (GITT). It consists of applying a C/10 current to lithiate or de-lithiate the material for a certain capacity increment (e.g. 5 % of the material capacity), followed by a long relaxation, usually 4 hours. Next, the obtained potential is then labeled as the OCV of the material at a certain lithiation level.

The test duration, which can take more than 2 weeks, is the first drawback of the GITT method. The second is its incapability of retracing accurately the phases transition, hence, not suitable for ICA validation [332]. For a clearer comparison of the two methods, the reader is invited to refer to Chen et al. [332].

The OCV-curves obtained from C/20 sollicitation are illustrated in in Figure 93, along with the SOL values calculated from the EBD tool (obtained in Chapter 6 at BOL).

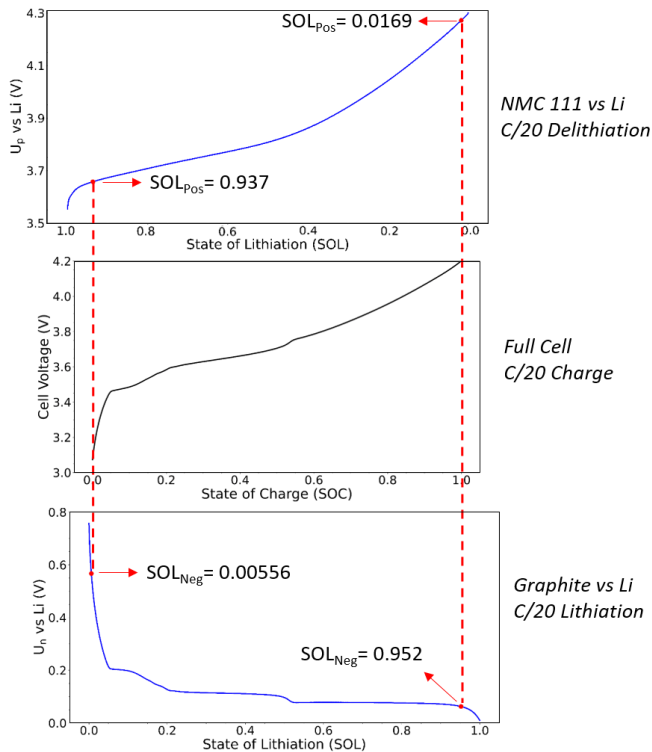


Figure 93. Cell-balancing issued from the EBD tool, showing the pseudo-OCV of the NMC and Graphite as well as the C/20 charging profile of the full cell

Tortuosity. By definition, the tortuosity is the ratio of the transport path distance in a porous medium, to the distance of a straight path [333]. It plays a crucial role in the charge and mass transport, and impacts mainly the resistance of the cell. In

other words, the higher the tortuosity, the higher the resistance. Its impact is mainly visualized at elevated current rates.

Numerous methods are found in literature to measure the tortuosity of the electrode material [333]–[337]. The chosen one is based on the works of Landesfeind [333], [337], who validated the methodology experimentally with 3D tomography for NMC and graphite based electrodes.

The methodology is based on an Electrochemical Impedance Spectroscopy (EIS) done on a symmetrical cell configuration with a blocking condition at the electrode surface. Such condition prevents the insertion of mobile ions, making it possible to study solely the pore phase.

The main assumption taken here is that the electronic resistance of the electrode is negligible, and the ionic transport in the electrolyte can be presented correctly by a transmission line model (TLM). The electrode tortuosity can then be determined by extracting the ionic resistance (R_{ion}) from the impedance spectrum [333], [337].

This methodology was applied for the PE. Unfortunately, the experiments couldn't be done on the NE due to material availability constraints. Its tortuosity is then estimated using the Bruggmann equation as shown in [338].

Imposing a blocking condition was achieved here by intercalating to the most the PE. Other methods require using a non-intercalating electrolyte [336].

Intercalating the PE to the most was made possible with the following protocol (illustrated in Figure 94). The PE was inserted in a half-cell setup, which was discharged to 2.5 V at C/10, with a floating condition, and then discharged again at C/50 till 2.3 V with the same floating condition (cutoff current at C/100) (Figure 94).

The next step was to build a coin-cell step with two fully-lithiated PE. This of course required to open up the half-cells, and retrieve the lithiated electrodes. A galvanostatic EIS experiment is then carried out with a frequency scan between 10 mHz and 200 kHz., with a current amplitude of 8 mA.

The used electrolyte was the one synthesized similarly to the full cell electrolyte composition. The process is illustrated in Figure 94. The tortuosity is measured using equation (56).

$$\tau_p = \frac{R_{ion} A \kappa \epsilon}{2d} \quad (56)$$

where

τ_p is the tortuosity of the PE

R_{ion} is ionic resistance (Ohm)

A is the surface area of the electrode (cm²)

κ is the electrolyte conductivity (S/cm)

ϵ is the porosity of the electrode

d is the thickness of the electrode (cm)

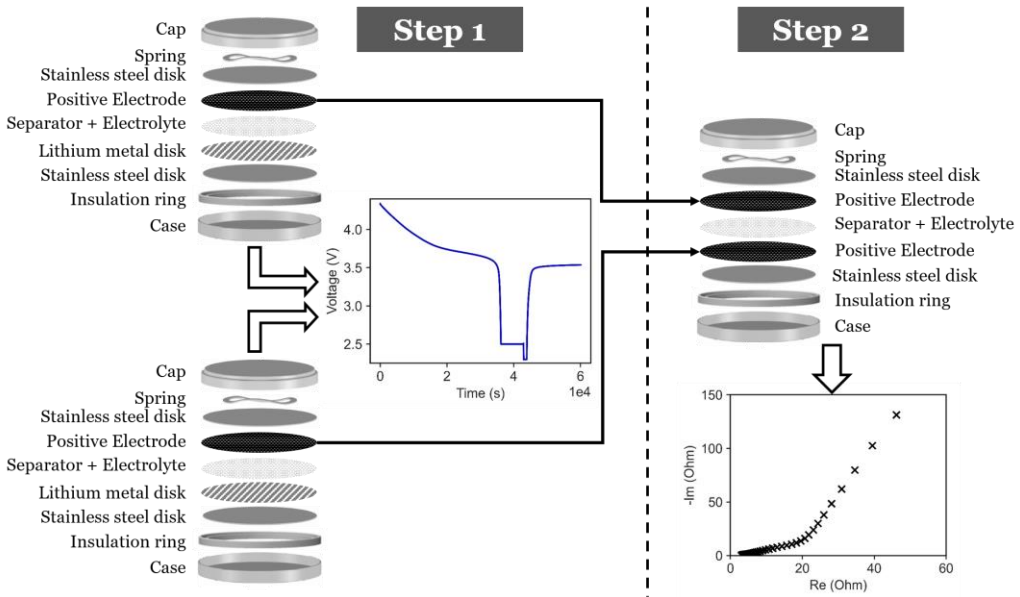


Figure 94. Tortuosity measurement experimental process

Here the conductivity is taken from part 2.5.2, for the temperatures in question ($\kappa=2.94\text{ mS/cm}$ at $T=-10^\circ\text{C}$ and $\kappa=2.05\text{ mS/cm}$ at $T=-20^\circ\text{C}$). R_{ion} is extracted from the Nyquist EIS spectrum via the low and high frequency linear extrapolation. The intersection of the extrapolations with the horizontal axis yields their respective resistances (high frequency resistance, R_{HF} ; low frequency resistance, R_{LF}). R_{ion} is then obtained using equation (57).

$$R_{LF} = \frac{R_{ion}}{3} + R_{HF} \quad (57)$$

It is then important to obtain a clear distinction between the high and low frequency phases. It was shown that a low temperature experiment ensures a clear distinction of both phases [334]. For this reason the measurement was done at -10 and -20°C . It should be noted that the tortuosity is independent of the testing temperature.

Figure 95 illustrates the obtained results. The tortuosity was then calculated showing values of 4.81 and 5.23 at -10°C and -20°C respectively, with a spread of 4.18%. The average of these two values is then chosen for the P2D modeling.

Diffusion of Li-ion through the active material. This is considered as one of the most important parameters in the P2D model [120], [213]. The method used is detailed exhaustively in the following publications [213], [339]–[341]. It consists of exciting the battery, set at equilibrium at a certain SOC, with a small and short constant current pulse (GITT). This induces the voltage to drop abruptly in the first milliseconds (IR drop), before following its evolution. It is assumed that the IR drop acts only as a constant that shifts the voltage value, but does not alter its evolution.

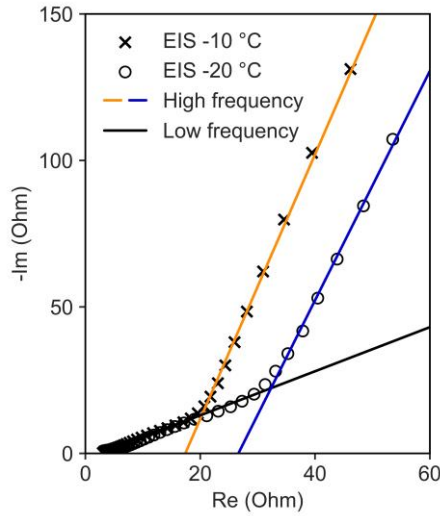


Figure 95. Electrochemical Impedance Spectroscopy (EIS) carried out on symmetric coin cell

This post-IR-drop voltage shape is considered to be a consequence of the concentration gradient formation in the solid state material. This will then be helpful in measuring the diffusion of Li^+ ions in the active material.

Applying a small current implies that the influence of the reaction kinetics can be neglected, underlining then the impact of diffusion. The diffusion is dependent on the lithiation level of the material. For this reason, the small and short current pulse is made at different stoichiometry levels.

Deducing the diffusion value from this post-IR drop voltage evolution is based on the short-time analysis explained by Wen et al. [339]. In this method, the concentration of the Li^+ ions at the electrolyte-electrode interface, which is hardly measured, is not needed. The derivation of the formula (equation (58)) is rather based on the stoichiometry values. In other terms, all the parameters needed are either known or experimentally measured, explaining the reason behind this choice.

$$D_1 = \frac{4r^2}{\pi t} \cdot \left(\frac{\Delta E_s}{\Delta E_t} \right)^2 \quad (58)$$

where

D_1 is the diffusion of the Li^+ ions in the active material

r is the particle radius

ΔE_s is change in the equilibrium voltage after the current pulse

ΔE_t is total change in voltage during the current solicitation minus the IR drop

Half-cell experiments were done using the same methodology explained in chapter 6 part 5.1.3, to undergo GITT experiments. The goal is to calculate the diffusion at different lithiation levels. For this reason, a current pulse of $C/10$ for 12 min followed

by a break of 4 hours, were applied to the coin cells through its entire voltage range. This ensures a diffusion value for each 2 % of SOL. A discharge current is applied for the graphite half-cell (lithiation of graphite) and a charge current is applied for the NMC half-cell (delithiation of NMC), to simulate a charging set up.

Figure 96 illustrated the diffusion value in function of the lithiation level. In the same graphs, literature results, obtained for similar material (Graphite and NMC 111) were plotted and compared to the actual case. They were extracted using the LiionDB tool [342].

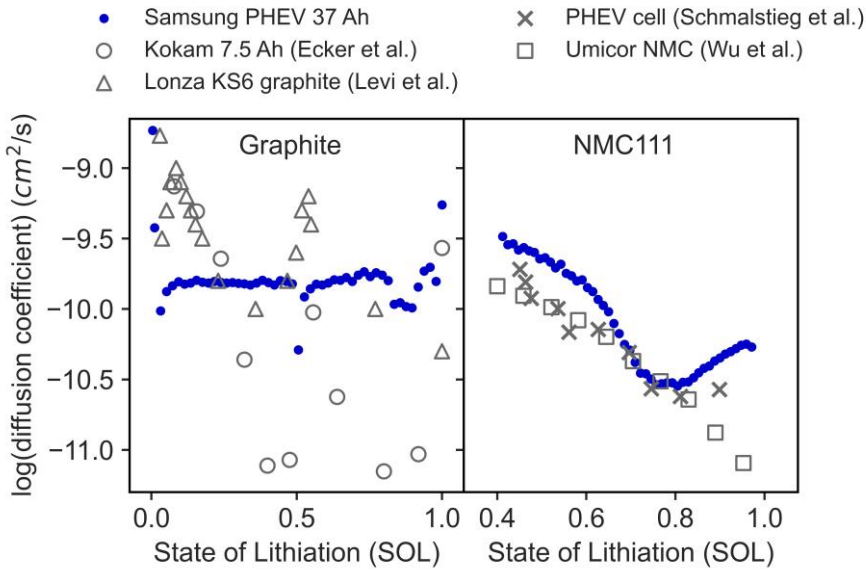


Figure 96. Logarithm of the diffusion coefficient of Li^+ ions versus the SOL of Graphite (left graph) and NMC111 (right graph). Extracted from: Ecker et al. [213], Levi et al. [343], Schmalstieg et al. [344] and Wu et al. [345]

The graphite diffusion values share in general the same shape in function of the material's SOL, and fluctuates within the same order of magnitude. The diffusion inside the Samsung's graphite seems to reach stability directly after the first points, unlike the other cases. The NMC 111 diffusion shared not only similar shapes but also very similar values, within a tiny range. The Samsung NMC 111 started with a tiny higher value though, and increased above an SOL of 0.8. This seems to follow the same trend of Schmalstieg et al. [344] who used PHEV cell material. Further analyses are needed to understand this last increase.

Exchange current density (i_0). Unfortunately, this parameter couldn't be obtained experimentally. It was adjusted to fit the 152 W charging voltage curve (Figure 99). The NMC111 exchange current density ($i_{0,p}$) was found to be 5.95 A/m^2 , and the Graphite ($i_{0,n}$) exchange current density was found to be 5.6 A/m^2 . This lie in the range of the results obtained experimentally in [346].

2.5.5 Parameters assessment

The entire parameters of the P2D model are listed in Table 18. Temperature dependent parameters are given at 25 °C. 73 % of the parameters were measured (Figure 97).

Table 18. Newman P2D model parameters for the Samsung 37 Ah SPHEV. The “Method” column labels the method used to evaluate the parameter: M = Measured, A = Assumed, L = Literature, Ad = Adjusted

Domain	Parameter	Symbol	Value	Method
Electrolyte	Conductivity	κ	6.90 mS/cm	M
	Apparent activation energy	Ea_{κ}	14.56	M
	Salt diffusivity	D_2	1.84×10^{-10} m ² /s	M
	Transference number	t_+^0	0.363	L [120]
	Activity coefficient	f_{\pm}	0	L [120]
	Reference lithium concentration	c_2^0	1 M	A
Separator	Porosity	ϵ_s	43.4 %	M
	Thickness	l_s	20.75 μ m	M
	Effective conductivity	κ^{eff}	0.99 mS/cm	M
	MacMullin number	N_{Mu}	6.95	M
Electrode	Thickness of active material	l_p	57 μ m	M
		l_n	59 μ m	M
	Surface	A_p	1.74 m ²	M
		A_n	1.58 m ²	M
	Porosity	ϵ_p	25.03 %	M
		ϵ_n	32.82 %	M
	Loading (per side)	Ld_p	18.2 mg/cm ²	M
		Ld_n	8.5 mg/cm ²	M
	Electronic conductivity	σ_p	0.17 S/m	L [347]
		σ_n	100 S/m	L [348]
Tortuosity	τ_p	5.02	M	
	τ_n	1.75	A	
Active material	Fraction of active material in the electrode	ϵ_p	94 %	M
		ϵ_n	96 %	M
	Diffusion coefficient in the active material	$D_{1,p}$	Figure 96	M
		$D_{1,n}$		M
	Exchange current density	$i_{0,p}$	5.95 A/m ²	Ad
		$i_{0,n}$	5.6 A/m ²	Ad
	Particle diameter	d_p	15 μ m	M
d_n		6 μ m	M	

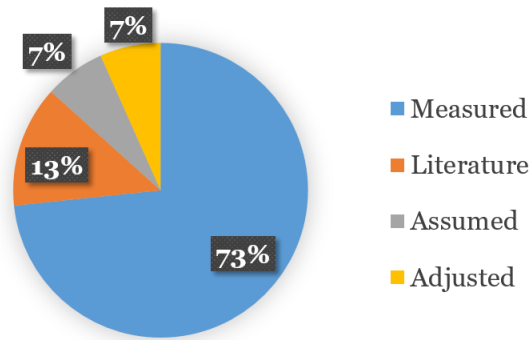


Figure 97. Parameters identification methods shares

3. Model validation

The first validation strategy requires comparing the model outcome of a C/20 charge with the experimental observations. To do so the two outcomes are plotted alongside each other in Figure 98 (A). The voltage absolute error is plotted in function of the capacity in Figure 98 (A'). The IC was derived for both the experimental and the model outcomes, and illustrated in Figure 98 (B). Finally the error sticks are drawn in Figure 98 (B'). The length of the sticks represents the relative difference between the peaks' intensities, and the width of the sticks represents the difference between the peaks' positions.

The comparison suggests that the model outcome is validated by the experimental observation. The voltage error is in general very close to 0, except for the very first start of the charge. The experimental capacity is 40.25 Ah, while the predicted capacity is 40.67 Ah, yielding an error of 1.04 %. The incremental capacity comparison shows a very tiny positional error. The peak at 3.77 V has an error of 8 mV, while the peak at 3.64 V shows a 9.8 mV error. The intensity error of the peaks seems to be in general less than 10 %, except for the peak and valley around 3.75 V (15.1 % and 14.9 % respectively). It was shown in Figure 44 of chapter 5 that these peak and valley vary significantly from a cell to another at BOL (13.4 % and 8.74 % respectively), which explains the discrepancy found here.

The second validation requires comparing the model outcome of real life charging scenarios. In Figure 99, the left panel represents the 65 W charging and the right panel represents the 152 W charging. The middle graph illustrates the voltage response, the lower graph illustrates the current and the upper one shows the voltage error, all with respect to the capacity.

For real life power charging technics, the model is able to describe accurately the experimental results, while maintaining an overall voltage error inferior to 1 %. In the very first stages of charging, the voltage error elevates up to 5 % for the 152 W charging. This points out at the limitation region of the model, where the hypotheses previously elaborated might not be valid.

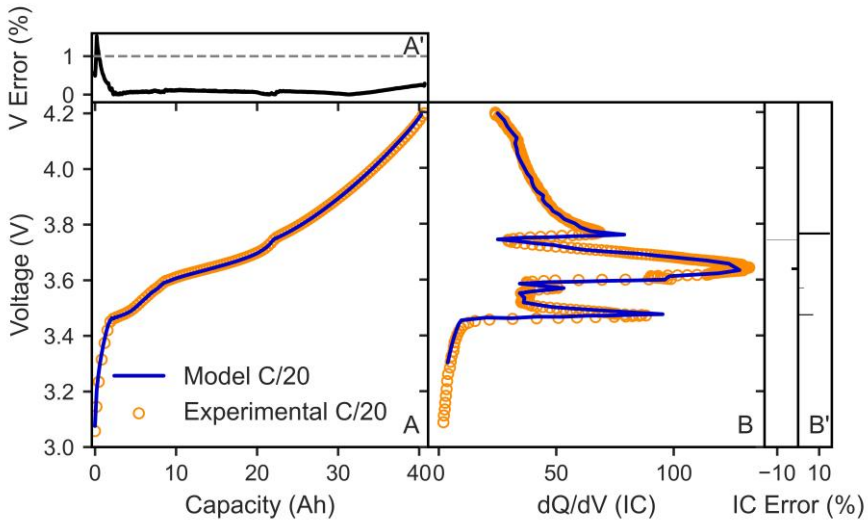


Figure 98. (A) Experimental C/20 galvanostatic charge curve (orange circles) along with the simulated results (blue line); (A') Experimental vs simulation voltage absolute error; (B) IC curve of the experimental C/20 charge along with the IC curve outcome of the simulation; (B') Experimental vs simulation IC peaks error.

This, however, isn't judged to be very alarming. It was shown in chapter 3 that the lower 20 % SOC margin (here below 8 Ah) are usually not reached during a PHEV operation.

For the 65 W charging, the predicted capacity is 39.3 Ah (vs 38.8 Ah, hence a capacity error of 1.3 %). For the 152 W charging, the predicted capacity is 38.0 Ah (vs 38.2 Ah, hence a capacity error of 0.5 %).

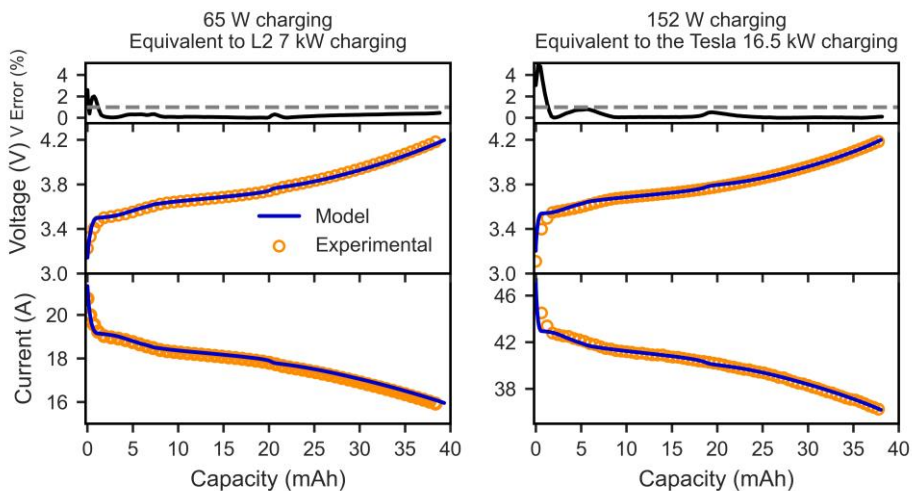


Figure 99. Power charging predictions from the P2D model compared to the experimental observations

4. Aging modeling

The Newman P2D performance model of the cell was developed and validated in the previous sections. The purpose of this one is to complement the model by aging mechanisms. These are interpreted as behavioral laws describing the evolution of some specific parameters, based on the conclusions made in chapter 6. The goal is to develop a “global model” that describes accurately the evolution of the performance criteria of the cell with time, depending on the aging conditions.

The following conditions are focused on, for the two temperatures (25 and 45 °C):

- Calendar aging at SOC 90 % without checkups (CU), depicted as Calendar SOC 90 no CU
- Calendar aging at SOC 90 % with checkups (CU), depicted as Calendar SOC 90 with CU
- Calendar aging at SOC 90 % + Short Trips + Long Trips (Urban scenario), depicted as Cal + ST + LT (U)
- Calendar aging at SOC 90 % + Short Trips + Long Trips (Highway scenario), depicted as Cal + ST + LT (H)

4.1 General principles and hypotheses

It was shown in chapter 6, that the LLI was always present during the mentioned aging scenarios. The lowest LLI level was found for the Calendar SOC 90 no CU condition. It was concluded that checkups originated some Li-deposition on the NE (negative electrode), which created additional surface for the formation and growth of a fresh SEI, inducing hence a higher LLI.

Cal + ST + LT scenarios showed a greater LLI too. ST and LT were the origin behind the cracking of the SEI layer [38]. This led to the creation of a new exchange surface, and therefore a creation of a secondary SEI layer, which grew at a relatively high rate, due to the Cal time at SOC 90 %.

The LAM_{pe} happened as often as the LLI. The positive electrode (PE), made out of NMC 111, is found to be unstable at high voltages. Therefore the Cal time of every scenario originated an LAM_{pe} . It was also found to increase slightly when the LLI intensified. A higher LLI on the NE induced higher potential values for the PE, hence, a faster PE decay.

Finally, LAM_{ne} was found out to occur at 45 °C. At calendar conditions it might have originated probably by the formation of gas bubbles, hence eclipsing its activity. For the Cal+ ST + LT (H) condition, post-mortem showed a decrease in the NE capacity.

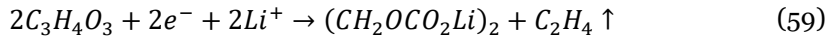
Thus, the dominant aging mechanism identified was the SEI layer. When checkups and cycling were added, other mechanisms happened, and lead to an increase of the exchange surface, hence a higher growth rate. The LAM_{pe} occurred too as often, and the LAM_{ne} happened mainly at 45 °C.

One hypothesis can then be drawn from this statement: the LLI was solely due to the SEI layer growth, which is the first aging model to be added. The active material surface of exchange was only fixed for the conditions that did not undergo checkups, and varied for the others. Modeling then the surface increase is another layer to be added. Finally, the LAM_{pe} and LAM_{ne} models can be included in an empirical fashion, deduced from the experimental data. They are assumed to evolve independently from the SEI.

4.2 The principals of the SEI model

The SEI model described in this subsection was elaborated many times in literature [13], [113], [120], [349], [350]. It involves the reaction between the EC of the electrolyte, and the lithium ions at the NE-SEI interface. It can be divided into three main steps:

1. Diffusion of the EC through the SEI layer
2. Decomposition of the EC at the graphite particle surface illustrated in equation (59) by [351]



3. SEI growth

Equation (59) is assumed to be the rate-determining step of this process. It yields a solid precipitation of ethylene dicarbonate (EDC) radical, associated to two Li-ions, to give the main component (assumed) of the SEI layer growth (Li_2EDC) [352].

This process takes into consideration that the SEI grows from the electrode-SEI interface, and it is strongly refuted by numerous experimental publications [38], [353], [354]. It was deduced experimentally that the SEI grows from the SEI-electrolyte interface, starting probably with an electron diffusion across the SEI layer. However, it was found that the previously described process models accurately enough the aging behavior of Li-ion batteries [120], [355].

The first step of the process, the diffusion of EC through the SEI layer, is modeled by the EC mass balance across the SEI film, given by equation (60) [113]:

$$\frac{\partial c_{EC}}{\partial t} = D_{EC} \frac{\partial^2 c_{EC}}{\partial r^2} - v \frac{\partial c_{EC}}{\partial r} \quad (60)$$

where

c_{EC} is the concentration of EC (mol/m³)

D_{EC} is the EC diffusion coefficient inside the SEI layer (m²/s)

v is SEI growth velocity (m/s)

Here, at the particle/SEI interface, $\partial c_{EC}/\partial t$ is set equal to the reaction rate of the SEI reaction (i_{SEI}/F) (equation (61)). At the SEI/electrolyte interphase, the concentration of EC is set equal to the electrolyte bulk concentration of EC (c_{EC}^0).

The kinetics of the second step, the decomposition of the EC to yield the Li_2EDC , is described by a Tafel equation.

$$i_{SEI} = -Fk_{0,SEI}c_{EC} \exp\left[-\frac{\alpha_{SEI}F}{RT}(\phi_1 - R_{SEI}i_t)\right] \quad (61)$$

where

i_{SEI} is current density of the SEI reaction (A/m²)

$k_{0,SEI}$ is the rate constant of the SEI reaction (m/s)

α_{SEI} is the symmetry factor of the SEI reaction

R_{SEI} is SEI ionic resistance ($\Omega \cdot m^2$)

i_t is total current density (A/m²)

The SEI resistance R_{SEI} is equal to the ratio of the SEI thickness to its ionic conductivity κ_{SEI} , assumed to be constant with time. The total current density (i_t), is the sum of the current density of the intercalation (i_n) and the current density of the SEI (i_{SEI}).

The third step, the SEI growth velocity, is described as in equation (62).

$$v = \frac{\partial \delta}{\partial t} = -\frac{i_{SEI} M_{SEI}}{n_e F \rho_{SEI}} \quad (62)$$

Where

v is the growth velocity (m/s)

δ is the layer thickness (m)

n_e is the number of involved electrons

M_{SEI} is the mass balance of the SEI components (kg/mol)

ρ_{SEI} is the density of the SEI component (kg/m³)

Finally, the capacity loss induced by this process is calculated as follows.

$$Q_{SEI} = \frac{V_{SEI} \rho_{SEI} n_e F}{M_{SEI}} \quad (63)$$

where

Q_{SEI} is loss of capacity caused by the SEI (Ah)

V_{SEI} is the SEI volume (m³)

In equation (63), V_{SEI} is given by the following.

$$V_{SEI} = \frac{\epsilon_{Gr} S_{particle}}{V_{particle}} V_{electrode} (1 - \epsilon_n) \int_{t_i}^{t_f} v dt \quad (64)$$

where

ϵ_{Gr} is volume fraction of the graphite

$S_{particle}$ is the particle exchange surface (m²)

$V_{particle}$ is the volume of the particle (m³)

$V_{electrode}$ is the volume of the electrode (m³), as in its surface times its thickness (Table 17)

ϵ_n is the porosity of the NE

t_i and t_f are the initial and final time, respectively, of the aging simulation

4.3 Parameterization and methodology

The methodology is illustrated in Figure 100.

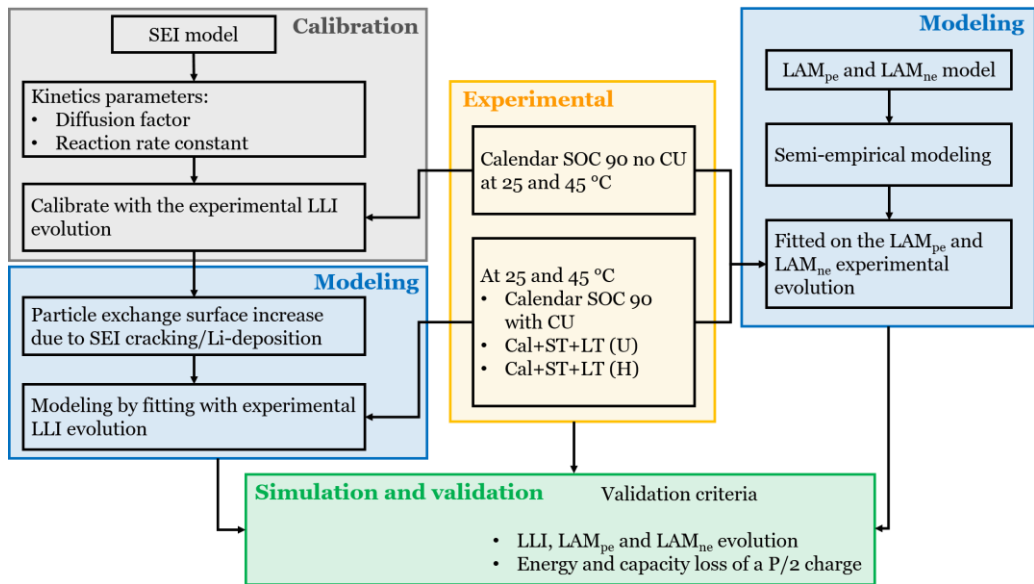


Figure 100. Describing the methodology used for the aging modeling

The SEI model described earlier depends on a series of parameters. While most of them are assumed from literature (Table 19), the kinetics parameters, i.e. the diffusion factor (D_{EC}) and the rate constant of the reaction ($k_{0,SEI}$), are calibrated as follows.

As seen previously, the aging condition that was concluded to undergo SEI growth without any surface change, is the Calendar SOC 90 no CU. It is also assumed that the SEI growth is the only mechanism that lead to LLI. For this reason, D_{EC} and $k_{0,SEI}$ are calibrated using the LLI experimental evolution of these conditions, taken from the results of the EBD tool of chapter 6. The calibration yields a set of parameters for each

of the two temperatures (25 and 45 °C), considered to be specific to the SEI layer of the cell in question, and the same for all the other conditions.

It was assumed that checkups and cycling tend to increase the particle exchange surface (equation (64)). Hence, modeling of the surface increase is done by fitting a linear equation on the LLI evolution of the conditions where checkups and cycling occurred.

Independently of the SEI growth, LAM_{pe} and LAM_{ne} are modeled. Their models are done by fitting semi-empirical equations on the experimental results issued from the EBD tool of chapter 6. Thus, a semi-empirical equation, in function of time, is fitted for each aging condition. The module “curve_fit” of the open source Python software SciPy [216] is used for the fitting.

These equations are included in the Newman P2D performance model to modify of the volume fraction (ε) of the positive (ε_{NMC}) and negative (ε_{Gr}) active materials in function of time and aging condition. For the 25 °C condition, LAM_{ne} did not seem to increase significantly and clearly, so it is assumed to be unaffected.

The validation of the model outcome is done on the basis of the final (end of test) energy and capacity values obtained from a 65 W charge. In other words, a checkup was replicated in the model, similarly to the experimental one, at the end of the simulation.

4.4 Calibration of the SEI model

4.4.1 General parameters

The SEI model elaborated earlier on relies on numerous parameters, listed in Table 19. It is assumed that these parameters are proper for the SEI of the cell in question, hence fixed for all the conditions, and the aging duration.

Table 19. SEI overall parameters, their source and their value

Parameter	Unit	Source	Value
Electrons number of reaction	-	Equation (59)	2
Diffusion coefficient of EC	m ² /s	Calibrated	-
Molar Mass	kg/mol	Equation (59)	0.162
Density	kg/m ³	[352]	1,680
Bulk concentration of EC	mol/m ³	[356]	4,541
Ionic Conductivity	S/m	[120]	5×10 ⁻⁶
Reaction Coefficient	mol/(m ² ·s)	Calibrated	-
Equilibrium potential	V	[357]	0.4
Symmetry Factor	-	[357]	0.5

4.4.2 Kinetics parameters calibration

As mentioned in the methodology section and in Table 19, the kinetics parameters are calibrated on the LLI evolution of the Calendar SOC 90 no CU condition. The results of the calibration are listed in Table 20, and their outcome is illustrated in Figure 101.

Table 20. Kinetics parameters calibrated on the LLI evolution of the Calendar SOC 90 no CU conditions

Parameter	Unit	Temperature	Value
Diffusion coefficient of EC	m ² /s	25 °C	2.8×10^{-22}
		45 °C	2.1×10^{-21}
Reaction Coefficient	mol/(m ² ·s)	25 °C	1×10^{-12}
		45 °C	7×10^{-9}

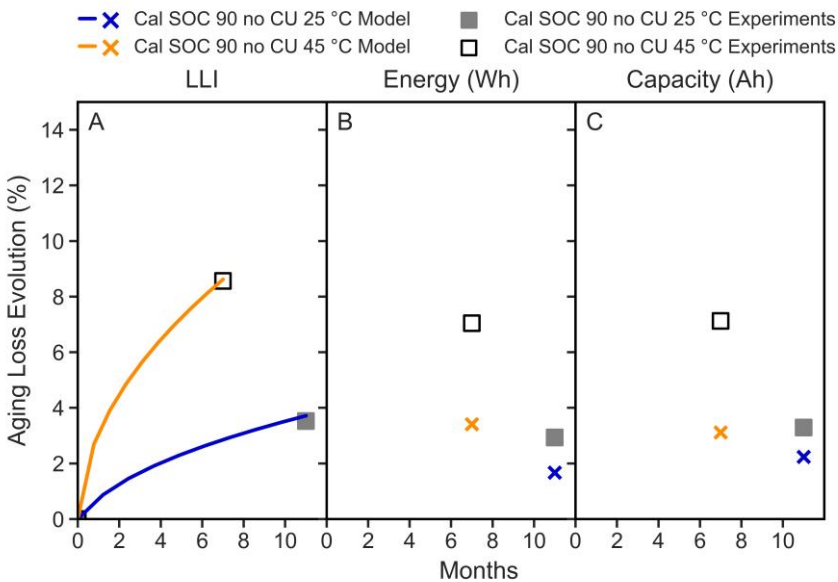


Figure 101. Calibration results of the SEI kinetics parameters on the no CU conditions: (A) the LLI evolution, (B) the energy loss and (C) the capacity loss obtained

With the kinetic parameters calibrated on the LLI evolution, the simulated loss in capacity and energy does not seem to fit with the experimental results. The kinetics parameters represent well the LLI evolution but underestimate the loss in energy/capacity. This is explained by the values obtained in Table 20, which are one to two order of magnitudes lower than literature values [120], [357]. Increasing the

kinetics values of Table 20, might probably make the energy/capacity loss fit the experimental observation, but will then overestimate the LLI.

4.5 LAM_{pe} and LAM_{ne} models

The LAM_{pe} and LAM_{ne} semi-empirical models are listed in the tables below including the fitting equation and the involved parameters.

As no CU conditions comprised only two points (beginning of test and end of test), a simple first order linear equation is chosen. For the other conditions, the LAM_{pe} seemed to evolve in a square root shape with time (chapter 6, Figure 58 and Figure 59), therefore a square root equation was fitted on the experimental data. The R² values were above 0.93 (Table 21).

Table 21. LAM_{pe} semi-empirical equations

Condition	Equation	Parameters	R ²
Calendar SOC 90 no CU 25 °C	$LAM_{pe} = At + B$	A = 6.95×10 ⁻¹⁰ B=0	1.00
Calendar SOC 90 no CU 45 °C		A = 2.56×10 ⁻⁰⁹ B=0	1.00
Calendar SOC 90 with CU 25 °C	$LAM_{pe} = A\sqrt{t}$	A = 3.98×10 ⁻⁰⁶	0.95
Cal + ST + LT (U) 25 °C		A = 6.6×10 ⁻⁰⁶	0.93
Cal + ST + LT (H) 25 °C		A = 7.33×10 ⁻⁰⁶	0.93
Calendar SOC 90 with CU 45 °C		A = 1.16×10 ⁻⁰⁵	0.99
Cal + ST + LT (U) 45 °C		A=1.47×10 ⁻⁰⁵	0.99
Cal + ST + LT (H) 45 °C		A=1.33×10 ⁻⁰⁵	0.98

The LAM_{ne} evolution modeling was trickier than the LAM_{pe} (chapter 6, Figure 58 and Figure 59). Polynomial fitting was used for most of the cases, except the last one, which seemed to follow a square root shape (Table 22). In general, a lower R² value was found when compared to the LAM_{pe}. Additional points are needed to identify a clearer shape for the evolution of the LAM_{ne}.

Table 22. LAM_{ne} semi-empirical equations

Condition	Equation	Parameters	R ²
Calendar SOC 90 no CU 45 °C	$LAM_{ne} = At + B$	A = 3.00×10^{-09} B=0	1.00
Calendar SOC 90 with CU 45 °C	$LAM_{ne} = At^2 + Bt + C$	A = 1.42×10^{-16} B = 1.26×10^{-09} C = 5.62×10^{-03}	0.91
Cal + ST + LT (U) 45 °C	$LAM_{ne} = At^3 + Bt^2 + Ct + D$	A= 1.72×10^{-23} B = 2.17×10^{-16} C = 2.82×10^{-09} D = 1.55×10^{-03}	0.89
Cal + ST + LT (H) 45 °C	$LAM_{ne} = A\sqrt{t}$	A= 4.28×10^{-06}	0.76

The LAM semi-empirical equations are added to the calibrated model of 4.4.2, and the results are illustrated in Figure 102. The estimation of the energy and capacity loss became more accurate when compared to the results of Figure 101.

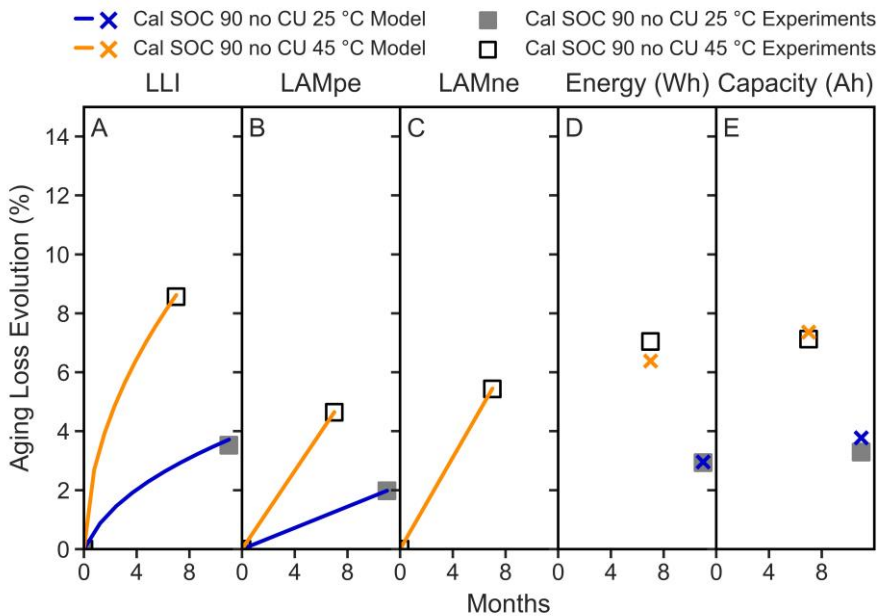


Figure 102. Calibrated SEI model and the LAM_{pe} and LAM_{ne} evolution laws results on the no CU conditions: (A) the LLI evolution, (B) the LAM_{pe} evolution, (C) the LAM_{ne} evolution (D) the energy loss and (E) the capacity loss obtained

4.6 SEI surface increase modeling

In the previous parts, the SEI model was calibrated, and the empirical equations of the LAM_{pe} and LAM_{ne} were parametrized. It was proved (Figure 102) that applying LAM_{pe} and LAM_{ne} evolution to the P2D model with the calibrated SEI helped in predicting more accurately the loss in energy/capacity. In this part, the evolution of the particle exchange surface is the last layer to be added to the model. It is applied to the cells that suffered from cycling (CU, ST and LT).

It is assumed that the surface increases linearly with aging. The rate of increase was fitted to the LLI experimental evolution of each condition (visualized in Figure 103 and Figure 104), and its value for each condition is listed in Table 23.

Table 23. Particle surface increase rate, expressed in percentage per month, listed in function of the aging condition

Condition	Particle exchange surface increase
	%/month
Calendar SOC 90 with CU 25 °C	0.91
Cal + ST + LT (U) 25 °C	8
Cal + ST + LT (H) 25 °C	40
Calendar SOC 90 with CU 45 °C	0.91
Cal + ST + LT (U) 45 °C	8
Cal + ST + LT (H) 45 °C	10

It can be seen that the highest the cycling intensity, the faster the surface increase. The impacts of the CU and the ST + LT (U) on the surface seems to be independent on the temperature value. The Cal + ST + LT (H) at 25 °C showed the highest surface increase rate.

Finally, the Cal + ST + LT (H) at 45 °C showed a smaller increase rate (10 %/month) when compared its 25 °C homologue (40 %/month). As seen in the chapter 5, the Cal + ST + LT (H) at 45 °C couldn't be completed properly due to an increase in the resistance value, reducing the duration of the LT phase. That might be linked to the smaller increase rate in surface found here.

4.7 Validation of the full model

The SEI calibrated model, along with the modeled increase in the particle exchange surface and the LAM evolution laws are added together in the P2D model. Validation is done by comparing the charging energy and capacity values to the experimental results (Figure 103 and Figure 104).

At 25 °C (Figure 103), the comparison suggests that the predictions of the models are confirmed by the experimental observations. The model describes accurately

enough the LLI and LAM_{pe} evolutions, as well as the value of energy and capacity loss at the end of the test with a minor error. However, the shape of the LLI evolution of the Cal + ST + LT (H) condition differs from the model's prediction. Even if the last two experimental points seem to follow the model's trend, the first three points show a brusque increase followed by a stabilization. This might either indicate that the increase in the particle exchange surface followed a nonlinear trend, or that another aging mechanisms was involved here. Some other mechanisms includes the particle micro-cracking, in which SEI grows at a higher rate. The kinetics parameters are here considered to be fixed. If a micro-crack happens, the formation and growth of the SEI might follow different kinetics.

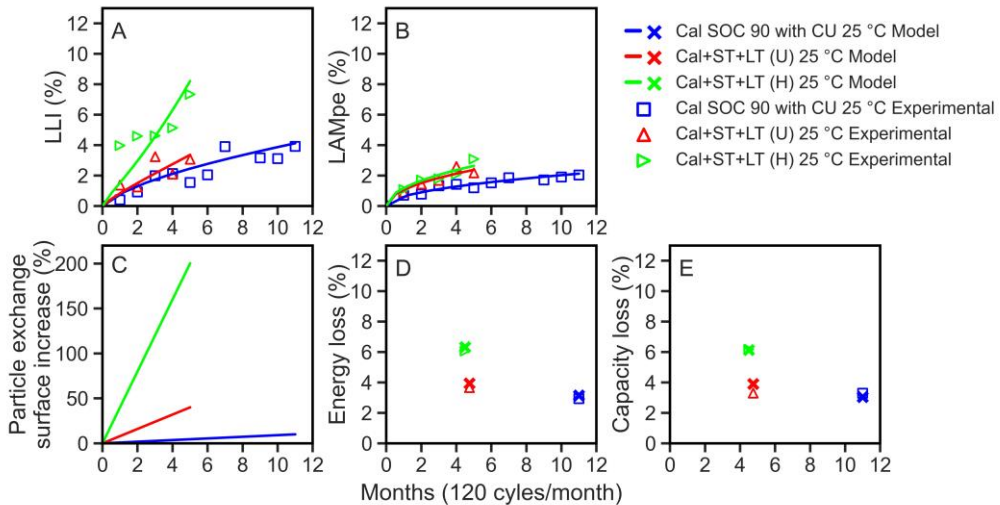


Figure 103. Simulation results when the calibrated SEI model, the LAM_{pe} evolution laws and the modeled increase in the particle exchange surface are added to the P2D model for the 25 °C conditions: (A) the LLI evolution, (B) the LAM_{pe} evolution, (C) the particle exchange surface evolution, (D) the energy loss and (E) the capacity loss obtained at the end of the test

At 45 °C (Figure 104), the model's predictions were not always confirmed by the observations. Starting with the Cal SOC 90 with CU condition, even if the LAM_{pe} , LAM_{ne} , the energy and capacity losses were well predicted, the LLI evolution shape was quite different from what the experiments depicted. Post-mortem analysis concluded that a considerable amount of Li-plating was formed. In this model, it is considered that the Li-plating only adds a certain surface of interaction for the formation of a fresh SEI, and does not alter directly the amount of cyclable lithium, which might be the reason behind this abrupt linear increase in LLI.

Concerning the Cal + ST + LT (U) condition, the model predictions were considered to be good enough, except for the capacity and energy loss values. The model underestimated the capacity and energy loss by about 1 %.

Finally, the Cal + ST + LT (H) condition seemed to be trickier to model. One issue might be due to the underestimation of the LAM_{ne} . Post-mortem analyses showed a NE capacity loss of more than 4 %. Here the EBD tool showed only 2 %. Another issue is related to the reduction of the LT phase due to an increase in internal resistance, when the number of cycles passed the 200 cycles mark. Further improvements should be done to model aging conditions with highway steps.

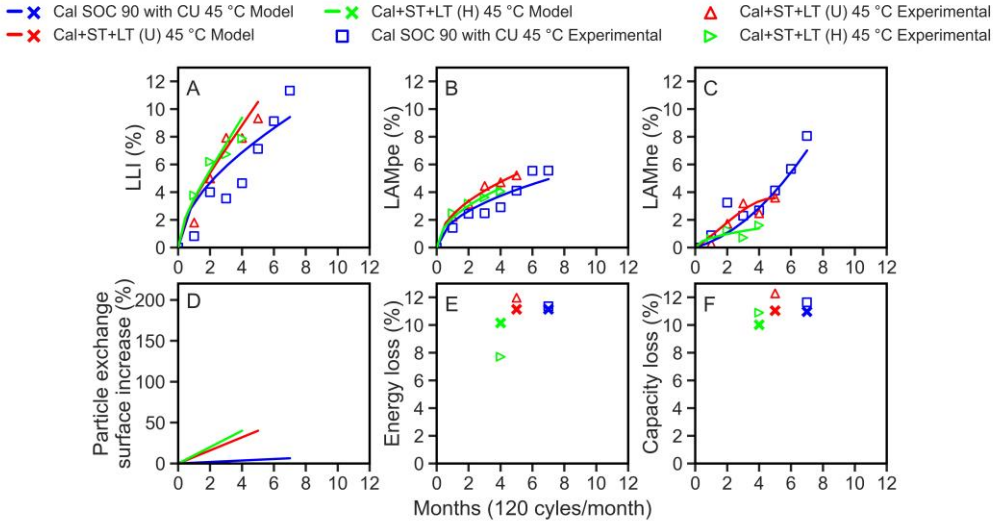


Figure 104. Simulation results when the calibrated SEI model, the LAM_{pe} evolution laws and the modeled increase in the particle exchange surface are added to the P2D model for the 45 °C conditions: (A) the LLI evolution, (B) the LAM_{pe} evolution, (C) the LAM_{ne} evolution, (D) the particle exchange surface evolution, (E) the energy loss and (F) the capacity loss obtained

5. Conclusion and perspectives

In this chapter, a Newman P2D model was developed for a Samsung 37 Ah PHEV cell. 73 % of the model parameters were measured experimentally, and the performance model seemed to describe accurately the behavior of the cell. The validation was done on incremental capacity (IC) curves, and on real life charging applications.

The aging modeling was done using a combined physics-mechanistic approach, in which the “classical” SEI model was coupled to LAM_{pe} and LAM_{ne} evolution laws. The SEI kinetics parameters were calibrated on the LLI experimental evolution, rather than on the capacity evolution. It was shown that the obtained values were lower than the literature results, and that they underestimated the loss in energy/capacity. Empirical LAM_{pe} and LAM_{ne} models were added to the SEI model and improved the model accuracy, showing that the SEI isn’t the only mechanism to impact the loss in energy/capacity.

The particle exchange surface was modeled to vary with aging due to SEI cracks formation, or metallic lithium deposition. Final results suggested that overall, the model described accurately the performance (energy and capacity) evolution of the cells.

Many improvements, though, can be made. Here the LAM_{pe} and LAM_{ne} models were simple semi-empirical equations describing their time evolution laws. More complex physical models can be made, describing more accurately the nature of the LAM (such as particle cracking, Mn dissolution, rock-salt formation etc.).

The particle exchange surface was also a very simple linear equation. Extra work should be done in this direction to try and model more accurately this surface evolution.

The kinetics of the SEI remained fixed throughout the aging duration. When particle micro-cracks occurs and a secondary SEI forms and grows, the kinetics might differ.

Furthermore, post-mortem analysis showed that lithium plating occurred during aging. Its impact here was considered to be a simple increase in the particle exchange surface, however, its contribution to the LLI was ignored. Adding lithium plating layer to the model can improve even more the predictions, especially concerning the impact of the checkups. Models like the one presented in [79] that takes into consideration the increase in the particle exchange surface can be quite interesting.

Chapter 8 – General conclusion and perspectives

As a reminder, the goal of the thesis was to develop a reliable methodology for the durability testing of Li-ion batteries related to their usage, in the purpose of a more accurate prediction of their lifetime. The Literature review of chapter 2 yielded two major conclusions concerning the existing works in the field of battery aging. Firstly, the current methods of accelerated aging lead to erroneous interpretations. Secondly, the cumulative damage approach is questionable. Overall, accelerated aging tests were found to be decorrelated from the real usage of EVs.

The first question asked is: how are the batteries used in real-world applications? An analysis of usage was done in chapter 3 and 4 to clarify the answer. The most critical stress factors encountered by the battery were identified using an RPN analysis, depending on the three types of EVs. The interdependence of these stress factors was underlined, and the major aging mechanisms were spotted. It was concluded that high SOC levels occurs often during the life of BEV and PHEV batteries, due to range anxiety. Temperatures below 10 °C and above 30 °C were found to be very critical during short trips. In general, they lead to an increase in the discharge rate, hence adding a new stress factor on the batteries.

This part yielded an accelerated aging protocol that mimics the stress factors found in usage (chapter 5). The interdependence between calendar and cycle aging was taken into consideration by replicating the most typical usage scenarios in a concentric way: Calendar (parking), Calendar + Short Trips and Calendar + Short Trips + Long Trips. Each phase was identified to have a certain impact on the energy loss. In general, the higher the intensity of the discharge (duration and rate) the higher the loss. Testing the WLTP range of the batteries was found to be a quite revealing and more usage-representative way of evaluating their “health”. This accelerated aging protocol was patented. This chapter answered to the second question: can accelerated aging tests be representative of real world applications.

Following the accelerated aging protocol, the goal was to identify the aging mechanisms that occurred. It was found that the loss of active material at the positive electrode was always present, as the Calendar condition was done at high SOC levels, similarly to the usage. The loss of lithium inventory was seen to increase with the discharge intensity, and that was allocated to the break, repair and growth process of the SEI. The loss of active material at the negative electrode was proved using the SEM technic. The mechanisms behind each phase of the life of the battery were identified.

Finally, a Newman P2D performance and aging model was developed for the cell in question. The performance model was validated using incremental capacity analysis and usage representative charging scenarios. Aging modeling was made by implementing the SEI growth model, a change in the exchange surface area of the SEI (to simulate the fracturing of the surface), and the loss of active material. With this, the expected loss of energy and capacity was validated by the experimental observations for most the cases. Some inaccuracy were found with the highway scenarios where it is expected that some particle fracturing can occur. The aging mechanisms consistency between the 25 °C and 45 °C was refuted.

The state-of-the-art methodology of accelerated aging testing was improved and made more reliable with the help of a usage analysis and a patented aging protocol. The aging mechanisms characterization indicated what are the mechanisms that might have decreased the energy capacity, and modeling these mechanisms was done.

The third and fourth question asked in the beginning were related to the aging mechanisms consistency and the modeling accuracy. This introduces the first perspective of this work. It was concluded that increasing the temperature was not a reliable accelerated factor. However, it was shown that Cal + ST + LT Highway profiles at 25 °C can play the role of a stress factor representative of real usage. Nevertheless, in order to validate the mechanisms' consistency, feedback from real-world aged cells is needed. Ideally, aging mechanisms should be compared between cells aged using this method, and cells aged in real life applications. The world is facing nowadays a huge increase in the sales of EVs, which makes it more feasible to validate the protocols.

In terms of modeling precision, the same can be said. Data from real world aging are being more and more accessible. The model developed here can ideally be applied to real world solicitations and compared.

However, the RPN analysis of chapter 3 (Table 5) needs to be regularly updating itself with these same real-world data. Consequently, accelerated aging protocols need to be regularly adapted to the usage, and aging models need to be constantly readjusted. It was seen that some usage parameters change with time. For example, the technology acceptance and its understanding from the public may vary, and range anxiety can disappear. High SOC could then no longer be critical. Charging infrastructure can improve and fast charging can be more accessible. It could then be considered as a stress factor.

This new paradigm of aging testing elucidates one of the market demands. As mentioned by [44], [130], the standards of battery testing need to be representative of real-world solicitations. The approach elaborated in this thesis can answer this need. It can eventually take the form of a battery testing standard on its own, as it can be applied to all kinds of batteries, not only automotive ones.

Scientific production

M. Haber, O. Raccurt, P. Azais, and S. Genies, “Identification of Li-ion batteries’ stress factors during vehicle’s service lifetime: Assessment and Analysis,” in Advanced Battery Power Conference, 2021 [Online]. Available: <https://battery-power.eu/poster2/533/>

M. Haber and O. Raccurt, “Procédé d’étalonnage d’un modèle d’estimation du vieillissement d’accumulateurs électrochimiques,” deposit number : FR2111401, 2021

M. Haber, P. Azais, S. Genies, and O. Raccurt, “Results and Analysis of a BEV Driving Campaign Comprising Three Types of Daily Uses Categorized by Home-to-Work Distance,” in AABC Europe, 2022 [Online]. Available: <https://www.advancedautobat.com/europe/poster-titles>

M. Haber, S. Genies, P. Azais, A. Martin, M. Chandesris, and O. Raccurt, “Parametrization of a Doyle-Fuller-Newman (DFN) Model for a Commercial 37Ah Li-Ion Battery and Validation with Incremental Capacity Analysis,” in 241st ECS Meeting, 2022 [Online]. Available: <https://ecs.confex.com/ecs/241/meetingapp.cgi/Paper/155496>

M. Haber, P. Azais, S. Genies, and O. Raccurt, “Assessment and Analysis of Li-ion batteries’ stress factors during electric vehicles’ service lifetime” , *Submission process ongoing*

Résumé de la thèse en Français

1. Chapitre 1 – Introduction

Le contexte de décarbonisation du secteur automobile, étant celui dans lequel se situe la thèse, est brièvement exposé dans ce premier chapitre. L'estimation du vieillissement et la durée de vie d'une batterie de véhicule électrique représentent un obstacle économique majeur quant à l'acceptation et le déploiement massif de cette technologie. La compréhension des mécanismes de dégradations d'une batterie lors de son usage est inévitable afin de passer cet obstacle. Cependant, cela demeure un sujet très compliqué et vaste, abondamment étudié dans la littérature.

L'objectif de cette thèse est de développer une méthodologie de prédiction de durée de vie des batteries Li-ion représentative de l'usage automobile, à travers des vieillissements accélérés et de la modélisation.

2. Chapitre 2 – Bibliographie

Ce chapitre a pour but d'investiguer l'état de l'art actuel sur le domaine du vieillissement et des méthodes d'estimation de durée de vie des batteries Li-ion. Cela couvre les différents mécanismes de dégradation des batteries, les méthodes de détections de ces mécanismes, ainsi que les types de vieillissement accéléré et les différents modèles associés.

Les conclusions de cette analyse bibliographique sont énumérées ci-dessous :

- Le type de vieillissement accéléré le plus répandu dans le domaine des batteries est l'« overstress ». Celui-ci consiste à appliquer un certain facteur de stress de façon plus intense à sa valeur en usage normal à la batterie. Il a été montré que cette technique engendre des mécanismes de dégradation différents de ceux observés avec un facteur de stress d'amplitude « normale ». La représentativité de ces vieillissements n'est donc pas validée, et peut expliquer les erreurs de modélisation démontrées dans certaines publications.
- Les vieillissements en cyclage et calendaire, qui engendrent chacun des mécanismes physiques différents, sont testés séparément. Des modèles associés à chacun de ces types de vieillissement sont alors calibrés, et un modèle de vieillissement « global » est constitué par la somme linéaire de ces deux modèles. L'hypothèse sous-jacente est ici de considérer l'impact des deux phases, cyclage et calendaire, comme un simple cumul de dommage. Il a été montré que cette approche n'est pas validée pour de longues durées (>

1 an), et donc devrait être rejetée, car il y a une interdépendance entre les phénomènes et les facteurs de stress entre les phases de calendrier et de cyclage de la batterie qui s'enchaînent de façon cyclique lors de l'usage.

- Les tests de vieillissement accéléré sont décorrélés de l'usage. En d'autres termes, ces tests, qui sont censés représenter les facteurs de stress les plus critiques lors de la vie d'une batterie, sont fait sans une analyse de l'usage préalable, limitant alors leur représentativité.

Ceci nous amène alors à la méthodologie de la thèse. La première étape de cette méthodologie consiste à mener une analyse de l'usage des batteries Li-ion d'application automobile (chapitres 3 et 4). La deuxième étape consiste à développer et mettre en place un protocole de vieillissement accéléré représentatif de l'usage, appliqué sur des cellules Samsung PHEV 37 Ah (chapitre 5). La troisième étape constitue une compréhension des mécanismes de dégradation qui se sont engendrés lors de ces vieillissements (chapitre 6). Finalement, la dernière étape consiste à développer un modèle de performance multi-physique de type Newman P2D, auquel viendront s'ajouter des modèles de dégradation afin de décrire le comportement des batteries durant leur vieillissement (chapitre 7).

3. Chapitre 3 – Facteurs de stress vus par une batterie Li-ion en fonction de l'usage dans un véhicule électrique (EV)

Ce chapitre porte sur la première étape de la méthodologie proposée dont le but est :

- 1- D'identifier les facteurs de stress auxquels sont soumises les batteries Li-ion des véhicules électriques (EV) en fonction de l'usage.
- 2- D'évaluer l'impact de ces facteurs de stress et donc leurs niveaux de criticité vis-à-vis de du vieillissement des cellules.

Pour cela, une étude exhaustive de la littérature portant sur l'usage des différents types de véhicules électriques a été menée. Ceux-ci sont divisés en 3 types : les tout électrique (BEV), les hybrides (HEV) ainsi que les hybrides rechargeables (PHEV). Cette étude a permis d'identifier les principaux facteurs de stress à savoir :

- 1- la température des cellules,
- 2- leur niveau d'état de charge (SOC : State of Charge),
- 3- leur profondeur de décharge (DOD : Depth of Discharge),
- 4- le taux de charge et de décharge.

L'analyse de ces facteurs de stress a été réalisée à partir de plusieurs campagnes de roulage dans différents pays issus de l'état de l'art. La distance parcourue cumulée de ces études est aux alentours de 228 millions de km, pour plus de 37,500 véhicules. Cette étude a permis, pour chaque facteur de stress d'identifier l'intensité et l'occurrence, et ceci pour les différents types de véhicules (BEV, HEV et PHEV). Elle

a permis également de mettre en avant les différences en fonction des zones géographiques et les usages associés.

Malgré ce travail de synthèse, la température des cellules n'est pas systématiquement accessible dans l'état de l'art, en particulier lors de phase de calendaire ou de charge. Or, c'est un stress qui impacte fortement le vieillissement. Afin d'avoir accès à la température des cellules, nous avons exploité les données issues d'une campagne de roulage menée au CEA de Grenoble sur un véhicule commercial (BMW_{i3} 60 Ah) de 2018 dans le cadre d'un précédent projet. L'analyse de ces données a permis de répondre en partie à ce besoin (cette étude est référencée par « Campagne CEA »). Dans cette étude, des thermocouples ont été mis sur les cellules du pack batteries du véhicule, et des mesures ont été faites durant les phases de roulage, de charge et de parking. Des mesures électriques et GPS ont aussi été faites. Ce véhicule a été utilisé comme véhicule de service CEA, et a parcouru 1,000 km.

Les résultats de cette synthèse ont permis de conclure plusieurs points intéressants. Il a été montré dans la campagne CEA que la température des cellules durant les phases de parking n'est pas forcément égale à la température ambiante, cela étant d'autant plus vrai pour les températures extrêmes ($< 10\text{ °C}$ et $> 35\text{ °C}$). À basse température ambiante, la température des cellules est plus élevée, et à haute température, celle-ci est plus basse. Ceci est dû à l'isolation thermique du pack batteries et son inertie thermique. Ceci dit, les mécanismes de dégradations lors des phases de parking (comme l'épaississement de la couche de SEI) sont très faiblement accélérés par l'amplitude des températures vues.

Pendant les phases de roulage, il a été montré que plus le trajet parcouru est long, plus la température des cellules se stabilise autour de 20 °C grâce à la thermalisation du pack batteries. Les courts trajets constituent une grande part des trajets effectués en Europe. Ils sont les plus critiques vis-à-vis de la température des cellules. Celle-ci n'a pas le temps de se stabiliser à 20 °C alors que les cellules subissent de fortes sollicitations. On a pu montrer qu'à basse température, les matériaux actifs des électrodes se dégradent par fracturation et augmentation de la couche de SEI (Surface Electrolyte Interface).

Nous avons également étudié la puissance de décharge à partir de la consommation énergétique du pack batteries (exprimées en Wh/km). Les résultats ont montré que la consommation énergétique est variable en fonction de la température ambiante. Plus la température ambiante est extrême, plus la consommation est élevée. Cette élévation est principalement due à la thermalisation du pack mais aussi de la distance parcourue. Pour un court trajet, la consommation peut être jusqu'à trois fois plus élevée que la consommation d'un long trajet. Ce phénomène met en exergue la notion de « pénalité d'énergie ». Nous avons pu voir que la masse du véhicule et sa vitesse jouent aussi sur l'augmentation de la puissance en décharge, montrant ainsi que ce stress peut être assez critique pour des véhicules lourds, roulant à

grande vitesse. Ceci dit, une grande valeur de puissance en décharge peut induire des changements brusques dans le volume des particules et donc, une fracturation de ces dernières. Ce mécanisme s'accélère durant les courts trajets du fait d'une plus forte consommation, plus particulièrement en hiver lorsque la température est basse et avant que la thermalisation du pack et donc des cellules ne soit efficace.

La puissance en charge est aussi un facteur de stress assez important étudié abondamment dans l'état de l'art du vieillissement des batteries Li-ion. Il a été prouvé que la méthode de charge la plus commune de nos jours se trouve aux alentours de 7 kW. Pour une capacité moyenne des batteries d'EV (actuellement de 61.7 kWh), ceci ne présente pas de stress majeur.

Finalement, le SOC et DOD ont également été étudiés. Il a été montré que la plage d'opération de SOC est différente d'un type d'EV à un autre. Pour les BEV, la plage d'opération se situe entre 90 % et 20 % de SOC. Dans le cas d'un HEV, la batterie opère normalement entre 70 % et 30 % de SOC suivant un mode de fonctionnement hybride, plus connue par « CS » pour « Charge Sustaining ». Finalement, dans un PHEV, la batterie opère entre un 90 et 30 % de SOC, similairement à la batterie d'un BEV, et entre un 20 et 40 % de SOC comme pour le mode « CS ». Il a été montré que pour un usage européen, les utilisateurs ont tendance à recharger la batterie très souvent ce qui reflète la peur de l'autonomie. Ainsi, la plage de SOC la plus courante se situe dans les valeurs élevées avec des DOD faibles.

Suite à cette analyse des facteurs de stress, une analyse de risque « Risk Probabilistic Analysis » (RPN) a été établie en adaptant la méthodologie développée dans d'autres domaines technologiques plus matures. Cette analyse a pour but de souligner le facteur de stress le plus critique dans la vie d'une batterie d'EV et a été réalisée dans le cas d'un usage en Europe. La RPN repose sur l'attribution pour chaque facteur de stress de trois grandeurs numériques :

- 1- Son niveau de sévérité (S), celui-ci a été établi en fonction de la température des cellules.
- 2- La probabilité d'occurrence de cette température (P_T),
- 3- La probabilité d'occurrence en fonction de l'application (P_x , où $x = \text{BEV}$ ou HEV ou PHEV).

Chacun de ces facteurs aura une valeur qui varie de 1 à 10, dépendamment de son impact. La valeur RPN est le produit de ces trois facteurs. Plus la valeur RPN est élevée, plus le facteur de stress est impactant dans la vie d'une batterie.

Les plages de température ont été divisées en 3 catégories : basse, < 10 °C, haute, > 35 °C, et moyenne, entre 10 et 30 °C. Les résultats de cette analyse sont présentés dans le Tableau 1.

Cette analyse montre que le stress le plus important dans la vie d'une batterie de BEV est le cyclage à haut SOC ainsi que la puissance en décharge à basse température. Dans le cas d'une batterie de HEV, la puissance en décharge est le stress le plus critique. Quant aux véhicules PHEV, les vitesses de charge et de décharge sont les plus critiques. En effet, la capacité du pack est beaucoup plus faible que celle d'un pack de BEV. Ceci induit aussi une utilisation plus complète de la plage de SOC, d'où une criticité de DOD élevé.

Tableau 1 : Analyse RPN pour les différents stress identifiés en fonction du type de véhicule et de l'usage

Driving/Charging Conditions				BEV		HEV		PHEV	
Cell Temperature	P _T	Stress Factor	S	P _x	RPN	P _x	RPN	P _x	RPN
High (>35 °C)	1	High mid-SOC	6	9	54	0	0	7	42
		Wide DOD	9	2	18	0	0	8	72
		Discharge power	8	5	40	10	80	6	48
		Charge power	8	2	16	0	0	2	24
Mild	6	High mid-SOC	5	9	270	0	0	7	210
		Wide DOD	7	2	84	0	0	8	336
		Discharge power	7	2	84	10	420	4	168
		Charge power	8	2	96	0	0	4	192
Low (<10 °C)	3	High mid-SOC	5	9	135	0	0	7	105
		Wide DOD	9	2	54	0	0	8	216
		Discharge power	8	7	168	10	240	8	192
		Charge power	9	2	54	0	0	2	53
Parking conditions									
Cell Temperature	P _T	Stress Factor	S	P _x	RPN	P _x	RPN	P _x	RPN
High (>35 °C)	1	High SOC	8	9	72	0	0	7	56
Mild	5		5	9	225	0	0	7	175
Low (<10 °C)	4		0	9	0	0	0	7	0

Il faut noter que cette analyse est propre à l'espace temporel dans lequel elle a été établie. Dans ce cas, en Europe, et dans une période où la peur de l'autonomie est toujours d'actualité. Dans l'avenir les usages changeront probablement, notamment vis-à-vis de la peur de l'autonomie. Dans ce cas, les valeurs de probabilité d'occurrence varieraient en modifiant ainsi les résultats de l'analyse RPN.

Cette analyse permet de souligner la criticité des facteurs de stress, et ainsi identifier les facteurs de stress pertinents à appliquer lors des vieillissements accélérés.

4. Chapitre 4 – Campagne de roulage sur un BEV

Comme discuté dans le chapitre précédent, la température des cellules est un facteur critique quant à leur vieillissement, mais difficilement accessible dans la littérature. Disposant d'un véhicule électrique instrumenté au CEA (BMW i3 de 2018) ayant déjà fait l'objet d'une étude de roulage dans le cas d'un précédent projet européen pour des profils de roulage spécifiques, il a été décidé d'utiliser ce véhicule pour compléter l'étude de l'usage.

L'objectif étant de mesurer la température des cellules ainsi que les autres paramètres lors d'un usage quotidien domicile-travail, une nouvelle campagne a été lancée sur ce véhicule dans le cadre de cette thèse. Trois types distance domicile-travail ont été identifiés dans le chapitre précédent : Court (< 10 km), Moyen (entre 10 et 20 km) et Long (entre 20 et 40 km). Les collaborateurs du CEA/DEHT ont été invités à participer à cette étude sur la base du volontariat et choisis de façon à représenter ces trois catégories. Chaque utilisateur devait conduire le véhicule pour ses trajets journaliers domicile-travail pour une durée de deux semaines. Des mesures électriques (courant, tension de plusieurs cellules du pack), de GPS ainsi que de température (ambiante et celle des cellules) ont été effectuées. Au total, 24 volontaires ont participé, 8 642 km ont été parcourus et 838 trajets ont été effectués.

Les résultats principaux de cette campagne de roulage sont les suivants. La peur de l'autonomie a été mise en évidence avec un rechargement après 33km pour un SOC de 77% en moyenne. Ce qui correspond à une recharge systématique après chaque trajet. Ce qui confirme l'analyse de la littérature, à savoir que les cellules subissent un stress important lié au niveau de SOC élevé. Nous avons également observé que la consommation d'énergie dépend de la température conformément à ce qui a été montré dans le chapitre précédent. La variation de la puissance délivrée du pack batterie a été tracée en fonction de la vitesse du véhicule, et de la température ambiante. Cette analyse montre qu'à partir de 80 km/h, la puissance peut devenir jusqu'à 3 fois plus élevée pour des températures inférieures à 5 °C. Ces conditions apparaissent pour des températures ambiantes basses et que le pack n'a pas eu le temps de se thermaliser (courts trajets).

La température des cellules a été tracée en fonction de la température ambiante pour les différents types de trajets. L'effet de la thermalisation a été identifié avec une grande partie des températures qui se retrouvent aux alentours de 25 °C après 20 km de roulage. Cependant, quelques cellules ont été trouvées à des températures entre 5 et 10 °C même pour les longs trajets. Ce qui montre que la thermalisation n'est dans ce cas pas toujours efficace sur la totalité du pack batterie.

Cette campagne de roulage a permis de délivrer une quantité d'informations suffisantes pour répondre aux manques de l'analyse de l'usage issue des analyses de l'état de l'art. Elle a aussi permis de confirmer certaines conclusions issues de l'analyse de l'état de l'art telles que l'anxiété de l'autonomie, la dépendance de la consommation et des puissances en fonction de la température. Ce qui permet d'avoir les éléments pour l'établissement des protocoles de vieillissement accélérés présentés dans le chapitre suivant.

5. Chapitre 5 – Campagne de vieillissement accéléré représentative

Suite à cette étude de l'usage synthétisé au chapitre précédent, nous avons les éléments nécessaires pour effectuer la deuxième étape de la méthodologie. À savoir, la réalisation d'une campagne de vieillissement accéléré en tenant compte de l'usage et de l'interdépendance des phases calendaires et de cyclage. Pour répondre à ce besoin, un protocole de vieillissement original a été développé. Il comporte trois étapes.

- Lors de la première étape, nous définissons l'application de la batterie (par exemple, dans le domaine de l'automobile, on compte au moins trois applications différentes : BEV, HEV et PHEV).
- La deuxième étape consiste à définir les phases d'usage et de les classer de la plus fréquente à la moins fréquente conformément à l'usage.
- La troisième étape consiste à les appliquer afin de réaliser un vieillissement accéléré en procédant de façon incrémentale (ou concentrique). En d'autres termes, une première série d'échantillons est soumise à un protocole de vieillissement composé d'une première phase correspondant à l'usage le plus fréquent.

Chaque niveau de vieillissement produira des données exploitables ensuite pour le développement de modèles de vieillissement, ce qui permettra de mieux comprendre l'interaction entre les différentes phases : calendaire, le cyclage correspondant à de courts trajets et le cyclage correspondant à de longs trajets.

Nous dérivons ensuite plus en détail la campagne expérimentale menée. Une cellule prismatique Samsung de 37 Ah dédiée à des applications de PHEV a été choisie dans le cadre de cette thèse. Le protocole a donc été défini en fonction de l'usage de ces cellules (PHEV) et de leurs caractéristiques.

La première phase de vieillissement identifiée est la phase inactive de la batterie, dans le scénario où le véhicule est garé (plus de 90 % de la vie d'un véhicule). Celle-ci est dénommée « Cal » pour faire référence au vieillissement calendaire. La deuxième phase est la phase de courts trajets, qui constitue plus de 70 % des trajets (estimés à 8 km) effectués en Europe. Cette dernière est référée par « ST » pour « Short Trip ». La phase des longs trajets constitue une phase moins fréquente, mais

toutefois existante dans la vie d'un véhicule, et donc est considérée comme la troisième phase du protocole (estimés à 10 km additionnels). Elle est notée « LT » pour « Long Trip ». Une dernière phase propre aux applications PHEV (et HEV) est celle où la batterie est utilisée pour accompagner le moteur thermique. Dans cette dernière, la batterie opère en maintien d'état de charge, ou « Charge Sustaining ». Des régimes de puissances en charge et décharge sont appliqués de telle sorte à ne pas réduire le SOC de la batterie, qui sera entre 20 et 40 % dans le cas d'un PHEV. Cette phase est nommée « HT » pour « Hybrid Trip ».

Pour résumer le protocole en question, les différentes phases sont listées ci-dessous et appliquées à deux différentes températures, 25 et 45 °C :

- Cal SOC 90 %, SOC 60 % et SOC 30 % (3 cellules par conditions)
- Cal SOC 90 % + ST (référé par Cal + ST) (2 cellules par conditions)
- Cal SOC 90 % + ST + LT (référé par Cal + ST + LT) (2 cellules par conditions)
- Cal SOC 30 % + HT (référé par Cal + HT) (2 cellules par conditions)

La paramétrisation du protocole, où les valeurs et la durée de puissance en décharge, est basée encore une fois sur l'application. La vitesse de décharge est dépendante de la longueur du trajet (ST et LT), de la température (extrême ou proche de l'ambiante) et du type de trajet (urbaines, autoroute et combiné). Des valeurs de consommation d'énergie basée sur l'usage sont utilisées pour déduire la puissance de décharge de chaque cellule. Le résumé du protocole est illustré dans la Figure 105.

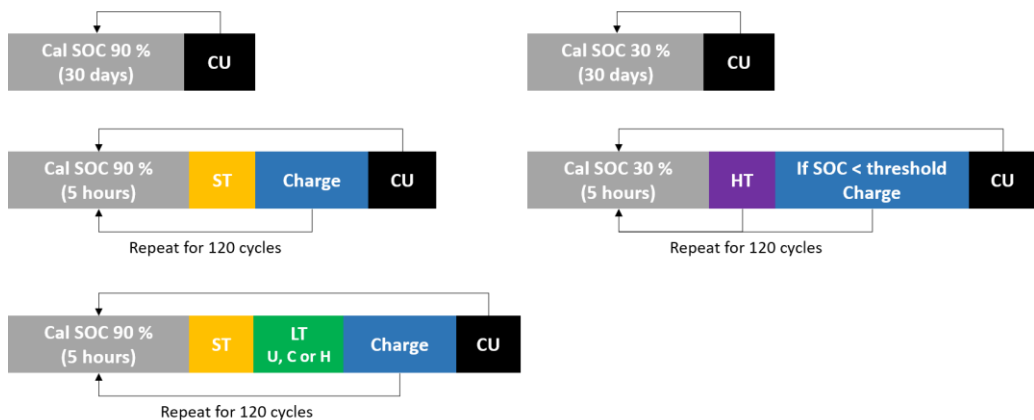


Figure 105. Schéma montrant la succession des phases du protocole de vieillissement accéléré. Avec Cal : calendrier, ST : short trip, LT : long trip, CU : check-up.

Les CU sont des protocoles de caractérisation de la batterie permettant de suivre la perte de performances au cours du vieillissement. Deux types de CU sont utilisés dans ce protocole. Le premier est appliqué tous les mois et consiste en une simple mesure de capacité à l'aide d'une décharge à puissance constante (65 W) suivie d'une charge et décharge à courant très faible (1,85 A, équivalent à C/20) afin d'effectuer un diagnostic non destructif de la batterie (cf. chapitre 6 décrivant l'exploitation de ces données). Le deuxième CU est appliqué uniquement en début et fin de vieillissement afin de mesurer de la perte d'autonomie de la batterie. Pour cela nous avons appliqué un profil WLTP adapté à la cellule dans les marges de SOC opérationnel (SOC 90 et SOC 30 %). Il est à noter que pour le vieillissement calendaire une cellule par condition n'a pas subi de CU ceci pour quantifier l'impact du CU sur le vieillissement.

Lors des essais, les cellules étaient comprimées à l'aide d'un montage spécifique développé dans cette thèse et adapté à des cellules de forts courants (allants jusqu'à 180 A).

Le suivi du vieillissement est représenté par la perte en énergie (Wh) calculée à partir d'une décharge à 65 W durant les phases de CU (Figure 106). Pour les cellules vieilles en calendaire à différents états de charge, il a été montré que plus le SOC est élevé, plus la perte en énergie est rapide. De plus, la température joue un rôle d'accélération additionnel quant à la perte de performance. Les cellules qui n'ont pas subi de CU mensuels ont vieilli moins vite que les cellules qui ont subi de CU. Cette différence s'est avérée d'autant plus importante que le SOC et la température sont élevés.

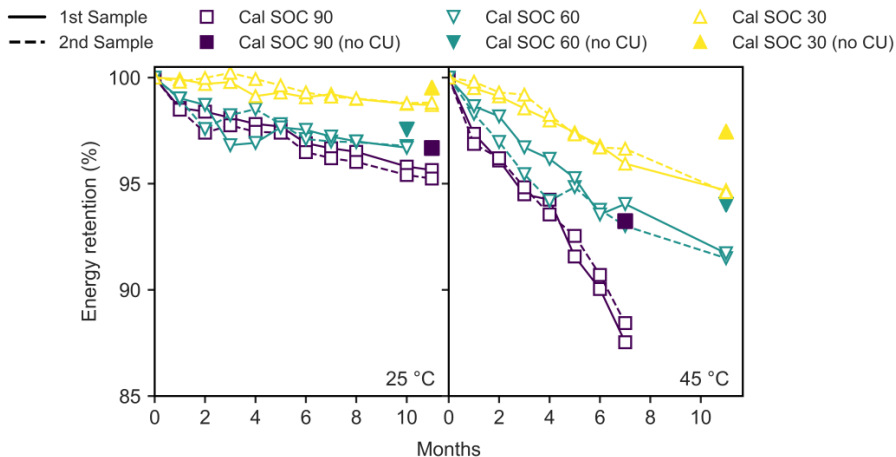


Figure 106. Perte en énergie des cellules vieilles en calendaire. Les deux échantillons de chaque condition sont montrés (lignes pleines et hachurées), et le point plein représente la perte en énergie de l'échantillon qui n'a pas subi de CU.

Les vieillissements incluant les profils Cal + ST + LT ont montré des résultats intéressants. Plus l'intensité (décharge de type H (Highway) par exemple) et la durée de la décharge (les décharges de types Long Trajets, ou LT) augmentent, plus le vieillissement est rapide. Ceci met en évidence l'impact des deux facteurs de stress que sont la puissance de décharge et le DOD.

Les tests de vieillissement en cyclage n'ont pas montré de différences marquantes comparées aux vieillissements à SOC 30 %, prouvant ainsi que, au moins pour la durée de l'étude, l'impact des cycles hybrides sur le vieillissement calendaire est très faible.

Les pertes en autonomie (km) mesurées à partir d'un profil WLTP ont permis de quantifier l'état de santé d'une batterie de façon plus représentative de l'usage. Ils ont également permis de montrer que la perte en énergie mesurée à travers une décharge constante n'est pas toujours équivalente à la perte en autonomie. Par exemple, les cellules vieillies en calendaire à SOC 90 % et à 25 °C ont perdu 5 % en énergie et presque 0 % en autonomie.

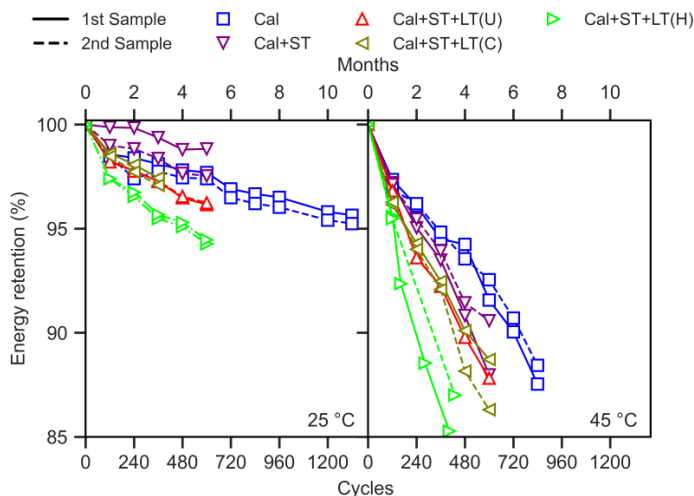


Figure 107. Perte en énergie des différentes conditions de vieillissement de type Cal SOC 90 % + ST + LT. Les deux échantillons de chaque condition sont montrés (lignes pleines et hachurées).

Pour conclure ce chapitre, un protocole accéléré original représentatif de l'usage et prenant en compte l'interaction des vieillissements calendaire et en cyclage a été appliqué sur des cellules d'application PHEV. Le comportement en vieillissement accéléré a montré que la perte en énergie est plus importante lorsque l'intensité et la profondeur de décharge augmentent. Nous avons pu également voir l'effet des différentes phases de roulage et leur combinaison sur le vieillissement. L'impact du

CU a également été mis en évidence par la comparaison des vieillissements des cellules en calendrier qui n'ont pas subi de CU.

L'étude des mécanismes de vieillissement par des diagnostics à partir des courbes électrochimiques et des analyses post-mortem est décrite dans le chapitre suivant.

6. Chapitre 6 – Identification des mécanismes de dégradation

Dans le chapitre 5 un vieillissement accéléré représentatif de l'usage a été mis en place et appliqué sur une Samsung 37 Ah PHEV. Le but de ce chapitre est d'identifier les mécanismes de dégradation causés par les différentes phases de calendrier (parking), court trajets (ST, short trip) et longs trajets (LT, long trip).

L'analyse se fait en deux niveaux. Le premier, le niveau « macro » en analysant les données électrochimiques, considère les modes de vieillissement et donc la perte de lithium (LLI, pour Loss of Lithium Inventory) ainsi que la perte de matières actives à l'électrode négative et à l'électrode positive (LAMne et LAMpe, pour Loss of Active Material on the Negative Electrode and the Positive Electrode). Deux outils numériques ont été utilisés pour cela : l'EBD (ou Electrode Balancing and Diagnosis, développé dans le cadre de cette thèse) et l'outil 'Alawa, développé par l'équipe de Matthieu Dubarry au HNEI et couramment utilisé dans la littérature.

Le deuxième niveau d'analyse considère les mécanismes physiques et électrochimiques de dégradation. Pour cela des analyses post-mortem ont été réalisées sur certaines cellules après vieillissement. Le protocole passe par une première analyse visuelle de l'état des électrodes après démontage, suivi par des analyses MEB et EDX ainsi que des analyses électrochimiques en piles boutons effectuées sur des échantillons prélevés sur les électrodes.

Commençons par le premier niveau d'analyse. Comme expliqué dans le chapitre précédent, un cycle lent (à un courant de 1.85 A ou C/20) a été appliqué durant les phases de CU. Ce dernier est utilisé pour effectuer un diagnostic de l'état de vieillissement. Celui-ci se base sur un recalibrage des courbes d'OCV des deux électrodes après vieillissements à partir des courbes de potentiel de chaque électrode obtenue en début de vie sur des piles boutons (appelé également « balancing » des électrodes par la communauté). Pour cela, un outil a été développé sur COMSOL dans le cadre de cette thèse. Il permet, à partir des courbes de potentiels et du «balancing» des électrodes, d'identifier les différents modes de vieillissement de la cellule correspondant aux pertes de lithium actif (LLI) et de matière active à l'électrode négative (LAMne) et positive (LAMpe). Les résultats obtenus sont présentés sur la Figure 108.

Les vieillissements à 25 °C n'ont pas montré de pertes significatives à l'électrode négative, les valeurs de LAMne oscillent à des valeurs inférieures à 2 %. Les analyses ont montré une évolution plus claire pour les valeurs de LAMpe. Celles-ci

augmentent au cours du temps pour tous les vieillissements avec une progression légèrement plus rapide pour les protocoles ST et LT. Cela permet de conclure que la perte de matière à l'électrode positive (LAMpe) est principalement due aux phases calendaires (Cal). Enfin, les résultats montrent une évolution plus forte de la perte en lithium (LLI). Celle-ci augmente d'autant que l'intensité et la durée des décharges sont plus élevées. Ainsi, ces résultats permettent de conclure que plus l'intensité des décharges est importante, plus les pertes lithium cyclables sont importantes.

A 45 °C, des résultats similaires concernant le LLI et la LAMpe sont observés, mais avec une intensité bien plus forte, mettant en valeur l'impact de la température. Contrairement au cas précédent, ici la LAMne est assez importante, montrant une évolution très similaire pour les différents types de vieillissement.

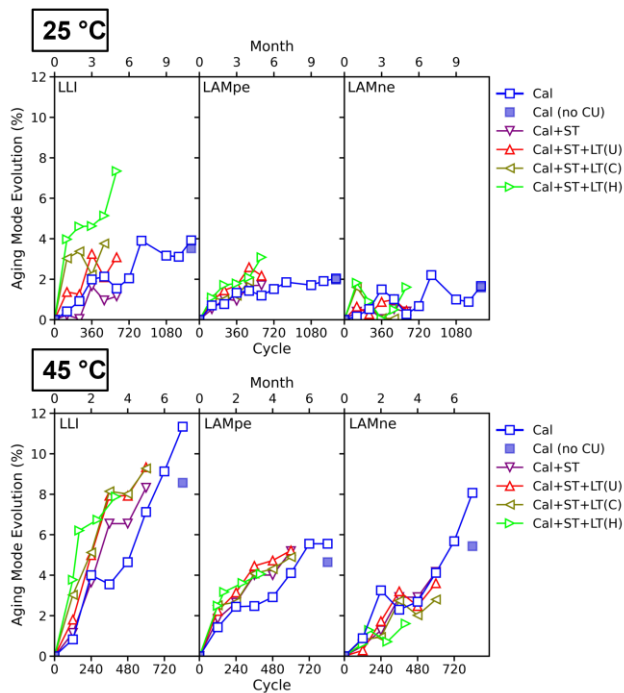


Figure 108. Évolution des modes de dégradations (LLI, LAMpe et LAMne) pour les différents scénarios de vieillissement à 25 °C et à 45 °C

L'outil 'Alawa a également été utilisé à des fins de comparaison avec l'outil développé dans cette thèse. Les résultats obtenus aboutissent à des conclusions très similaires.

Cependant, ces outils ne permettent d'obtenir que des résultats qualitatifs. Résultats qu'il faut confirmer par des analyses post-mortem afin de faire le lien entre les modifications de comportement électrochimique et les mécanismes de dégradation (LLI, LAMe et LAMp). Pour cela des analyses post-mortem ont été réalisées sur plusieurs cellules : celles vieilles en Calendaire SOC 90 % à 45 °C, avec et sans CU,

ainsi que les cellules vieilles en Cal + ST + LT (H) à 45 °C. Nous présentons ci-dessous un résumé des résultats obtenus.

Le premier résultat obtenu à partir des cellules vieilles en calendrier a permis de montrer que le CU n'est pas neutre. Celui-ci induit la formation de lithium métallique sur l'électrode négative (appelé « Li-plating »). Ce dépôt n'a pas été observé sur les cellules n'ayant pas subi de CU lors du vieillissement.

Le deuxième résultat concernant les cellules après cyclage est que les phases de fortes décharges induisent un certain stress mécanique sur l'électrode négative. Des fracturations de la surface des électrodes ont été identifiées par des analyses MEB, montrant ainsi l'origine de la perte de matière active.

Les résultats des tests électrochimiques sur piles boutons face au lithium ont permis de confirmer la perte de matière active à l'électrode positive. Les valeurs obtenues lors de ces analyses postmortem sont très proches de celles obtenues avec l'outil EBD à partir des CU sur cellule complète. Ceci permet de valider les hypothèses. Par ailleurs, d'autres tests électrochimiques sur piles boutons ont permis de quantifier la perte de lithium dû à la croissance de SEI sur l'électrode négative.

L'ensemble de ces analyses a permis d'identifier les mécanismes de dégradation et leurs différentes relations en fonction de la sollicitation. Celles-ci ont été synthétisées sous la forme d'un schéma (Figure 109). Celui-ci permet de montrer le lien entre les sollicitations appliquées sur la cellule aux mécanismes et les modes de vieillissement.

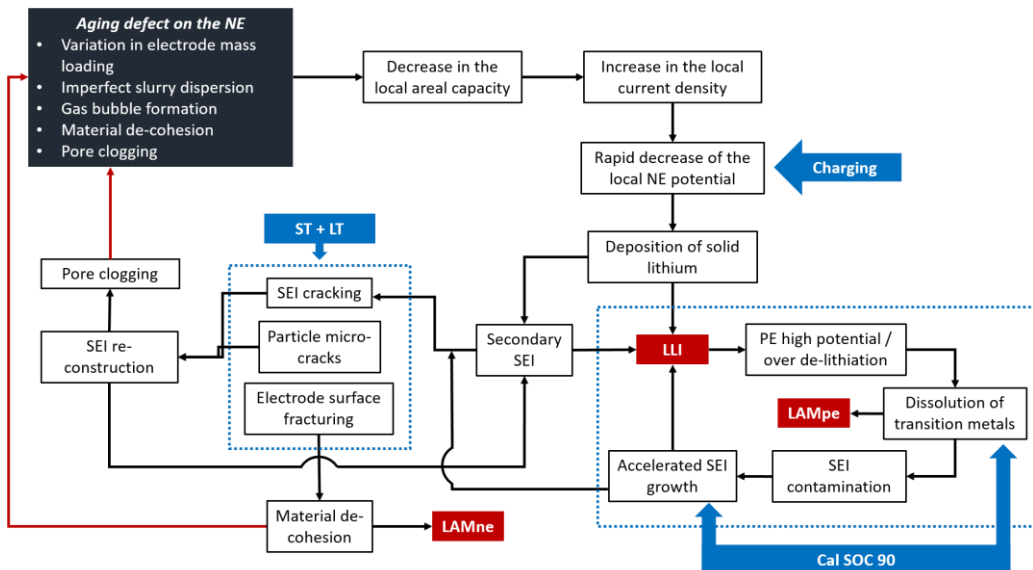


Figure 109. Schéma du cycle de vieillissement montrant l'interdépendance des mécanismes et des modes de dégradation par rapport à un scénario général Cal + ST + LT

Les analyses post-mortem ont également permis de montrer que le vieillissement est très hétérogène, principalement au niveau de l'électrode négative. Ces défauts, pouvant provenir de plusieurs sources, réduisent la capacité surfacique locale, et en conséquence, la densité de courant locale. Quand une charge est appliquée, localement, le potentiel de l'électrode négative passera en dessous de la limite de 0 V vs Li. Ce qui correspond à une situation favorable à la formation de lithium métallique (lithium plating). Par conséquent, le potentiel de l'électrode positive augmentera à cause d'une sur-dé-lithiation, causant alors une perte à l'électrode positive. Le mécanisme originaire de cette perte est souvent la dissolution des métaux de transition qui migrent et se déposent sur l'électrode négative. Une fois déposés, ces derniers ont tendance à contaminer la couche de SEI et à accélérer sa croissance. La croissance de la couche de SEI et la dissolution des métaux de transition sont activées par les phases de Calendaire à SOC 90 %.

Le dépôt de lithium, lié à une sur dé-lithiation de l'électrode positive, engendre également la création de surfaces additionnelles pour la formation et croissance d'une SEI secondaire.

Les mécanismes de dégradation engendrés par les décharges appliquées ont été identifiés :

- la fracturation de la SEI, créant plus de surfaces accessibles et accélérant alors sa croissance,
- la formation de microcracks au niveau des particules
- et la fracturation de la surface de l'électrode, comme cela a été confirmé par observation en microscopie électronique à balayage (MEB).

Ces mécanismes sont alors à l'origine d'une perte à l'électrode négative, et donc d'un nouveau défaut qui accentuera le reste des mécanismes évoqués.

La modélisation de ces mécanismes de dégradation fera l'objet du chapitre suivant.

7. Chapitre 7 – Modélisation de la performance et du vieillissement

Nous avons pu identifier au chapitre 6 que trois modes de dégradation apparaissent lors du vieillissement accéléré des cellules : la perte de lithium (LLI), la perte de matière active aux électrodes négative (LAMne) et positive (LAMpe). Ces pertes ont été assimilées à la croissance de SEI, au dépôt de Lithium métallique ainsi qu'à la fracturation des particules. Le but de ce chapitre est d'utiliser ces résultats pour développer des modèles de dégradation multiphysiques.

En premier lieu, un modèle de performance doit être établi et validé. Pour cela, un modèle, électrochimique de type Newman P2D (Pseudo 2D) a été développé. Ce modèle, basé sur le concept d'électrode poreuse, considère les différents composants internes de la cellule (collecteurs de courant, électrodes séparatrices et électrolyte)

comme un continuum entre les phases solides et la phase liquide. Le modèle considère le transport des ions lithium à travers le « sandwich » élémentaire constitué de trois couches imprégnées d'électrolyte : l'électrode positive, le séparateur, et l'électrode négative. Ce qui correspond à la première dimension du modèle. Dans cette dimension, les équations sont définies suivant une direction de l'espace suivant un axe orthogonal à la surface des électrodes. La diffusion des ions Lithium au sein des particules de la matière active (considérée comme sphérique), suivant la dimension radiale, constitue la pseudo deuxième dimension du modèle.

Durant une sollicitation de charge ou de décharge, des équations de transport dans le sandwich et dans la particule, des équations de balance de masse et de courant, ainsi qu'une équation cinétique de type « Buttlar-Volmer » sont résolues afin de trouver les inconnues du système.

Celles-ci sont :

- la concentration du lithium dans l'électrolyte et dans les matériaux actifs,
- la densité de courant dans ces deux éléments,
- le potentiel des deux électrodes.

Une synthèse des équations du modèle ainsi que la liste des paramètres et des variables sont décrites dans le manuscrit (cf. tableau 16). La résolution de ces équations se fait à l'aide du logiciel *COMSOL 5.5* couplé avec le logiciel *Matlab* et le module *Live Link*.

L'extraction des paramètres du modèle est critique pour une représentation précise du comportement de la batterie. Dans ce travail de thèse, nous avons extrait plus de 70 % des paramètres du modèle expérimentalement par des mesures directes (e.g. dimensions des électrodes), soit par des mesures indirectes (e.g. des mesures d'impédance en pile bouton pour les valeurs de tortuosité). L'OCV des électrodes est issue des courbes de potentiel à régime lent ($C/20$), et l'équilibrage des électrodes a été effectué grâce à l'outil EBD élaboré dans le chapitre antécédent. Une synthèse de tous les paramètres se trouve dans le tableau 18 du manuscrit. Les 30% des paramètres restant ont été déterminés à partir de la littérature connaissant la composition et les dimensions internes de la cellule obtenue lors des analyses antemortem.

La validation du modèle de performance s'est faite à partir des données expérimentales effectuées sur la cellule complète en utilisant la réponse en tension lors d'un cycle de charge/décharge lente et d'une sollicitation de charges rapides à puissance constante. Ces deux conditions sont représentatives d'une application automobile. Pour chacune de ces sollicitations, une validation du modèle par une analyse incrémentale (dQ/dV) d'une charge lente a été effectuée (ICA/DVA). Ces comparaisons entre le modèle et les courbes expérimentales montrent un très bon accord avec une erreur inférieure à 1% sur la quasi-totalité de la plage de capacité

(Figure 110). Il est à remarquer que la validation du modèle par les analyses ICA/DVA permet de garantir la bonne représentativité du modèle.

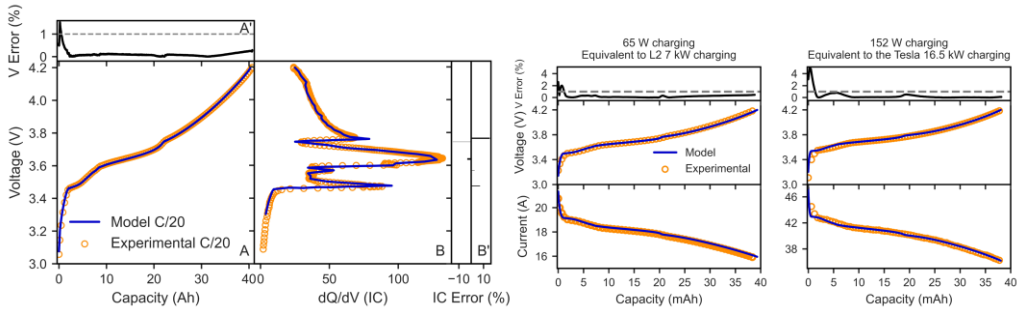


Figure 110. Comparaison des résultats du modèle avec les résultats expérimentaux

Après validation du modèle de performance, l'étape suivante consiste à rajouter des lois de vieillissement à ce modèle. La stratégie de vieillissement se base sur les pertes en lithium (LLI) et les pertes en matières actives (LAMne et LAMpe) conclues de l'outil EBD du chapitre précédent.

La première hypothèse porte sur l'attribution de la perte de lithium (LLI) à la croissance de la SEI. Celle-ci a été modélisée tout d'abord à partir de l'approche la plus répandue dans la littérature qui se base sur la diffusion de l'éthylène carbonate (EC) à travers la couche de SEI et sa réaction avec le lithium sur la surface graphite-SEI. Étant donné que dans notre cas nous avons observé une fracturation des particules, une deuxième hypothèse a été ajoutée à la première afin de prendre en compte ce phénomène. Pour cela nous supposons que le taux de croissance de SEI est affecté par la surface rajoutée lors de la fracturation de la SEI, la fracturation de la matière et le dépôt de lithium solide. Nous avons donc modélisé ce phénomène par l'ajout d'un coefficient sur la loi de croissance de la SEI du fait de l'augmentation de l'interface. La troisième hypothèse se base sur le fait que la perte de matière active aux deux électrodes peut se modéliser avec des lois de comportement semi-empirique en fonction du temps. Celles-ci ont été établies à partir des résultats obtenus avec l'outil EBD présenté au chapitre 6.

La majorité des paramètres du modèle de croissance de SEI sont issus de la littérature. Les paramètres cinétiques (diffusion de l'EC et la constante de cinétique) sont optimisés afin de représenter la perte en lithium des cellules vieilles en calendrier sans check up obtenus expérimentalement. Pour les vieillissements avec check up et ceux avec cyclage, l'augmentation de la surface d'échange est optimisée pour représenter cette perte en lithium additionnelle. Finalement, la LAMpe est modélisée par une loi en racine carrée en fonction du temps, différente pour chaque sollicitation, et la LAMne est modélisée par des équations polynomiales.

Les figures 111 et 112 ci-dessous montrent que le modèle représente assez bien les résultats expérimentaux à 25 °C que ce soit pour la perte en énergie et la perte en

capacité. Cependant, à 45 °C, la comparaison n'est pas satisfaisante, surtout pour la perte en énergie.

À l'issue de cette thèse, nous avons identifié plusieurs perspectives d'amélioration. La première consisterait à modéliser plus précisément l'augmentation du fait de la fracturation qui n'est probablement pas linéaire. Le deuxième porterait sur l'ajout dans le modèle d'équations décrivant le phénomène de « lithium plating ». La troisième devrait prendre en compte l'impact sur la résistance interne du fait des mécanismes de dégradation décrits précédemment. Celle-ci devrait induire une perte additionnelle en énergie.

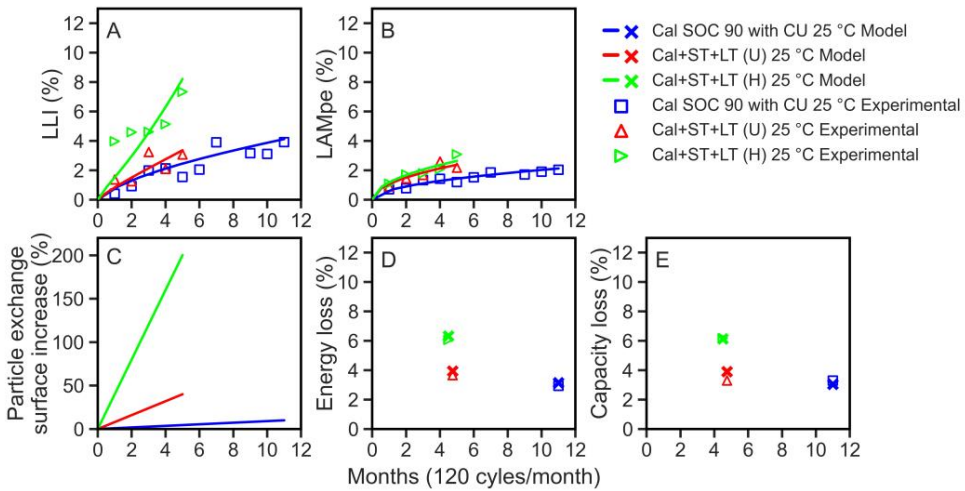


Figure 111. Résultats de simulation confrontés aux résultats expérimentaux à 25 °C montrant la perte de lithium, LLI, (croissance de SEI + augmentation de surface d'échange), la perte de matière active à l'électrode positive, LAMpe, ainsi que l'augmentation de surface d'échange, induisant une perte d'énergie et une perte de capacité

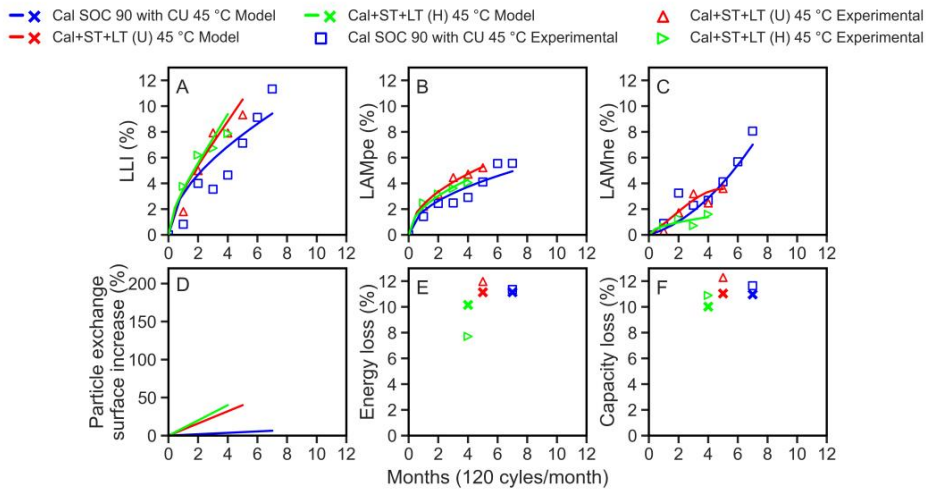


Figure 112. Résultats de simulation confrontés aux résultats expérimentaux à 25 °C montrant la perte de lithium, LLI, (croissance de SEI + augmentation de surface d'échange), la perte de matière active à l'électrode positive, LAMpe, ainsi que l'augmentation de surface d'échange, induisant une perte d'énergie et une perte de capacité

8. Conclusion

En conclusion, les chapitres 3 et 4 ont permis d'identifier les facteurs de stress les plus critiques durant la vie d'une batterie Li-ion d'application automobile, grâce à l'analyse RPN. Ces facteurs doivent être utilisés durant les tests de vieillissement accéléré afin d'améliorer leurs représentativités. Dans le chapitre 5, un nouveau protocole de vieillissement accéléré a été mis en place en garantissant la représentativité avec l'usage, et le chapitre 6 a permis d'identifier les mécanismes de dégradations. Finalement, un modèle multiphysique associé à des modèles de vieillissement a été développé en tenant compte des mécanismes de dégradation identifiés.

Reference list

- [1] European-Parliament, “CO₂ emissions from cars: facts and figures (infographics).” 2022 [Online]. Available: <https://www.europarl.europa.eu/news/en/headlines/society/20190313STO31218/co2-emissions-from-cars-facts-and-figures-infographics>
- [2] Transport and Environment, “How clean are electric cars? T&E’s analysis of electric car lifecycle CO₂ emissions,” Transport & Environment, Apr. 2020.
- [3] C. Grey and D. Hall, “Prospects for lithium-ion batteries and beyond—a 2030 vision,” *Nature Communications*, vol. 11, p. 6279, 2020.
- [4] I. Tsiropoulos, D. Tarvydas, and N. Lebedeva, “Li-ion batteries for mobility and stationary storage applications,” European Commission, 2018 [Online]. Available: <https://ec.europa.eu/jrc/en/publication/eur-scientific-and-technical-research-reports/li-ion-batteries-mobility-and-stationary-storage-applications>
- [5] J. Miler, “Electric car costs to remain higher than traditional engines.” *Financial Times*, Aug-2020 [Online]. Available: <https://www.ft.com/content/a7e58ce7-4fab-424a-b1fa-f833ce948cb7>
- [6] M. Wayland, “Stellantis CEO warns of electric vehicle battery shortage, followed by lack of raw materials.” CNBC, 2022 [Online]. Available: <https://www.cnbc.com/2022/05/24/stellantis-ceo-warns-of-ev-battery-shortage-lack-of-raw-materials.html>
- [7] P. LeBeau, “EV battery costs could spike 22% by 2026 as raw material shortages drag on.” CNBC, 2022 [Online]. Available: <https://www.cnbc.com/2022/05/18/ev-battery-costs-set-to-spike-as-raw-material-shortages-drags-on.html>
- [8] J. Jiang and C. Zhang, *Fundamentals and application of lithium-ion batteries in electric drive vehicles*. 2015, pp. 1–280.
- [9] S. Grolleau, “Vieillessement calendaire des accumulateurs Lithium-Ion : modélisation et analyse,” 2013 [Online]. Available: <http://www.theses.fr/2013CAEN2079>
- [10] P. Ralon, M. Taylor, and A. Ilas, “Electricity Storage and Renewables: Costs and Markets to 2030,” IRENA, 2017 [Online]. Available: <https://www.irena.org/publications/2017/Oct/Electricity-storage-and-renewables-costs-and-markets>
- [11] L. J. Song, F. Chen, and V. Mehrotra, “NiMH Supercapacitor Design, Modeling and HEV Applications,” *ECS Transactions*, vol. 41, no. 22, pp. 3–12, Dec. 2019.
- [12] M. V. Reddy, A. Mauger, C. Julien, A. Paoella, and K. Zaghbi, “Brief History of Early Lithium-Battery Development,” *Materials*, vol. 13, no. 8, p. 1884, 2020.
- [13] C. Delacourt, C. Ades, and Q. Badey, “Vieillessement des accumulateurs lithium-ion dans l’automobile,” *Techniques de l’ingénieur Machines thermiques et systèmes de production d’énergie électrique*, vol. base documentaire : TIB167DUO., no. ref. article : re231, 2014 [Online]. Available: <https://www.techniques-ingenieur.fr/base-documentaire/mecanique-th7/machines-thermiques-et-systemes-de-production-d-energie->

- electrique-42167210/vieillissement-des-accumulateurs-lithium-ion-dans-l-automobile-re231/
- [14] R. Korthauer, Ed., *Lithium-Ion Batteries: Basics and Applications*. Springer-Verlag Berlin Heidelberg, 2018 [Online]. Available: <https://www.springer.com/gp/book/9783662530696>
- [15] A. Mauger, C. M. Julien, J. B. Goodenough, and K. Zaghib, "Tribute to Michel Armand: from Rocking Chair – Li-ion to Solid-State Lithium Batteries," *Journal of The Electrochemical Society*, vol. 167, no. 7, p. 070507, Dec. 2019.
- [16] M. Lazzari and B. Scrosati, "A Cyclable Lithium Organic Electrolyte Cell Based on Two Intercalation Electrodes," *Journal of The Electrochemical Society*, vol. 127, no. 3, p. 773, Mar. 1980.
- [17] L. Wang, Q. Liu, S. Xu, Y. Du, and X. Ren, "Research and Development on the Separators of Li-ion Batteries," *IOP Conference Series: Earth and Environmental Science*, vol. 770, no. 1, p. 012011, May 2021.
- [18] A. Li, A. C. Y. Yuen, W. Wang, I. M. De Cachinho Cordeiro, C. Wang, T. B. Y. Chen, J. Zhang, Q. N. Chan, and G. H. Yeoh, "A Review on Lithium-Ion Battery Separators towards Enhanced Safety Performances and Modelling Approaches," *Molecules*, vol. 26, no. 2, 2021.
- [19] M. Meeus, "Overview of Battery Cell Technologies." European Commission, 2018 [Online]. Available: https://www.zeroemission.eu/wp-content/uploads/2018/04/report_batteries-workshop_january-11-12_final.pdf
- [20] K. Möller, Nationale Plattform Elektromobilität (NPE), 2016 [Online]. Available: <https://www.acatech.de/publikation/roadmap-integrierte-zell-und-batterieproduktion-deutschland/>
- [21] R. Schröder, M. Aydemir, and G. Seliger, "Comparatively Assessing different Shapes of Lithium-ion Battery Cells," *Procedia Manufacturing*, vol. 8, pp. 104–111, 2017.
- [22] X.-G. Yang, T. Liu, and C.-Y. Wang, "Thermally modulated lithium iron phosphate batteries for mass-market electric vehicles," *Nature Energy*, vol. 6, p. 176, Jan. 2021.
- [23] L. Xie, D. Ren, L. Wang, C. Zonghai, T. Guangyu, A. Khalil, and H. Xiangming, "A Facile Approach to High Precision Detection of Cell-to-Cell Variation for Li-ion Batteries," *Scientific Reports*, vol. 10, no. 7182, 2020.
- [24] R. Folkson, *Alternative fuels and advanced vehicle technologies for improved environmental performance: Towards zero carbon transportation*. Elsevier, 2014, pp. 708–709.
- [25] L. Mathieu, "Electric Surge: Carmaker's electric car plans across Europe 2019-2025," *Transport & Environment*, 2019 [Online]. Available: https://www.transportenvironment.org/sites/te/files/publications/2019_07_TE_electric_cars_report_final.pdf
- [26] J. Asamer, A. Graser, B. Heilmann, and M. Ruthmair, "Sensitivity analysis for energy demand estimation of electric vehicles," *Transportation Research Part D: Transport and Environment*, vol. 46, pp. 182–199, 2016.
- [27] C. Corchero, R. Gumara, M. Cruz-Zambrano, M. Sanmarti, D. Gkatzoflias, P. Dilara, I. Drossinos, and A. Donati, "Data Collection and Reporting Guidelines for European electro-mobility projects," Publications Office of the

- European Union, 2014 [Online]. Available: <http://publications.jrc.ec.europa.eu/repository/handle/JRC92972>
- [28] “Electric Vehicle Database.” EV Database, 2020 [Online]. Available: <https://ev-database.org/>
- [29] A. A. Pesaran, “Choices and Requirements of Batteries for EVs, HEVs, PHEVs.” NREL, Apr-2011 [Online]. Available: <https://www.nrel.gov/docs/fy11osti/51474.pdf>
- [30] A. Abdellahi, S. Rahimian, B. Blizanac, and B. Sisk, “Exploring the Opportunity Space For High-Power Li-Ion Batteries in Next-Generation 48V Mild Hybrid Electric Vehicles,” 2017.
- [31] “How Do Plug-In Hybrid Electric Cars Work?” US Department of Energy [Online]. Available: <https://afdc.energy.gov/vehicles/how-do-plug-in-hybrid-electric-cars-work>
- [32] J. Axsen, A. F. Burke, and K. S. Kurani, “CHAPTER SIXTEEN - Batteries for PHEVs: Comparing Goals and the State of Technology,” in *Electric and Hybrid Vehicles*, G. Pistoia, Ed. Amsterdam: Elsevier, 2010, pp. 405–427 [Online]. Available: <http://www.sciencedirect.com/science/article/pii/B9780444535658000166>
- [33] S. Pelletier, O. Jabali, G. Laporte, and M. Veneroni, “Battery degradation and behaviour for electric vehicles: Review and numerical analyses of several models,” *Transportation Research Part B: Methodological*, vol. 103, pp. 158–187, 2017.
- [34] B. Matadi, “Study of the aging mechanisms of Li-ion batteries in low-temperature cycling and high-temperature storage: understanding of the origins and aging modeling,” Université Grenoble Alpes, 2017 [Online]. Available: <https://tel.archives-ouvertes.fr/tel-01792293>
- [35] C. Argue, “Que peut nous dire l’étude de 6 300 véhicules électriques sur la santé des batteries des VE?” 2021 [Online]. Available: <https://www.geotab.com/fr/blog/ve-batterie/>
- [36] M. M. Kabir and D. E. Demirocak, “Degradation mechanisms in Li-ion batteries: a state-of-the-art review,” *International Journal of Energy Research*, vol. 41, no. 14, pp. 1963–1986, 2017 [Online]. Available: <https://www.scopus.com/inward/record.uri?eid=2-s2.0-85018913817&doi=10.1002%2fer.3762&partnerID=40&md5=95a47f6906fbb8cb883d2a71a014bf34>
- [37] A. Barré, B. Deguilhem, S. Grolleau, M. Gérard, F. Suard, and D. Riu, “A review on lithium-ion battery ageing mechanisms and estimations for automotive applications,” *Journal of Power Sources*, vol. 241, pp. 680–689, 2013.
- [38] E. Peled and S. Menkin, “Review—SEI: Past, Present and Future,” *Journal of The Electrochemical Society*, vol. 164, no. 7, pp. A1703–A1719, 2017 [Online]. Available: <https://doi.org/10.1149%2F2.1441707jes>
- [39] C. R. Birkel, M. R. Roberts, E. McTurk, P. G. Bruce, and D. A. Howey, “Degradation diagnostics for lithium ion cells,” *Journal of Power Sources*, vol. 341, pp. 373–386, 2017.
- [40] T. Waldmann, A. Iturrondobeitia, M. Kasper, N. Ghanbari, F. Aguesse, E. Bekaert, L. Daniel, S. Genies, I. J. Gordon, M. W. Lölle, E. D. Vito, and M.

- Wohlfahrt-Mehrens, “Review—Post-Mortem Analysis of Aged Lithium-Ion Batteries: Disassembly Methodology and Physico-Chemical Analysis Techniques,” *Journal of The Electrochemical Society*, vol. 163, no. 10, pp. A2149–A2164, 2016.
- [41] J. Edge, S. O’Kane, R. Prosser, N. Kirkaldy, A. Patel, A. Hales, A. Ghosh, W. Ai, J. Chen, J. Jiang, S. Li, M.-C. Pang, L. Bravo Diaz, A. Tomaszewska, M. Marzook, K. Radhakrishnan, H. Wang, Y. Patel, B. Wu, and G. Offer, “Lithium Ion Battery Degradation: What you need to know,” *Physical Chemistry Chemical Physics*, vol. 23, 2021.
- [42] M. Dubarry, N. Qin, and P. Brooker, “Calendar aging of commercial Li-ion cells of different chemistries – A review,” *Current Opinion in Electrochemistry*, vol. 9, pp. 106–113, 2018 [Online]. Available: <https://www.sciencedirect.com/science/article/pii/S2451910318300929>
- [43] S. E. J. O’Kane, W. Ai, G. Madabattula, D. Alonso-Alvarez, R. Timms, V. Sulzer, J. S. Edge, B. Wu, G. J. Offer, and M. Marinescu, “Lithium-ion battery degradation: how to model it,” *Phys. Chem. Chem. Phys.*, vol. 24, no. 13, pp. 7909–7922, 2022.
- [44] V. Ruiz, “Standards for the performance and durability assessment of electric vehicle batteries,” European Commission, 2018.
- [45] *ISO 12405-4: Electrically propelled road vehicles – Test specification for lithium-ion traction battery packs and systems – Part 4: Performance testing*. 2018.
- [46] *IEC 62660-1: Rechargeable Cells Standards Publication Secondary lithium-ion cells for the propulsion of electric road vehicles. Part 1: Performance testing*. 2010.
- [47] USABC, “United States Advanced Battery Consortium Battery Test Manual For Electric Vehicles,” U.S. Department of Energy, 2020 [Online]. Available: <https://uscar.org/usabc/>
- [48] G. Mulder, N. Omar, S. Pauwels, F. Leemans, B. Verbrugge, W. D. Nijs, P. V. den Bossche, D. Six, and J. V. Mierlo, “Enhanced test methods to characterise automotive battery cells,” *Journal of Power Sources*, vol. 196, no. 23, pp. 10079–10087, 2011.
- [49] E. Sarasketa-Zabala, F. Aguesse, I. Villarreal, L. M. Rodriguez-Martinez, C. M. López, and P. Kubiak, “Understanding Lithium Inventory Loss and Sudden Performance Fade in Cylindrical Cells during Cycling with Deep-Discharge Steps,” *The Journal of Physical Chemistry C*, vol. 119, no. 2, pp. 896–906, 2015 [Online]. Available: <https://doi.org/10.1021/jp510071d>
- [50] N. Lin, Z. Jia, Z. Wang, H. Zhao, G. Ai, X. Song, Y. Bai, V. Battaglia, C. Sun, J. Qiao, K. Wu, and G. Liu, “Understanding the crack formation of graphite particles in cycled commercial lithium-ion batteries by focused ion beam - scanning electron microscopy,” *Journal of Power Sources*, vol. 365, pp. 235–239, 2017.
- [51] M. Dotoli, R. Rocca, M. Giuliano, M. Sgroi, L. Belforte, N. Li Pira, G. Mangione, E. Milo, G. Nicol, and F. Parussa, “Physical-Chemical Characterization of Cycle Aged Commercial Cells of Automotive Interest,” in *WCX SAE World Congress Experience*, 2022.
- [52] R. Xu, Y. Yang, F. Yin, P. Liu, P. Cloetens, Y. Liu, F. Lin, and K. Zhao, “Heterogeneous damage in Li-ion batteries: Experimental analysis and

- theoretical modeling,” *Journal of the Mechanics and Physics of Solids*, vol. 129, pp. 160–183, 2019.
- [53] T. Sasaki, T. Abe, Y. Iriyama, M. Inaba, and Z. Ogumi, “Formation mechanism of alkyl dicarbonates in Li-ion cells,” *Journal of Power Sources*, vol. 150, pp. 208–215, 2005.
- [54] A. Barai, K. Uddin, M. Dubarry, L. Somerville, A. McGordon, P. Jennings, and I. Bloom, “A comparison of methodologies for the non-invasive characterisation of commercial Li-ion cells,” *Progress in Energy and Combustion Science*, vol. 72, pp. 1–31, 2019.
- [55] D. Liu, Z. Shadike, R. Lin, K. Qian, H. Li, K. Li, S. Wang, Q. Yu, M. Liu, S. Ganapathy, X. Qin, Q.-H. Yang, M. Wagemaker, F. Kang, X.-Q. Yang, and B. Li, “Review of Recent Development of In Situ/Operando Characterization Techniques for Lithium Battery Research,” *Advanced Materials*, vol. 31, no. 28, p. 1806620, 2019.
- [56] J. Barker, M. Y. Saidi, and J. L. Swoyer, “Performance Evaluation of the Electroactive Material, γ -LiV₂O₅, Made by a Carbothermal Reduction Method,” *Journal of The Electrochemical Society*, vol. 150, no. 9, p. A1267, Aug. 2003.
- [57] M. Dubarry, C. Truchot, B. Y. Liaw, K. Gering, S. Sazhin, D. Jamison, and C. Michelbacher, “Evaluation of commercial lithium-ion cells based on composite positive electrode for plug-in hybrid electric vehicle applications. Part II. Degradation mechanism under 2C cycle aging,” *Journal of Power Sources*, vol. 196, no. 23, pp. 10336–10343, 2011 [Online]. Available: <http://www.sciencedirect.com/science/article/pii/S0378775311016247>
- [58] M. Dubarry, C. Truchot, and B. Y. Liaw, “Synthesize battery degradation modes via a diagnostic and prognostic model,” *Journal of Power Sources*, vol. 219, pp. 204–216, 2012.
- [59] M. Dubarry, C. Truchot, M. Cugnet, B. Y. Liaw, K. Gering, S. Sazhin, D. Jamison, and C. Michelbacher, “Evaluation of commercial lithium-ion cells based on composite positive electrode for plug-in hybrid electric vehicle applications. Part I: Initial characterizations,” *Journal of Power Sources*, vol. 196, no. 23, pp. 10328–10335, 2011.
- [60] M. Dubarry, V. Svoboda, R. Hwu, and B. Y. Liaw, “Incremental Capacity Analysis and Close-to-Equilibrium OCV Measurements to Quantify Capacity Fade in Commercial Rechargeable Lithium Batteries,” *Electrochemical and Solid-State Letters*, vol. 9, no. 10, p. A454, 2006.
- [61] S. Lee, J. B. Siegel, A. G. Stefanopoulou, J.-W. Lee, and T.-K. Lee, “Electrode State of Health Estimation for Lithium Ion Batteries Considering Half-cell Potential Change Due to Aging,” *Journal of The Electrochemical Society*, vol. 167, no. 9, p. 090531, Jan. 2020.
- [62] H. Ekström, “Electrode Balancing of a Lithium-Ion Battery with COMSOL.” May-2019 [Online]. Available: <https://www.comsol.com/blogs/electrode-balancing-of-a-lithium-ion-battery-with-comsol>
- [63] I. Baghdadi, “Aging modes taking into account in the modeling of lithium-ion batteries performance for lifetime assessment in automotive usage,” Université de Bordeaux, 2017 [Online]. Available: <https://tel.archives-ouvertes.fr/tel-01578752>

- [64] C. Edouard, " Vieillissement des batteries Li-ion de traction : des mécanismes vers le vieillissement accéléré," 2015 [Online]. Available: <http://www.theses.fr/2015COMP2221>
- [65] E. Peled, "The Electrochemical Behavior of Alkali and Alkaline Earth Metals in Nonaqueous Battery Systems—The Solid Electrolyte Interphase Model," *Journal of The Electrochemical Society*, vol. 126, no. 12, pp. 2047–2051, Dec. 1979 [Online]. Available: <https://doi.org/10.1149%2F1.2128859>
- [66] R. Deshpande and D. Bernardi, "Modeling Solid-Electrolyte Interphase (SEI) Fracture: Coupled Mechanical/Chemical Degradation of the Lithium Ion Battery," *Journal of The Electrochemical Society*, vol. 164, pp. A461–A474, 2017.
- [67] C. Lin, A. Tang, H. Mu, W. Wang, and C. Wang, "Aging Mechanisms of Electrode Materials in Lithium-Ion Batteries for Electric Vehicles," *Journal of Chemistry*, vol. 2015, p. 104673, Jun. 2015 [Online]. Available: <https://doi.org/10.1155/2015/104673>
- [68] T. Waldmann, B.-I. Hogg, M. Kasper, S. Grolleau, C. Gutierrez, K. Trad, B. Matadi, and M. Wohlfahrt-Mehrens, "Interplay of Operational Parameters on Lithium Deposition in Lithium-Ion Cells: Systematic Measurements with Reconstructed 3-Electrode Pouch Full Cells," *Journal of The Electrochemical Society*, vol. 163, pp. A1232–A1238, 2016.
- [69] F. Ringbeck, C. Rahe, G. Fuchs, and D. U. Sauer, "Identification of Lithium Plating in Lithium-Ion Batteries by Electrical and Optical Methods," *Journal of The Electrochemical Society*, vol. 167, no. 9, p. 090536, May 2020 [Online]. Available: <https://doi.org/10.1149/1945-7111/ab8f5a>
- [70] S. P. Rangarajan, Y. Barsukov, and P. P. Mukherjee, "Anode potential controlled charging prevents lithium plating," *J. Mater. Chem. A*, vol. 8, no. 26, pp. 13077–13085, 2020 [Online]. Available: <http://dx.doi.org/10.1039/DoTA04467A>
- [71] K. Persson, V. A. Sethuraman, L. J. Hardwick, Y. Hinuma, Y. S. Meng, A. van der Ven, V. Srinivasan, R. Kostecki, and G. Ceder, "Lithium Diffusion in Graphitic Carbon," *The Journal of Physical Chemistry Letters*, vol. 1, no. 8, pp. 1176–1180, 2010 [Online]. Available: <https://doi.org/10.1021/jz100188d>
- [72] K. Persson, Y. Hinuma, Y. S. Meng, A. Van der Ven, and G. Ceder, "Thermodynamic and kinetic properties of the Li-graphite system from first-principles calculations," *Phys. Rev. B*, vol. 82, no. 12, p. 125416, Sep. 2010 [Online]. Available: <https://link.aps.org/doi/10.1103/PhysRevB.82.125416>
- [73] X.-B. Cheng, R. Zhang, C.-Z. Zhao, F. Wei, J.-G. Zhang, and Q. Zhang, "A Review of Solid Electrolyte Interphases on Lithium Metal Anode," *Advanced Science*, vol. 3, no. 3, p. 1500213, 2016.
- [74] A. Manthiram, "A reflection on lithium-ion battery cathode chemistry," *Nature Communications*, vol. 11, 2020.
- [75] R. Jung, M. Metzger, F. Maglia, C. Stinner, and H. A. Gasteiger, "Oxygen Release and Its Effect on the Cycling Stability of LiNixMnyCozO2 (NMC) Cathode Materials for Li-Ion Batteries," *Journal of The Electrochemical Society*, vol. 164, no. 7, p. A1361, May 2017.
- [76] C. Zhan, T. Wu, J. Lu, and K. Amine, "Dissolution, migration, and deposition of transition metal ions in Li-ion batteries exemplified by Mn-based cathodes – a critical review," *Energy Environ. Sci.*, vol. 11, no. 2, pp. 243–257, 2018.

- [77] Y. Xia, Y. Zhou, and M. Yoshio, "Capacity Fading on Cycling of 4 V Li / LiMn₂O₄ Cells," *Journal of The Electrochemical Society*, vol. 144, no. 8, p. 2593, Aug. 1997.
- [78] X. Li, A. M. Colclasure, D. P. Finegan, D. Ren, Y. Shi, X. Feng, L. Cao, Y. Yang, and K. Smith, "Degradation mechanisms of high capacity 18650 cells containing Si-graphite anode and nickel-rich NMC cathode," *Electrochimica Acta*, vol. 297, pp. 1109–1120, 2019.
- [79] X.-G. Yang, Y. Leng, G. Zhang, S. Ge, and C.-Y. Wang, "Modeling of lithium plating induced aging of lithium-ion batteries: Transition from linear to nonlinear aging," *Journal of Power Sources*, vol. 360, pp. 28–40, 2017.
- [80] X. Zhao, Y. Yin, Y. Hu, and S.-Y. Choe, "Electrochemical-thermal modeling of lithium plating/stripping of Li(Ni_{0.6}Mn_{0.2}Co_{0.2})O₂/Carbon lithium-ion batteries at subzero ambient temperatures," *Journal of Power Sources*, vol. 418, pp. 61–73, 2019.
- [81] W. Vermeer, G. R. Chandra Mouli, and P. Bauer, "A Comprehensive Review on the Characteristics and Modeling of Lithium-Ion Battery Aging," *IEEE Transactions on Transportation Electrification*, vol. 8, no. 2, pp. 2205–2232, 2022.
- [82] S. Zhang, K. Zhao, T. Zhu, and J. Li, "Electrochemomechanical degradation of high-capacity battery electrode materials," *Progress in Materials Science*, vol. 89, pp. 479–521, 2017.
- [83] M. Ochida, T. Doi, Y. Domi, S. Tsubouchi, H. Nakagawa, T. Yamanaka, T. Abe, and Z. Ogumi, "Effects of Electrolyte Additives on the Suppression of Mn Deposition on Edge Plane Graphite for Lithium-Ion Batteries," *Journal of The Electrochemical Society*, vol. 160, no. 2, p. A410, Jan. 2013.
- [84] C. Delacourt, A. Kwong, X. Liu, R. Qiao, W. L. Yang, P. Lu, S. J. Harris, and V. Srinivasan, "Effect of Manganese Contamination on the Solid-Electrolyte-Interphase Properties in Li-Ion Batteries," *Journal of The Electrochemical Society*, vol. 160, no. 8, p. A1099, May 2013.
- [85] D. Li, H. Li, D. Danilov, L. Gao, J. Zhou, R.-A. Eichel, Y. Yang, and P. H. L. Notten, "Temperature-dependent cycling performance and ageing mechanisms of C₆/LiNi_{1/3}Mn_{1/3}Co_{1/3}O₂ batteries," *Journal of Power Sources*, vol. 396, pp. 444–452, 2018.
- [86] J. M. Reniers, G. Mulder, and D. A. Howey, "Review and Performance Comparison of Mechanical-Chemical Degradation Models for Lithium-Ion Batteries," *Journal of The Electrochemical Society*, vol. 166, no. 14, p. A3189, Sep. 2019.
- [87] W. Nelson, "Chapter 1: Introduction and Background," in *Accelerated Testing: Statistical Models, Test Plans, and Data Analysis*, John Wiley & Sons, 1990, pp. 1–50 [Online]. Available: <https://books.google.co.uk/books?id=AfdQAAAAMAAJ>
- [88] E. Sarasketa-Zabala, E. Martinez-Laserna, M. Bercibar, I. Gandiaga, L. M. Rodriguez-Martinez, and I. Villarreal, "Realistic lifetime prediction approach for Li-ion batteries," *Applied Energy*, vol. 162, pp. 839–852, 2016 [Online]. Available: <http://www.sciencedirect.com/science/article/pii/S0306261915013513>
- [89] M. D. Gennaro, E. Paffumi, G. Martini, A. Giallonardo, S. Pedroso, and A. Loisel-Lapointe, "A case study to predict the capacity fade of the battery of

- electrified vehicles in real-world use conditions,” *Case Studies on Transport Policy*, vol. 8, no. 2, pp. 517–534, 2020.
- [90] *USABC Electric Vehicle Battery Test Procedures Manual Revision 3*. 2015.
- [91] *Battery Test Manual For 48 Volt Mild Hybrid Electric Vehicles Rev 0*. 2017.
- [92] T. Gewalt, M. Lienkamp, D. Lehmkuhl, and A. Hahn, “Accelerated aging characterization of lithium-ion cells: Limitation of arrhenius dependency,” in *2019 14th International Conference on Ecological Vehicles and Renewable Energies, EVER 2019*, 2019.
- [93] I. Baghdadi, O. Briat, J.-Y. Delétage, P. Gyan, and J.-M. Vinassa, “Lithium battery aging model based on Dakin’s degradation approach,” *Journal of Power Sources*, vol. 325, pp. 273–285, 2016 [Online]. Available: <http://www.sciencedirect.com/science/article/pii/S0378775316307388>
- [94] M. Broussely, S. Herreyre, P. Biensan, P. Kasztejna, K. Nechev, and R. . Staniewicz, “Aging mechanism in Li ion cells and calendar life predictions,” *Journal of Power Sources*, vol. 97–98, pp. 13–21, 2001 [Online]. Available: <http://www.sciencedirect.com/science/article/pii/S0378775301007224>
- [95] J. Wang, J. Purewal, P. Liu, J. Hicks-Garner, S. Soukazian, E. Sherman, A. Sorenson, L. Vu, H. Tataria, and M. W. Verbrugge, “Degradation of lithium ion batteries employing graphite negatives and nickel–cobalt–manganese oxide + spinel manganese oxide positives: Part 1, aging mechanisms and life estimation,” *Journal of Power Sources*, vol. 269, pp. 937–948, 2014 [Online]. Available: <http://www.sciencedirect.com/science/article/pii/S037877531401074X>
- [96] S. Grolleau, “Veilleissement calendaire des accumulateurs Lithium-ion Modelisation et analyses,” Université de Caen Basse-Normandie, 2013.
- [97] W. Diao, Y. Xing, S. Saxena, and M. Pecht, “Evaluation of Present Accelerated Temperature Testing and Modeling of Batteries,” *Applied Sciences*, vol. 8, p. 1786, 2018.
- [98] D.-I. Stroe, M. Swierczynski, S. K. Kær, and R. Teodorescu, “Degradation Behavior of Lithium-Ion Batteries During Calendar Ageing—The Case of the Internal Resistance Increase,” *IEEE Transactions on Industry Applications*, vol. 54, no. 1, pp. 517–525, 2018.
- [99] C. M. Snyder, “The effects of c-rate on Li ion degradation.,” 2016 [Online]. Available: <https://www.osti.gov/biblio/1397110>
- [100] J. Wang, P. Liu, J. Hicks-Garner, E. Sherman, S. Soukiajian, M. Verbrugge, H. Tataria, J. Musser, and P. Finamore, “Cycle-life model for graphite-LiFePO₄ cells,” *Journal of Power Sources*, vol. 196, no. 8, pp. 3942–3948, 2011 [Online]. Available: <https://www.sciencedirect.com/science/article/pii/S0378775310021269>
- [101] M. Petit, E. Prada, and V. Sauviant-Moynot, “Development of an empirical aging model for Li-ion batteries and application to assess the impact of Vehicle-to-Grid strategies on battery lifetime,” *Applied Energy*, vol. 172, pp. 398–407, 2016 [Online]. Available: <https://www.sciencedirect.com/science/article/pii/S0306261916304500>
- [102] J. de Hoog, J.-M. Timmermans, D. Ioan-Stroe, M. Swierczynski, J. Jaguemont, S. Goutam, N. Omar, J. V. Mierlo, and P. V. D. Bossche, “Combined cycling and calendar capacity fade modeling of a Nickel-Manganese-Cobalt Oxide Cell with real-life profile validation,” *Applied*

- Energy*, vol. 200, pp. 47–61, 2017 [Online]. Available: <http://www.sciencedirect.com/science/article/pii/S0306261917305251>
- [103] J. Schmalstieg, S. Käbitz, M. Ecker, and D. U. Sauer, “A holistic aging model for Li(NiMnCo)O₂ based 18650 lithium-ion batteries,” *Journal of Power Sources*, vol. 257, pp. 325–334, 2014 [Online]. Available: <http://www.sciencedirect.com/science/article/pii/S0378775314001876>
- [104] F. Herb, “Aging mechanisms in lithium-ion batteries and PEM fuel cells and their influence on the properties of hybrid systems made thereof,” University of Ulm, Germany, 2010 [Online]. Available: <https://www.osti.gov/etdeweb/biblio/21478490>
- [105] B. Carlsson, “Chapter 4.2 - Initial Risk Analysis of Potential Failure Modes,” in *Performance and Durability Assessment*, M. Köhl, B. Carlsson, G. Jorgensen, and A. W. Czanderna, Eds. Amsterdam: Elsevier, 2004, pp. 147–157 [Online]. Available: 4
- [106] Voltaiq, “Myths and Realities in Battery Engineering for EVs,” 2020.
- [107] L. De Sutter, G. Berckmans, M. Marinaro, J. Smekens, Y. Firouz, M. Wohlfahrt-Mehrens, J. Van Mierlo, and N. Omar, “Comprehensive Aging Analysis of Volumetric Constrained Lithium-Ion Pouch Cells with High Concentration Silicon-Alloy Anodes,” *Energies*, vol. 11, 2018.
- [108] A. Barré, F. Suard, M. Gérard, M. Montaru, and D. Riu, “Statistical analysis for understanding and predicting battery degradations in real-life electric vehicle use,” *Journal of Power Sources*, vol. 245, pp. 846–856, 2014.
- [109] Y. Zhang, R. Xiong, H. He, X. Qu, and M. Pecht, “State of charge-dependent aging mechanisms in graphite/Li(NiCoAl)O₂ cells: Capacity loss modeling and remaining useful life prediction,” *Applied Energy*, vol. 255, p. 113818, 2019.
- [110] C. Chen and M. Pecht, “Prognostics of lithium-ion batteries using model-based and data-driven methods,” in *Proceedings of the IEEE 2012 Prognostics and System Health Management Conference (PHM-2012 Beijing)*, 2012, pp. 1–6.
- [111] G. Suri and S. Onori, “A control-oriented cycle-life model for hybrid electric vehicle lithium-ion batteries,” *Energy*, vol. 96, pp. 644–653, 2016.
- [112] M. Einhorn, V. F. Conte, C. Kral, J. Fleig, and R. Permann, “Parameterization of an electrical battery model for dynamic system simulation in electric vehicles,” in *2010 IEEE Vehicle Power and Propulsion Conference*, 2010, pp. 1–7.
- [113] C. Delacourt and M. Safari, “Mathematical Modeling of Aging of Li-Ion Batteries,” in *Physical Multiscale Modeling and Numerical Simulation of Electrochemical Devices for Energy Conversion and Storage: From Theory to Engineering to Practice*, A. A. Franco, M. L. Doublet, and W. G. Bessler, Eds. London: Springer London, 2016, pp. 151–190 [Online]. Available: https://doi.org/10.1007/978-1-4471-5677-2_5
- [114] N. Dufour, M. Chandesris, S. Geniès, M. Cugnet, and Y. Bultel, “Lithiation heterogeneities of graphite according to C-rate and mass-loading: A model study,” *Electrochimica Acta*, vol. 272, pp. 97–107, 2018.
- [115] E. Redondo Iglesias, “Study of lithium-ion batteries ageing in electric vehicle applications: calendar and cycling ageing combination effects,” Université

- de Lyon, 2017 [Online]. Available: <https://tel.archives-ouvertes.fr/tel-01668529>
- [116] Y. Chen, Y. He, Z. Li, and L. Chen, "A combined multiple factor degradation model and online verification for electric vehicle batteries," *Energies*, vol. 12, no. 22, 2019 [Online]. Available: <https://www.scopus.com/inward/record.uri?eid=2-s2.0-85075986516&doi=10.3390%2fen12224376&partnerID=40&md5=5e03bd69cd86e2f1e06e3891e7128b58>
- [117] J. Purewal, J. Wang, J. Graetz, S. Soukiazian, H. Tataria, and M. W. Verbrugge, "Degradation of lithium ion batteries employing graphite negatives and nickel-cobalt-manganese oxide + spinel manganese oxide positives: Part 2, chemical-mechanical degradation model," *Journal of Power Sources*, vol. 272, pp. 1154-1161, 2014 [Online]. Available: <http://www.sciencedirect.com/science/article/pii/S0378775314010726>
- [118] E. Sarasketa-Zabala, I. Laresgoiti, I. Alava, M. Rivas, I. Villarreal, and F. Blanco, "Validation of the methodology for lithium-ion batteries lifetime prognosis," in *2013 World Electric Vehicle Symposium and Exhibition (EVS27)*, 2013, pp. 1-12.
- [119] P. Cygan and J. R. Laghari, "Models for insulation aging under electrical and thermal multistress," *IEEE Transactions on Electrical Insulation*, vol. 25, no. 5, pp. 923-934, 1990.
- [120] N. Dufour, "Modélisation multi-physique de l'électrode de graphite au sein d'une batterie lithium-ion : Etude des hétérogénéités et des mécanismes de vieillissement," Université Grenoble Alpes, 2019 [Online]. Available: <https://tel.archives-ouvertes.fr/tel-02148211>
- [121] M. Doyle, T. F. Fuller, and J. Newman, "Modeling of Galvanostatic Charge and Discharge of the Lithium/Polymer/Insertion Cell," *Journal of The Electrochemical Society*, vol. 140, no. 6, pp. 1526-1533, Jun. 1993.
- [122] J. Li, K. Adewuyi, N. Lotfi, R. G. Landers, and J. Park, "A single particle model with chemical/mechanical degradation physics for lithium ion battery State of Health (SOH) estimation," *Applied Energy*, vol. 212, pp. 1178-1190, 2018.
- [123] S. Carelli and W. G. Bessler, "Prediction of Reversible Lithium Plating with a Pseudo-3D Lithium-Ion Battery Model," *Journal of The Electrochemical Society*, vol. 167, no. 10, p. 100515, Jun. 2020.
- [124] Q. Badey, "Study of mechanisms and modeling of lithium-ion battery ageing for an automotive usage," Université Paris Sud - Paris XI, 2012 [Online]. Available: <https://tel.archives-ouvertes.fr/tel-00693344>
- [125] J. J. Kauzlarich, "The Palmgren-Miner rule derived," in *Tribological Design of Machine Elements*, vol. 14, D. Dowson, C. Taylor, M. Godet, and D. Berthe, Eds. Elsevier, 1989, pp. 175-179.
- [126] J. de Hoog, J.-M. Timmermans, D. Ioan-Stroe, M. Swierczynski, J. Jaguemont, S. Goutam, N. Omar, J. [Van Mierlo], and P. [Van D. Bossche], "Combined cycling and calendar capacity fade modeling of a Nickel-Manganese-Cobalt Oxide Cell with real-life profile validation," *Applied Energy*, vol. 200, pp. 47-61, 2017.
- [127] A. Cordoba-Arenas, S. Onori, Y. Guezennec, and G. Rizzoni, "Capacity and power fade cycle-life model for plug-in hybrid electric vehicle lithium-ion

- battery cells containing blended spinel and layered-oxide positive electrodes,” *Journal of Power Sources*, vol. 278, pp. 473–483, 2015.
- [128] B. Epding, B. Rumberg, H. Jahnke, I. Stradtman, and A. Kwade, “Investigation of significant capacity recovery effects due to long rest periods during high current cyclic aging tests in automotive lithium ion cells and their influence on lifetime,” *Journal of Energy Storage*, vol. 22, pp. 249–256, 2019.
- [129] E. Redondo-Iglesias, P. Venet, and S. Pelissier, “Calendar and cycling ageing combination of batteries in electric vehicles,” *Microelectronics Reliability*, vol. 88–90, pp. 1212–1215, 2018.
- [130] P. Ohlund, *Input for EVE concerning durability requirements on electrified vehicles - WLTP-SG-EV-18-05 Vehicle durability*. UNECE - EVE Group, 2017 [Online]. Available: <https://wiki.unece.org/display/trans/18th+Meeting+of+WLTP+Sub+Group+EV>
- [131] B. Carlsson, “Chapter 4.1 - General Methodology,” in *Performance and Durability Assessment*, M. Köhl, B. Carlsson, G. Jorgensen, and A. W. Czanderna, Eds. Amsterdam: Elsevier, 2004, pp. 141–145.
- [132] S. Mathew, M. Alam, and M. Pecht, “Identification of Failure Mechanisms to Enhance Prognostic Outcomes,” *Journal of Failure Analysis and Prevention*, vol. 12, no. 1, pp. 66–73, 2012.
- [133] C. Hendricks, N. Williard, S. Mathew, and M. Pecht, “A failure modes, mechanisms, and effects analysis (FMMEA) of lithium-ion batteries,” *Journal of Power Sources*, vol. 297, pp. 113–120, 2015 [Online]. Available: <https://www.sciencedirect.com/science/article/pii/S0378775315301233>
- [134] R. Li, J. Wu, H. Wang, J. Guo, and G. Li, “Reliability assessment and failure analysis of lithium iron phosphate batteries,” *Information Sciences*, vol. 259, pp. 359–368, 2014 [Online]. Available: <https://www.sciencedirect.com/science/article/pii/S0020025513004738>
- [135] J. W. A. Catton, S. B. Walker, P. McInnis, M. Fowler, R. A. Fraser, S. B. Young, and B. Gaffney, “Design and Analysis of the Use of Re-Purposed Electric Vehicle Batteries for Stationary Energy Storage in Canada,” *Batteries*, vol. 5, no. 1, 2019 [Online]. Available: <https://www.mdpi.com/2313-0105/5/1/14>
- [136] Y. Hua, X. Liu, S. Zhou, Y. Huang, H. Ling, and S. Yang, “Toward Sustainable Reuse of Retired Lithium-ion Batteries from Electric Vehicles,” *Resources, Conservation and Recycling*, vol. 168, p. 105249, 2021 [Online]. Available: <https://www.sciencedirect.com/science/article/pii/S0921344920305644>
- [137] A. Rohatgi, “Webplotdigitizer: Version 4.5.” 2021 [Online]. Available: <https://automeris.io/WebPlotDigitizer>
- [138] G. Pasaoglu, D. Fiorello, A. Martino, G. Scarcella, A. Alemanno, A. Zubaryeva, and C. Thiel, “Driving and parking patterns of European car drivers – a mobility survey,” European Commission, European Commission, Publications Office of the European Union, 2012.
- [139] Y. Wang, S. Huang, and D. Infield, “Investigation of the potential for electric vehicles to support the domestic peak load,” in *2014 IEEE International Electric Vehicle Conference, IEVC 2014*, 2014.

-
- [140] M. Haber, O. Raccurt, P. Azais, and S. Genies, "Identification of Li-ion batteries' stress factors during vehicle's service lifetime: Assessment and Analysis," in *Advanced Battery Power Conference*, 2021 [Online]. Available: <https://battery-power.eu/poster2/533/>
- [141] A. Blömeke, A. Hebing, and D. U. Sauer, "Data compression techniques applied to long-term recordings of battery data from electric vehicles," 2021 [Online]. Available: <https://2021.battery-power.eu/poster2/519/>
- [142] J. Schoch, "Battery Life Optimal Operation of Electric Vehicles," *Karlsruher Institut für Technologie (KIT)*, 2018 [Online]. Available: <https://publikationen.bibliothek.kit.edu/1000083119/13974324>
- [143] P. Dost, P. Spichartz, and C. Sourkounis, "Temperature influence on state-of-the-art electric vehicles' consumption based on fleet measurements," in *2015 International Conference on Electrical Systems for Aircraft, Railway, Ship Propulsion and Road Vehicles (ESARS)*, 2015, pp. 1–6.
- [144] A. Donati, P. Dilara, C. Thiel, A. Spadario, D. Gkatzoflias, and I. Drossinos, "Individual mobility: From conventional to electric cars," *European Commission Joint Research Centre*, 2015.
- [145] NAF, "20 popular EVs tested in Norwegian winter conditions." NAF, Mar-2020 [Online]. Available: <https://www.naf.no/elbil/aktuelt/elbiltest/ev-winter-range-test-2020/>
- [146] P. Ashkrof, G. H. de Almeida Correia, and B. van Arem, "Analysis of the effect of charging needs on battery electric vehicle drivers' route choice behaviour: A case study in the Netherlands," *Transportation Research Part D: Transport and Environment*, vol. 78, p. 102206, 2020 [Online]. Available: <http://www.sciencedirect.com/science/article/pii/S1361920919309757>
- [147] L. Mathieu, "Recharge EU: how many charge points will Europe and its Member States need in the 2020s," *Transport & Environment*, 2020 [Online]. Available: <https://www.transportenvironment.org/wp-content/uploads/2021/07/01%202020%20Draft%20TE%20Infrastructure%20Report%20Final.pdf>
- [148] E. Labeye, M. Hugot, C. Brusque, and M. A. Regan, "The electric vehicle: A new driving experience involving specific skills and rules," *Transportation Research Part F: Traffic Psychology and Behaviour*, vol. 37, pp. 27–40, 2016 [Online]. Available: <http://www.sciencedirect.com/science/article/pii/S1369847815001898>
- [149] T. Franke and J. F. Krems, "Understanding charging behaviour of electric vehicle users," *Transportation Research Part F: Traffic Psychology and Behaviour*, vol. 21, pp. 75–89, 2013 [Online]. Available: <https://www.sciencedirect.com/science/article/pii/S1369847813000776>
- [150] C. C. Rolim, G. N. Gonçalves, T. L. Farias, and Ó. Rodrigues, "Impacts of Electric Vehicle Adoption on Driver Behavior and Environmental Performance," *Procedia - Social and Behavioral Sciences*, vol. 54, pp. 706–715, 2012 [Online]. Available: <http://www.sciencedirect.com/science/article/pii/S1877042812042504>
- [151] C. De Cauwer, M. Messagie, S. Heyvaert, T. Coosemans, and J. Van Mierlo, "Electric vehicle use and energy consumption based on real world electric vehicle fleet trip and charge data its impact on existing EV research models," *World Electric Vehicle Journal*, vol. 7, pp. 436–446, 2015.

- [152] MAHLE, “MAHLE Powertrain High Charge Rate 48 V Battery Pack,” MAHLE Powertrain, 2020 [Online]. Available: <https://www.mahle-powertrain.com/media/mahle-powertrain/experience/48v-battery-pack/mpt-48-v-battery.pdf>
- [153] Y. Al-Wreikat, C. Serrano, and J. R. Sodr e, “Effects of ambient temperature and trip characteristics on the energy consumption of an electric vehicle,” *Energy*, vol. 238, p. 122028, 2022 [Online]. Available: <https://www.sciencedirect.com/science/article/pii/S0360544221022763>
- [154] P. Weldon, P. Morrissey, J. Brady, and M. O’Mahony, “An investigation into usage patterns of electric vehicles in Ireland,” *Transportation Research Part D: Transport and Environment*, vol. 43, pp. 207–225, 2016 [Online]. Available: <https://www.sciencedirect.com/science/article/pii/S1361920915002230>
- [155] K. Smith, E. Wood, S. Santhanagopalan, G. Kim, Y. Shi, and A. Pesaran, “Predictive Models of Li-ion Battery Lifetime (Presentation),” 2014 [Online]. Available: <https://www.osti.gov/biblio/1156987>
- [156] E. Wood, J. Neubauer, A. D. Brooker, J. Gonder, and K. A. Smith, “Variability of Battery Wear in Light Duty Plug-In Electric Vehicles Subject to Ambient Temperature, Battery Size, and Consumer Usage: Preprint,” 2012 [Online]. Available: <https://www.nrel.gov/docs/fy12osti/53953.pdf>
- [157] J. Taggart, “Ambient temperature impacts on real-world electric vehicle efficiency range,” in *2017 IEEE Transportation Electrification Conference and Expo (ITEC)*, 2017, pp. 186–190.
- [158] M. Klippenstein, “Nissan Leaf, Chevy Volt Range Loss In Winter: New Data From Canada.” Dec-2013 [Online]. Available: https://www.greencarreports.com/news/1089160_nissan-leaf-chevy-volt-range-loss-in-winter-new-data-from-canada
- [159] AAA, “AAA ELECTRIC VEHICLE RANGE TESTING,” American Automobile Association, Inc, 2019 [Online]. Available: <https://www.aaa.com/AAA/common/AAR/files/AAA-Electric-Vehicle-Range-Testing-Report.pdf>
- [160] ABRP, “Tesla Model 3 Performance vs RWD consumption - Real Driving Data from 233 Cars.” ABetterRoutePlanner, 2018 [Online]. Available: <https://forum.abetterrouteplanner.com/blogs/entry/22-tesla-model-3-performance-vs-rwd-consumption-real-driving-data-from-233-cars/>
- [161] C. Morris, “A BETTER ROUTEPLANNER Plots Tesla Range in Relation to Speed And Temperature.” Jul-2018 [Online]. Available: <https://evannex.com/blogs/news/a-better-routeplanner-plots-tesla-range-in-relation-to-speed-and-temperature>
- [162] Z. Jiang, H. Tian, M. J. Beshir, R. Sibagatullin, and A. Mazloomzadeh, “Statistical analysis of Electric Vehicles charging, station usage and impact on the grid,” in *2016 IEEE Power Energy Society Innovative Smart Grid Technologies Conference (ISGT)*, 2016, pp. 1–5.
- [163] FleetCarma, “EV300 Final Report,” Toronto Atmospheric Fund, 2013 [Online]. Available: <http://taf.ca/wp-content/uploads/2015/05/EV300-CrossChasm-report.pdf>

-
- [164] J. G. Smart and S. D. Salisbury, "Plugged In: How Americans Charge Their Electric Vehicles," 2015 [Online]. Available: <https://www.osti.gov/biblio/1369632>
- [165] L. Hu, J. Dong, and Z. Lin, "Modeling charging behavior of battery electric vehicle drivers: A cumulative prospect theory based approach," *Transportation Research Part C-emerging Technologies*, vol. 102, pp. 474–489, 2019.
- [166] J. Smart and S. Schey, "Battery Electric Vehicle Driving and Charging Behavior Observed Early in The EV Project," *SAE International Journal of Alternative Powertrains*, vol. 1, 2012.
- [167] S. Zoepf, D. MacKenzie, D. Keith, and W. Chernicoff, "Charging choices and fuel displacement in a large-scale demonstration of plug-in hybrid electric vehicles," *Transportation Research Record: Journal of the Transportation Research Board*, pp. 1–10, 2013 [Online]. Available: [http://web.mit.edu/sloan-auto-lab/research/beforeh2/files/Zoepf et al TRR 2385.pdf](http://web.mit.edu/sloan-auto-lab/research/beforeh2/files/Zoepf_et_al_TRR_2385.pdf)
- [168] X. Hao, H. Wang, Z. Lin, and M. Ouyang, "Seasonal effects on electric vehicle energy consumption and driving range: A case study on personal, taxi, and ridesharing vehicles," *Journal of Cleaner Production*, vol. 249, p. 119403, 2020 [Online]. Available: <http://www.sciencedirect.com/science/article/pii/S0959652619342738>
- [169] Y. Zou, S. Wei, F. Sun, X. Hu, and Y. Shiao, "Large-scale deployment of electric taxis in Beijing: A real-world analysis," *Energy*, vol. 100, pp. 25–39, 2016 [Online]. Available: <https://www.sciencedirect.com/science/article/pii/S036054421600092X>
- [170] Y. Yang, Z. Tan, and Y. Ren, "Research on Factors That Influence the Fast Charging Behavior of Private Battery Electric Vehicles," *Sustainability*, vol. 12, no. 8, 2020 [Online]. Available: <https://www.mdpi.com/2071-1050/12/8/3439>
- [171] X.-H. Sun, T. Yamamoto, and T. Morikawa, "Charge timing choice behavior of battery electric vehicle users," *Transportation Research Part D: Transport and Environment*, vol. 37, pp. 97–107, 2015 [Online]. Available: <http://www.sciencedirect.com/science/article/pii/S1361920915000395>
- [172] M. S. Islam, J. Sardi, and M. Nadarajah, "Distribution grid impact of large number of EV charging with improved characterization," *2017 Australasian Universities Power Engineering Conference (AUPEC)*, pp. 1–6, 2017 [Online]. Available: <https://ieeexplore.ieee.org/document/8282440>
- [173] G. Wager, J. Whale, and T. Braunl, "Driving electric vehicles at highway speeds: The effect of higher driving speeds on energy consumption and driving range for electric vehicles in Australia," *Renewable and Sustainable Energy Reviews*, vol. 63, pp. 158–165, 2016 [Online]. Available: <http://www.sciencedirect.com/science/article/pii/S1364032116301721>
- [174] F. Jabeen, D. Olaru, B. Smith, T. Braunl, and S. Speidel, "Electric vehicle battery charging behaviour: Findings from a driver survey," *Australasian Transport Research Forum, ATRF 2013 - Proceedings*, 2013 [Online]. Available: https://www.australasiantransportresearchforum.org.au/sites/default/files/2013_jabeen_olaru_smith_braunl_speidel.pdf

- [175] M. Stevens, "EV Performance in Canada: Real-World Performance in the Cold," 2015 [Online]. Available: http://emc-mec.ca/wp-content/uploads/TS2_6_EV-PERFORMANCE-IN-CANADA-ANALYSIS-FROM-5-MILLION-KMS-IN-38C-TO-+46C.pdf
- [176] C. Argue, "To what degree does temperature impact EV range?" GEOTAB, May-2020 [Online]. Available: <https://www.geotab.com/blog/ev-range/>
- [177] "Understanding micro, mild, full and plug-in hybrid electric vehicles." x-engineer, 2020 [Online]. Available: <https://x-engineer.org/automotive-engineering/vehicle/hybrid/micro-mild-full-hybrid-electric-vehicle/>
- [178] "BMW's iPerformance plug-in hybrid electric vehicle (PHEV) powertrain architecture." x-engineer, 2020 [Online]. Available: <https://x-engineer.org/automotive-engineering/vehicle/hybrid/bmw-iperformance-plug-in-hybrid-electric-vehicle-phev-powertrain-architecture/>
- [179] "Daimler developing new dedicated architecture for battery-electric vehicles; debut at Paris Motor Show in September; 500 km." Green Car Congress, 2016 [Online]. Available: <https://www.greencarcongress.com/2016/06/20160613-daimler4.html>
- [180] F. Chopard, C. Blanchard, C. Huillet, and G. Helder De Campos, "Dynamic Insulating System for Battery," in *32nd Electric Vehicle Symposium (EVS32)*, 2019 [Online]. Available: <https://papers.evs32.org/download.php?f=papers/evs32-2610227.pdf>
- [181] Z. Wang, X. Li, G. Zhang, Y. Lv, J. He, J. Luo, C. Yang, and C. Yang, "Experimental study of a passive thermal management system for three types of battery using copper foam saturated with phase change materials," *RSC Adv.*, vol. 7, no. 44, pp. 27441–27448, 2017 [Online]. Available: <http://dx.doi.org/10.1039/C7RA03963H>
- [182] G. Landucci, V. Cozzani, and M. Birk, "5 - Heat Radiation Effects," in *Domino Effects in the Process Industries*, G. Reniers and V. Cozzani, Eds. Amsterdam: Elsevier, 2013, pp. 70–115 [Online]. Available: <https://www.sciencedirect.com/science/article/pii/B9780444543233000051>
- [183] Á. Lakatos, A. Csík, and I. Csarnovics, "Experimental verification of thermal properties of the aerogel blanket," *Case Studies in Thermal Engineering*, vol. 25, p. 100966, 2021 [Online]. Available: <https://www.sciencedirect.com/science/article/pii/S2214157X21001295>
- [184] MatWeb, "Overview of materials for Silicone Foam." 2022 [Online]. Available: https://www.matweb.com/search/datasheet_print.aspx?matguid=c5a00eo b46c045ce981ac96fe6cea51
- [185] D. S. W. Pau, C. M. Fleischmann, M. J. Spearpoint, and K. Y. Li, "Thermophysical properties of polyurethane foams and their melts," *Fire and Materials*, vol. 38, no. 4, pp. 433–450, 2014 [Online]. Available: <https://onlinelibrary.wiley.com/doi/abs/10.1002/fam.2188>
- [186] H. Yamada, "Contribution of evaporative emissions from gasoline vehicles toward total VOC emissions in Japan," *Science of The Total Environment*, vol. 449, pp. 143–149, 2013 [Online]. Available: <http://www.sciencedirect.com/science/article/pii/S0048969713001009>

-
- [187] K. Scott, J. Simpson, and E. Mcpherson, "Effects of tree cover on parking lot microclimate and vehicle emissions," *J Arboriculture*, vol. 25, 1998.
- [188] C. M. Martini G Grigoratos T, "An experimental study to investigate typical temperature conditions in fuel tanks of European vehicles," *Environmental Science and Pollution Research*, vol. 26, 2019 [Online]. Available: <https://pubmed.ncbi.nlm.nih.gov/31025279/>
- [189] M. Maures, Y. Zhang, C. Martin, J.-Y. Delétage, J.-M. Vinassa, and O. Briat, "Impact of temperature on calendar ageing of Lithium-ion battery using incremental capacity analysis," *Microelectronics Reliability*, vol. 100–101, p. 113364, 2019 [Online]. Available: <https://www.sciencedirect.com/science/article/pii/S0026271419304731>
- [190] J. Rugh, A. Pesaran, and K. Smith, "Electric Vehicle Battery Thermal Issues and Thermal Management Techniques." NREL, 2013 [Online]. Available: <https://www.nrel.gov/docs/fy13osti/52818.pdf>
- [191] A. Pesaran, "Addressing the Impact of Temperature Extremes on Large Format Li-Ion Batteries for Vehicle Applications." NREL, Mar-2013 [Online]. Available: <https://www.nrel.gov/docs/fy13osti/58145.pdf>
- [192] A. Harris and C. A. V. Hughes, "Development of a thermal management control system for electric vehicles," in *Vehicle Thermal Management Systems Conference and Exhibition (VTMS10)*, Woodhead Publishing, 2011, pp. 363–372 [Online]. Available: <http://www.sciencedirect.com/science/article/pii/B9780857091727500324>
- [193] C. Huber and R. Kuhn, "13 - Thermal management of batteries for electric vehicles," in *Advances in Battery Technologies for Electric Vehicles*, B. Scrosati, J. Garche, and W. Tillmetz, Eds. Woodhead Publishing, 2015, pp. 327–358 [Online]. Available: <http://www.sciencedirect.com/science/article/pii/B9781782423775000133>
- [194] Y.-T. Luo, C.-Y. Lang, and B.-E.-S. Luo, "Investigation into heating system of lithium-ion battery pack in low-temperature environment," vol. 44, pp. 100–106, 2016.
- [195] R. Khan, M. Swierczynski, and S. Kær, "Towards an Ultimate Battery Thermal Management System: A Review," *Batteries*, vol. 3, p. 9, 2017.
- [196] E. Henriques, P. Peças, and A. Silva, *Technology and Manufacturing Process Selection: the Product Life Cycle Perspective*. Springer Science & Business Media, 2014.
- [197] A. Pesaran, "Battery Thermal Management in EVs and HEVs: Issues and Solutions," *Battery Man*, vol. 43, 2001.
- [198] M. Akbarzadeh, T. Kalogiannis, J. Jagueмонт, L. Jin, H. Behi, D. Karimi, H. Beheshti, J. V. Mierlo, and M. Berecibar, "A comparative study between air cooling and liquid cooling thermal management systems for a high-energy lithium-ion battery module," *Applied Thermal Engineering*, vol. 198, p. 117503, 2021 [Online]. Available: <https://www.sciencedirect.com/science/article/pii/S1359431121009352>
- [199] X. Hu, Y. Zheng, D. A. Howey, H. Perez, A. Foley, and M. Pecht, "Battery warm-up methodologies at subzero temperatures for automotive applications: Recent advances and perspectives," *Progress in Energy and*

- Combustion Science*, vol. 77, p. 100806, 2020 [Online]. Available: <http://www.sciencedirect.com/science/article/pii/S0360128519301169>
- [200] E. Wood, J. Neubauer, A. D. Brooker, J. Gonder, and K. A. Smith, "Variability of Battery Wear in Light Duty Plug-In Electric Vehicles Subject to Ambient Temperature, Battery Size, and Consumer Usage: Preprint," 2012 [Online]. Available: <https://www.osti.gov/biblio/1050097>
- [201] A. Bizzarri, "Thermal management for batteries in E-mobility applications." Priatherm, 2018 [Online]. Available: <https://fhi.nl/app/uploads/sites/38/2018/06/11.00-Priatherm-Batenburg.pdf>
- [202] W. L. Zhang J Wang F, "Design of electric air-heated box for batteries in electric vehicles," *Journal of Power Sources*, vol. 37, 2013 [Online]. Available: <https://www.semanticscholar.org/paper/Design-of-electric-air-heated-box-for-batteries-in-Li-fang/8aa918a83747affb32d3b41foa8a75957545a8fd>
- [203] Q. Wang, B. Jiang, B. Li, and Y. Yan, "A critical review of thermal management models and solutions of lithium-ion batteries for the development of pure electric vehicles," *Renewable and Sustainable Energy Reviews*, vol. 64, pp. 106–128, 2016 [Online]. Available: <http://www.sciencedirect.com/science/article/pii/S1364032116301435>
- [204] "Mitsubishi to begin offering customers test drives of North American spec i-MiEV in November." Green Car Congress, Oct-2011 [Online]. Available: <https://www.greencarcongress.com/2011/10/imiev-20111010.html>
- [205] K. C. Colwell, "Tested: How Cold Weather Affects EV Range." CAR AND DRIVER, May-2018 [Online]. Available: <https://www.caranddriver.com/features/a20915996/tested-how-cold-weather-affects-ev-range-feature/>
- [206] C. Zhan, T. Wu, J. Lu, and K. Amine, "Dissolution, migration, and deposition of transition metal ions in Li-ion batteries exemplified by Mn-based cathodes – a critical review," *Energy Environ. Sci.*, vol. 11, no. 2, pp. 243–257, 2018.
- [207] K. Chen, Z. Yu, S. Deng, Q. Wu, J. Zou, and X. Zeng, "Evaluation of the low temperature performance of lithium manganese oxide/lithium titanate lithium-ion batteries for start/stop applications," *Journal of Power Sources*, vol. 278, pp. 411–419, 2015 [Online]. Available: <https://www.sciencedirect.com/science/article/pii/S0378775314020795>
- [208] T. Rauhala, K. Jalkanen, T. Romann, E. Lust, N. Omar, and T. Kallio, "Low-temperature aging mechanisms of commercial graphite/LiFePO₄ cells cycled with a simulated electric vehicle load profile—A post-mortem study," *Journal of Energy Storage*, vol. 20, pp. 344–356, 2018 [Online]. Available: <https://www.sciencedirect.com/science/article/pii/S2352152X18303694>
- [209] F. P. McGrogan, S. N. Raja, Y.-M. Chiang, and K. J. V. Vliet, "Electrochemomechanical Fatigue: Decoupling Mechanisms of Fracture-Induced Performance Degradation in LilessubgreaterXless/subgreaterMnlesssubgreater2less/subgreaterOlesssubgreater4less/subgreater," *Journal of The Electrochemical Society*, vol. 165, no. 11, pp. A2458–A2466, 2018 [Online]. Available: <https://doi.org/10.1149/2.0191811jes>

-
- [210] P. Li, Y. Zhao, Y. Shen, and S.-H. Bo, "Fracture behavior in battery materials," *Journal of Physics: Energy*, vol. 2, no. 2, p. 022002, Apr. 2020 [Online]. Available: <https://doi.org/10.1088/2515-7655/ab83e1>
- [211] Y. Motoaki, W. Yi, and S. Salisbury, "Empirical analysis of electric vehicle fast charging under cold temperatures," *Energy Policy*, vol. 122, pp. 162–168, 2018 [Online]. Available: <https://www.sciencedirect.com/science/article/pii/S0301421518304828>
- [212] R. German, P. Delarue, and A. Bouscayrol, "Battery pack self-heating during the charging process," in *2018 IEEE International Conference on Industrial Technology (ICIT)*, 2018, pp. 2049–2054.
- [213] M. Ecker, T. Tran, P. Dechent, S. Käbitz, A. Warnecke, and D. Sauer, "Parameterization of a Physico-Chemical Model of a Lithium-Ion Battery: I. Determination of Parameters," *Journal of the Electrochemical Society*, vol. 162, pp. A1836–A1848, 2015.
- [214] T. Li, X. Yuan, L. Zhang, D. Song, K. Shi, and C. Block, "Degradation Mechanisms and Mitigation Strategies of Nickel-Rich NMC-Based Lithium-Ion Batteries," *Electrochemical Energy Reviews*, vol. 3, pp. 43–80, 2020 [Online]. Available: <https://doi.org/10.1007/s41918-019-00053-3>
- [215] H. Ge, T. Aoki, N. Ikeda, S. Suga, T. Isobe, Z. Li, Y. Tabuchi, and J. Zhang, "Investigating Lithium Plating in Lithium-Ion Batteries at Low Temperatures Using Electrochemical Model with NMR Assisted Parameterization," *Journal of The Electrochemical Society*, vol. 164, pp. A1050–A1060, 2017.
- [216] P. Virtanen, R. Gommers, T. E. Oliphant, M. Haberland, T. Reddy, D. Cournapeau, E. Burovski, P. Peterson, W. Weckesser, J. Bright, S. J. van der Walt, M. Brett, J. Wilson, K. J. Millman, N. Mayorov, A. R. J. Nelson, E. Jones, R. Kern, E. Larson, C. J. Carey, Ihan Polat, Y. Feng, E. W. Moore, J. VanderPlas, D. Laxalde, J. Perktold, R. Cimrman, I. Henriksen, E. A. Quintero, C. R. Harris, A. M. Archibald, A. H. Ribeiro, F. Pedregosa, P. van Mulbregt, and S. 1. . Contributors, "SciPy 1.0: Fundamental Algorithms for Scientific Computing in Python," *Nature Methods*, vol. 17, pp. 261–272, 2020.
- [217] *MODEL S OWNER'S MANUAL*. TESLA, 2021 [Online]. Available: https://www.tesla.com/sites/default/files/model_s_owners_manual_north_america_en_us.pdf
- [218] "Addendum 15: United Nations Global Technical Regulation No. 15," United Nations, ECE/TRANS/180/Add.15/Amend.5, 2019 [Online]. Available: <https://unece.org/transport/documents/2021/01/standards/addendum-15-united-nations-global-technical-regulation-no-15>
- [219] J. GORZELANY, "COMPARING ALL 2019 ELECTRIC VEHICLES." myev.com, 2019 [Online]. Available: <https://www.myev.com/research/buyers-sellers-advice/comparing-all-2019-electric-vehicles>
- [220] F. Badin, F. L. Berr, H. Briki, J. Dabadie, M. Petit, S. Magand, and E. Condemine, "Evaluation of EVs energy consumption influencing factors, driving conditions, auxiliaries use, driver's aggressiveness," in *2013 World Electric Vehicle Symposium and Exhibition (EVS27)*, 2013, pp. 1–12.

- [221] B. Reick, A. Konzept, A. Kaufmann, R. Stetter, and D. Engelmann, "Influence of Charging Losses on Energy Consumption and CO₂ Emissions of Battery-Electric Vehicles," *Vehicles*, vol. 3, no. 4, pp. 736–748, 2021 [Online]. Available: <https://www.mdpi.com/2624-8921/3/4/43>
- [222] Mercedes-Benz, "Classe E Berline 300 de / 300 e - Hybride rechargeable." 2022 [Online]. Available: <https://www.mercedes-benz.fr/passengercars/mercedes-benz-cars/models/e-class/saloon-w213-fl/hybride-rechargeable/legal-loi-lom-wt-price.module.html>
- [223] Volvo-Cars, "XC60 Recharge." Jul-2022 [Online]. Available: <https://www.volvocars.com/fr/cars/xc60-hybrid/>
- [224] Land-Rover, "Range Rover Sport | (PHEV), Electric SUV." 2022 [Online]. Available: <https://www.landroverusa.com/vehicles/phev/phev-vehicles/range-rover-sport.html>
- [225] Volkswagen, "Nouveau Touareg R." [Online]. Available: <https://www.volkswagen.fr/fr/modeles-et-configurateur/touareg-r.html>
- [226] Y. Preger, H. M. Barkholtz, A. Fresquez, D. L. Campbell, B. W. Juba, J. Romàn-Kustas, S. R. Ferreira, and B. Chalamala, "Degradation of Commercial Lithium-Ion Cells as a Function of Chemistry and Cycling Conditions," *Journal of The Electrochemical Society*, vol. 167, no. 12, p. 120532, Sep. 2020 [Online]. Available: <https://iopscience.iop.org/article/10.1149/1945-7111/abae37>
- [227] S. Sun, T. Guan, X. Cheng, P. Zuo, Y. Gao, C. Du, and G. Yin, "Accelerated aging and degradation mechanism of LiFePO₄/graphite batteries cycled at high discharge rates," *RSC Adv.*, vol. 8, no. 45, pp. 25695–25703, 2018 [Online]. Available: <http://dx.doi.org/10.1039/C8RA04074E>
- [228] E. Paffumi, M. D. Gennaro, and G. Martini, "European-wide study on big data for supporting road transport policy," *Case Studies on Transport Policy*, vol. 6, no. 4, pp. 785–802, 2018.
- [229] S. M. Arif, T. T. Lie, B. C. Seet, S. Ayyadi, and K. Jensen, "Review of Electric Vehicle Technologies, Charging Methods, Standards and Optimization Techniques," *Electronics*, vol. 10, no. 16, 2021 [Online]. Available: <https://www.mdpi.com/2079-9292/10/16/1910>
- [230] K. Brodd, "An Overview of Electric Vehicles and Charging Stations." Nov-2020 [Online]. Available: <https://www.advancedenergy.org/2020/11/01/an-overview-of-electric-vehicles-and-charging-stations/>
- [231] C. Lilly, "EV connector types." Apr-2022 [Online]. Available: <https://www.zap-map.com/charge-points/connectors-speeds/>
- [232] A. Brown, A. Schayowitz, and E. White, "Electric Vehicle Charging Infrastructure Trends from the Alternative Fueling Station Locator: Fourth Quarter 2021," NREL, Sep. 2021 [Online]. Available: https://afdc.energy.gov/fuels/electricity_infrastructure_trends.html
- [233] G. Falchetta and M. Noussan, "Electric vehicle charging network in Europe: An accessibility and deployment trends analysis," *Transportation Research Part D: Transport and Environment*, vol. 94, p. 102813, 2021 [Online]. Available: <https://www.sciencedirect.com/science/article/pii/S1361920921001164>

-
- [234] D. Herron, "Range Confidence: Charge Fast, Drive Far, with your Electric Car: Electric vehicle charging scenarios." 2008 [Online]. Available: <https://greentransportation.info/ev-charging/range-confidence/chap3/3-ev-charging-scenarios.html>
- [235] E. W. Wood, C. L. Rames, A. Bedir, N. Crisostomo, and J. Allen, "California Plug-In Electric Vehicle Infrastructure Projections: 2017-2025 - Future Infrastructure Needs for Reaching the State's Zero Emission-Vehicle Deployment Goals," 2018.
- [236] P. Chakraborty, R. Parker, T. Hoque, J. Cruz, L. Du, S. Wang, and S. Bhunia, "Addressing the range anxiety of battery electric vehicles with charging en route," *Scientific Reports*, vol. 12, p. 5588, 2022.
- [237] D. Pevec, J. Babic, A. Carvalho, Y. Ghiassi-Farrokhfal, W. Ketter, and V. Podobnik, "Electric Vehicle Range Anxiety: An Obstacle for the Personal Transportation (R)evolution?," in *2019 4th International Conference on Smart and Sustainable Technologies (SpliTech)*, 2019, pp. 1–8.
- [238] A. Tomaszewska, Z. Chu, X. Feng, S. O'Kane, X. Liu, J. Chen, C. Ji, E. Endler, R. Li, L. Liu, Y. Li, S. Zheng, S. Vetterlein, M. Gao, J. Du, M. Parkes, M. Ouyang, M. Marinescu, G. Offer, and B. Wu, "Lithium-ion battery fast charging: A review," *eTransportation*, vol. 1, p. 100011, 2019 [Online]. Available: <http://www.sciencedirect.com/science/article/pii/S2590116819300116>
- [239] Z. Guo, B. Y. Liaw, X. Qiu, L. Gao, and C. Zhang, "Optimal charging method for lithium ion batteries using a universal voltage protocol accommodating aging," *Journal of Power Sources*, vol. 274, pp. 957–964, 2015 [Online]. Available: <https://www.sciencedirect.com/science/article/pii/S0378775314018047>
- [240] A. Pesaran, "Battery Requirements for Plug-In Hybrid Electric Vehicles – Analysis and Rationale." NREL, Dec-2007 [Online]. Available: <https://www.nrel.gov/transportation/assets/pdfs/42469.pdf>
- [241] V. V. Viswanathan and M. C. Kintner-Meyer, "Repurposing of batteries from electric vehicles," in *Advances in Battery Technologies for Electric Vehicles*, 1st ed., B. Scrosati, J. Garche, and W. Tillmetz, Eds. Woodhead Publishing, 2015.
- [242] P. Keil, S. Schuster, J. Wilhelm, J. Travi, A. Hauser, R. Karl, and A. Jossen, "Calendar Aging of Lithium-Ion Batteries: I. Impact of the Graphite Anode on Capacity Fade," *Journal of The Electrochemical Society*, vol. 163, pp. A1872–A1880, 2016.
- [243] G. Mulder, "Draft White Paper Test methods for improved battery cell understanding," European Community, 2018.
- [244] A. Masias, "Electrochemical Prozac: Relieving Battery Anxiety through Life and Safety Research," in *Frontiers of Engineering: Reports on Leading-Edge Engineering from the 2014 Symposium*, 2015.
- [245] J. Belt, I. Bloom, M. Conte, F. V. Conte, K. Morita, T. Ikeya, and J. Groot, "Ageing Testing Procedures on Lithium Batteries in an International Collaboration Context," *World Electric Vehicle Journal*, vol. 4, 2011.
- [246] D. Zhang, L. D. Couto, R. Drummond, S. Sripad, and V. Viswanathan, "Cell-Level State of Charge Estimation for Battery Packs Under Minimal Sensing," 2021 [Online]. Available: <https://arxiv.org/abs/2109.08332>

- [247] A. Loiselle, S. Pedroso, and M. Christenson, "Impacts of Mileage Accumulation and Charge Rate on EV Range and Energy Usage," *Transport Canada*, 2017 [Online]. Available: <https://wiki.unece.org/download/attachments/35356710/EVE-20-06e.pdf?api=v2>
- [248] D. Marconi, A. Simma, and M. Gindraux, "The Swiss Microcensus 2005: An International Comparison on Travel Behaviour," in *Swiss Transport Research Conference*, 2004.
- [249] J. Smart, W. Powell, and S. Schey, "Extended Range Electric Vehicle Driving and Charging Behavior Observed Early in the EV Project," 2013.
- [250] B. Dalla Chiara, F. Deflorio, M. Pellicelli, L. Castello, and M. Eid, "Perspectives on Electrification for the Automotive Sector: A Critical Review of Average Daily Distances by Light-Duty Vehicles, Required Range, and Economic Outcomes," *Sustainability*, vol. 11, no. 20, 2019 [Online]. Available: <https://www.mdpi.com/2071-1050/11/20/5784>
- [251] "National Household Travel Survey." 2017 [Online]. Available: <https://nhts.ornl.gov/>
- [252] E. Wikner, E. Björklund, J. Fridner, D. Brandell, and T. Thiringer, "How the utilised SOC window in commercial Li-ion pouch cells influence battery ageing," *Journal of Power Sources Advances*, vol. 8, p. 100054, 2021 [Online]. Available: <https://www.sciencedirect.com/science/article/pii/S2666248521000093>
- [253] S. Saxena, D. Roman, V. Robu, D. Flynn, and M. Pecht, "Battery Stress Factor Ranking for Accelerated Degradation Test Planning Using Machine Learning," *Energies*, vol. 14, no. 3, 2021 [Online]. Available: <https://www.mdpi.com/1996-1073/14/3/723>
- [254] T. Waldmann, M. Wilka, M. Kasper, M. Fleischhammer, and M. Wohlfahrt-Mehrens, "Temperature dependent ageing mechanisms in Lithium-ion batteries – A Post-Mortem study," *Journal of Power Sources*, vol. 262, pp. 129–135, 2014 [Online]. Available: <http://www.sciencedirect.com/science/article/pii/S0378775314004352>
- [255] C. Avenel, O. Raccurt, J.-L. Gardette, and S. Therias, "Review of accelerated ageing test modelling and its application to solar mirrors," *Solar Energy Materials and Solar Cells*, vol. 186, pp. 29–41, 2018.
- [256] E. Sarasketa-Zabala, I. Gandiaga, L. M. Rodriguez-Martinez, and I. Villarreal, "Calendar ageing analysis of a LiFePO₄/graphite cell with dynamic model validations: Towards realistic lifetime predictions," *Journal of Power Sources*, vol. 272, pp. 45–57, 2014 [Online]. Available: <http://www.sciencedirect.com/science/article/pii/S0378775314013068>
- [257] E. Wikner and T. Thiringer, "Extending Battery Lifetime by Avoiding High SOC," *Applied Sciences*, vol. 8, no. 10, 2018 [Online]. Available: <https://www.mdpi.com/2076-3417/8/10/1825>
- [258] E. Wikner, E. Björklund, J. Fridner, D. Brandell, and T. Thiringer, "How the utilised SOC window in commercial Li-ion pouch cells influence battery ageing," *Journal of Power Sources Advances*, vol. 8, p. 100054, 2021 [Online]. Available: <https://www.sciencedirect.com/science/article/pii/S2666248521000093>

-
- [259] Y. Gao, J. Jiang, C. Zhang, W. Zhang, Z. Ma, and Y. Jiang, "Lithium-ion battery aging mechanisms and life model under different charging stresses," *Journal of Power Sources*, vol. 356, pp. 103–114, 2017 [Online]. Available: <https://www.sciencedirect.com/science/article/pii/S0378775317305876>
- [260] M. Montaru, S. Fiette, J.-L. Koné, and Y. Bultel, "Calendar ageing model of Li-ion battery combining physics-based and empirical approaches," *Journal of Energy Storage*, vol. 51, p. 104544, 2022 [Online]. Available: <https://www.sciencedirect.com/science/article/pii/S2352152X22005618>
- [261] N. M. Johnson, "19 - Battery technology for CO₂ reduction," in *Alternative Fuels and Advanced Vehicle Technologies for Improved Environmental Performance*, R. Folkson, Ed. Woodhead Publishing, 2014, pp. 582–631 [Online]. Available: <https://www.sciencedirect.com/science/article/pii/B9780857095220500194>
- [262] "USABC electric vehicle Battery Test Procedures Manual. Revision 2," 1996.
- [263] E. Martinez-Laserna, I. Gandiaga, E. Sarasketa-Zabala, J. Badedo, D.-I. Stroe, M. Swierczynski, and A. Goikoetxea, "Battery second life: Hype, hope or reality? A critical review of the state of the art," *Renewable and Sustainable Energy Reviews*, vol. 93, pp. 701–718, 2018 [Online]. Available: <http://www.sciencedirect.com/science/article/pii/S1364032118302491>
- [264] S. Saxena, C. L. Floch, J. MacDonald, and S. Moura, "Quantifying EV battery end-of-life through analysis of travel needs with vehicle powertrain models," *Journal of Power Sources*, vol. 282, pp. 265–276, 2015.
- [265] ThePandasDevelopmentTeam, "pandas-dev/pandas: Pandas." Zenodo, Feb-2020 [Online]. Available: <https://doi.org/10.5281/zenodo.3509134>
- [266] C. R. Harris, K. J. Millman, S. J. van der Walt, R. Gommers, P. Virtanen, D. Cournapeau, E. Wieser, J. Taylor, S. Berg, N. J. Smith, R. Kern, M. Picus, S. Hoyer, M. H. van Kerkwijk, M. Brett, A. Haldane, J. F. del Río, M. Wiebe, P. Peterson, P. Gérard-Marchant, K. Sheppard, T. Reddy, W. Weckesser, H. Abbasi, C. Gohlke, and T. E. Oliphant, "Array programming with NumPy," *Nature*, vol. 585, no. 7825, pp. 357–362, Sep. 2020 [Online]. Available: <https://doi.org/10.1038/s41586-020-2649-2>
- [267] J. D. Hunter, "Matplotlib: A 2D graphics environment," *Computing in Science & Engineering*, vol. 9, no. 3, pp. 90–95, 2007.
- [268] M. L. Waskom, "seaborn: statistical data visualization," *Journal of Open Source Software*, vol. 6, no. 60, p. 3021, 2021.
- [269] PlotlyTechnologiesInc., "Collaborative data science." Plotly Technologies Inc., Montreal, QC, 2015 [Online]. Available: <https://www.plotly.com>
- [270] M. Coudiène and D. Levy, "De plus en plus de personnes travaillent en dehors de leur commune de résidence," INSEE, 2016.
- [271] C. Pan, W. Dai, L. Chen, L. Chen, and L. Wang, "Driving range estimation for electric vehicles based on driving condition identification and forecast," *AIP Advances*, vol. 7, no. 10, p. 105206, 2017.
- [272] L. Noel, G. Z. de Rubens, B. K. Sovacool, and J. Kester, "Fear and loathing of electric vehicles: The reactionary rhetoric of range anxiety," *Energy Research & Social Science*, vol. 48, pp. 96–107, 2019.

- [273] M. Haber and O. Raccurt, “Procédé d’étalonnage d’un modèle d’estimation du vieillissement d’accumulateurs électrochimiques,” deposit number : FR2111401, 2021.
- [274] S. SDI, “Prismatic Lithium ion battery cells.” 2022 [Online]. Available: <https://www.samsungsdi.com/automotive-battery/products/prismatic-lithium-ion-battery-cell.html>
- [275] C. Beckx, S. Broekx, B. Degraeuwe, B. Beusen, and L. I. Panis, “Limits to active transport substitution of short car trips,” *Transportation Research Part D: Transport and Environment*, vol. 22, pp. 10–13, 2013.
- [276] R. L. Mackett, “Why do people use their cars for short trips?,” *Transportation*, vol. 30, no. 3, pp. 329–349, 2003.
- [277] J. Belt, “Battery Test Manual For Plug-In Hybrid Electric Vehicles,” 2010.
- [278] J. P. Christophersen, “U.S. Department of Energy Vehicle Technologies Program: Battery Test Manual For Plug-In Hybrid Electric Vehicles,” 2014.
- [279] Z. Li, J. Huang, B. Y. Liaw, and J. Zhang, “On state-of-charge determination for lithium-ion batteries,” *Journal of Power Sources*, vol. 348, pp. 281–301, 2017.
- [280] M. Dubarry, V. Svoboda, R. Hwu, and B. Y. Liaw, “Capacity loss in rechargeable lithium cells during cycle life testing: The importance of determining state-of-charge,” *Journal of Power Sources*, vol. 174, no. 2, pp. 1121–1125, 2007.
- [281] C. Truchot, M. Dubarry, and B. Y. Liaw, “State-of-charge estimation and uncertainty for lithium-ion battery strings,” *Applied Energy*, vol. 119, pp. 218–227, 2014.
- [282] J. P. Christophersen, “Battery Test Manual For Electric Vehicles, Revision 3,” 2015.
- [283] W. Diao, J. Jiang, C. Zhang, H. Liang, and M. Pecht, “Energy state of health estimation for battery packs based on the degradation and inconsistency,” *Energy Procedia*, vol. 142, pp. 3578–3583, 2017.
- [284] T. R. Board, *Tires and Passenger Vehicle Fuel Economy: Informing Consumers, Improving Performance – Special Report 286*. Washington, DC: The National Academies Press, 2006.
- [285] O. A. Hjelkrem, P. Arnesen, T. A. Bø, and R. S. Sondell, “Estimation of tank-to-wheel efficiency functions based on type approval data,” *Applied Energy*, vol. 276, p. 115463, 2020.
- [286] A. G. Stefanopoulou and Y. Kim, “10 - System-level management of rechargeable lithium-ion batteries,” in *Rechargeable Lithium Batteries*, A. A. Franco, Ed. Woodhead Publishing, 2015, pp. 281–302.
- [287] M. Dubarry and G. Baure, “Perspective on Commercial Li-ion Battery Testing, Best Practices for Simple and Effective Protocols,” *Electronics*, vol. 9, no. 1, 2020.
- [288] PennState, “STAT 200 3.2 Identifying Outliers: IQR Method.” [Online]. Available: <https://online.stat.psu.edu/stat200/lesson/3/3.2#:text=To%20build%20this%20fence%20we,above%20Q3%20are%20considered%20outliers>.
- [289] P. K. Dunn, *Scientific Research Methods: Software manual*. Bookdown, 2019 [Online]. Available: <https://bookdown.org/pkaldunn/SRM-software/>

-
- [290] NIST, "What are outliers in the data?" [Online]. Available: <https://www.itl.nist.gov/div898/handbook/prc/section1/prc16.htm>
- [291] M. Lewerenz, A. Marongiu, A. Warnecke, and D. U. Sauer, "Differential voltage analysis as a tool for analyzing inhomogeneous aging: A case study for LiFePO₄|Graphite cylindrical cells," *Journal of Power Sources*, vol. 368, pp. 57–67, 2017.
- [292] M. Lewerenz, J. Münnix, J. Schmalstieg, S. Käbitz, M. Knips, and D. U. Sauer, "Systematic aging of commercial LiFePO₄|Graphite cylindrical cells including a theory explaining rise of capacity during aging," *Journal of Power Sources*, vol. 345, pp. 254–263, 2017.
- [293] B. Gyenes, D. A. Stevens, V. L. Chevrier, and J. R. Dahn, "Understanding Anomalous Behavior in Coulombic Efficiency Measurements on Li-Ion Batteries," *Journal of The Electrochemical Society*, vol. 162, no. 3, pp. A278–A283, Dec. 2014.
- [294] M. Klett, R. Eriksson, J. Groot, P. Svens, K. C. Högstöm, R. W. Lindström, H. Berg, T. Gustafson, G. Lindbergh, and K. Edström, "Non-uniform aging of cycled commercial LiFePO₄//graphite cylindrical cells revealed by post-mortem analysis," *Journal of Power Sources*, vol. 257, pp. 126–137, 2014.
- [295] J. Cannarella and C. B. Arnold, "Stress evolution and capacity fade in constrained lithium-ion pouch cells," *Journal of Power Sources*, vol. 245, pp. 745–751, 2014.
- [296] S. Lv, X. Wang, W. Lu, J. Zhang, and H. Ni, "The Influence of Temperature on the Capacity of Lithium Ion Batteries with Different Anodes," *Energies*, vol. 15, no. 1, 2022.
- [297] X. Han, M. Ouyang, L. Lu, J. Li, Y. Zheng, and Z. Li, "A comparative study of commercial lithium ion battery cycle life in electrical vehicle: Aging mechanism identification," *Journal of Power Sources*, vol. 251, pp. 38–54, 2014.
- [298] S. Zheng, C. Hong, X. Guan, Y. Xiang, X. Liu, G.-L. Xu, R. Liu, G. Zhong, F. Zheng, Y. Li, X. Zhang, Y. Ren, Z. Chen, K. Amine, and Y. Yang, "Correlation between long range and local structural changes in Ni-rich layered materials during charge and discharge process," *Journal of Power Sources*, vol. 412, pp. 336–343, 2019.
- [299] E. Sarasketa-Zabala, I. Gandiaga, E. Martinez-Laserna, L. M. Rodriguez-Martinez, and I. Villarreal, "Cycle ageing analysis of a LiFePO₄/graphite cell with dynamic model validations: Towards realistic lifetime predictions," *Journal of Power Sources*, vol. 275, pp. 573–587, 2015.
- [300] M. Dubarry, M. Bercibar, A. Devie, D. Anseán, N. Omar, and I. Villarreal, "State of health battery estimator enabling degradation diagnosis: Model and algorithm description," *Journal of Power Sources*, vol. 360, pp. 59–69, 2017.
- [301] M. Bercibar, F. Devriendt, M. Dubarry, I. Villarreal, N. Omar, W. Verbeke, and J. V. Mierlo, "Online state of health estimation on NMC cells based on predictive analytics," *Journal of Power Sources*, vol. 320, pp. 239–250, 2016.
- [302] B. Stiaszny, J. C. Ziegler, E. E. Krauß, J. P. Schmidt, and E. Ivers-Tiffée, "Electrochemical characterization and post-mortem analysis of aged LiMn₂O₄-Li(Ni_{0.5}Mn_{0.3}Co_{0.2})O₂/graphite lithium ion batteries. Part I: Cycle aging," *Journal of Power Sources*, vol. 251, pp. 439–450, 2014.

- [303] R. Jung, M. Metzger, F. Maglia, C. Stinner, and H. A. Gasteiger, "Oxygen Release and Its Effect on the Cycling Stability of LiNi_{0.8}Mn_{0.15}Co_{0.05}O₂ Cathode Materials for Li-Ion Batteries," *Journal of The Electrochemical Society*, vol. 164, no. 7, pp. A1361–A1377, 2017.
- [304] M. D. Radin, S. Hy, M. Sina, C. Fang, H. Liu, J. Vinckeviciute, M. Zhang, M. S. Whittingham, Y. S. Meng, and A. Van der Ven, "Narrowing the Gap between Theoretical and Practical Capacities in Li-Ion Layered Oxide Cathode Materials," *Advanced Energy Materials*, vol. 7, no. 20, p. 1602888, 2017.
- [305] A. Shellikeri, V. Watson, D. Adams, E. E. Kalu, J. A. Read, T. R. Jow, J. S. Zheng, and J. P. Zheng, "Investigation of Pre-lithiation in Graphite and Hard-Carbon Anodes Using Different Lithium Source Structures," *Journal of The Electrochemical Society*, vol. 164, no. 14, pp. A3914–A3924, 2017.
- [306] Q. Liu, S. Li, S. Wang, X. Zhang, S. Zhou, Y. Bai, J. Zheng, and X. Lu, "Kinetically Determined Phase Transition from Stage II (LiC₁₂) to Stage I (LiC₆) in a Graphite Anode for Li-Ion Batteries," *The Journal of Physical Chemistry Letters*, vol. 9, no. 18, pp. 5567–5573, 2018.
- [307] C. Hogrefe, T. Waldmann, M. B. Molinero, L. Wildner, P. Axmann, and M. Wohlfahrt-Mehrens, "Cross-Sectional In Situ Optical Microscopy with Simultaneous Electrochemical Measurements for Lithium-Ion Full Cells," *Journal of The Electrochemical Society*, vol. 169, no. 5, p. 050519, May 2022.
- [308] D. Mohanty, E. Hockaday, J. Li, D. K. Hensley, C. Daniel, and D. L. Wood, "Effect of electrode manufacturing defects on electrochemical performance of lithium-ion batteries: Cognizance of the battery failure sources," *Journal of Power Sources*, vol. 312, pp. 70–79, 2016.
- [309] L. David, R. E. Ruther, D. Mohanty, H. M. Meyer, Y. Sheng, S. Kalnaus, C. Daniel, and D. L. Wood, "Identifying degradation mechanisms in lithium-ion batteries with coating defects at the cathode," *Applied Energy*, vol. 231, pp. 446–455, 2018.
- [310] U. Janakiraman, T. R. Garrick, and M. E. Fortier, "Review—Lithium Plating Detection Methods in Li-Ion Batteries," *Journal of The Electrochemical Society*, vol. 167, no. 16, p. 160552, Dec. 2020.
- [311] M. Broussely, P. Biensan, F. Bonhomme, P. Blanchard, S. Herreyre, K. Nechev, and R. J. Staniewicz, "Main aging mechanisms in Li ion batteries," *Journal of Power Sources*, vol. 146, no. 1, pp. 90–96, 2005.
- [312] Y. Merla, B. Wu, V. Yufit, N. P. Brandon, R. F. Martinez-Botas, and G. J. Offer, "Novel application of differential thermal voltammetry as an in-depth state-of-health diagnosis method for lithium-ion batteries," *Journal of Power Sources*, vol. 307, pp. 308–319, 2016.
- [313] T. Joshi, K. Eom, G. Yushin, and T. F. Fuller, "Effects of Dissolved Transition Metals on the Electrochemical Performance and SEI Growth in Lithium-Ion Batteries," *Journal of The Electrochemical Society*, vol. 161, no. 12, pp. A1915–A1921, 2014.
- [314] J. Park, J. H. Seo, G. Plett, W. Lu, and A. M. Sastry, "Numerical Simulation of the Effect of the Dissolution of LiMn₂O₄ Particles on Li-Ion Battery

- Performance,” *Electrochemical and Solid-State Letters*, vol. 14, no. 2, p. A14, 2011.
- [315] B. Matadi, S. Geniès, A. Delaille, C. Chabrol, E. De Vito, M. Bardet, J.-F. Martin, L. Daniel, and Y. Bultel, “Irreversible Capacity Loss of Li-Ion Batteries Cycled at Low Temperature Due to an Untypical Layer Hindering Li Diffusion into Graphite Electrode,” *Journal of The Electrochemical Society*, vol. 164, pp. A2374–A2389, 2017.
- [316] D. Anseán, M. Dubarry, A. Devie, B. Y. Liaw, V. M. García, J. C. Viera, and M. González, “Operando lithium plating quantification and early detection of a commercial LiFePO₄ cell cycled under dynamic driving schedule,” *Journal of Power Sources*, vol. 356, pp. 36–46, 2017.
- [317] E. E. Petersen, “Diffusion in a pore of varying cross section,” *AIChE Journal*, vol. 4, no. 3, pp. 343–345, 1958 [Online]. Available: <https://aiche.onlinelibrary.wiley.com/doi/abs/10.1002/aic.690040322>
- [318] TESLA, “Charging Connectors.” 2022 [Online]. Available: https://www.tesla.com/en_EU/support/charging-connectors
- [319] F. W. Karasek and R. E. Clement, “Chapter 4 - Gas Chromatography – Mass Spectrometry,” in *Basic Gas Chromatography – Mass Spectrometry*, F. W. Karasek and R. E. Clement, Eds. Amsterdam: Elsevier, 1988, pp. 79–159.
- [320] Y. Chen, G. Xu, X. Liu, Q. Pan, Y. Zhang, D. Zeng, Y. Sun, H. Ke, and H. Cheng, “A gel single ion conducting polymer electrolyte enables durable and safe lithium ion batteries via graft polymerization,” *RSC Adv.*, vol. 8, no. 70, pp. 39967–39975, 2018.
- [321] W. Nelson, “Models for Life Tests with Constant Stress,” in *Accelerated Testing*, John Wiley & Sons, Ltd, 1990, pp. 51–111 [Online]. Available: <https://onlinelibrary.wiley.com/doi/abs/10.1002/9780470316795.ch2>
- [322] T. Xu, C. Zhou, H. Zhou, Z. Wang, and J. Ren, “Synthesis of Alumina-Coated Natural Graphite for Highly Cycling Stability and Safety of Li-Ion Batteries,” *Chinese Journal of Chemistry*, vol. 37, no. 4, pp. 342–346, 2019.
- [323] Y. Tran, C. Täubert, M. Fleischhammer, P. Axmann, L. Küppers, and M. Wohlfahrt-Mehrens, “LiMn₂O₄ Spinel/LiNi_{0.8}Co_{0.15}Al_{0.05}O₂ Blends as Cathode Materials for Lithium-Ion Batteries,” *Journal of The Electrochemical Society*, vol. 158, pp. A556–A561, 2011.
- [324] J. Kasnatscheew, S. Röser, M. Börner, and M. Winter, “Do Increased Ni Contents in LiNixMnyCozO₂ (NMC) Electrodes Decrease Structural and Thermal Stability of Li Ion Batteries? A Thorough Look by Consideration of the Li⁺ Extraction Ratio,” *ACS Applied Energy Materials*, vol. 2, no. 11, pp. 7733–7737, 2019.
- [325] H. Kobayashi, Y. Arachi, S. Emura, H. Kageyama, K. Tatsumi, and T. Kamiyama, “Investigation on lithium de-intercalation mechanism for Li_{1-y}Ni_{1/3}Mn_{1/3}Co_{1/3}O₂,” *Journal of Power Sources*, vol. 146, no. 1, pp. 640–644, 2005.
- [326] B. D. McCloskey, “Attainable Gravimetric and Volumetric Energy Density of Li–S and Li Ion Battery Cells with Solid Separator-Protected Li Metal Anodes,” *The Journal of Physical Chemistry Letters*, vol. 6, no. 22, pp. 4581–4588, 2015.

- [327] Designerdata, “Styrene-butadiene rubber.” [Online]. Available: <https://designerdata.nl/materials/plastics/rubbers/styrene-butadiene-rubber>
- [328] Entegris, “Graphite Properties and Characteristics.” [Online]. Available: <https://poco.entegris.com/>
- [329] MSESUPPLIES, “50g SUPER C65 Nano Carbon Black Conductive Additive for Battery Cathode and Anode.” [Online]. Available: <https://www.msesupplies.com/products/super-c65-carbon-black-conductive-additive-for-lithium-ion-battery-cathode-and-anode-50g?variant=31262541709370>
- [330] Designerdata, “PVDF.” [Online]. Available: <https://designerdata.nl/materials/plastics/thermo-plastics/polyvinylidene-fluoride>
- [331] H. Al-Shammari and S. Farhad, “Performance of Cathodes Fabricated from Mixture of Active Materials Obtained from Recycled Lithium-Ion Batteries,” *Energies*, vol. 15, no. 2, 2022 [Online]. Available: <https://www.mdpi.com/1996-1073/15/2/410>
- [332] C.-H. Chen, F. B. Planella, K. O’Regan, D. Gastol, W. D. Widanage, and E. Kendrick, “Development of Experimental Techniques for Parameterization of Multi-scale Lithium-ion Battery Models,” *Journal of The Electrochemical Society*, vol. 167, no. 8, p. 080534, Jan. 2020.
- [333] J. Landesfeind, J. Hattendorff, A. Ehrl, W. A. Wall, and H. A. Gasteiger, “Tortuosity Determination of Battery Electrodes and Separators by Impedance Spectroscopy,” *Journal of The Electrochemical Society*, vol. 163, no. 7, p. A1373, Apr. 2016.
- [334] N. Ogihara, S. Kawauchi, C. Okuda, Y. Itou, Y. Takeuchi, and Y. Ukyo, “Theoretical and Experimental Analysis of Porous Electrodes for Lithium-Ion Batteries by Electrochemical Impedance Spectroscopy Using a Symmetric Cell,” *Journal of The Electrochemical Society*, vol. 159, no. 7, p. A1034, Jul. 2012.
- [335] F. L. E. Usseglio-Viretta, A. Colclasure, A. N. Mistry, K. P. Y. Claver, F. Pouraghajan, D. P. Finegan, T. M. M. Heenan, D. Abraham, P. P. Mukherjee, D. Wheeler, P. Shearing, S. J. Cooper, and K. Smith, “Resolving the Discrepancy in Tortuosity Factor Estimation for Li-Ion Battery Electrodes through Micro-Macro Modeling and Experiment,” *Journal of The Electrochemical Society*, vol. 165, no. 14, p. A3403, Nov. 2018.
- [336] T.-T. Nguyen, A. Demortière, B. Fleutot, B. Delobel, C. Delacourt, and S. J. Cooper, “The electrode tortuosity factor: why the conventional tortuosity factor is not well suited for quantifying transport in porous Li-ion battery electrodes and what to use instead,” *npj Computational Materials*, vol. 6, no. 1, Aug. 2020 [Online]. Available: <https://hal.archives-ouvertes.fr/hal-03095260>
- [337] J. Landesfeind, M. Ebner, A. Eldiven, V. Wood, and H. A. Gasteiger, “Tortuosity of Battery Electrodes: Validation of Impedance-Derived Values and Critical Comparison with 3D Tomography,” *Journal of The Electrochemical Society*, vol. 165, no. 3, p. A469, Feb. 2018.
- [338] B. Tjaden, S. J. Cooper, D. J. Brett, D. Kramer, and P. R. Shearing, “On the origin and application of the Bruggeman correlation for analysing transport

- phenomena in electrochemical systems,” *Current Opinion in Chemical Engineering*, vol. 12, pp. 44–51, 2016.
- [339] C. J. Wen, B. A. Boukamp, R. A. Huggins, and W. Weppner, “Thermodynamic and Mass Transport Properties of “LiAl,” *Journal of The Electrochemical Society*, vol. 126, no. 12, p. 2258, Dec. 1979.
- [340] A. Nickol, T. Schied, C. Heubner, M. Schneider, A. Michaelis, M. Bobeth, and G. Cuniberti, “GITT Analysis of Lithium Insertion Cathodes for Determining the Lithium Diffusion Coefficient at Low Temperature: Challenges and Pitfalls,” *Journal of The Electrochemical Society*, vol. 167, no. 9, p. 090546, Jun. 2020.
- [341] W. Weppner and R. A. Huggins, “Determination of the Kinetic Parameters of Mixed-Conducting Electrodes and Application to the System Li₃Sb,” *Journal of The Electrochemical Society*, vol. 124, no. 10, p. 1569, Oct. 1977.
- [342] A. A. Wang, S. E. J. O’Kane, F. B. Planella, J. L. Houx, K. O’Regan, M. Zyskin, J. Edge, C. W. Monroe, S. J. Cooper, D. A. Howey, E. Kendrick, and J. M. Foster, “Review of parameterisation and a novel database (LiionDB) for continuum Li-ion battery models,” *Progress in Energy*, vol. 4, no. 3, p. 032004, May 2022.
- [343] M. D. Levi and D. Aurbach, “Diffusion Coefficients of Lithium Ions during Intercalation into Graphite Derived from the Simultaneous Measurements and Modeling of Electrochemical Impedance and Potentiostatic Intermittent Titration Characteristics of Thin Graphite Electrodes,” *The Journal of Physical Chemistry B*, vol. 101, no. 23, pp. 4641–4647, 1997.
- [344] J. Schmalstieg and D. U. Sauer, “Full Cell Parameterization of a High-Power Lithium-Ion Battery for a Physico-Chemical Model: Part II. Thermal Parameters and Validation,” *Journal of The Electrochemical Society*, vol. 165, no. 16, pp. A3811–A3819, 2018 [Online]. Available: <https://doi.org/10.1149/2.0331816jes>
- [345] S.-L. Wu, W. Zhang, X. Song, A. K. Shukla, G. Liu, V. Battaglia, and V. Srinivasan, “High Rate Capability of Li(Ni_{1/3}Mn_{1/3}Co_{1/3})O₂ Electrode for Li-Ion Batteries,” *Journal of The Electrochemical Society*, vol. 159, no. 4, p. A438, Jan. 2012.
- [346] O. Chaouachi, J.-M. Réty, S. Génies, M. Chandesris, and Y. Bultel, “Experimental and theoretical investigation of Li-ion battery active materials properties: Application to a graphite/Ni_{0.6}Mn_{0.2}Co_{0.2}O₂ system,” *Electrochimica Acta*, vol. 366, p. 137428, 2021.
- [347] F. Cadiou, T. Douillard, F. Willot, J.-C. Badot, B. Lestriez, and E. Maire, “Effective Electronic and Ionic Conductivities of Dense EV-Designed NMC-Based Positive Electrodes using Fourier Based Numerical Simulations on FIB/SEM Volumes,” *Journal of The Electrochemical Society*, vol. 167, no. 14, p. 140504, Oct. 2020.
- [348] T. A. Yemata, Q. Ye, H. Zhou, A. K. K. Kyaw, W. S. Chin, and J. Xu, “6 - Conducting polymer-based thermoelectric composites: Principles, processing, and applications,” in *Hybrid Polymer Composite Materials*, V. K. Thakur, M. K. Thakur, and A. Pappu, Eds. Woodhead Publishing, 2017, pp. 169–195 [Online]. Available: <https://www.sciencedirect.com/science/article/pii/B9780081007853000061>

- [349] M. Safari and C. Delacourt, "Simulation-based analysis of aging phenomena in a commercial graphite/LiFePO₄ cell," *Journal of the Electrochemical Society*, vol. 158, no. 12, pp. A1436–A1447, 2011 [Online]. Available: <https://www.scopus.com/inward/record.uri?eid=2-s2.0-81355163921&doi=10.1149%2f2.103112jes&partnerID=40&md5=3fd3ea336f56c7194142c31e1934407c>
- [350] A. Kamal, "Physical modeling of lithium-ion aging for automotive applications," Michigan Technological University, 2018 [Online]. Available: <https://digitalcommons.mtu.edu/etdr/735/>
- [351] S. J. An, J. Li, C. Daniel, D. Mohanty, S. Nagpure, and D. L. Wood, "The state of understanding of the lithium-ion-battery graphite solid electrolyte interphase (SEI) and its relationship to formation cycling," *Carbon*, vol. 105, pp. 52–76, 2016.
- [352] O. Borodin, G. D. Smith, and P. Fan, "Molecular Dynamics Simulations of Lithium Alkyl Carbonates," *The Journal of Physical Chemistry B*, vol. 110, no. 45, pp. 22773–22779, 2006.
- [353] A. J. Smith, J. C. Burns, X. Zhao, D. Xiong, and J. R. Dahn, "A High Precision Coulometry Study of the SEI Growth in Li/Graphite Cells," *Journal of The Electrochemical Society*, vol. 158, no. 5, p. A447, 2011.
- [354] P. Verma, P. Maire, and P. Novák, "A review of the features and analyses of the solid electrolyte interphase in Li-ion batteries," *Electrochimica Acta*, vol. 55, no. 22, pp. 6332–6341, 2010.
- [355] M. Safari and C. Delacourt, "Simulation-Based Analysis of Aging Phenomena in a Commercial Graphite/LiFePO₄ Cell," *Journal of The Electrochemical Society*, vol. 158, no. 12, p. A1436, 2011 [Online]. Available: <https://doi.org/10.1149%2F2.103112jes>
- [356] H. J. Ploehn, P. Ramadass, and R. E. White, "Solvent Diffusion Model for Aging of Lithium-Ion Battery Cells," *Journal of The Electrochemical Society*, vol. 151, no. 3, p. A456, 2004.
- [357] M. Safari, M. Morcrette, A. Teyssot, and C. Delacourt, "Multimodal physics-based aging model for life prediction of Li-Ion batteries," *Journal of the Electrochemical Society*, vol. 156, no. 3, pp. A145–A153, 2009 [Online]. Available: <https://www.scopus.com/inward/record.uri?eid=2-s2.0-59349083200&doi=10.1149%2f1.3043429&partnerID=40&md5=0dc7d93444f3395eb3a8dff613c4ee8>